

Technical Report ECOM C-0423-10

Wind Tunnel Studies and Simulations  
of Turbulent Shear Flows Related to  
Atmospheric Science and Associated Technologies

TECHNICAL REPORT

AN INVESTIGATION OF FLOW OVER HIGH ROUGHNESS

TASK I: STUDY OF AIRFLOW IN  
SIMULATED TEMPERATE AND  
TROPICAL FOREST CANOPIES

FORT HUACHUCA

by

T. KAWATANI\* and W. Z. SADEH\*\*

Fluid Dynamics and Diffusion Laboratory  
Department of Civil Engineering  
Colorado State University  
Fort Collins, Colorado

Prepared jointly for  
U. S. Army Electronics Command  
Contract No. DAAB07-68-C-0423

and

Office of Naval Research  
Contract No. N0014-68-A-0493-0001.

August 1971

CER71-72TK-WZS3

\*Research Assistant. Presently Assistant Professor, Department of  
Civil Engineering, Kobe University, Kobe, JAPAN.

\*\*Associate Professor of Engineering.



U18401 0576134

## ACKNOWLEDGEMENTS

This work was supported by Atmospheric Science Laboratory, U.S. Army Electronic Command (Contract DAAB07-68C-0423) under the supervision of Dr. J. H. Shinn. This support, together with support in preparing this report by project THEMIS under the supervision of Mr. R. D. Cooper (Fluid Dynamics Branch, Office of Naval Research, Contract N00014-A-0393-0001) is gratefully acknowledged.

## ABSTRACT

An experimental investigation of the atmospheric boundary-layer flow on high roughness was conducted by simulating the flow over a forest canopy in a meteorological wind tunnel. The model forest canopy used consisted of plastic simulated-evergreen trees. The measurements were carried out at constant free-stream velocity and under thermally neutral conditions. Two canopy densities were tested to explore the effects of the roughness density on the flow. One roughness density was half of the other.

The results indicate that the mean velocity profiles within the fully developed flow region can be described by generalized logarithmic relationships. For the flow in the inner zone, the free-stream velocity and the roughness height are the similarity parameters for the velocity and the vertical distance, respectively. In the outer zone the free-stream velocity and the momentum thickness are the scaling parameters. The roughness density has a strong influence on the momentum loss and the upward flow displacement in the transition region. The shape of the roughness element affects the mean velocity distribution inside the canopy, i.e., jetting effect.

The internal boundary-layer thickness was determined based on the turbulent shear-stress distribution. It is found that the flow near the canopy leading edge has two-dimensional wake-like characteristics. The latter are due to the canopy frontal area which is a drastic step obstruction.

The existence of an inertial subrange in the fully developed flow region is doubtful although local isotropy occurs for eddies smaller than

2% of the total boundary-layer thickness. The evolution of turbulent energy associated with various size eddies along the canopy can be successfully described by a discretized-energy analysis.

## LIST OF SYMBOLS

$A, A_i, A_o$	Constant
$B, B_i, B_o$	Constant
$B_w$	Filter bandwidth
$C, C_o, C_1, C_2, C_r$	Constant
$c_f$	Local skin friction
$D$	Pipe diameter
$d$	Zero-plane displacement
$E$	Mean voltage
$E_o$	Mean voltage in still air
$E_p$	Rate of turbulent-energy production per unit mass ( $L^2/T^3$ )
$e$	Voltage fluctuation
$e_{45}, e_{135}$	Voltage fluctuations for yaw-angle of $45^\circ$ and $135^\circ$
$e_{\alpha\alpha}$	Turbulent kinetic energy per unit mass in $\alpha$ -direction ( $L^2/T^2$ )
$F(n)$	Frequency density function
$f(n)$	One-dimensional frequency density function
$H$	Shape factor
$h$	Roughness height
$k$	Wave number
$k_d$	Wave number corresponding to lower limit of energy-dissipation range
$k_e$	Wave number corresponding to upper bound of energy-containing range
$k_\ell$	Lower bound of wave number for the existence of local isotropy

$L$	Wavelength (eddy size)
$L_s$	Length scale
$L_u$	Upper limit of the eddy size for the existence of local isotropy
$l$	Mixing length
$M$	Constant
$n$	Frequency, exponent in Eq. (2.1)
$P$	Static pressure
$P_\infty$	Static pressure in the free stream
$p$	Pressure fluctuation
$T_u, T_w$	Turbulent intensity based on local mean velocity in x- and z-directions
$T_{u_\infty}, T_{w_\infty}$	Turbulent intensity based on the free-stream velocity in x- and z-directions
$t$	Time
$U, W$	Local mean velocity in x- and z-directions
$U_e$	Instantaneous effective velocity for hot-wire cooling
$U_s$	Velocity scale
$U_\infty$	Free-stream velocity
$U_*$	Friction velocity
$U_{*h}$	Friction velocity for $d = h$
$\Delta U$	Velocity deviation on rough wall from that on smooth wall
$u, w$	Velocity fluctuation in x- and z-directions
$\overline{u^2[k]}$	Turbulent kinetic energy per unit mass within a wave number interval 0 to $k$ ( $L^2/T^2$ )
$\overline{u^2[L]}$	Turbulent kinetic energy per unit mass at eddy size $L$

$\overline{u_i^2[n_i]}$	Discretized turbulent kinetic energy per unit mass at frequency $n_i$
$\overline{u_0^2[L]}$	$\overline{u^2[L]}$ at $(\tilde{x}, \tilde{z}) = (0, 1)$
$\vec{V}$	Velocity vector
$x$	Longitudinal distance (downstream distance) from the canopy leading edge
$y$	Lateral distance from the canopy center line
$z$	Vertical distance from the wall
$z_k$	Height of the kink in logarithmic velocity profile
$z_o$	Roughness length
$z_{oh}$	Roughness length when $d = h$
$\beta$	Constant
$\delta$	Boundary-layer thickness
$\delta^*$	Displacement thickness
$\delta_d^*$	Displacement thickness for the flow below $z = d$
$\delta_h^*$	Displacement thickness for the flow within the canopy
$\delta_i$	Internal boundary-layer thickness
$\epsilon$	Rate of turbulent-energy dissipation per unit mass ( $L^2/T^3$ )
$\epsilon[k]$	Rate of turbulent-energy dissipation per unit mass within a wave number interval 0 to $k$
$\theta$	Momentum thickness
$\theta_h$	Momentum thickness for the flow within the canopy
$\kappa$	von Kármán's constant
$\nu$	Kinematic viscosity ( $L^2/T$ )
$\pi$	Profile parameter

$\pi_1$	Profile parameter calculated by Eq. (5.11)
$\pi_f$	Profile parameter for the best fitting to experimental data
$\rho$	Fluid density
$\tau_0$	Wall shear stress
$\phi[k]$	One-dimensional wave number density function
$\omega$	Wake function

#### Superscripts

$\sim$	Dimensionless
$\_$	Time-averaged

#### Subscripts

d	Deduced from experimental data (friction velocity)
m	Measured (friction velocity)
j	j direction
rms	Root mean square
$\alpha$	$\alpha$ direction

## LIST OF FIGURES

<u>Figure</u>		<u>Page</u>
3.1	Sketch of the model forest canopy and model tree element . . . . .	85
3.2	Overall view of the Meteorological Wind Tunnel . . .	86
3.3	View of the model forest canopy . . . . .	87
4.1	Typical normal hot-wire calibration curve . . . . .	88
4.2	Typical yawed hot-wire calibration curve . . . . .	89
4.3	Block diagram of hot-wire anemometer measuring system . . . . .	90
4.4	General view of hot-wire anemometer system and additional equipment . . . . .	91
5.1	Power law representation of upstream velocity profile . . . . .	92
5.2	Logarithmic law representation of upstream velocity profile. . . . .	93
5.3a	Mean velocity profiles within and above the canopy for FDC case . . . . .	94
5.3b	Mean velocity profiles within and above the canopy for FDC case . . . . .	95
5.4a	Mean velocity profiles within and above the canopy for HDC case . . . . .	96
5.4b	Mean velocity profiles within and above the canopy for HDC case . . . . .	97
5.5	Mean velocity variation along isoheights above the canopy; FDC and HDC . . . . .	98
5.6	Mean velocity profiles inside the canopy at 6 selected stations; FDC and HDC . . . . .	99
5.7	Lateral variation in the mean velocity and turbulent intensity for FDC case over a distance of 30 cm off the center line . . . . .	100

<u>Figure</u>		<u>Page</u>
5.8	Lateral variation in the mean velocity and turbulent intensity for HDC case over a distance of 30 cm off the center line . . . . .	101
5.9	Boundary-layer thickness growth and the boundary between the transition and fully developed flow regions; FDC and HDC . . . . .	102
5.10	Growth of displacement thickness and momentum thickness along the canopy; FDC and HDC . . . . .	103
5.11	Variation of the ratios of the displacement and momentum thicknesses within the canopy to the local total displacement and momentum thicknesses along the roughness; FDC and HDC . . . . .	104
5.12	Variation in the shape factor along the canopy; FDC and HDC . . . . .	105
5.13	Power law variation of the mean velocity above the canopy within the fully developed flow region; FDC and HDC . . . . .	106
5.14	Change in logarithmic law velocity representation with the zero-plane displacement; HDC case . . . . .	107
5.15	Variation of the mixing length with height; FDC and HDC . . . . .	108
5.16	Sample of modified logarithmic law description of the mean velocity profiles above the canopy within the fully developed flow region for HDC case . . . . .	109
5.17	Modified logarithmic law description of the mean velocity within the inner zone ( $z = 1.0$ to $1.85$ ); FDC and HDC . . . . .	110
5.18	Defect velocity profiles within the fully developed flow region in terms of the modified wake function; FDC case . . . . .	111
5.19	Defect velocity profiles within the fully developed flow region in terms of the modified wake function; HDC case . . . . .	112
5.20	Mean velocity profiles above the canopy within the fully developed flow region according to the generalized logarithmic law; FDC case . . . . .	113

<u>Figure</u>		<u>Page</u>
5.21	Mean velocity profiles above the canopy in the fully developed flow region according to the generalized logarithmic law; HDC case . . . . .	114
5.22	Mean velocity profiles in the outer zone within the fully developed flow region described by the generalized logarithmic law; FDC case . . . . .	115
5.23	Mean velocity profiles in the outer zone within the fully developed flow region described by the generalized logarithmic law; HDC case . . . . .	116
5.24	Mean velocity profiles above a peg canopy within the fully developed flow region according to the generalized logarithmic law . . . . .	117
5.25	Mean velocity profiles above a peg canopy in the outer zone within the fully developed flow region described by the generalized logarithmic law . . . . .	118
5.26a	Turbulent shear-stress distributions within and above the canopy; FDC case . . . . .	119
5.26b	Turbulent shear-stress distribution within and above the canopy; FDC case . . . . .	120
5.27a	Turbulent shear-stress distributions within and above the canopy; HDC case . . . . .	121
5.27b	Turbulent shear-stress distributions within and above the canopy; HDC case . . . . .	122
5.28	Momentum balance in the transition region; HDC case . . . . .	123
5.29	Momentum balance in the fully developed flow region; HDC case . . . . .	124
5.30	Longitudinal pressure gradient above the canopy; HDC case . . . . .	125
5.31	Growth of the internal and total boundary layer thicknesses . . . . .	126
5.32	Variation in longitudinal turbulent intensity above the canopy along isoheights; FDC case . . . . .	127

<u>Figure</u>		<u>Page</u>
5.33	Variation in longitudinal turbulent intensity above the canopy along isoheights; HDC case . . . . .	128
5.34	Variation in vertical turbulent intensity above the canopy along isoheights; FDC case . . . . .	129
5.35	Variation in vertical turbulent intensity above the canopy along isoheights; HDC case . . . . .	130
5.36	Coefficient of anisotropy for the model forest canopy and for real forests . . . . .	131
5.37	Wave-number spectra above the canopy; FDC case . . .	132
5.38	Wave-number spectra above the canopy; HDC case . . .	133
5.39	Variation of energy-containing spectrum and energy-dissipation spectrum at two selected heights; FDC case . . . . .	134
5.40	Variation in turbulent kinetic energy and energy dissipation as function of the wave number; FDC case . . . . .	135
5.41	Variation in turbulent kinetic energy and energy dissipation as function of the wave number; HDC case . . . . .	136
5.42	Variations in energy dissipation, energy production and their ratio as function height; FDC and HDC . . . . .	137
5.43a	Variation in the discretized energy at four eddy sizes; FDC case . . . . .	138
5.43b	Variation in the discretized energy at four eddy sizes; FDC case . . . . .	139
5.44a	Variation in the discretized energy at four eddy sizes; HDC case . . . . .	140
5.44b	Variation in the discretized energy at four eddy sizes; HDC case . . . . .	141
A.1	Hot wire yawed to the mean flow . . . . .	142

## TABLE OF CONTENTS

	<u>Page</u>
1. INTRODUCTION . . . . .	1
2. THEORETICAL CONSIDERATIONS . . . . .	4
3. EXPERIMENTAL APPARATUS . . . . .	14
3.1 Model forest canopy . . . . .	16
3.2 Wind tunnel . . . . .	17
4. EXPERIMENTAL TECHNIQUE AND INSTRUMENTATION . . . . .	19
4.1 Pressure and velocity measurement . . . . .	19
4.2 Mean velocity and turbulence measurement . . . . .	19
5. EXPERIMENTAL RESULTS . . . . .	25
5.1 Establishment of the flow . . . . .	26
5.2 Mean velocity survey . . . . .	27
5.3 Shear stress and turbulence survey . . . . .	53
5.4 Turbulent-energy survey . . . . .	62
6. SUMMARY AND CONCLUSIONS. . . . .	72
APPENDIX I - YAWED HOT WIRE . . . . .	76
REFERENCES . . . . .	79
FIGURES . . . . .	85
APPENDIX II - TABLES . . . . .	143

## 1. INTRODUCTION

The flow characteristics within the atmospheric boundary layer vary depending upon the nature and configuration of the ground. Particularly, the turbulence features in the atmospheric surface layer where the frictional drag force of the ground is dominant depend considerably upon the properties of the ground roughness. The shapes of roughness elements, their geometrical arrangement and the roughness density are main factors to determine the velocity field. As roughness becomes higher and larger, the turbulent motion is greatly increased. The various exchange processes in the resulting turbulent flow are governed strongly by the turbulence characteristics. In an urban area, the exchange processes are closely related to air-pollution problems. In the flow inside and above forest or vegetative canopy the turbulence determines soil erosion, evaporation and rates of carbon dioxide exchange. Moreover, large velocity fluctuations cause significant aerodynamic effects on buildings and/or structures. Consequently, the study of velocity field in the atmospheric boundary layer is of utmost importance for a better understanding of various transport processes and wind loading on structures.

Theoretical analysis of the atmospheric-boundary-layer flow is extremely difficult because of the complexity of the interaction between the velocity field and the ground roughness. Hence, it is necessary to perform detailed experimental studies. Field measurements are inherently difficult due to the unsteadiness of weather conditions and the relatively high cost involved in setting up measurement stations. On the other hand, a suitable wind tunnel can now provide satisfactory conditions for simulating the atmospheric boundary layer. The flow conditions can be

maintained unchanged over enough time for carrying out adequate investigation. Moreover, suitable instrumentation and measurement technique are easily available.

Studies of air flow inside and above forest and/or vegetative canopies have been initiated in the Fluid Dynamics and Diffusion Laboratory at Colorado State University. The flow on a forest canopy was investigated by using a model forest canopy composed of plastic simulated-evergreen trees in a meteorological wind tunnel. The measurements were performed at a constant free-stream velocity and under thermally neutral conditions.

The mean velocity within a fully developed turbulent boundary layer on small roughness elements, e.g., sand or gravel, is described usually by employing a power law and/or a logarithmic law. However, when roughness elements are relatively high compared with the total boundary-layer thickness (10% or more), the flow is highly disturbed. The overall flow characteristics must be determined by the momentum transport due to the velocity fluctuations and the processes of the turbulent energy production and dissipation. Generally, the flow on high roughness elements is quite different from that on small elements. Therefore, in order to provide a reasonable description of the mean velocity distribution on high roughness, the feasibility of the aforementioned laws must be examined. A generalized law for describing the velocity variation above high roughness elements is sought. Furthermore for a close examination of the turbulence structure, it is necessary to survey the turbulent shear stress, turbulence intensities and turbulent energy.

The canopy frontal area, which is a drastic and sudden obstruction, has a strong effect on the flow. It is important to investigate the flow characteristics in the transition domain to discern how the flow attains its fully developed regime. Thus, it is necessary to examine the mean velocity evolution along the canopy and the variations in the turbulent shear stress, turbulence intensity and turbulent energy within this region.

The roughness density, as mentioned previously, strongly affects the velocity field. In order to explore the influence of the roughness density on the flow, two canopy densities were tested.

Theories related to this work are surveyed in the following section. Subsequently, the experimental results and relevant discussions are presented.

The data used in this work are included in Appendix II.

## 2. THEORETICAL CONSIDERATIONS

The mean velocity profiles within a turbulent boundary layer over a flat plate are usually described by using a power law and/or a logarithmic law.

The power law suggested by Prandtl [1] is

$$\frac{U}{U_{\infty}} = \left(\frac{z}{\delta}\right)^{1/n}, \quad (2.1)$$

where  $U$  denotes the mean velocity,  $U_{\infty}$  designates the free-stream velocity,  $z$  is the vertical distance from the wall and  $\delta$  stands for the local boundary-layer thickness. This power law is based on the assumption that the local skin-friction coefficient

$$c_f = \frac{\tau_o}{\frac{1}{2} \rho U_{\infty}^2}, \quad (2.2)$$

where  $\tau_o$  is the shear stress at the wall and  $\rho$  denotes the fluid density, is proportional to some power of the Reynolds number based on  $\delta$  and  $U_{\infty}$ . The value of  $1/7$  was suggested for the exponent  $1/n$  in Eq. (2.1). However, it is found that the exponent varies from  $1/10$  to  $1/3$  depending upon the Reynolds number [2]. The validity of Eq. (2.1) is restricted to Reynolds numbers smaller than  $10^5$  [1].

In order to express the dependence of the exponent in Eq. (2.1) on the Reynolds number, the power law was generalized by employing two integral characteristic parameters, i.e., momentum thickness  $\theta$  and displacement thickness  $\delta^*$  [3]. Thus,

$$\frac{U}{U_{\infty}} = \left\{ \left( \frac{z}{\theta} \right) \frac{H-1}{H(H+1)} \right\}^{(H-1)/2}, \quad (2.3)$$

where  $H$  designates the shape factor, i.e.,  $\delta^*/\theta$ .

In reality, the Reynolds number often exceeds the aforesaid range of validity of these power laws. Moreover, analytically, the dependence of the exponent in Eq. (2.1) on the Reynolds number is not known yet. To overcome these difficulties, the law of wall (or the logarithmic law) was introduced on the basis of the mixing-length concept [4]. In this law, the mixing-length is assumed to be proportional to the vertical distance from the wall. In addition, the shear stress is postulated to be constant with height. The generalized law of wall is expressed by

$$\frac{U}{U_{\infty}} = F \left[ \frac{U_* z}{\nu} \right], \quad (2.4)$$

where the friction velocity denoted by  $U_*$  is defined as

$$U_* = \sqrt{\tau_0 / \rho}. \quad (2.5)$$

On the other hand, under the assumption that the mixing-length is independent of the magnitude of velocity and the shear stress changes linearly with the vertical distance from the wall, a velocity defect law was proposed by von Kármán [1]. This law is based on the similarity assumption of velocity fluctuations. The generalized form of the velocity defect law is

$$\frac{U_{\infty} - U}{U_*} = G \left[ \frac{z}{\delta} \right]. \quad (2.6)$$

When there is a region, no matter how limited, where Eqs. (2.4) and (2.6) are valid simultaneously, the functional form for both law of wall and velocity defect law is logarithmic [5]. Then, for a flow on a smooth surface, the law of wall is expressed by

$$\frac{U}{U_*} = \frac{1}{\kappa} \ln \frac{zU_*}{\nu} + C_1, \quad (2.7)$$

where  $\kappa$  is von Kármán's constant and  $C_1$  is an integration constant. The value of the latter is determined by matching the velocity distribution to the velocity at the outer edge of the viscous sublayer.

Nikuradse [6] made extensive measurements on the flow in smooth and sand-roughened pipes. The numerical value of von Kármán's constant was found to be 0.4. Moreover, it was observed that the velocity profile on the rough surface deviated from that on the smooth wall with increasing Reynolds number. This deviation depends upon the Reynolds number and the relative scale of roughness  $h/D$ , where  $h$  is the roughness-element height and  $D$  is the pipe diameter. When the Reynolds number based on the roughness height and friction velocity, i.e.,  $\frac{hU_*}{\nu}$ , is larger than 70, the deviation becomes a function of the relative scale of roughness alone [3]. In other words, when roughness elements are very high, the roughness height is the governing factor of the flow pattern. Similar results are reported in Refs. 7, 8, 9, 10 and 11. In order to describe the velocity profiles on a rough wall by means of Eq. (2.7), a roughness function was introduced [2]. Then, Eq. (2.7) becomes

$$\frac{U}{U_*} = \frac{1}{\kappa} \ln \frac{U_* z}{\nu} + C_1 - \frac{\Delta U}{U_*} , \quad (2.8)$$

where  $\Delta U/U_*$  is a roughness function which represents the mean velocity deviation on rough wall from that on smooth wall. It was shown experimentally that the roughness function for flow on fully rough wall depends on the Reynolds number based on the roughness height and friction velocity. Thus, the roughness function is [11]

$$\frac{\Delta U}{U_*} = \frac{1}{\kappa} \ln \frac{U_* h}{\nu} + C_2 , \quad (2.9)$$

where  $C_2$  is a constant. Substitution of Eq. (2.9) into Eq. (2.8) leads to the following logarithmic law

$$\frac{U}{U_*} = \frac{1}{\kappa} \ln \frac{z}{h} + C_R , \quad (2.10)$$

where  $C_R$  is a positive constant for a given roughness.

In the atmospheric surface layer, the wind is affected by various types of roughness elements such as grass, crops, trees, buildings and so on. The height of this layer is typically between 20 and 200 m [12]. Above the surface layer, with increasing vertical distance, the velocity deviation from the geostrophic wind speed disappears gradually. The atmospheric boundary layer (or the planetary boundary layer) is defined as the distance from the ground where the mean velocity attains the geostrophic wind speed. The thickness of this layer is about 500 to 1000 m depending upon the particular latitude [13].

In order to represent the mean velocity profiles within the atmospheric surface layer by a logarithmic law, it is assumed that the effects of the roughness on the mixing-length are confined to a layer where the vertical distance from the ground and the roughness length are comparable [14]. The latter is a length scale which describes the influence of the roughness on the flow. When the vertical distance is sufficiently large compared with the roughness length, the mean velocity profile is written by

$$\frac{U}{U_*} = \frac{1}{\kappa} \ln \frac{z}{z_0} \quad , \quad (2.11)$$

where  $z_0$  denotes the roughness length.

Usually, this relationship is applied to the velocity profiles on either bare ground or very short vegetation, e.g., not exceeding a few centimeters [13]. To describe the velocity distribution over high roughness elements, the aforementioned equation is modified introducing a zero-plane displacement [14,15]. The modified logarithmic law is

$$\frac{U}{U_*} = \frac{1}{\kappa} \ln \frac{z-d}{z_0} \quad , \quad (2.12)$$

where  $d$  stands for the zero-plane displacement. The latter is considered as a datum level above which the turbulent exchange processes occur. It is noteworthy that the roughness length and the zero-plane displacement are interdependent since the logarithmic law is obtained by integrating a first order differential equation describing the shear stress distribution based on the mixing-length hypothesis. In spite of

this fact, Deacon [16] determined the zero-plane displacement and the roughness length independently in order to provide the best fit curve to measured velocities. Then, it seems that Eq. (2.12) can represent the velocity profiles between 1 and 13 m over area covered with high grass.

The flow in the atmospheric boundary layer may be simulated by the flow within the boundary layer on a flat plate. Thus, it is important to examine the eventual equivalence of the two length parameters in Eq. (2.11) and (2.12) i.e.,  $z_0$  and  $d$ , to  $C_r$  and  $h$  in Eq. (2.10). The roughness length in Eq. (2.11) can be expressed in terms of the roughness height and a constant  $C_r$  in Eq. (2.10) by the relationship

$$z_0 = h/C_0 \quad , \quad (2.13)$$

where  $C_0 = \exp(\kappa C_r)$ . Thus, the roughness length is constant for a given roughness. Moreover, since the constant  $C_r$  is positive, the roughness length is smaller than the roughness height. Next, it was found that the logarithmic profile represented by Eq. (2.10) is universal for either smooth or rough surface if the origin of the vertical coordinate is properly selected somewhere between the top and bottom of the roughness elements [2,10]. Thus, the zero-plane displacement introduced into Eq. (2.12) is considered as an adjustment of the vertical-coordinate origin such that the measured velocities are described by the logarithmic law.

In the turbulent boundary layer on a flat plate, the velocity distribution in the lower 10 to 20% of boundary-layer thickness

can be described by the logarithmic law [2]. The general form of the velocity profile throughout the entire boundary layer is expressed by a combination of the logarithmic law and the law of the wake [17]

$$\frac{U}{U_*} = \frac{1}{\kappa} \ln \frac{U_* z}{\nu} + C_1 + \frac{\pi[x]}{\kappa} \omega\left[\frac{z}{\delta}\right] \quad (2.14)$$

where  $\pi[x]$  is a profile parameter. The function  $\omega\left[\frac{z}{\delta}\right]$  is referred to as the law of the wake and supposedly common to all two-dimensional turbulent boundary-layer flows. Based on existing data, the wake function  $\omega\left[\frac{z}{\delta}\right]$  is subjected to the following normalizing conditions

$$\omega(0) = 0 \quad , \quad (2.15a)$$

$$\omega(1) = 2 \quad , \quad (2.15b)$$

and

$$\int_0^1 \omega d\left(\frac{z}{\delta}\right) = 1 \quad . \quad (2.15c)$$

Thus, in terms of the wake function, the velocity-defect law is

$$\frac{U_\infty - U}{U_*} = -\frac{1}{\kappa} \ln \frac{z}{\delta} + \frac{\pi[x]}{\kappa} (2 - \omega\left[\frac{z}{\delta}\right]) \quad (2.16)$$

Since Eq. (2.14) satisfies the boundary condition  $U = U_\infty$  at  $z = \delta$  and by the condition (2.15b) the profile parameter can be evaluated by

$$\frac{2\pi[x]}{\kappa} = \frac{U_\infty}{U_*} - \frac{1}{\kappa} \ln \frac{U_* \delta}{\nu} - C_1, \quad (2.17)$$

where  $C_1$  was estimated to be 5.1 [17].

The use of the mixing-length concept in analyzing a turbulent boundary-layer flow permits description of the average properties of flow, e.g., the mean velocity profiles and the shear stress exerted on the wall. However, the turbulent-energy production, transfer and dissipation cannot be explained by this concept. In order to account for these mechanisms, it is necessary to examine the energy equation for both mean flow and turbulence. Derivation and extensive discussion of both mean and turbulent energy equations can be found in Refs. 3, 12, and 18.

The kinetic energy extracted from the mean flow due to its retardation caused by roughness appears in the form of fluctuating energy. Through a cascade process [19], the latter is converted into heat by direct action of viscous stresses. Generally, this process does not occur in the same place since the eddies are conveyed by the mean velocity. Consequently, the balance between the energy production and energy dissipation is not necessarily a local process. Depending upon their relative magnitude, the difference can be made up at some downwind position. These mechanisms can be explained by examining the turbulent energy equation in an arbitrary direction  $\alpha$  under thermally neutral condition [12]

$$\begin{aligned} \frac{\partial \bar{e}_{\alpha\alpha}}{\partial t} = & - \overline{u_{\alpha} u_j} \frac{\partial U_{\alpha}}{\partial x_j} - \nu \left( \frac{\partial u_{\alpha}}{\partial x_j} + \frac{\partial u_j}{\partial x_{\alpha}} \right) \frac{\partial u_{\alpha}}{\partial x_j} - \frac{1}{\rho} u_{\alpha} \frac{\partial p}{\partial x_{\alpha}} \\ & + \frac{\partial}{\partial x_j} \left( - \bar{e}_{\alpha\alpha} U_j - \overline{e_{\alpha\alpha} u_j} + \nu \frac{\partial \bar{e}_{\alpha\alpha}}{\partial x_j} + \nu \overline{u_{\alpha} \frac{\partial u_j}{\partial x_{\alpha}}} \right) , \end{aligned} \quad (2.18)$$

where  $j = 1, 2, 3$ , the dummy index  $\alpha$  is not to be summed upon and  $e_{\alpha\alpha} = u_{\alpha}^2/2$ . In this equation, the mean velocity is denoted by  $U$  and the fluctuating velocity by  $u$ . Terms in the final bracket express the energy transfer from one place to another since their volume integral vanishes at all points on a sufficiently distant surface [12]. The third term on the right-hand side of Eq.(2.18) accounts for the transfer of energy among the turbulent velocity components by the fluctuating pressure forces. The second term is the total rate of work against viscous forces in the  $\alpha$ -direction and represents the energy dissipation directly to heat, i.e., the dissipation term. The first term on the right-hand side indicates the energy supply from the mean motion to the fluctuating velocity and is usually referred to as the production term. The production term can be rewritten as [12]

$$\overline{u_{\alpha} u_j} \frac{\partial U_{\alpha}}{\partial x_j} + U_{\alpha} \overline{u_j \frac{\partial u_{\alpha}}{\partial x_j}} = \frac{\partial}{\partial x_j} \overline{(u_{\alpha} u_j U_{\alpha})} . \quad (2.19)$$

The term on the right-hand side is the divergence of the fluctuating energy transport. Its integration in space is equal to zero. Hence the two terms on the left-hand side represent the energy balance.

This indicates that the energy extracted from the mean motion in the  $\alpha$ -direction by  $-U_\alpha u_j \frac{\partial u_\alpha}{\partial x_j}$  becomes the fluctuating energy in the same direction through  $-u_\alpha u_j \frac{\partial U_\alpha}{\partial x_j}$ .

All the terms in Eq. (2.18) but the pressure transport term were measured within two-dimensional turbulent boundary layer [20,21]. These results show that the various transport terms are of secondary importance with respect to the production and dissipation terms near the wall. In other words, the production and dissipation are nearly in balance, i.e., most energy produced locally can dissipate locally [12,18]. As a result, near the ground within a two-dimensional turbulent boundary layer, the energy balance can be approximated by

$$-\overline{uw} \frac{\partial U}{\partial z} \approx \epsilon, \quad (2.20)$$

where  $\epsilon$  stands for the energy dissipation and,  $u$  and  $w$  are the fluctuating velocities in the  $x$ - and  $z$ -direction, respectively.

### 3. EXPERIMENTAL APPARATUS

The objective of the experimental program was to study the flow within and, in particular, above high roughness elements randomly distributed. This was to be achieved by using a model forest canopy consisting of plastic simulated evergreen trees in a meteorological wind tunnel. The flow within the atmospheric boundary layer changes its characteristics depending on the shape of prevailing roughness elements, their stiffness and configuration. Therefore, the flow over forest canopies can hardly be studied from measurements using a single tree or a small number of trees. Unfortunately, field measurements do not yet yield adequate results for a systematic analysis of flow. This is due to the continuous variation of weather conditions and the high cost in setting up adequate field measurement stations. On the other hand, the wind tunnel flow provides satisfactory conditions to simulate the atmospheric boundary layer [22]. The flow conditions can be kept unchanged over a long enough time period for performing adequate measurements. Moreover, suitable instrumentation and measurement techniques are easily available.

Many investigations of flows using various types of trees and forest canopies were conducted in wind tunnels and in field [23,24,25, 26,27]. The wind-tunnel data show reasonable agreement with field data. However, most of these studies are limited to particular aspects. Consequently, they do not supply a general picture of the flow field caused by high roughness spreading over wide area, such as a forest canopy or any vegetative canopy. Investigation of the flow inside and above forest canopies using a wind tunnel was recently initiated at the Fluid Dynamics and Diffusion Laboratory, Colorado State University.

First, flexible roughness elements were used [28]. Next, pegs were employed to simulate vegetative canopies [29,30]. Following that, drag measurements of model trees [31] and preliminary velocity and diffusion measurements [32,33] were performed by employing simulated forest canopy. The latter is generally similar to the canopy used in the present work.

Since the flow in the wind tunnel is of different scale than the full-scale flow, the flow similarity conditions must be satisfied. Thus, geometrical, dynamic, kinematic and thermal similarity must be achieved [22,34]. For dynamical similarity, the Rossby, Reynolds and Froude numbers must be the same for both model and field flow. The model forest used in this experiment does not have any specific prototype so that geometrical similarity is irrelevant. Neither thermal similarity nor the Froude number equality needs to be considered since the experiment was carried out under thermally neutral conditions. The condition for the Rossby number can be disregarded if the horizontal length scale of the full-scale forest is smaller than about 150 km [22].

The Reynolds number equality is of prime importance in the case of laminar flow. However, the flow about sharp-edged bodies or tree-like roughness is turbulent and, hence, inertially dominated. Flow separation occurs on each one of the roughness elements. In other words, the roughness element acts as vortex generators and counteracts the damping effect of the viscosity [3]. Then, it can be assumed that the flow pattern is independent of the Reynolds number. Recent experimental investigations seem to indicate that drag coefficient and wake characteristics of tree elements are approximately independent of the Reynolds number [23,24,28,30,32,33]. In general, it is reasonable to assume that

the flow in the atmospheric surface layer is inertially dominated. Similarly, the wind tunnel flow reported herein is inertially dominated. Therefore, the flow over model forest can simulate the full-scale forest canopy flow although the Reynolds number in the model canopy is smaller than that in a similar field flow.

Finally, to satisfy kinematic similarity, the upstream velocity should vary according to the logarithmic law characteristics of the lower atmosphere. Moreover, the model forest canopy is to be placed in a turbulent boundary layer simulating the atmospheric surface layer. Accordingly, the upstream boundary layer must be artificially thickened.

### 3.1 Model forest canopy

A model forest canopy 1100 cm long and 183 cm wide was used. A schematic diagram of the canopy and of the model tree is displayed in Fig. 3.1. The model tree used is 18 cm high and, roughly, the largest diameter of the crown was measured at a height of about 13.5 cm, i.e., at 75% of the canopy height. The system of coordinates used and all important dimensions are also shown in this figure. The canopy base consists of 18 identical aluminum plates 0.5 cm thick. On the face of these plates, holes of 0.5 cm in diameter were drilled at intervals of 1.27 cm. Model trees made from plastic simulated evergreen boughs were inserted into these holes. These roughness elements were selected based on the results reported in Ref. 32. The model trees were randomly distributed so that no definite rows were evident. Two roughness densities, i.e., the number of trees per unit area, were employed. The first was approximately 1 tree per 46 cm<sup>2</sup>, whereas the other was nearly 1 tree per 92 cm<sup>2</sup>. Hereafter, the former

is referred to as full-density canopy or FDC and the latter as half-density canopy or HDC. In the former density, the base plates were completely covered by the tree crowns. It is, further, possible to define a volumetric density number. This was defined as the ratio of the volume occupied by the trees to the total volume of the canopy. If the trunk is represented by a cylinder and the crown by a cone, as shown in Fig. 3.1(d), then the crown volume is about 222 times larger than the trunk volume. Consequently, the latter can be neglected. Then, the volumetric density was approximately 0.26 for the full-density canopy and 0.13 for the half-density canopy.

### 3.2 Wind tunnel

The experiment reported herein was conducted in the Army Meteorological Wind Tunnel [35]. This is a closed circuit wind tunnel with a 27 m long test section and a cross-section of 183 x 183 cm. Its contraction ratio is 9:1. Air speed up to about 36 m/sec is generated by a propeller driven by a 250 hp DC motor. The air speed can be changed continuously by adjusting the pitch of propeller blades and/or the motor speed. A schematic diagram of the wind tunnel including the system of coordinates used and all important dimensions is shown in Fig. 3.2.

The leading edge of the canopy was located 15 m downstream of the test section entrance. To satisfy the requirement for kinematic similarity, turbulence was generated by gravel installed upstream of the entrance, i.e., in the contraction section. However, the turbulent boundary layer generated by this roughness was not thick enough at the canopy leading edge. Consequently, an additional turbulence generator was placed along the first 3 m of the wind-tunnel test

section. The turbulence generator was made from flexible plastic strips of 10 cm high, 0.63 cm wide and 0.019 cm thick. Thus, an adequate turbulent boundary layer was obtained.

The wind tunnel ceiling is sectionally adjustable such that any desirable longitudinal pressure gradient can be obtained. For this adjustment, eight static-pressure taps located 244 cm apart were employed.

An electrically driven traversing mechanism permitted continuous movement of various measurement probes in the x, y, and z-directions. The position of probes can be controlled within 1 mm.

A photograph of the full density canopy installed in the wind tunnel is displayed in Fig. 3.3.

#### 4. EXPERIMENTAL TECHNIQUE AND INSTRUMENTATION

##### 4.1 Pressure and velocity measurement

The pressure gradient in the wind direction is negligibly small in the atmospheric boundary layer. Consequently, the experiment was carried out under approximately zero pressure gradient condition. The latter was achieved by an extensive series of trails in which the slope of the wind tunnel ceiling along the model canopy was sectionally adjusted. For this purpose, the static pressure taps located along the ceiling were utilized. The pressure at the first tap located 900 cm downstream of the test section entrance was used as the reference static pressure. The difference between the reference pressure and the pressure at other taps was adjusted within 0.002 mm Hg. An electronic pressure meter of capacitance type (Trans-Sonic Equibar Type 120 A) was employed for the pressure measurement. This meter is a differential micromanometer with a range up to 30 mm Hg and a resolution of 0.0001 mm Hg.

The experiment was carried out at a constant free-stream velocity of 6 m/sec. The freestream velocity was measured by means of a Pitot-static tube located 1 m upstream of the model forest and 1 m above the wind tunnel floor. A similar Trans-Sonic pressure meter was utilized to monitor the Pitot-static tube reading. A standard Pitot-static tube of hemispherical type with an impact orifice of 1/8-in diameter was utilized [36].

##### 4.2 Mean velocity and turbulence measurement

The mean velocity distribution within and above the forest canopy was measured by a single hot-wire anemometer. Simultaneously, the

longitudinal turbulence intensity was also measured. The hot-wire anemometer used in this experiment is a new system conceived, designed and built at the Fluid Dynamics and Diffusion Laboratory, Colorado State University [37]. This is a fully transistorized unit of constant temperature type (CT). The noise level of the unit is less than 200  $\mu\text{v}$ . The signal to noise ratio (S/N) is from 4 to 200 depending on the output signal. Its frequency response is as high as 100 kHz. A copper-plated tungsten wire of 0.00875 mm in diameter and of an aspect ratio of approximately 170 was used.

The hot-wire calibration indicated that the square of the actual voltage drop across the wire  $E$  is nearly proportional to the square root of the undisturbed velocity  $U$ . That is, the so-called King's law [38] was found to be reasonably satisfied within the velocity range of the present experiment. A typical calibration curve is displayed in Fig. 4.1. For practical purposes, the relation between the voltage drop and the undisturbed velocity may be written as [39]

$$E^2 = E_0^2 + MU^{\frac{1}{2}}, \quad (4.1)$$

where  $E_0$  is the voltage drop in still air (or shielded hot-wire). The constant  $M$  varies with wire configuration, wire properties and air properties. This constant is experimentally determined from calibration for each particular wire employed. Moreover, both  $E_0$  and  $M$  depend on the resistance ratio  $N$ . The latter is the ratio of the heated-wire resistance under working condition  $R_w$  to its cold resistance in still air  $R_{wco}$ . It is important to note that Eq. (4.1) does not hold at very low velocity, say, smaller than 0.10 m/sec [39].

When a hot-wire probe is placed in the turbulent flow, the instantaneous effective velocity  $U_e$  causing the actual voltage drop can be expressed by

$$U_e = [(U + u)^2 + w^2]^{\frac{1}{2}} . \quad (4.2)$$

In the above relationship,  $U$  is the mean or time-averaged velocity,  $u$  is the component of the fluctuating velocity parallel to  $U$  and  $w$  is the lateral component of the fluctuating velocity perpendicular to the hot wire. The component parallel to hot-wire axis  $v$  contributes negligibly to the heat loss of a hot wire [18,40]. Thus, Eq. (4.1) becomes

$$E^2 = E_0^2 + MU_e^{\frac{1}{2}} . \quad (4.3)$$

Under the condition of relatively small fluctuation,  $w$  is assumed to be negligible compared with  $(U + u)$ . Thus, Eq. (4.3) reduces to

$$(\bar{E} + e)^2 = E_0^2 + M(U + u)^{\frac{1}{2}} , \quad (4.4)$$

where  $\bar{E}$  is the time-averaged (DC) voltage necessary to balance the bridge under steady conditions and  $e$  stands for the AC instantaneous voltage drop proportional to the fluctuating velocity  $u$ . Next, by performing a binomial expansion, the quadratic and high order terms in  $e$  and  $u$  can be neglected in Eq. (4.4) on the assumption of small fluctuations. Separating the bridge voltage into its DC and AC parts, and taking square-root of both fluctuating quantities, the turbulence

intensity is given by [39]

$$\frac{u_{rms}}{U} = \frac{4\overline{E^2}}{\overline{E^2} - E_0^2} \frac{e_{rms}}{\overline{E}}, \quad (4.5)$$

where the subscript rms denotes square-root of mean square value, i.e.,  $(\overline{u^2})^{1/2}$  and  $(\overline{e^2})^{1/2}$ . The error in using Eq. (4.5) is at most 10% for turbulence intensity of 60%. Turbulence intensities of this order of magnitude were monitored only at several stations.

In addition to the condition of small fluctuations, the mean velocity must be high enough to satisfy the relation  $E - E_0/E_0 > 0.2$  for Eq. (4.5) to be valid [39]. The measurement of large fluctuations in the low velocity range can be carried out by using the method developed by Sadeh [39]. This method needs an adequate linearizer unit. Since the measurements in our work were made without a linearizer, the results in the high turbulence intensity region are not so reliable.

A yawed wire probe was employed for measurements of the vertical fluctuating velocity  $w$  and the turbulent shear stress  $\overline{uw}$ . When a hot wire is placed successively in the  $x$ - $z$  plane at two different yaw angles, say,  $45^\circ$  and  $135^\circ$ , to the mean flow direction,  $\overline{uw}$  and  $\overline{w^2}$  are given by the relationships (see Appendix I)

$$\frac{\overline{uw}}{U^2} = \frac{4\overline{E^2} (\overline{e_{45}^2} - \overline{e_{135}^2})}{(\overline{E^2} - E_0^2)^2}, \quad (4.6)$$

and

$$\frac{\overline{w^2}}{U^2} = \frac{8 \overline{E^2} (\overline{e_{45}^2} + \overline{e_{135}^2})}{(\overline{E^2} - E_0^2)^2} - \frac{\overline{u^2}}{U^2}, \quad (4.7)$$

where  $e$  denotes the AC instantaneous voltage drop across the yawed wire caused by  $u$  and  $w$ , and the subscripts 45 and 135 stand for the yaw angle of the hot wire to the mean flow. In Eq. (4.7)  $\overline{u^2}$  is obtained from a normal wire measurement at the same location. It is important to notice that in deriving Eqs. (4.6) and (4.7), the King's law is assumed to be valid for a hot wire yawed to the mean flow direction. Calibrations of a  $45^\circ$ -yawed wire showed that the aforementioned assumption is reasonably satisfied. A sample of the calibration curves obtained is provided by Fig. 4.2.

The frequency-spectra survey was performed by means of a recording wave analyzer (General Radio, Recording Sound and Vibration Analyzer, Type 1911-A). The fraction of energy at each frequency, i.e., the frequency density function, calculated in terms of the mean-square output of a wave analyzer is

$$F[n] = \frac{1}{B_w} \overline{e^2[n, B_w]}, \quad (4.8)$$

where  $\overline{e^2[n, B_w]}$  is the square of the rms output at any selected frequency  $n$ ,  $B_w$  stands for the filter bandwidth and  $n$  is the central frequency within the bandwidth. A constant-percentage bandwidth of 1/3 octave (23%) was used throughout this survey. In this case, the

bias error when changes of the mean-square values are smaller than  $\pm 15$  db/octave is estimated to be less than 5% [41].

Both normal and yawed wire were calibrated employing a calibrator (Thermo-System Calibrator, Model 1125). Air velocity in this calibrator ranges from about 0.15 m/sec to 300 m/sec. The accuracy of the reproduction of velocity in this calibrator is  $\pm 2\%$  for velocity larger than 3 m/sec. At smaller velocity, the accuracy is approximately  $\pm 5\%$ .

Other auxiliary equipment used in this experiment were: (1) A digital DC voltmeter (Hewlett-Packard, Model 3440 A) for monitoring of various output voltages; (2) A true root-mean-square meter, TRMS (DISA, Type 55D35) for measurement of rms values; (3) A dual-beam oscilloscope (Tektronix, Type 502A) for quick assessment of the output signal pattern, calibration and monitoring of instantaneous AC signal; (4) A tape recorder (Ampex, Model FR 1300) for recording of various output signal for further analysis; (5) An integrator (CSU) for obtaining the time-averaged value of hot-wire output voltage; (6) An x-y recorder (Moseley Autograf, Model 135) for recording TRMS output voltages. A simplified block diagram of the equipment utilized is shown in Fig. 4.3. A general view of the hot-wire anemometer and the additional equipment, is provided by Fig. 4.4.

## 5. EXPERIMENTAL RESULTS

The flow within and, particularly, above the model forest canopy was investigated. The experiment was performed at constant free-stream velocity, i.e., approximately vanishing longitudinal pressure gradient, under thermally neutral conditions. The main purposes of the work reported herein were:

- (1) To study the mean velocity evolution along the canopy.
- (2) To investigate the turbulence intensity variation along the canopy.
- (3) To explore the turbulent energy distribution and turbulence structure.
- (4) To examine the high roughness effects on both mean velocity and turbulence.

The system of coordinates used in the presentation of the results is portrayed in Figs. 3.1 and 3.2. The origin is at the geometrical center of the canopy leading edge. Generally, the results are presented in dimensionless form. Dimensionless variables are denoted by a tilde placed over the symbols used. The dimensionless coordinates are defined by

$$\tilde{x}, \tilde{y}, \tilde{z} = x/h, y/h, z/h, \quad (5.1)$$

where  $h$  is the canopy height,  $h = 18$  cm. The velocities are referred to the constant free-stream velocity used in this experiment

$$\tilde{\vec{V}} = \vec{V}/U_{\infty}, \quad (5.2)$$

where  $U_{\infty} = 6$  m/sec . If other reference length or velocity is utilized, they are mentioned as they are introduced.

The results for both canopy densities, FDC and HDC, are presented simultaneously for the sake of comparison and for assessing the effects of canopy density. As the experimental results are presented, relevant discussions are interspersed wherever it is deemed helpful for proper interpretations of the results.

### 5.1 Establishment of the flow

To begin with, longitudinal zero-pressure gradient was obtained by adjusting sectionally the wind-tunnel ceiling as described in Sec. 3.2. The free-stream velocity which was maintained at 6 m/sec was measured at 1 m upstream of the canopy, i.e., at  $x = -1$  m in the plane  $y = 0$  (see Fig. 3.1). Basically, due to the zero-pressure gradient, the free-stream velocity should remain constant along the model forest. However, a slight increase of about 2.5% in its value was monitored up to 1 m downstream of the canopy leading edge, i.e., up to  $x = 1$  m. Beyond this point, the variation in the free-stream velocity was negligibly small, less than about 1%.

It was found that the velocity distribution at  $x = -1$  m, which is displayed in Fig. 5.1, is reasonably described by a power law (see Eq. (2.1)). In this figure the vertical distance is made dimensionless using the local boundary layer thickness  $\delta$  . The numerical value of the exponent was found to be approximately 0.18. Field measurements also indicate that the velocity profile can be expressed by a power law. Generally, the value of the exponent depends on the surface roughness [42]. For instance, in Ref. 43 a value of 0.28 is suggested for wooded

area and  $\delta$  of 0.16 for open country. The value of the exponent for the upstream velocity is about 12% larger than the aforementioned value for open country. Furthermore, based on field measurements, the value of the exponent can vary daily and/or seasonally [42]. The seasonal variation seems to depend on the location of the measurement probes.

Simultaneously, it was found that the upstream velocity varies satisfactorily according to the logarithmic law (see Eq. (2.11)) as shown in Fig. 5.2. The estimated value of the friction velocity and of the roughness length are about 36 cm/sec and 0.093 cm, respectively. In accordance with the suggested value of roughness length for various natural surfaces [16], the upstream surface in this experiment would correspond to a desert area. Consequently, the velocity distribution in the atmospheric surface layer over smooth surface was simulated adequately by the upstream flow.

## 5.2 Mean velocity survey

The mean velocity in both FDC and HDC cases was measured at 14 locations along the canopy center line, i.e., along the x-axis in the plane  $y = 0$ , from 1 m upstream of the canopy to 1 m downstream of it. At each location, for the FDC case, the measurements along the z-axis were carried out at 14 to 17 stations over a height of 119 to 132 cm. On the other hand, the measurements for HDC case were performed at 13 to 16 stations over a height of 102 to 132 cm. Within the canopy height the mean velocity was measured at 4 or 5 stations at each location.

The measured mean velocity variation for FDC case is shown in Figs. 5.3a and 5.3b whereas for the HDC case in Figs. 5.4a and 5.4b. In both cases, a similar velocity variation with height was obtained. When the

flow encounters the canopy, the lower part of the flow is deflected upward by the canopy frontal area. Hence, in the vicinity of roughness a relatively drastic velocity change with height is observed. Away from the canopy the velocity increased gradually exhibiting a change similar to the upstream velocity.

In order to examine the mean velocity evolution above the canopy, the velocity variation along 6 isoheights for both canopy densities, FDC and HDC, is displayed in Fig. 5.5. The flow retardation due to the roughness, which is stronger close to the canopy than far from it, is clearly discerned. Most of the velocity deceleration occurs over a longitudinal distance of about 15 to 20 roughness heights within a region extending approximately up to one roughness height above the canopy ( $\tilde{z} = 2$ ). Beyond 20 roughness heights from the canopy leading edge, the velocity change up to about  $1.5h$  above the roughness is practically negligible. Away from the roughness, the flow retardation extends over longer distances. With increasing height above the canopy, a longer adjustment range to the new roughness conditions is needed. The region throughout which most of the deceleration develops can be defined as a transition region. On the other hand, the fully developed flow region is arbitrarily defined as the region where the mean velocity deviates by less than 5% from the local mean velocity at  $\tilde{x} = 45$ . Within this domain, the flow reaches a state of relative equilibrium. According to the above definitions, the extents of the transition and the fully developed flow regions for both FDC and HDC are shown by the broken lines in Fig. 5.5. It is important to remark that the transition region for FDC stretches over a shorter distance than for HDC. Roughly, it stretches in the former case up to  $\tilde{x} = 16$  to 32 and in the latter case

up to  $\tilde{x} = 19$  to 38 over a height range from  $\tilde{z} = 1$  to 5 . This is due to the dependence of the momentum loss on roughness density. As the density is higher, the momentum loss is greater and, hence, the transition domain is shorter. Thus, the extent of the transition region depends upon the roughness density and increases with height above the canopy. Toward the trailing edge of the canopy, a slight acceleration over a distance of about  $5h$  was observed. It is due to the flow adjustment to the smooth surface leeward of the canopy.

It is, further, worthwhile to notice the effect of the roughness-element shape on the velocity variation within the canopy. Recall that the trunk extends over 28% of the roughness height and the crown over 72% of it (see Fig. 3.1). The mean velocity change with height inside the canopy at 6 selected stations is shown in Fig. 5.6. Generally, higher velocities were monitored along the trunk zone than along the crown. As the flow approaches the canopy, it is divided into two distinct parts due to crown stagnation effects. An upward flow displacement above the canopy and a downward deflection into the trunk spacing arise simultaneously. Accordingly, the largest velocities within the canopy were monitored at about 1/2 of the trunk height throughout the beginning of the transition region. This region of relatively large velocities is called the jet region. On the other hand, the smallest velocities were generally measured at  $\tilde{z} = 0.7$ , i.e., at about half of the crown height ( $z = 13.6$  cm). The jetting vanishes gradually as  $x$  increases. Within the canopy, the fully developed flow region is defined as the domain where the jet effect is not discernible. In the FDC case the jetting was observed up to about 1.5 m ( $\tilde{x} = 8.33$ ) from the leading edge while for HDC up to about 2 m ( $\tilde{x} = 11.11$ ) . Once the jetting

effect fades, similar velocity profiles were obtained at all measurement stations inside the canopy. Furthermore, the velocity along the lower half of the canopy is almost constant with height. Near the trailing edge of the canopy, due to the flow adjustment to the canopy-leeward smooth surface, the flow is displaced downward and repenetrates into the canopy. Therefore, a slight jetting redevelops as the canopy trailing edge is approached.

Basically, the flow in the neighborhood of the canopy center line, i.e., in the vicinity of the plane  $y = 0$ , can be assumed to be similar to two-dimensional flow through a channel. Consequently, it is important to examine the mean velocity and turbulence intensity change off the center line. It should be recalled that the latter was measured simultaneously with the former. The results for both FDC and HDC cases over a distance of 30 cm off the center line at two stations, i.e.,  $\tilde{x} = 16.66$  and 38.88, are portrayed in Figs. 5.7 and 5.8, respectively. In these figures the mean velocity is normalized using the free-stream velocity in the plane  $y = 0$  ( $U_{\infty c} = U_{\infty}(y=0) = 6$  m/sec) and the longitudinal turbulence intensity ( $T_u$ ) is based on the local mean velocity. A lateral variation in the mean velocity of less than 5% is discerned. Similarly, the transversal change in the turbulence intensity is smaller than about 3%. Thus, in the vicinity of the canopy center line, i.e., within about  $y = \pm 30$  cm, the flow is practically two-dimensional.

The boundary-layer thickness growth for both FDC and HDC cases is depicted in Fig. 5.9. The boundary between the transition and fully developed flow regions is also shown in this figure. The boundary-layer thickness was defined, as commonly done, as the distance from the wall

where  $U/U_\infty = 0.99$ . The results indicated, as expected, that the growth rate in the FDC case is larger than that for the HDC case. This is due to the dependence of the upward flow displacement on canopy density. As the latter is higher, the former is larger. The adjustment of the boundary-layer thickness downstream of the canopy is also clearly discerned in Fig. 5.9.

It is, further, important to examine the variation of the displacement and momentum thickness,  $\delta^*$  and  $\theta$ , along the canopy. The results for both FDC and HDC are shown in Fig. 5.10. As anticipated, their growth rates for FDC case are slightly larger than for HDC. This result is in agreement with the boundary-layer thickness change. Due to the drastic flow retardation throughout the transition region, a strong increase in the momentum thickness is expected to occur within this region. This is not substantiated by the obtained momentum thickness change. Since most of the momentum thickness loss and the flow upward displacement are caused by the roughness, it is important to find out the contribution of the flow within the canopy to total local momentum and displacement thicknesses. These results are displayed in Fig. 5.11. In this figure,  $\delta_h^*$  and  $\theta_h$  designate the fraction of the displacement and momentum thicknesses, respectively, over the canopy height. In the transition region, the contribution of the flow inside the roughness to the momentum thickness reduces from 50 to about 10% over a distance of 20 to 30h from the canopy leading edge. Hence, the severe flow retardation is mainly due to the large momentum loss inside the roughness. It is inferred that the latter is mainly caused by the stagnation flow effects on the canopy frontal area rather than by the friction at the canopy surface. Within the fully developed flow region, the contribution

of the flow inside the canopy to the momentum thickness levels off to about 10%. In this region, the flow is already adjusted to the new roughness conditions and the momentum loss is mostly due to friction along the canopy fuzzy surface. This result agrees with the drag measurements reported in Ref. 31. It is important to remark that the fraction of momentum thickness within the canopy depends upon its density. The contribution in FDC case is always smaller than for HDC case. As the roughness is denser, the upward flow displacement is larger. In the FDC case, it reduces to 10% at about  $\tilde{x} = 20$  whereas in the HDC case at approximately  $\tilde{x} = 30$ . The variation of the roughness contribution to the local total displacement thickness reveals a similar behavior. It diminishes from roughly 60% at the canopy leading edge to about 40% at  $\tilde{x} = 30$  to 35. Similar to momentum thickness variation, the roughness contribution to total displacement thickness throughout the transition region is larger for HDC than for FDC. This contribution reduces to about 40% at  $\tilde{x} = 30$  for FDC whereas at  $\tilde{x} = 35$  for HDC. Within the fully developed flow region, the roughness contribution to the displacement thickness occurs more gradually than to the momentum loss.

In order to examine the roughness effects on the flow displacement and momentum loss, it is important to evaluate the shape factor, i.e., the ratio of displacement thickness to momentum thickness, ( $H = \delta^*/\theta$ ). The shape factor variation along the canopy is displayed in Fig. 5.12. At the very beginning of the transition region, the shape factor for FDC reveals a steeper increase than that for HDC. In the former case it reaches a maximum value of about 3.50 at  $\tilde{x} = 5.55$  while for HDC it is approximately 3.35 at  $\tilde{x} = 10$ . After the maximum value is attained, in both cases the shape factor diminishes gradually to a value of about

2.65 in the fully developed flow region. As the trailing edge is approached, the shape factor reduces slightly due to the smooth surface downwind of the canopy.

The shape factor depends upon the wall conditions through the friction velocity. It can be expressed by the relationship [11]

$$H = \left(1 - C \frac{U_*}{U_\infty}\right)^{-1}, \quad (5.3)$$

where  $C$  is assumed to be a universal constant for flows without pressure gradient. For flow over both smooth and rough surfaces (fine roughness: sand or gravel), the shape factor ranges from 1.4 to 2.6. In this case the value of  $C$  was estimated to be 6.1 [11]. On the other hand, depending upon the particular logarithmic law used to describe the velocity distribution, the value of  $C$  can vary from 4.88 to 5.4 [18]. Since in this work the roughness is relatively high, it is important to evaluate the value of  $C$  in Eq. (5.3). For the sake of comparison, the results at three stations in the fully developed flow region for both FDC and HDC cases are summarized below:

$\bar{x}$	$x$ (m)	C	
		FDC	HDC
38.88	7.0	13.1	9.8
47.22	8.5	13.0*	9.9
52.77	9.5	15.0	10.7

---

\* Obtained by interpolation

In computing the values of  $C$  the local friction velocity was estimated from the shear stress measurement (see Sec. 5.3). The values of  $C$  obtained are about 1.5 to 2.4 times larger than that for fine roughness, viz., 6.1 in Ref. 11 which is the best fitted experimental approximation. Hence, the high roughness affects strongly the value of so-called universal constant  $C$ . Moreover, if the latter value is employed in Eq. (5.3), the shape factor would be about 50 to 60% smaller than its values shown in Fig. 5.12. When the shape factor is estimated for the flow above the roughness, i.e.,  $H = (\delta^* - \delta_h^*) / (\theta - \theta_h)$ , its value in the fully developed flow is about 1.65.

Generally, in the fully developed flow region the mean velocity above the canopy can be represented by a  $1/n$ -power law and/or a logarithmic law (see Eqs. (2.1) and (2.11)). The value of the exponent  $1/n$  in the power law varies drastically with the flow Reynolds number [2] and, hence, the possibility of obtaining a similar velocity distribution is limited. Furthermore, the validity of such a representation for flow over high roughness elements was not yet adequately investigated. For flow over high roughness an adjusted power law where the vertical distance is measured from the roughness surface was suggested [28]. Thus,

$$\tilde{U} = \left( \frac{\tilde{z}-1}{\delta-1} \right)^{1/n}, \quad (5.4)$$

where  $\tilde{\delta} = \delta/h$ . Samples of the velocity distribution in the fully developed flow region for both FDC and HDC using Eq. (5.4) are displayed in Fig. 5.13. The values of  $n$  were found to be 2.8 and 2.5 for FDC and HDC, respectively. Basically, if the exponent is properly evaluated, the velocity seems to be satisfactorily described by Eq. (5.4). On the other hand, it is practically impossible to determine an adequate value

for  $n$  since its exact dependence on roughness condition is not known. Moreover, the use of Eq. (5.4) in the vicinity of the roughness surface ( $\tilde{z} = 1.28$  to  $1.35$  or  $\frac{\tilde{z}-1}{\tilde{\delta}-1} = 0.05$  to  $0.07$ ) does not yield reliable results. Usually, the measured velocity is larger than the value obtained from this equation.

It might be surmised that the use of the power law in terms of the shape factor as given by Eq. (2.3) [3] would eliminate some of the difficulties related to the  $1/n$ -power law. In this equation the exponent is expressed directly in terms of the shape factor. The latter can be easily computed from the measured velocity. When Eq. (2.3) was used employing the computed values of  $H$  and  $\theta$  significant discrepancies between the calculated (based on  $H$ ) and measured velocities were obtained. For instance, within  $\tilde{z} = 1$  to  $6$ , differences up to 10% were obtained. For increasing distance from the canopy the disagreement augmented.

The velocity variation above the roughness depends on the roughness element shape and, particularly, on the roughness density and arrangement. Recall that the crown is largest around  $\tilde{z} = 0.75$  and that in all cases a minimum velocity was monitored at  $\tilde{z} = 0.7$ . Thus, it was attempted to use Eq. (2.3) when the origin of the vertical coordinate was selected at  $\tilde{z} = 0.75$ . This endeavor did not lead to any acceptable improvement. It is suspected that this disagreement is caused by the strong dependence of the exponent in Eq.(2.3) on the value of the shape factor. Hence, the use of the latter as the single overall parameter for flow over high roughness is questionable.

The logarithmic law in its various formulations is widely used for describing the velocity within a turbulent boundary layer on rough surfaces. This law was proposed as a similarity solution for the boundary-layer flow. In the logarithmic law (see Eq. (2.11)), the similarity parameters are expressed by the friction velocity and roughness length. The former is equal to the square-root of the wall shear stress per unit mass which plays a very important role since it supplies the energy to the turbulence [2]. Its value and effect depend strongly upon the roughness features, i.e., on roughness shape, density and distribution. It is, further, important to remark that the direct measurement of the wall shear stress is extremely difficult. Consequently, under the assumption of constant shear stress layer [1] the friction velocity is usually deduced from the measured velocity variation. Similarly, the roughness length which is used as a length scale parameter is also estimated from the velocity measurement. In using the logarithmic law for rough walls, the vertical coordinate can be measured from a virtual surface which lies somewhere between the top and bottom of the roughness. Furthermore, this surface is presumably unique and experimentally determinable for each given roughness [2]. Particularly, in the case of flow on relatively high roughness, the adjustment of the vertical-coordinate origin is provided by the zero-plane displacement  $d$  leading to a modified logarithmic law (see Eq. (2.12)) [14,15]. The zero-plane displacement is a third similarity parameter characteristic to relatively high roughness. Its value is numerically evaluated in the same manner as the friction velocity and roughness length. Such a scheme can lead to erroneous

and physically unacceptable negative value for the zero-plane displacement [44,45].

Samples of the results obtained using the logarithmic law ( $d = 0$ ) and the modified logarithmic law ( $d \neq 0$ ) for HDC at  $\tilde{x} = 38.88$  are shown in Fig. 5.14. When the logarithmic law was employed, a kink is observed at about  $\tilde{z} = 2$ . Thus, two zones of logarithmic velocity variation are obtained (curve denoted by I in Fig. 5.14). The first extends from  $\tilde{z} = 0.75$  to 2 whereas the second above  $\tilde{z} = 2$ . Next, this kink can be eliminated by using the modified logarithmic law. Thus, it was attempted to encompass the entire boundary layer by employing this law. Unfortunately, this endeavor led, as expected, to a negative zero-plane displacement, i.e.,  $\tilde{d} = -0.7$  (curve II in Fig. 5.14). This result is physically unacceptable.

As mentioned earlier, the origin of the vertical coordinate used in the logarithmic law ought to be determined experimentally and is located somewhere within the roughness [2]. Therefore, it is interesting to examine if the origin (or the zero-plane displacement) can be determined when the friction velocity is known. In carrying out this examination, a value of 0.4, as commonly done, was used for the so-called universal von Kármán's constant  $\kappa$ . Thus, the slope of the modified logarithmic law  $U_* / \kappa$  is known. The friction velocity can be evaluated from the turbulent shear stress measured at the roughness surface by means of the relationship  $U_{*m} = (|\overline{uw}|_1)^{1/2}$  where  $U_{*m}$  is referred to as the measured friction velocity and  $(|\overline{uw}|_1)$  denotes the value of the shear stress at  $\tilde{z} = 1$ . Recall that the logarithmic law can express the velocity variation close to the wall, viz.,

within the inner 10 to 20% of the boundary layer [2]. When the zero-plane displacement is adjusted such that the required slope based on the measured friction velocity  $U_{*m}$  is satisfied, it was found that the inner layer extends about 20 to 30% of the boundary layer. Under these constraints the velocity variation obeys the modified logarithmic law over the inner 25% of the boundary-layer thickness when  $\tilde{d} = 0.75$ . The results of this computation are illustrated by curve III in Fig. 5.14. A kink is observed at  $\tilde{z} = 2.1$  (or  $\tilde{z} - \tilde{d} = 1.35$ ). Furthermore, for  $\tilde{z} > 2.1$ , the velocity also exhibits a logarithmic variation. On the other hand, the friction velocity for a given zero-plane displacement can be deduced from the slope of the velocity variations presented according to the modified logarithmic law. The friction velocity so obtained is referred to as the deduced friction velocity and designated by  $U_{*d}$ . For the sake of comparison, both deduced and measured friction velocities for all three cases are tabulated below:

Case	$\tilde{d}$	$\tilde{z}$	$\tilde{U}_*$	$\tilde{z}_0$
I	0	$2.0 \geq \tilde{z} \geq 0.75$	0.146	0.50
		$4.8 \geq \tilde{z} \geq 2.0$	0.197	0.73
II	-0.7	$4.8 \geq \tilde{z} \geq 0.75$	0.240	1.13
III	0.75	$2.0 \geq \tilde{z} > 1.1$	0.065†	0.06
		$4.8 \geq \tilde{z} \geq 2.0$	0.163	0.40

Note that  $\tilde{U}_* = U_*/U_\infty$  and  $\tilde{z}_0 = z_0/h$  where  $U_\infty = 6$  m/sec and  $h = 18$  cm. In carrying out all these computations  $\kappa = 0.4$  was employed.

In all the aforesaid three cases, the mean velocity changes according to a logarithmic law within limited zones although their slopes are different. Basically, the various combinations of the three similarity parameters  $U_*$ ,  $z_0$  and  $d$  can yield a logarithmic

†Measured friction velocity.

velocity variation. Particularly, since the selection of the zero-plane displacement for high roughness is practically arbitrary, different values of  $U_*$  and  $z_0$  can be obtained from a single measured velocity variation. Thus, it is very difficult to relate them to the roughness characteristics. This problem is discussed in Refs. 46 and 47 when field data and wind tunnel measurements, respectively, are analyzed. As a result, it is impossible to conclude, except in the case of negative  $d$ , what combination of the three similarity parameters is correct and/or what law provides a better representation.

Due to the relatively large uncertainty in evaluating the similarity parameters, it is surmised that the so-called universal constant  $\kappa$  would reveal a large scattering in its value. From a measured velocity profile, the three quantities  $U_*/\kappa$ ,  $z_0$  and  $d$  can be obtained solving three simultaneous equations assuming a logarithmic velocity variation. Then, if either  $U_*$  or  $\kappa$  is known, the other can be estimated from any combination of  $z_0$  and  $d$ . However, since it is practically impossible to relate them properly to the roughness characteristics, various values for  $\kappa$  are obtained even when  $U_*$  is measured. As a matter of fact, even von Kármán found that  $\kappa$  lies between 0.37 to 0.38 [4]. The value of 0.4 is commonly accepted on the basis of Nikuradse's experiment [6]. Results of several investigations tabulated in Ref. 48 reveal that  $\kappa$  ranges from 0.34 to 0.49 depending upon the particular source. When the field measurements reported in Ref. 49 are analyzed using the logarithmic law, the value of  $\kappa$  can vary from 0.25 to 0.49 depending on the data reduction. On the other hand, a value of 0.41 is employed for  $\kappa$  in Ref. 49. In Ref. 17, it is suggested that  $\kappa$  lies between 0.39 and 0.41 when the logarithmic law is used. Values of  $\kappa$  outside this range are

usually considered as a result from operations or assumptions which change the definition of this constant [17].

The large uncertainty in the value of von Kármán's constant for flow on high roughness elements is illustrated when its value is evaluated from wall shear-stress measurement. In Ref. 31, using similar roughness elements as in this work, the wall shear stress was measured by means of a shear plate. Simultaneously, the velocity change was monitored. Based on the data reported in Ref. 31, it was found that the velocity variation throughout almost the entire boundary layer in the fully developed flow region ( $x = 5, 6$  and  $7$  m) can be represented by the logarithmic law ( $d = 0$ ). The estimated value of  $U_* / \kappa$  is 225 cm/sec while the shear plate measurement yielded  $U_* = 50$  cm/sec. Thus,  $\kappa = 0.22$ . However, if the modified logarithmic law is employed when  $\tilde{d} = 0.7$ , the value of this constant becomes again 0.4 in the inner zone. In this case, a kink is observed at  $\tilde{z} = 1.85$ . This result indicates clearly that the experimental determination of  $\kappa$  based on either the logarithmic law or the modified logarithmic law cannot lead to any definite conclusion about the supposed universality of von Kármán's constant.

Further, it is worth pointing out that the constant  $\kappa$  was introduced in both Prandtl's mixing-length theory and von Kármán's similarity hypothesis as an empirical dimensionless coefficient of proportionality for the mixing length  $\ell$ . [1]. In the former  $\ell = \kappa z$  whereas in the latter  $\ell = \kappa \frac{dU}{dz} / \left( \frac{d^2U}{dz^2} \right)$ . When the shear stress and velocity variations are measured it is conceivable to evaluate the mixing-length change with height using the shear stress relationship [1]

$$\ell^2 = \frac{-\overline{uw}}{\left| \frac{dU}{dz} \right| \frac{dU}{dz}} \quad (5.5)$$

Under the assumption of linear variation of the mixing length with the distance from the wall close to the roughness [4], the value of  $\kappa$  can be computed using the shear-stress data (see Sec. 5.3). This computation was carried out in order to compare the value of  $\kappa$  for high roughness with its value for fine roughness [1,6]. Samples of the results of this computation within the fully developed flow region at three stations for both HDC and FDC cases are shown in Fig. 5.15. In both cases, the mixing length exhibits a linear variation with height from  $\tilde{z} = 0.75$  to 2.0. Extrapolation of the linear portion leads to  $\tilde{z} = 0.25$  at  $\ell = 0$ . Thus, if  $\ell$  is proportional to  $z$  it follows that an imaginary wall is possibly located at  $\tilde{z} = 0.25$ , i.e.,  $\ell = \kappa(\tilde{z} - 0.25)$ . Based on the results presented in Fig. 5.15 and using the aforementioned adjusted relationship for  $\ell$ , it was found that  $\kappa = 0.19$  for HDC and 0.165 for FDC. For the sake of comparison, the mixing length variation for  $\kappa = 0.4$  is also portrayed in Fig. 5.15. The obtained values of  $\kappa$  are quite different from the generally accepted value of 0.4. These results indicate that von Kármán's constant  $\kappa$  is not a universal constant for flow on high roughness elements. The turbulence structure for flow on rough walls, particularly, on high roughness elements, is strongly affected by the wall roughness. Hence, it is not reasonable to expect a similar mixing-length variation with height for all roughnesses. It appears that  $\kappa$  can be considered as a dimensionless scaling coefficient for the friction velocity determined by the particular roughness configuration and distribution.

In order to overcome the difficulties related to the estimation of zero-plane displacement, it was proposed in Ref. 28 to approximate the latter by the roughness height, i.e.,  $d = h$ , where  $h$  denotes the roughness height. Then,

$$\frac{U}{U_*} = \frac{1}{\kappa} \ln \frac{z - h}{z_0}, \quad (5.6)$$

where it is assumed that  $\kappa = 0.4$ . Thus, the origin of the vertical coordinate is located exactly at the roughness surface. A sample of the results using the modified logarithmic law where  $d = h$  is displayed in Fig. 5.16. In this figure the velocity distribution in the fully developed flow region for HDC case is shown. As previously, two zones of linear velocity variation with the logarithm of height are observed. A kink was obtained at about  $\tilde{z} = 2.0$ . Similar results were obtained for the FDC case. The friction velocities in two zones were deduced from the velocity data assuming  $\kappa = 0.4$ . It is interesting to compare the computed values of the friction velocity with its measured values at the roughness surface. The latter are provided by the shear stress measurement, i.e.,  $U_{*m} = (|\overline{uw}|_1)^{1/2}$  (see Sec. 5.3). The deduced and measured values of the friction velocity for both FDC and HDC cases are summarized below:

Zone	$\tilde{z}$	$\tilde{U}_{*d}$		$\tilde{x}$	$x$ (m)	$\tilde{U}_{*m}$	
		FDC	HDC			FDC	HDC
I	$2.0 > \tilde{z} > 1.0$	0.037	0.033	38.88	7.0	0.052	0.065
II	$\tilde{z} > 2.0$	0.122	0.138	52.77	9.5	0.045	0.058

Note that  $\tilde{U}_{*d}$ ,  $\tilde{U}_{*m} = U_{*d}/U_\infty$ ,  $U_{*m}/U_\infty$  and  $\tilde{x}$ ,  $\tilde{z} = x/h$ ,  $z/h$  where  $U_\infty = 6$  m/sec and  $h = 18$  cm. No agreement is observed with the measured friction velocity in either lower or upper zone.

The modified logarithmic law, Eq. (2.12), is based on the far-reaching assumption that the friction velocity is locally constant with height. Furthermore, the roughness length and zero-plane displacement are assumed to be determinable for given roughness and flow conditions. Basically, these assumptions are not modified even if the zero-plane displacement is replaced by the roughness height. On the other hand, due to the arbitrary approximation of  $d$  by  $h$ , it is doubtful if the local constancy of the other two similarity parameters is satisfied. Presumably, both Eqs. (2.12) and (5.6) can be used to describe the same velocity variation. Then, by equating these two relationships, the friction velocity employed in Eq. (5.6) is

$$U_{*h} = U_* \frac{\ln\left(\frac{z-d}{z_0}\right)}{\ln\left(\frac{z-h}{z_{oh}}\right)}. \quad (5.7)$$

In this equation the subscript  $h$  denotes the similarity parameters used in the modified logarithmic law when  $d$  is approximated by the roughness height. Since both  $U_*$  and  $z_0$  are assumed of being locally constant in Eq. (2.12), it ensues that  $U_{*h}$  is no longer locally constant but a function of height. A similar result about the roughness length used in Eq. (5.6) i.e.,  $z_{oh}$ , is obtained employing the same approach. Calculation of both the friction

velocity and roughness length by means of Eq. (5.6) over successive small intervals (about 1 to 2 cm) substantiated the aforesaid conclusions [33]. This computation was carried out for flow on similar roughness as employed in this investigation. It was found that both  $U_{*h}$  and  $z_{oh}$  vary drastically with height [33]. When a similar computation was performed using Nikuradse's data [6], the assumption of local constancy of friction velocity and roughness length was satisfied. These results are presented in Ref. 33. Recall that the height of the roughness elements utilized in this work and in Ref. 33 is more than 15% of the boundary layer thickness. On the other hand, the roughness used in Ref.6 ranged from 0.8 to 6.7% of the latter. Hence, the use of the modified logarithmic law under the assumption that  $d$  is approximated by the roughness height is not feasible for flow on high roughness.

Generally, a turbulent boundary layer on a plate can be viewed as a wake-like flow constrained by a wall [17]. As a result, the velocity variation throughout the entire boundary layer can be described by a linear combination of the logarithmic law (the law latter accounts for the departure of the velocity variation from the logarithmic law within the outer part of the boundary layer [3]). As mentioned earlier, it is suggested to use the logarithmic law, particularly, in the inner part of the boundary layer, i.e., within the lower 10 to 20% of the boundary layer-thickness [2]. Thus, the constraints on using the logarithmic law to express the velocity variation over high roughness are retained in Eq.(2.14).

Consequently, in order to use Eq. (2.14) for flow on high roughness, it is necessary to introduce the zero-plane displacement. It follows that the latter must be used as the virtual origin of the vertical distance for the wake function. Then, the modified law of the wake in terms of the velocity defect law is

$$\frac{U_{\infty} - U}{U_*} = \frac{1}{\kappa} \ln \frac{z-d}{\delta-d} + \frac{\pi[x]}{\kappa} (2 - \omega[\frac{z-d}{\delta-d}]) . \quad (5.8)$$

where  $\pi[x]$  is the profile parameter and  $\omega[\frac{z-d}{\delta-d}]$  denote the modified wake function. The normalized conditions for the latter, similar to those of the wake function in Ref. 17, are

$$\omega = 0 \quad \text{at} \quad z = d , \quad (5.9a)$$

and

$$\omega = 2 \quad \text{at} \quad z = \delta , \quad (5.9b)$$

and

$$\int_0^1 \omega d(\frac{z-d}{\delta-d}) = 1 . \quad (5.9c)$$

As previously mentioned,  $d$  can be approximated based on the shear stress measurements (see Sec. 5.3) and using the modified logarithmic law (Eq. (2.12)). Since the local friction velocity is known, i.e.,  $U_{*m} = (|\overline{uw}|_1)^{1/2}$ , the slope of the velocity variation in the modified logarithmic law is  $U_{*m}/\kappa$ , where it is assumed that  $\kappa = 0.4$  for consistency with the results presented in Ref. 17. Then, the zero-plane displacement was approximated by successive trials until the linear

logarithmic variation agreed reasonably with the required slope. In carrying out this procedure, the velocity measured within the inner 20% of the boundary layer, i.e.,  $\tilde{z} = 1$  to 1.85 ( $z = 18$  to 33 cm), was employed. The results of this computation for both FDC and HDC cases within the fully developed flow region are shown in Fig. 5.17. Recall that the result of a similar computation for HDC is shown in Fig. 5.14. It was found that  $\tilde{d} = 0.85$  for FDC and 0.75 for HDC, respectively.

Now, once  $\tilde{d}$  is determined, the modified law of the wake (Eq. (5.8)) can be used. The wake function was computed using the table in Ref. 17 when the modified argument  $\frac{z-\tilde{d}}{\delta-\tilde{d}}$  was employed. In order to present the measured velocity according to Eq. (5.8), the measured friction velocity at roughness top, i.e.,  $U_{*m} = (|\overline{uw}|_1)^{1/2}$ , is used to normalize the defect velocity. The vertical distance is made dimensionless employing the boundary-layer thickness which is measured from the virtual origin. The mean velocities obtained in the fully developed flow regions for FDC and HDC cases are shown in Figs. 5.18 and 5.19, respectively. Notice that terms on the right hand-side of Eq. (5.8) except the profile parameter  $\pi[x]$  can be evaluated when the boundary-layer thickness and virtual origin are known. Thus, once the normalized defect velocity is obtained experimentally, the profile parameter for the best fitting curve to the measured velocity can be evaluated. Next, using this evaluated profile parameter, the defect velocity variation throughout the entire boundary layer is calculated by means of Eq. (5.8), and is displayed by solid line in Figs. 5.18 and 5.19. The computed profile parameters for the best fitting are tabulated below.

$\tilde{x}$	x (m)	$\pi[x]$	
		FDC	HDC
38.88	7.0	1.10	0.92
47.22	8.5	---	0.92
52.77	9.5	1.32	1.12

On the other hand, the profile parameter is related to the local friction velocity at the wall by Eq. (2.17). Then, using the normalized condition of the modified wake function, i.e., Eq. (5.9b), Eq. (2.17) becomes

$$\frac{2\pi[x]}{\kappa} = \frac{U_{\infty}}{U_{*}} - \frac{1}{\kappa} \ln \left\{ \frac{(\delta-d)U_{*}}{\nu} \right\} - C_1 \quad (5.10)$$

In Eq. (2.17), the constant  $C_1$  was determined empirically to fit the velocity data presented in Ref 17 and a value of 5.1 is proposed. However, it is questionable to utilize this value for  $C_1$  in Eq. (5.10) since the roughness elements in this work are extremely high compared with those in Ref. 17. As a matter of fact, if  $C_1 = 5.1$  is used in Eq. (5.10), the profile parameter would become negative. For instance, the profile parameter at  $\tilde{x} = 38.88$  ( $x = 7.0$  m) in HDC would be -2.85. Therefore, Eq. (5.10) cannot be used to estimate  $\pi[x]$ . The profile parameter can be also obtained by utilizing the relationship [17]

$$\pi[x] + 1 = \kappa \frac{\delta^* U}{\delta U_{*}} \quad (5.11)$$

Note that all the quantities in this equation can be evaluated from

the velocity measurements. For flow on high roughness, Eq. (5.11) is modified due to the virtual origin of the vertical distance. Thus,

$$\pi[x] + 1 = \kappa \frac{(\delta^* - \delta_d^*)U}{(\delta - d)U_*}, \quad (5.12)$$

where  $d$  is the zero-plane displacement,  $\delta_d^*$  is the fraction of the displacement thickness below the virtual origin ( $z = 0$  to  $d$ ) and  $U_*$  is approximated by the measured friction velocity at the roughness surface  $U_{*m} = (|\overline{uw}|)_1^{1/2}$ . The computed profile parameters by means of Eq. (5.12) are compared with those computed for the best fitting curves in the table below:

$\tilde{x}$	x (m)	FDC		HDC	
		$\pi_1$	$\pi_1/\pi_f$	$\pi_1$	$\pi_1/\pi_f$
38.88	7.0	1.60	1.45	0.86	0.93
47.22	8.5	---	---	0.97	1.05
52.77	9.5	1.96	1.48	1.47	1.33

In the above table,  $\pi_1$  denotes the profile parameter calculated by means of Eq. (5.12) whereas  $\pi_f$  designates the value determined for the best fitting to the experimental data. It is important to mention that the non-modified relationship for the profile parameter, i.e., Eq. (5.11), always yields larger value than Eq. (5.12). At  $\tilde{x} = 38.88$  and 42.77 for HDC, the differences between  $\pi_1$  and  $\pi_f$  are negligibly small while at the other locations they are rather large. No definite trend can be observed.

Notice that the velocity variation in the fully developed flow region are well expressed by means of Eq. (5.8) if the five parameters,

viz.,  $U_\infty$ ,  $U_*$ ,  $\delta$ ,  $d$  and  $\pi[x]$ , are known. The relationships among these five parameters are yet to be found. Moreover, it seems that the relationships used to determine the profile parameter from the velocity measurements do not yield acceptable results. Therefore, the use of modified law of the wake, i.e., Eq. (5.8), for flow over high roughness elements is limited by the relatively large number of undetermined parameters.

The results presented concerning both the logarithmic law and the law of the wake indicate clearly the difficulties and uncertainties in evaluating the various similarity parameters. Particularly, the estimation of  $U_*$  and  $d$  is most critical. It appears that these shortcomings can preclude their use. Consequently, it is important to postulate such similarity parameters which can be easily obtained from the velocity measurement. The evaluation of the zero-plane displacement  $d$  and, hence, the location of the origin for the vertical distance is the most crucial problem. Recall that  $d$  was introduced to account for the presence of the roughness. In order to overcome this problem, it is suggested to define the origin of the vertical distance exactly at the wall. Obviously, such an approach does not include the effects of the roughness on the vertical coordinate. On the other hand, it is expected to account for the roughness through appropriate similarity parameters.

As mentioned previously, the use of a power law to describe the velocity within a turbulent boundary layer is commonly accepted and experimentally verified. When the origin of the vertical coordinate is at the wall, the generalized power law can be written in the form

$$\frac{U}{U_s} = B \left( \frac{z}{L_s} \right)^n, \quad (5.13)$$

In this relationship  $U_s$  and  $L_s$  are the velocity and length scales, respectively, which must be determined, and  $B$  is a coefficient of proportionality. The exponent  $n$  depends on the flow Reynolds number and decreases as the latter increases [1]. On the average, the Reynolds number based on  $U_\infty$  and  $\delta$  ranges from 200,000 to 300,000. Next, expansion of Eq. (5.12) into Taylor series with respect to  $n$ , when quadratic and high order terms are neglected since  $n$  is smaller than unity, leads to a logarithmic expression,

$$\frac{U}{U_s} = B + A \ln \frac{z}{L_s}, \quad (5.14)$$

where  $A = nB$ . This relationship is practically an asymptotic form of the power law when the exponent is small enough.

In order to use such a generalized logarithmic relationship it is essential to determine the velocity and length similarity parameters, i.e.,  $U_s$  and  $L_s$ . To start with, it is postulated to use the free-stream velocity as the velocity scale. Basically, the free-stream velocity can be easily measured. As a length scale, it is proposed to employ the roughness height which is generally known. The velocity distributions in the fully developed flow region using the aforesaid scales are shown in Figs. 5.20 and 5.21 for FDC and HDC, respectively. At all measurement stations, the velocity profile exhibits a kink. Moreover, with increasing downstream distance the kink is monitored

at higher elevation above the roughness. For instance, the height of the kink  $z_k$  within the fully developed flow region for both FDC and HDC cases is summarized in the table below:

$\tilde{x}$	x (m)	$\tilde{z}_k$	
		FDC	HDC
27.77	5.0	1.6	1.5
38.88	7.0	1.9	2.0
47.22	8.5	---	2.4
52.77	9.0	1.9	2.7

Note that  $\tilde{z}_k = z_k/h$  where  $h = 18$  cm. Based on this change in slope, the boundary layer is divided into two domains. The zone below the kink is called the inner zone whereas the zone above it is defined as the outer zone. This distinction is solely based on the kink in the mean velocity variation. Thus, the inner zone is not related to the so-called internal boundary layer [50].

Within the inner zone, all the profiles collapse on a single line as observed in Figs. 5.20 and 5.21. Therefore, the postulated scales, i.e.,  $U_\infty$  and  $h$ , are similarity parameters. Then, in the inner zone the generalized logarithmic law is

$$\frac{U}{U_\infty} = B_i + A_i \ln \frac{z}{h}, \quad (5.15)$$

where  $A_i$  and  $B_i$  are constants to be determined. The values of these two constants depend upon the flow conditions, namely, the free-stream velocity and the roughness structure. In the FDC case  $A_i = 0.312$

and  $B_i = 0.330$  whereas in the HDC case  $A_i = 0.346$  and  $B_i = 0.260$ . Recall that in both cases the same free-stream velocity was used.

When the free-stream velocity and roughness length are utilized as the similarity parameters for the outer zone, the velocity profiles do not coincide on a single curve. At each position a logarithmic variation is obtained. Moreover, the velocity profiles at all stations possess exactly the same slope as clearly seen in Figs. 5.20 and 5.21. This indicates the validity of the free-stream velocity as a similarity parameter. On the other hand, the vertical translation of each velocity profile is due to the use of the roughness height as the length scale. The roughness height is not a characteristic property of the boundary layer. The overall properties of the boundary layer are functions of the longitudinal position. Consequently, it is feasible to use one of the integral characteristics of the flow as a length scale. The momentum thickness depends on the flow above the canopy to a larger extent than the displacement thickness as shown in Fig. 5.11. Hence, it is suggested to utilize the momentum thickness, which can be easily evaluated from velocity measurement, as the length similarity parameter. As a result, for the outer zone, the generalized logarithmic law becomes

$$\frac{U}{U_\infty} = B_0 + A_0 \ln \frac{z}{\theta}, \quad (5.16)$$

where  $\theta$  is the local total momentum thickness, and  $A_0$  and  $B_0$  are constants to be determined. The velocity profiles in the outer zone using Eq. (5.16) for both FDC and HDC are shown in Figs. 5.22 and 5.23.

All the velocity distributions do collapse on a single curve. As previously, their values depend on the free-stream velocity and roughness structure. The values of  $A_0$  and  $B_0$  in FDC case are 0.424 and 0.176, respectively. In the HDC case,  $A_0$  is 0.486 and  $B_0$  is 0.076. Thus, in the outer zone the free-stream velocity and momentum thickness can be used as similarity parameters.

In order to substantiate these results, a similar approach was employed using the data for flow over pegs [30]. When Eq. (5.15) was utilized, similar velocity variations were obtained for the inner zone. The velocity changes are shown in Fig. 5.24. Within the outer zone, the velocity profiles are described by non-coincident parallel lines. Thus, a similar result as for the flow over the canopies is obtained. Next, using Eq. (5.16) for the outer zone all the velocity profiles are represented by a single curve as portrayed in Fig. 5.25.

*The important aspect of these results is the feasibility of the generalized logarithmic relationships. The similarity parameters, i.e., free-stream velocity, roughness height and momentum thickness, can be easily obtained. One of the problems related to the generalized logarithmic relationships is the determination of the two constants A and B. These constants can be easily determined experimentally for a given roughness.*

### 5.3 Shear stress and turbulence survey

The longitudinal fluctuating velocity component, i.e.,  $u$  and its energy spectra were measured using a normal hot wire simultaneously with the mean velocity measurements. The lateral and vertical fluctuating components, i.e.,  $v$  and  $w$ , and the turbulent shear

stress  $-\overline{uw}$  were monitored by means of a yawed hot-wire probe as described in Section 4.2. The yawed-wire measurements for the FDC case were carried out at 13 locations along the canopy centerline over a distance of 12 m ( $x = -1$  to 11 m). At each location, the measurements along the  $z$ -axis were performed at 11 to 15 stations over a height up to 73-112 cm among which 4 to 5 stations were located in the canopy. For the HDC case, the yawed-wire survey was conducted at 13 locations over a distance of 12 m ( $x = 0$  to 12 m). At each location, the measurements were performed at 11 to 15 stations over a height up to 73-110 cm among which 3 to 5 stations were situated inside the roughness.

The energy extracted from the mean flow is supplied to the longitudinal velocity fluctuation through the work of the turbulent shear stress. In the energy equation this is expressed by the production term, i.e.,  $-\overline{uw} \frac{\partial U}{\partial z}$ . Then, by the action of the pressure fluctuation, the longitudinal turbulent energy is partly distributed to the vertical and lateral components depending upon their dissipation rates [2].

In order to assess the effect of the canopy on the turbulent shear stress the latter is normalized with respect to its value at the top of the canopy leading edge, i.e, at  $\tilde{x}, \tilde{z} = 0,1$  denoted by  $\overline{uw}[0,1]$ . The distributions of the turbulent shear stress along the  $z$ -axis are displayed in Figs. 5.26a and 5.26b for the FDC case whereas Figs. 5.27a and 5.27b represent HDC. At the very beginning of the transition region, a drastic amplification of the turbulent shear stress is observed in the vicinity of the canopy surface. Up to  $\tilde{x} = 27.77$  ( $x = 5$  m), each turbulent shear stress profile possesses a maximum. The latter is not observed beyond  $\tilde{x} = 27.77$ . These maxima shift outward as the downstream distance increases. The change in the position of the maxima along the

x-axis and the longitudinal variation of the maximum shear stress are shown by the inserts in Figs. 5.26a and 5.27a.

Generally, the turbulent shear stress distribution is strongly affected by the longitudinal pressure gradient [51]. In boundary-layer theory, the vertical pressure variation is usually neglected [1]. This experiment was conducted at constant pressure in the free stream and, hence, the longitudinal pressure gradient in the boundary layer should be zero. When the pressure gradient is zero or favorable, the maximum shear stress in flow on smooth walls is obtained at the wall [51]. Then, in flow on rough surfaces maximum stress is expected at the roughness top. On the other hand, the measured shear stress indicates clearly, as shown in Figs. 5.26a and 5.27a, that its maximum value occurred away from the roughness surface. The canopy boundary layer is highly turbulent and thick compared with that on fine roughness elements (e.g., sands or gravels). Within such a thick boundary layer the fluctuating velocities can affect the vertical pressure gradient and, hence, the local longitudinal pressure gradient, i.e.,  $P(x,z)$ . When an adverse pressure gradient exists in flow on smooth walls, the maximum turbulent shear stress occurs some place away from the wall [51]. Consequently, it is surmised that a local adverse pressure gradient exists across the boundary layer and, particularly, a relatively large pressure gradient prevails up to  $\tilde{x} = 30$  (within the so-called transition region) although the pressure in the freestream flow is presumably constant.

The pressure variation within the boundary layer can be estimated through momentum balance of the equation of motion. The flow in the transition region is not strictly two-dimensional. However, the results

shown in Figs. 5.7 and 5.8 indicate that in the neighborhood of the canopy centerline ( $y \leq |30 \text{ cm}|$ ) the flow is approximately two-dimensional. The vertical component of the momentum equation for two-dimensional steady flow in a dimensionless form is

$$\tilde{U} \frac{\partial \tilde{W}}{\partial \tilde{x}} + \tilde{W} \frac{\partial \tilde{W}}{\partial \tilde{z}} = - \frac{\partial \tilde{P}}{\partial \tilde{z}} + \frac{1}{\text{Re}_h} \left( \frac{\partial^2 \tilde{W}}{\partial \tilde{x}^2} + \frac{\partial^2 \tilde{W}}{\partial \tilde{z}^2} \right) - \left( \frac{\partial \tilde{uw}}{\partial \tilde{x}} + \frac{\partial \tilde{w}^2}{\partial \tilde{z}} \right), \quad (5.17)$$

where  $\text{Re}_h$  denote the Reynolds number based on the free-stream velocity and roughness height. Its value is about 57,000 ( $\nu = 0.189 \text{ cm}^2/\text{sec}$ ). In this equation, the velocity components are referred to the free-stream velocity  $U_\infty$ , the pressure to the free-stream dynamic pressure. Similarly,  $\tilde{uw} = \overline{uw}/U_\infty^2$  and  $\tilde{w} = \overline{w^2}/U_\infty^2$ . All the terms in Eq. (5.17) but the vertical pressure gradient were computed from the measured data. Samples of the momentum balance in the HDC case are provided by Fig. 5.28 for the transition region and by Fig. 5.29 for the fully developed flow region. The momentum balance was computed graphically and numerically. In these figures the viscous shear stress terms are not shown since it was found that they are completely negligible with respect to the inertia and turbulent contributions, i.e., less than 1% of the latter terms. Furthermore, in the fully developed flow region (Fig. 5.29) the longitudinal gradient of  $\overline{-uw}$  is disregarded because it was found to be totally insignificant compared with the other terms. The vertical mean velocity was evaluated by integrating the two-dimensional continuity equation graphically. Within the boundary layer, as observed in Fig. 5.5, the longitudinal gradient of the horizontal velocity  $U$  is either negative or zero. The former slope is prevalent throughout the transition region. In the fully developed region the streamwise gradient of the

horizontal velocity is practically zero but slightly negative far away from the roughness. Consequently, the vertical component  $W$  increases monotonically with height. The vertical velocity computed by this method becomes a constant value as the longitudinal gradient of  $U$  approaches zero. It is important to remark that  $W = 0$  at the wall. Moreover, for sufficiently large distance from the boundary layer, where the flow is presumably uniform, the vertical velocity should be zero. The latter condition implies that the streamwise gradient of  $U$  should be positive away from the boundary layer. Thus, it is surmised that the horizontal velocity component will increase slightly with downstream distance over rather large vertical distance. The value of the vertical velocity component at the outer edge of the boundary layer decreases gradually from about  $0.1 U_\infty$  in the transition region to less than  $0.01 U_\infty$  in the fully developed flow domain. Hence, the longitudinal gradient of  $W$ , i.e.,  $\partial \tilde{W} / \partial \tilde{z}$ , is finite in the transition region and becomes negligibly small in the fully developed flow region. Within the transition region, the vertical pressure gradient  $\partial \tilde{P} / \partial \tilde{z}$  shown by the broken line in Fig. 5.28, is mainly balanced by the inertia term  $\tilde{U} \partial \tilde{W} / \partial \tilde{x}$  in the outer part of the boundary layer ( $\tilde{z} > 2$ ) and by the turbulent term  $\underline{\underline{\partial w^2 / \partial \tilde{z}}}$  within its inner part. In the fully developed flow region, the vertical pressure gradient displayed by the broken line in Fig. 5.29 is balanced by  $\underline{\underline{\partial w^2 / \partial \tilde{x}}}$  throughout the entire boundary layer since the inertia term  $\tilde{U} \partial \tilde{W} / \partial \tilde{x}$  is negligibly small. Recall that in the transition region a drastic increase in the turbulent shear stress occurs below  $\tilde{z} = 2$  up to  $\tilde{x} = 8.33$  as observed in Figs. 5.28 and 5.30. Therefore, to assess the effect of the pressure on the turbulent shear stress distribution, the equation of motion can be simplified for

both the fully developed flow region and the lower part of the transition domain by

$$\frac{\partial \tilde{P}}{\partial \tilde{z}} = - \frac{\partial \overline{w^2}}{\partial \tilde{z}} \quad (5.18)$$

A similar relationship, for thin boundary layer on flat plate based on order of magnitude considerations, is suggested in Ref. 3. Integration of Eq. (5.18) when  $P = P_\infty = \text{const.}$  and  $\overline{w^2} = 0$  at sufficiently large vertical distance leads to

$$\tilde{P} = \tilde{P}_\infty - \overline{w^2} \quad (5.19)$$

Thus, by differentiating Eq. (5.19) the longitudinal pressure gradient is

$$\frac{\partial \tilde{P}}{\partial \tilde{x}} = - \frac{\partial \overline{w^2}}{\partial \tilde{x}} \quad (5.20)$$

According to this relationship, the local longitudinal pressure gradient can be evaluated directly from the measured streamwise distribution of the vertical fluctuating velocity  $\overline{w^2}$ . Samples of the results at five locations in the HDC case are displayed in Fig. 5.30. Within the beginning of the transition region, relatively high adverse pressure gradient is observed near the roughness surface. With increasing vertical distance, the streamwise pressure gradient becomes favorable. As the outer edge of the boundary layer is approached the latter vanishes gradually. The adverse pressure gradient becomes negligible

with downstream distance. These results indicate that the strong adverse pressure gradient is caused by the roughness which is a drastic step obstruction. This pressure gradient leads to local occurrence of maximum turbulent shear stress somewhere away from the roughness top. In addition, due to eventual flow separation from each roughness element, weak adverse pressure gradient arises in the immediate vicinity of the roughness surface. This phenomenon occurs not only in the transition region but in the fully developed flow domain. For instance, in the latter region, dimensionless adverse pressure gradient of order of  $10^{-4}$  was monitored up to  $\tilde{z} = 1.75$ . However, this weak adverse pressure gradient may be sufficient to cause the materialization of the maximum turbulent shear stress away from the roughness surface. Similar distribution of the turbulent shear stress were obtained in flow on fine roughness [52].

The increase of the turbulent shear stress, which represents the rate of turbulent momentum transport, indicates the canopy effect on momentum flux (see Figs. 5.26a to 5.27b). Generally, when a fully developed turbulent flow encounters a change in surface roughness, the effects of the change are felt within a so-called internal boundary layer [50]. This layer grows in depth with downstream distance. Most of the published studies about the internal boundary layer are based on the mean velocity variation. The change in the turbulence characteristics, particularly, the turbulent shear stress, due to new roughness conditions were treated indirectly employing the friction velocity. For instance, in Refs. 50 and 53, the internal boundary layer thickness is computed assuming logarithmic variation of the mean velocity and using von Karman's integral momentum equation. In Refs. 54 and 55, the

displacement of streamlines is used to estimate the growth of the internal boundary layer. It is important to remark that the flow within the beginning of the internal boundary layer is in a transitory state. In the latter state, both friction velocity and roughness length change with downwind distance for a given roughness [33]. Hence, it is questionable to employ a logarithmic velocity distribution for evaluating the internal boundary-layer thickness under the assumption that the two aforesaid scale parameters remain unchanged. The concept of the internal boundary layer is based on the assumption that the rate of adjustment of the turbulent shear stress to the new roughness is sufficiently rapid below a certain interface [53]. Above this interface, neither velocity nor stress has time to change. Consequently, it is theorized that the development of the internal boundary layer must be determined on the basis of the turbulent shear stress variation caused by the new roughness. The extent of the internal boundary layer is estimated from the shear stress evolution due to the new roughness as compared with the stress upstream of the roughness discontinuity. Then, the internal boundary-layer thickness  $\delta_i$  can be defined as the height where the new turbulent shear stress is equal to that at  $\tilde{x} = 0$ , i.e.,  $\delta_i$  is the height where  $\overline{uw}[x]/\overline{uw}[0] = 1$ . According to this definition, the growth of the internal boundary layer is displayed in Fig. 5.31. No difference in the growth of the internal boundary layer between FDC and HDC is noticeable up to  $\tilde{x} = 20$ , ( $x = 3.6$  m). Beyond the latter, the internal boundary-layer thickness is about 90% of the total boundary-layer thickness for FDC case and 97% for HDC case. Thus, the internal boundary layer thickness is significant up to  $\tilde{x} = 20$ . Within this region it was found that the internal boundary layer grows proportionally

to a power of downstream distance

$$\tilde{\delta}_i \propto \tilde{x}^{0.54} \quad , \quad (5.21)$$

where  $\tilde{\delta}_i = \delta_i/h$  and  $\tilde{x} = x/h$ . Thus, the internal boundary layer grows similarly to the width of a two-dimensional wake which is proportional to the square-root of the downwind distance [1]. In Ref. 56, assuming a power law variation of mean velocity, i.e.,  $U \propto z^{1/2}$ , the same result is obtained. This indicates, as previously pointed out, that the flow in the transition region has two-dimensional wake-like characteristics due to the large step obstruction (the canopy). On the other hand, in Refs. 50 and 53 where the internal boundary layer is determined from the mean velocity profiles based on a logarithmic law, its growth is expressed by  $\tilde{\delta}_i \propto \tilde{x}^{0.8}$  for  $\tilde{x} > 10^3$  where  $\tilde{\delta}_i = \delta_i/z_0$  and  $\tilde{x} = x/z_0$ . The origin of  $x$  is exactly at the roughness discontinuity and  $z_0$  designates the roughness length for the new roughness. Note that this variation is not valid in the region close to the roughness change, e.g.,  $x < 10$  m [50].

It is important to examine the change in the turbulence intensity along the canopy. The variation of longitudinal turbulence intensity based on the free-stream velocity, i.e.,  $T_{u\infty} = u_{rms}/U_\infty$  where  $U_\infty = 6$  m/sec, are shown along seven isoheights in Fig. 5.32 for FDC and in Fig. 5.33 for HDC. The variations of turbulence intensity for FDC and HDC cases are qualitatively similar. In the inner part ( $\tilde{z} \leq 2$ ) the turbulence augmentation occurs mostly up to  $\tilde{x} = 10$ . In the outer portion, the increase is more gradual extending up to  $x = 50$  at

$\tilde{z} = 6$ . By and large, at the same heights, the fluctuating velocity is smaller in the HDC case than in the FDC case. Below  $\tilde{z} = 3$ , the turbulence intensity along isoheights exhibits an oscillatory variation.

The vertical turbulence intensities, i.e.,  $T_{w\infty} = w_{rms}/U_{\infty}$ , along six isoheights are depicted in Figs. 5.34a and 5.34b for FDC case whereas in Fig. 5.35 for HDC. The overall variation of the vertical turbulence intensity is qualitatively similar to that of the longitudinal component. Change is noticeable up to  $\tilde{z} = 3$ .

The coefficient of anisotropy, which is defined by  $w_{rms}/u_{rms}$ , is a measure of the anisotropy of turbulence. The values of the coefficient in the fully developed flow region are displayed in Fig. 5.36 for both FDC and HDC cases. For the sake of comparison, the results obtained in and above a jungle-like forest [57], and those for a deciduous forest [58] are shown in the same figure. A reasonable agreement between the wind-tunnel data and field measurements results is observed.

#### 5.4 Turbulent-energy survey

The turbulent flow field cannot be described in detail due to its inherent randomness. Thus, a statistical description under the assumption of ergodicity [59,60] is necessary to express the characteristics of the turbulent flow. It is possible to describe the turbulent motion by means of frequency spectral analysis. Through this analysis, the kinetic energy of the fluctuating velocity is considered as being the sum of the energy associated with each frequency. Since the longitudinal turbulent velocity is predominant the results of the spectrum measurements for it are presented.

The one-dimensional wave-number density function  $\phi[k]$  is defined as [18]

$$1 = \int_0^{\infty} \phi[k] dk , \quad (5.22)$$

where  $\phi[k]dk$  is the amount of kinetic energy within the wave number from  $k$  to  $k + dk$  normalized by the total kinetic energy per unit mass  $\overline{u^2}$ . This quantity is called the energy-containing spectrum. Then, the dimensionless kinetic energy (or the energy-containing spectrum) within a wave number interval  $0$  to  $k$  is expressed by

$$\frac{\overline{u^2}[k]}{\overline{u^2}} = \frac{\overline{u^2}[k]}{\overline{u^2}} = \int_0^k \phi[k] dk . \quad (5.23)$$

The turbulent energy spectrum can be obtained experimentally in the frequency domain. The frequency spectrum is connected with the spacial correlation function by Taylor's hypothesis [61]. In terms of the frequency  $n$  and the local mean velocity  $U$ , the wave number is

$$k = \frac{2\pi n}{U} , \quad (5.24)$$

and the wave length (or eddy size) is

$$L = \frac{U}{n} . \quad (5.25)$$

Hence, the turbulent flow is considered as being composed of infinite number of eddies of various sizes.

At large Reynolds numbers, Kolmogoroff postulated that the turbulent motion is locally isotropic independent of the anisotropy of the large scale motions, i.e., local isotropy [62]. Moreover, for sufficiently

high Reynolds numbers, there is a subrange within the energy spectrum where the inertial transfer of energy is the dominating process, i.e., the inertial subrange [63]. The turbulence within the latter is statistically independent of the energy-containing eddies and strong dissipation [18]. Under the assumption of local isotropy within the inertial subrange, the wave-number density function, by dimensional arguments, is [18]

$$\phi[k] = \frac{1}{u^2} \beta \epsilon^{2/3} k^{-5/3}, \quad (5.26)$$

since  $\phi[k]$  as defined in Eq. (5.22) is normalized by  $\overline{u^2}$ . In this equation,  $\epsilon$  stands for the energy dissipation rate whose dimension is  $(\text{length})^2/(\text{time})^3$  (see Eq. (5.28)) and  $\beta$  is assumed to be a universal constant. The latter is about 0.5 [12].

The frequency spectra were measured using a recording wave analyzer (see Eq. (4.8)). Each spectrum was normalized by the mean square value of output voltage corresponding to the total kinetic energy per unit mass  $\overline{u^2}$ . This normalized spectrum is the one-dimensional frequency density function which is denoted by  $f[n]$ . The one-dimensional wave-number density function  $\phi[k] = (U/2\pi)f[n]$  [18]. In the following discussion, the results in the fully developed flow region at  $\tilde{x} = 38.88$  ( $x = 7$  m) are presented. The wave number spectra for FDC case at five selected heights and for HDC at four selected heights are displayed in Figs. 5.37 and 5.38, respectively. The curve corresponding to  $k^{-5/3}$  is also shown in these figures. Since, at first glance, a  $k^{-5/3}$  curve appears to provide a reasonable fit to the measured spectra within most parts of the wave number range, it is assumed that each spectrum possesses

an inertial subrange. However, it is pointed out in Ref. 64 that the Reynolds numbers for common laboratory flows are not sufficiently high so that an inertial subrange can occur. Particularly, in the boundary-layer flow, local isotropy and, hence, inertial subrange may not be obtained [18]. Consequently, it is of importance to examine the eventual existence of local isotropy and/or inertial subrange.

The rate of turbulent energy dissipation for isotropic turbulence in terms of the one-dimensional wave number density function is [64]

$$\epsilon = 15\nu \overline{u^2} \int_0^{\infty} k^2 \phi[k] dk, \quad (5.27)$$

since  $\phi[k]$  in Eq. (5.22) is normalized by  $\overline{u^2}$ . Note that Eq. (5.27) is derived from the three-dimensional wave-number density function by assuming that  $\phi[k]$  is proportional to  $k^{-7}$  for very large wave numbers and  $\phi[k]$  and  $\frac{\partial\phi[k]}{\partial k}$  are finite as  $k \rightarrow 0$ . In Eq. (5.27),  $\nu$  is the kinematic viscosity and  $k^2\phi[k]$  is referred to as the dissipation spectrum. The fraction of the normalized energy dissipation within the wave number interval 0 to  $k$  is defined as

$$\tilde{\epsilon}[k] = \frac{\epsilon[k]}{\epsilon} = \frac{\int_0^k k^2 \phi[k] dk}{\int_0^{\infty} k^2 \phi[k] dk}. \quad (5.28)$$

Both energy-containing spectra and dissipation spectra multiplied by  $k$ , i.e.,  $k\phi[k]$  and  $k^3\phi[k]$ , are portrayed in Fig. 5.39 for the FDC case at  $\tilde{z} = 1.03$  and  $3.19$  ( $z = 18.5$  and  $57.5$  cm). The areas under these curves represent the total turbulent kinetic energy and the rate of energy dissipation, respectively, since  $\phi dk = k\phi d(\ln k)$  and

$k^2\phi = k^3\phi d(\ln k)$ . The basic condition for the occurrence of an inertial subrange is that the contributions within at least one decade range to both energy-containing and energy-dissipation spectra are negligibly small [64]. In other words, the energy-dissipation range must be widely separated from the energy-containing range. The results shown in Fig. 5.39 reveal that the aforementioned condition is not adequately satisfied. At all heights, for both FDC and HDC cases, similar situations were observed. Moreover, as vertical distance increases, both energy-containing and energy-dissipation ranges shift to smaller wave number range (larger eddy size range). For instance, the value of  $k\phi[k]$  is maximum for  $k = 0.17 \text{ cm}^{-1}$  at  $\tilde{z} = 1.03$  and for  $k = 0.065 \text{ cm}^{-1}$  at  $\tilde{z} = 3.19$ . The value of  $k^3\phi[k]$  is maximum for  $k = 10 \text{ cm}^{-1}$  at  $\tilde{z} = 1.03$  while for  $k = 7 \text{ cm}^{-1}$  at  $\tilde{z} = 3.19$ . In order to examine this shift, the values of  $\underline{u^2}[k]$  and  $\tilde{\epsilon}[k]$  at various heights were calculated by means of Eqs. (5.23) and (5.28), respectively, where the integrals were evaluated graphically. The results are portrayed in Fig. 5.40 for the FDC case and in Fig. 5.41 for the HDC case. Both energy-containing and energy-dissipation ranges shift continuously toward larger eddy size domain with increasing vertical distance.

It is possible, from Figs. 5.40 and 5.41, to estimate how widely the dissipation range is separated from the energy-containing range. For this purpose, it is proposed to neglect the last 15% of the total kinetic energy in the energy-containing range and the first 15% of the energy dissipation in the dissipation range. In other words, only the kinetic energy  $\underline{u^2}[k]$  within the wave number range 0 to  $k_e$ , where  $k_e$  corresponds to 0.85 of the total kinetic energy, is considered. Similarly, the energy-dissipation within the wave number interval 0 to  $k_d$ , where

$k_d$  corresponds to 0.15 of the total energy dissipation, is neglected. These limits are shown by broken lines in Figs. 5.40 and 5.41. Thus,  $k_e$  is considered as the upper bound of the energy-containing range whereas  $k_d$  as the lower limit of the energy dissipation range. As mentioned previously, when  $k_d$  is separated from  $k_e$  by more than one decade, the condition for the existence of an inertial subrange is satisfied. The ratios of  $k_d$  to  $k_e$  at different heights are summarized below:

	FDC		HDC
$\tilde{z}$	$k_d/k_e$	$\tilde{z}$	$k_d/k_e$
1.03	2.15	1.07	2.7
2.25	2.17	2.96	7.8
4.82	4.25	4.18	14.1

At all heights but  $\tilde{z} = 4.18$  for HDC, these two ranges are separated by less than one decade. Therefore, the aforesaid basic conditions are not sufficiently satisfied and the existence of local isotropy is highly questionable. Even if the measured spectrum can be approximated by a  $k^{-5/3}$  curve, an inertial subrange does not necessarily occur. Such an approximation must be made cautiously. Otherwise, it might result in misleading conclusions.

It is, further, important to estimate the lower limit of the wave number (or the largest eddy size) for the occurrence of local isotropy. This limit can be roughly evaluated from the relationship [65]

$$\overline{u^2} \int_0^k k^2 \phi[k] dk \gg \left( \frac{dU}{dz} \right)^2 . \quad (5.29)$$

Assuming that  $\overline{u^2 \phi[k]}$  can be approximated by Eq. (5.26), substitution of

the latter into inequality (5.29) leads to the condition for the existence of local isotropy

$$k \gg \frac{4}{3} \left\{ \frac{\left(\frac{dU}{dz}\right)^2}{\beta \epsilon^{2/3}} \right\}^{3/4} . \quad (5.30)$$

Next, in the fully developed flow region it can be assumed that the energy dissipation is approximately equal to the energy production [12]. Then, the inequality (5.30) is written substituting the energy production for the energy dissipation.

$$k \gg \left\{ \frac{4}{3} \frac{\left(\frac{dU}{dz}\right)^2}{\beta E_p^{2/3}} \right\}^{3/4} = k_\ell , \quad (5.31)$$

where  $k_\ell$  is the lower bound of the wave number, and the energy production is

$$E_p = -\overline{uw} \frac{dU}{dz} . \quad (5.32)$$

The estimated value of  $k_\ell$  for both FDC and HDC cases are tabulated below:

$\tilde{z}$	FDC		HDC	
	$k_\ell$ (cm <sup>-1</sup> )	$L_u$ (cm)	$k_\ell$ (cm <sup>-1</sup> )	$L_u$ (cm)
1.5	0.50	13	0.39	16
2.0	0.40	16	0.33	19
3.0	0.30	21	0.33	19
4.0	0.28	22	0.30	21

In this table,  $L_u$  designates the eddy size corresponding to the wave number  $k_\ell$  (see Eqs. (5.24) and (5.25)), i.e., the largest eddy (or the upper limit). According to the relationship (5.31), local isotropy is expected to occur for wave numbers much larger than the lower bound  $k_\ell$ , say, at least one order of magnitude larger. In other words, the turbulence may be locally isotropic when the eddy size is one order of magnitude smaller than the upper limit  $L_u$ , e.g., about  $1-2 \text{ cm}(k=3-6 \text{ cm}^{-1})$ . Thus, local isotropy may occur within the dissipation range for the eddy size smaller than 2% of the boundary-layer thickness even though the existence of an inertial subrange is questionable.

As mentioned previously, in the inner part of the fully developed boundary layer, the energy dissipation is assumed approximately equal to the energy production. The former, under the assumption of isotropy, can be evaluated by means of Eq. (5.27). On the other hand, regardless of the isotropy, the turbulent energy production rate can be estimated by Eq. (5.32). Hence, by comparing the energy dissipation with the energy production in the fully developed flow region, the validity of the isotropy assumption can be examined. The variations in the energy dissipation rate and the energy production rate with height are shown in Fig. 5.42 for both FDC and HDC cases. In this figure, the ratio of the energy dissipation to the energy production is also displayed. It is observed that the energy dissipation estimated on the assumption of isotropy is much larger than the energy production although the turbulent energy is expected to be in balance at least close to the canopy top. This result indicates that the validity of the isotropy assumption is doubtful.

The turbulent energy associated with an eddy of a given size can be described by means of a discretized spectral analysis [66]. The latter is dependent of the existence of local isotropy and/or an inertial sub-range. Then the turbulent energy at a fixed point is written by

$$\overline{u^2} = \sum_{i=1}^{\infty} \overline{u_1^2}[n_i] , \quad (5.33)$$

where  $\overline{u_1^2}[n_i]$  is the portion of the total energy contributed by the turbulent fluctuation at the specific frequency  $n_i$ . The discretized energy  $\overline{u_1^2}[n_i]$  is proportional to the frequency-density function at each particular frequency, i.e.,  $\overline{u_1^2}[n_i] \sim f(n_i)_{\infty}$ . Given an eddy size, the corresponding frequency at each measurement station can be calculated by Eq. (5.25). Then, the discretized kinetic energy at this frequency can be obtained from the frequency-spectrum measurements. The variation of the discretized energy at four selected eddy sizes, viz.,  $L = 62.8, 12.6, 3.15$  and  $0.63$  cm ( $k = 0.1, 0.5, 2$  and  $10$  cm<sup>-1</sup>) were examined. These four eddy sizes were selected to cover the whole measured wave number range. The first eddy size represents the energy-containing range whereas the third one corresponds to the larger eddies in the dissipation range. The last size is typical to the eddies within the dissipation range. The discretized energies at these four scales are displayed in Figs. 5.43a and 5.43b for FDC and in Figs. 5.44a and 5.44b for HDC. In these figures, the energy at the eddy size  $L$  is denoted by  $\overline{u^2}[L]$  and its value at  $(\tilde{x}, \tilde{z}) = (0,1)$  is designated by  $\overline{u_0^2}[L]$ . In consistency with the presentation of the turbulent shear stress, the energy is normalized by  $\overline{u_0^2}[L]$ . The energy of the smallest eddy

( $L = 0.63$  cm) is affected most strongly by the canopy. In the immediate vicinity of the canopy surface ( $\tilde{z} = 1.5$ ) for both FDC and HDC cases, the change in the energy due to the canopy lessens as the eddy size increases. Near the middle of the boundary-layer thickness ( $\tilde{z} = 2.5$  and  $3.5$ ), the energy amplification at the largest eddy ( $L = 62.8$  cm) is more than at the middle size eddies ( $L = 12.6$  and  $3.15$  cm). With increasing vertical distance, overall effects of the canopy on the energy change at all four eddies diminish. In the transition region, a drastic increase in the energy at the smallest eddy size is observed. This indicates that the energy dissipation is highly intensified in the transition region. At the same height, the amplification of energy associated with all eddies is larger in FDC case than in HDC case.

Consequently, the energy variation associated with different-size eddies can be described successfully by means of the discretized-energy analysis which is independent of local isotropy and existence of inertial subrange.

## 6. SUMMARY AND CONCLUSIONS

The experimental results presented in this work indicate that the mean velocity in the fully developed flow region can be described by generalized logarithmic relationships. For the flow in the inner zone, viz., 30 to 45% of the boundary-layer thickness, the free-stream velocity and the roughness height are the scaling parameters for the velocity and the vertical distance from the wall, respectively. In the outer zone, the free-stream velocity and the momentum thickness are the similarity parameters. These scaling parameters can be easily determined from the mean velocity measurement. The power laws and/or the logarithmic laws examined herein cannot be satisfactorily employed to describe the mean-velocity profiles on high roughness elements. The use of either the modified logarithmic law or the modified law of the wake depends on knowing the friction velocity, roughness length and zero-plane displacement. Their dependence on the surface roughness is not known yet. Furthermore, the so-called von Kármán's constant is not a universal constant but can be considered as a scaling parameter of the friction velocity. Its numerical value would vary depending on the roughness.

The mean-velocity distributions inside the canopy within the transition region are strongly affected by the shape of the roughness element. The velocity in the trunk zone is higher than that in the crown zone. Particularly, the highest velocities were measured at about 1/2 of the trunk height, i.e., the jetting effect. Moreover, the drastic flow retardation in the beginning of the transition region is attributed to the large momentum loss of the flow inside the canopy.

The roughness density affects the upward flow displacement and the momentum loss. As the roughness density is higher, both displacement thickness and momentum thickness become larger. Due to greater momentum loss, the transition domain for the full-density-canopy case is shorter than for the half-density-canopy case. Since the upward flow displacement for denser canopy is larger, the contribution of the flow within the canopy to both total displacement thickness and momentum thickness becomes smaller in the full density canopy than in the half density canopy.

The flow characteristics within the fully developed flow region are determined by the flow development throughout the transition region. The latter stretches up to 20 to 30 roughness heights downstream of the canopy leading edge. Within the transition region the flow is characterized, particularly, by its turbulence structure. The internal boundary-layer thickness is defined based on the turbulent shear stress but not on the mean velocity. The canopy frontal area which is a drastic step obstruction has a strong influence on the turbulent shear-stress distribution and, hence, the growth of the internal boundary layer. An adverse pressure gradient generated by this obstruction leads to local occurrence of maximum turbulent shear stress away from the roughness top. The flow near the canopy leading edge reveals two-dimensional wake-like characteristics. As a result, the growth of the internal boundary layer up to 20 roughness heights is similar to the increase of the width of a two-dimensional wake. Beyond this distance, the internal boundary layer practically merges with the total boundary layer (90-97% of the total boundary-layer thickness).

The turbulence in the fully developed flow region may be locally isotropic when the eddy size is sufficiently small, e.g., less than 2% of the boundary layer thickness. However, the existence of an inertial subrange is questionable. The approximation of the measured energy spectra by a  $k^{-5/3}$  curve must be made cautiously. Otherwise, such an approximation might result in a misleading conclusion that both local isotropy and inertial subrange exist. In order to assess the energy variation associated with different-size eddies, regardless of the existence of local isotropy and inertial subrange, the discretized-energy analysis can be a satisfactory tool. The results of this analysis indicate that a large energy dissipation occurs in the transition region. In the fully developed flow region, the turbulent energy associated with various-size eddies reaches an equilibrium state.

It is reported in Ref. 67 that comparisons of the mean-velocity data obtained in and above a jungle-like coastal forest with wind-tunnel results for the full density canopy show a reasonable agreement. Moreover, a similar variation in the coefficient of anisotropy with height are observed for the wind-tunnel simulated flow and field data. Generally, the mean velocity field and overall turbulence features within and above forest canopies can be satisfactorily simulated. The results presented herein can provide valuable information in studying the problems associated with dispersal of agricultural chemicals and seed, exchange rates of water vapor and carbon dioxide and, to some extent, forest-fire problems. More generally, the canopy flow investigated in this work may represent the flow characteristics over high roughness elements like buildings and/or structures. Hence, the knowledge can be

---

extended to study the problems related to air pollution over urban areas or aerodynamic effects on buildings and structures.

To summarize, the main conclusions of this investigation are:

(1) The mean velocity profiles in the fully developed turbulent boundary layer above the canopy can be described by generalized logarithmic relationships.

(2) Inside the canopy within the transition region, the highest velocities were measured at about 1/2 of the trunk height, i.e., the jetting effects.

(3) Flow retardation in the beginning of the transition region is mainly due to the momentum loss of the flow inside the canopy.

(4) The internal boundary layer defined based on the turbulent shear stress distribution grows in the nearly same manner as the width of a two-dimensional wake.

(5) The turbulence in the fully developed flow region may be locally isotropic for sufficiently small eddies. However, the existence of an inertial subrange is doubtful.

(6) The turbulent energy variation associated with a particular size eddy can be analyzed using a discretized-energy method.

(7) The so-called von Kármán's constant can be considered as a scaling parameter for the friction velocity.

(8) As the roughness density is higher, the upward flow displacement becomes larger.

## APPENDIX I

## YAWED HOT WIRE

When a hot wire is positioned normal to the mean velocity direction in a flow with a small velocity fluctuation, the fluctuation in hot-wire cooling is produced, essentially, by the velocity fluctuation parallel to the mean velocity. On the other hand, if a hot wire is placed at an angle to the mean velocity direction, the fluctuation in the wire cooling is caused by both longitudinal and transversal fluctuating velocity components. A sketch of a hot wire placed at a yawed angle  $\psi$  to the mean velocity direction in the x-z plane is depicted in Fig. A.1. The instantaneous directions of the fluctuating velocity components are arbitrarily assumed. The yaw angle is measured clockwise from the mean velocity direction. The simplified and operational form of the so-called King's law for a yawed wire is [18]

$$(\bar{E} + e_{\psi})^2 - E_0^2 = MU_e^{\frac{1}{2}} \quad , \quad (A.1)$$

where  $U_e$  is the effective cooling velocity and  $M$  is a constant. The value of the latter depends on wire configuration and material, the selected resistance ratio and the air properties. The time-averaged (DC) voltage necessary to balance the bridge under steady conditions is denoted by  $\bar{E}$  whereas  $E_0$  designates the voltage drop in still air (at zero velocity). The value of  $E_0$  is constant for chosen operating conditions. The instantaneous AC voltage caused by the fluctuating velocity for a chosen yaw angle is denoted by  $e_{\psi}$ .

Generally, according to the cosine law [68,69], the hot wire is assumed to be most sensitive to the normal component of the resultant

velocity. In other words, the latter is considered most effective for cooling the hot wire. Furthermore, it is noteworthy that the wire cooling is not affected by any small fluctuating velocity component perpendicular to the x-z plane, i.e., v-component, as long as the mean velocity is large compared with v [40]. Thus, as a first approximation, neglecting the v-component, the normal component in the x-z plane is considered as the effective cooling velocity. Therefore, (see Fig. A.1)

$$U_e = U_{txz} \sin(\psi + \beta) = (U + u) \sin \psi + w \cos \psi, \quad (\text{A.2})$$

where  $U_{txz}$  is the total velocity in the x-z plane and  $U$  is the mean velocity. The fluctuating velocity components in x- and z-directions are denoted by  $u$  and  $w$ , respectively. The angles between the total velocity and the mean velocity are designated by  $\beta$ . Substitution of Eq. (A.2) into Eq. (A.1) leads, after some manipulation, to the following equation:

$$(\bar{E} + e_\psi)^2 - E_0^2 = M(U \sin \psi)^{\frac{1}{2}} \left(1 + \left(\frac{u}{U} + \frac{w}{U} \cot \psi\right)^{\frac{1}{2}}\right)^{\frac{1}{2}}. \quad (\text{A.3})$$

Under the assumption of small fluctuations, i.e.,  $u^2/U^2 \ll 1$  and  $w^2/U^2 \ll 1$ , and, hence,  $e^2\psi/E^2 \ll 1$ , quadratic and higher order terms in the binomial expansions of  $(\bar{E} + e_\psi)^2$  and  $(1 + (\frac{u}{U} + \frac{w}{U} \cot \psi))^{\frac{1}{2}}$  are neglected. Then Eq. (A.3) reduces to

$$\frac{\bar{E} e_\psi}{\bar{E}^2 - E_0^2} = \frac{u \sin \psi + w \cos \psi}{4 U \sin \psi}, \quad (\text{A.4})$$

where the relationship  $\overline{E}^2 - E_0^2 = M (U \sin \psi)^{\frac{1}{2}}$  was used for the mean values. Taking the mean-square of Eq. (A.4), we obtain

$$\frac{\overline{E}^2}{(\overline{E}^2 - E_0^2)^2} \overline{e_\psi^2} = \frac{\overline{u^2 \sin^2 \psi} + \overline{uw \sin 2\psi} + \overline{w^2 \cos^2 \psi}}{16 U^2 \sin \psi}, \quad (\text{A.5})$$

where the overbar denotes time-averaged (or mean) values. Subsequent positionings of the wire at the same location at two different yaw angles, say,  $45^\circ$  and  $135^\circ$ , respectively, lead to the following relationships for the shear stress and vertical component of the fluctuating velocity

$$\frac{\overline{uw}}{U^2} = \frac{4\overline{E}^2}{(\overline{E}^2 - E_0^2)^2} (\overline{e_{45}^2} - \overline{e_{135}^2}), \quad (\text{A.6})$$

and

$$\frac{\overline{w^2}}{U^2} = \frac{8\overline{E}^2}{(\overline{E}^2 - E_0^2)^2} (\overline{e_{45}^2} + \overline{e_{135}^2}) - \frac{\overline{u^2}}{U^2}. \quad (\text{A.7})$$

The longitudinal turbulence intensity in Eq. (A.7) is obtained by employing a normal hot-wire at the very same location. Notice that Eq. (A.6) and (A.7) are based on the assumption that the hot wire at each yaw angle monitors the same values of  $u$ ,  $w$  and  $\overline{uw}$ . In other words, it is assumed that the turbulent flow is uniform over the wire length. To satisfy this condition it is desirable to use a hot wire of relatively small aspect ratio.

## REFERENCES

1. Schlichting, H., Boundary Layer Theory, McGraw-Hill Book Co., Inc., New York, 4th ed. (1960).
2. Clauser, F. H., "The turbulent boundary layer," Advances in Applied Mechanics, (Dryden, H. L. and von Kármán, Th., editors), Academic Press Inc., Publishers, New York, N.Y., Vol. 4, 1-51 (1956).
3. Rotta, J. C., "Turbulent boundary layers in incompressible flow," Progress in Aeronautical Sciences, (Ferri, A., et al., editors), The Macmillan Company, New York, N.Y., Vol. 2, 1-219 (1962).
4. Prandtl, L., "The mechanics of viscous fluids," Div. G., Aerodynamic Theory, (Durand, W. F., editor), Dover Publications, Inc., New York, N.Y., Vol. 3, 34-208 (1963).
5. Millikan, C. B., "A critical discussion of turbulent flows in channels and circular tubes," Proc. Fifth Intern. Congress Appl. Mech., Harvard Univ., Cambridge, Mass., 386-392 (1938).
6. Nikuradse, J., "Laws of flow in rough pipes," NACA TM 1292 (1950).
7. Ludwig, H. and Tillmann, W., "Investigation of the wall-shearing stress in turbulent boundary layers," NACA TM 1285 (1950).
8. Klebanoff, P. S. and Diehl, Z. W., "Some features of artificially thickened fully developed turbulent boundary layers with zero pressure gradient," NACA TN 2475 (1951).
9. van Driest, E. R., "On turbulent flow near a wall," Journal of the Aeronautical Sciences, 23, 1007-1011 (1956).
10. Moore, W. L., "An experimental investigation of the boundary layer development along a rough surface," Ph.D. Dissertation, The State University of Iowa, Iowa City, Iowa (1951).
11. Hama, F. R., "Boundary layer characteristics for smooth and rough surfaces," Trans. Soc. Nav. Arch. and Marine Engrs., 62, 333-358 (1954).
12. Lumley, J. L. and Panofsky, H. A., The Structure of Atmospheric Turbulence, Interscience Publishers, New York, N.Y. (1964).
13. Sutton, O. G., Micrometeorology, McGraw-Hill Book Co., Inc., New York, N.Y. (1953).

14. Rossby, C. G. and Montgomery, R. B., "The layers of frictional influence in wind and ocean currents," *Papers in Physical Oceanography and Meteorology*, MIT and Woods Hole Oceanographic Institution, 3, No. 3 (1935).
15. Tan, H. S. and Ling, S. C., "Quasi-steady micro-meteorological atmospheric boundary layer over a wheat field," Lemon, E. R. (editor), "The energy budget at the earth's surface," Part II, U.S. Dept. of Agric. Res. Serv., Prod. RR72 (1963).
16. Deacon, E. L., "Vertical profiles of mean wind in the surface layers of the atmosphere," *Geophys. Mem.* 11, 91 (1953).
17. Coles, D., "The law of the wake in the turbulent boundary layer," *Journal of Fluid Mechanics*, 1, 2, 191-226 (1956).
18. Hinze, J. O., Turbulence: An Introduction to its Mechanism and Theory, McGraw-Hill Book Co., Inc., New York (1959).
19. Corrsin, S., "Turbulent flow," *American Scientist*, 49, 3, 300-325 (1961).
20. Townsend, A. A., The Structure of Turbulent Shear Flow, Cambridge University Press, England (1956).
21. Klebanoff, P. S., "Characteristics of turbulence in a boundary layer with zero pressure gradient," NACA TN 3178 (1954).
22. Cermak, J. E., Sandborn, V. A., Plate, E. J., Binder, G. H., Chuang, H., Meroney, R. N. and Ito, S., "Simulation of atmospheric motion by wind-tunnel flow," *Fluid Dynamics and Diffusion Laboratory*, Colorado State University, Fort Collins, Colorado, TR CER66JEC-VAS-EJP-GHB-RNM-SI-17 (1966).
23. Iizuka, H., "On the width of a windbreak," *Bulletin of the Government Forest Experiment Station*, No. 56, Tokyo, Japan (1952).
24. Woodruff, N. P. and Zingg, A. W., "Wind tunnel studies of fundamental problems related to windbreaks," U.S. Dept. of Agric., Soil Cons. Service, Rep. SCS-TP-112 (1952).
25. Hirata, T., "Fundamental studies of the formation of cutting series on the center pressure, the drag coefficient of a tree and one effect of shelter belts," *Bulletin of Forest.*, 45, 61-87, Tokyo University (1953).
26. Walshe, D. E. and Fraser, A. I., "Wind tunnel tests on a model forest," NPL, Teddington, Middlesex, England, Aero. Rep. 1078 (1963).
27. Lai, W., "Aerodynamic drag of several broadleaf tree species," U.S. Dept. Agric., Forest Service, Internal TR AFSWP-863 (1955).

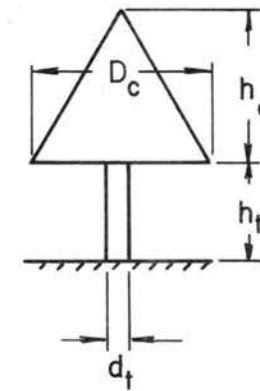
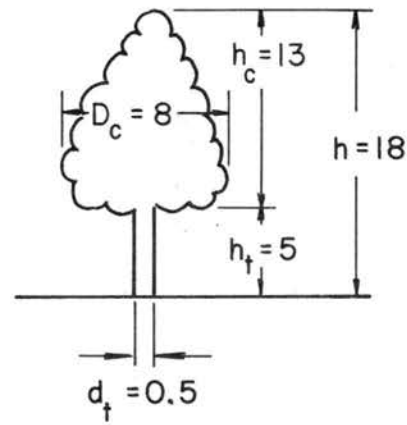
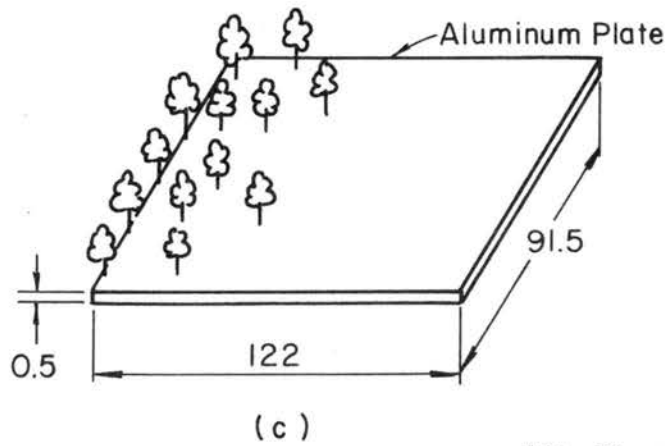
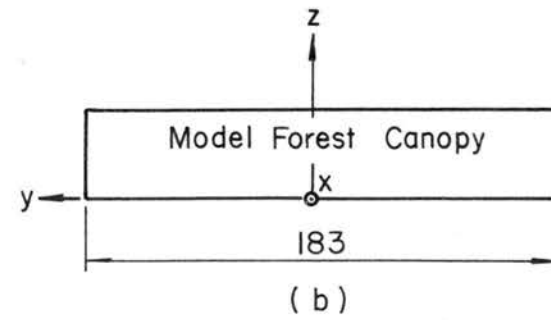
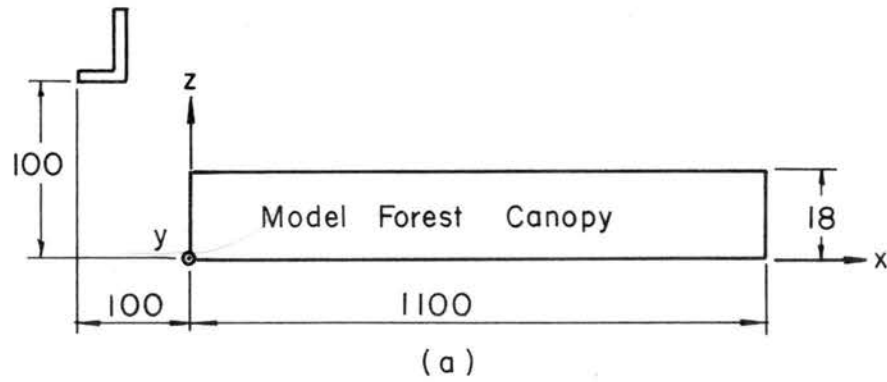
28. Plate, E. J. and Quaraishi, A. A., "Modeling of velocity distributions inside and above tall crops," *Journal of Applied Meteorology*, 4, 400-408 (1965).
29. Yano, M., "The turbulent diffusion in a simulated vegetative cover," Ph.D. Dissertation, Colorado State University, Fort Collins, Colorado (1966).
30. Kawatani, T. and Meroney, R. N., "Turbulence and wind speed characteristics within a model canopy flow field," *Agricultural Meteorology*, 7, 143-158 (1970).
31. Hsi, G. and Nath, J. H., "Wind drag within a simulated forest canopy," Fluid Dynamics and Diffusion Laboratory, Colorado State University, Fort Collins, Colorado, TR CER 68-69GH-JHN6 (1968).
32. Meroney, R. N., "Characteristics of wind and turbulence in and above model forests," *Journal of Applied Meteorology*, 7, No. 5, 780-788 (1968).
33. Sadeh, W. Z., Cermak, J. E. and Kawatani, T., "Flow over high roughness elements," *Boundary-Layer Meteorology*, 1, 3, 321-344 (1971).
34. McVehil, G. E., Ludwig, G. R. and Sundaram, T. R., "On the feasibility of modeling small-scale atmospheric motions," Cornell Aero. Lab., Buffalo, New York, TR ZB-23228-P-1 (1967).
35. Plate, E. J. and Cermak, J. E., "Micrometeorological wind tunnel facility," Fluid Dynamics and Diffusion Laboratory, Colorado State University, Fort Collins, Colorado, TR CER63EJP-JEC9 (1963).
36. Pankhurst, R. C. and Holder, D. W., Wind Tunnel Technique, Sir Issac Pitmand & Sons, Ltd., London (1952).
37. Sadeh, W. Z. and Finn, C. L., "A new hot-wire anemometer system," (to be published).
38. King, L. V., "On the convection of heat from small cylinders in a stream of fluid," *Phil. Trans. Roy. Soc., London, A.*, 214, 373-432 (1914).
39. Sadeh, W. Z., Maeder, P. F. and Sutera, S. P., "A hot wire-method for low velocity with large fluctuations," *The Review of Scientific Instruments*, 41, 9, 1295-1298 (1970).
40. Sandborn, V. A., "Metrology of fluid mechanics," College of Engineering, Colorado State University, Fort Collins, Colorado, Rep. CER66-67VAS32 (1966).

41. Rasmussen, C. G., "Measurement of turbulence characteristics," DISA Inf. Bul., 3 (1966).
42. Geiger, R., The Climate near the Ground, Harvard University Press, Cambridge, Massachusetts (1966).
43. Davenport, A. G., "The relationship of wind structure to wind loading," Proc. Symposium on Wind Effects on Buildings and Structures, Teddington, Middlesex, England, 1, 53-102 (1963).
44. Kung, E., "Deviation of roughness parameter from wind profile data above all vegetation," Studies of the Three-dimensional Structure of the Planetary Boundary Layer, University of Wisconsin, Madison, Wisconsin, 27-35 (1961).
45. Robinson, S. M., "A method for machine computation of wind profile parameters," Studies of the Three-dimensional Structure of the Planetary Boundary Layer, University of Wisconsin, Madison, Wisconsin, 63-70 (1961).
46. Hanna, S. R., "Turbulence and diffusion in the atmospheric boundary layer over urban areas," Notes of Seminar presented at Syracuse University (1970).
47. Perry, A. E., Schofield, W. H. and Joubert, P. N., "Rough wall turbulent boundary layers," Journal of Fluid Mechanics, 37, 2, 383-413 (1969).
48. Thwaites, B., (editor), Incompressible Aerodynamics, Oxford at the Clarendon Press, p. 57 (1960).
49. Rider, N. E., "Eddy diffusion of momentum, water vapour, and heat near the ground," Philosophical Transactions of the Royal Society of London, A., 246, 481-501 (1954).
50. Elliot, W. P., "The growth of the atmospheric internal boundary layer," Transactions of American Geophysical Union, 39, 6, 1048-1054 (1958).
51. Schubauer, G. B. and Klebanoff, P. S., "Investigation of separation of the turbulent boundary layer," NACA TR 1030 (1951).
52. Kung, R. J. and Plate, E. J., "Boundary layer development over equally spaced fences," Fluid Dynamics and Diffusion Laboratory, Colorado State University, Fort Collins, Colorado, TR CER69-70RJK-EJP-33 (1970).
53. Panofsky, H. A. and Townsend, A. A., "Change of terrain roughness and the wind profile," The Quarterly Journal of the Royal Meteorological Society, 90, 384, 147-155 (1964).

54. Townsend, A. A., "The response of a turbulent boundary layer to abrupt changes in surface conditions," *Journal of Fluid Mechanics*, 22, 4, 799-822 (1965).
55. Townsend, A. A., "The flow in a turbulent boundary layer after a change in surface roughness," *Journal of Fluid Mechanics*, 26, 2, 255-266 (1966).
56. Antonia, R. A. and Luxton, R. E., "The response of a turbulent boundary layer to an upstanding step change in surface roughness," *Transactions of the ASME, Journal of Basic Engineering*, Paper No. 70-FE-17 (1970).
57. Shinn, J. H., "Analysis of wind data from a South Carolina Coastal Forest," U.S. Army Electronics Command, Atmos. Sci. Lab., Res. Div., Fort Huachuca, Arizona, RD TR ECOM-6036 (1969).
58. Tourin, M. H. and Shen, W. C., "Deciduous forest diffusion study," Applied Science Division, Litton Systems, Inc., Minneapolis, Minnesota, Rep. 3004, Vol. 1 (1966).
59. Batchelor, G. K., Homogeneous Turbulence, Cambridge University Press (1967).
60. Papoulis, A., Probability, Random Variables and Stochastic Processes, McGraw-Hill Book Co., Inc., New York (1965).
61. Taylor, G. I., "The spectrum of turbulence," *Proc. Royal Society, A*, 164, 476-490 (1938).
62. Kolmogoroff, A., "The local structure of turbulence in incompressible viscous fluid for very large Reynolds' number," *Compt. rend. Acad. Sci. U.R.S.S.*, 30, 301-305 (1941).
63. Lin, C. C., Statistical Theories of Turbulence, Princeton University Press, Princeton, N.J. (1961).
64. Grant, H. L., Stewart, R. W. and Moilliet, A., "Turbulence spectra from a tidal channel," *Journal of Fluid Mechanics*, 12, 2, 241-263 (1962).
65. Pond, S., Stewart, R. W., and Burling, R. W., "Turbulence spectra in the wind over waves," *Journal of the Atmospheric Sciences*, 20, 319-324 (1963).
66. Sadeh, W. Z., Suter, S. P. and Maeder, P. F., "An investigation of vorticity amplification in stagnation flow," *Zeitschrift für angewandte Mathematik und Physik (ZAMP)*, 21, 5, 717-742 (1970).

67. Shinn, J. H., "Steady-state two-dimensional air flow in forests and the disturbance of surface layer flow by a forest wall," Ph.D. Dissertation, The University of Wisconsin, Madison, Wis. (1971).
68. Champagne, F. H., Sleicher, C. A. and Wehrmann, O. H., "Turbulence measurements and inclined hot-wires," Part 1, Journal of Fluid Mechanics, 28, 1, 153-175 (1967).
69. Champagne, F. H. and Sleicher, C. A., "Turbulence measurements with inclined hot-wires," Part 2, Journal of Fluid Mechanics, 28, 1, 177-182 (1967).

Pitot-Static Tube



All Dimensions in Centimeters

Fig. 3.1 Sketch of the model forest canopy and model tree element.

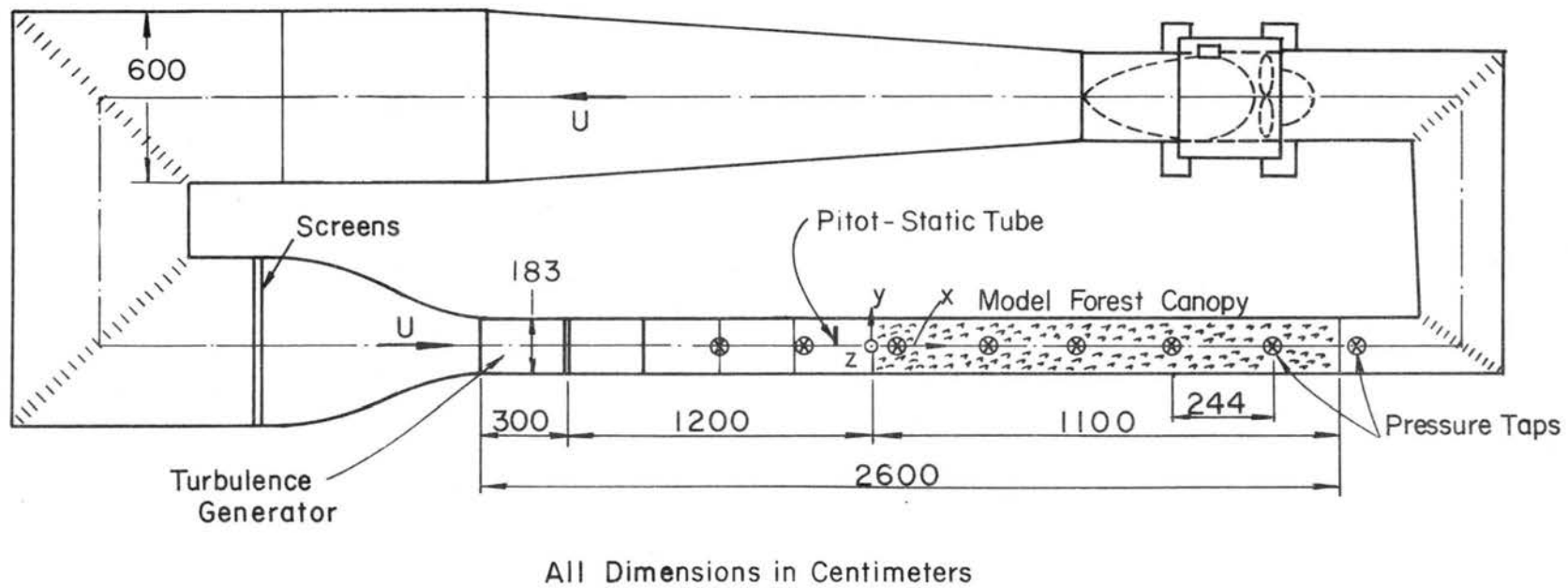


Fig. 3.2 Overall view of the Meteorological Wind Tunnel.

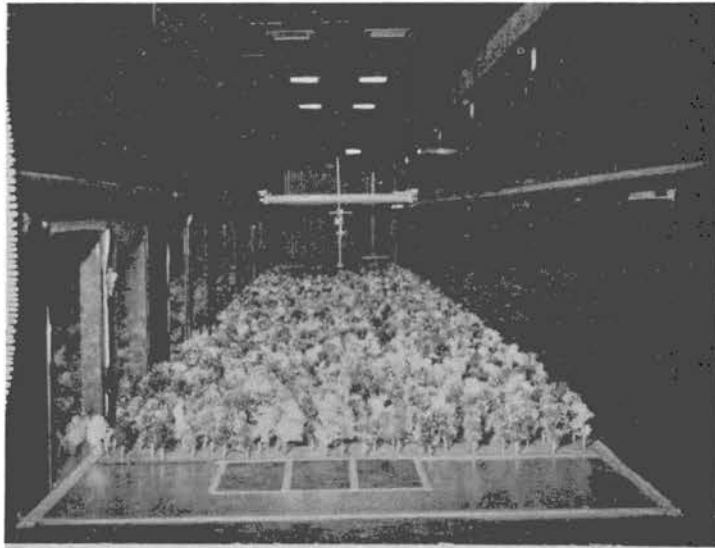


Fig. 3.3 View of the model forest canopy.

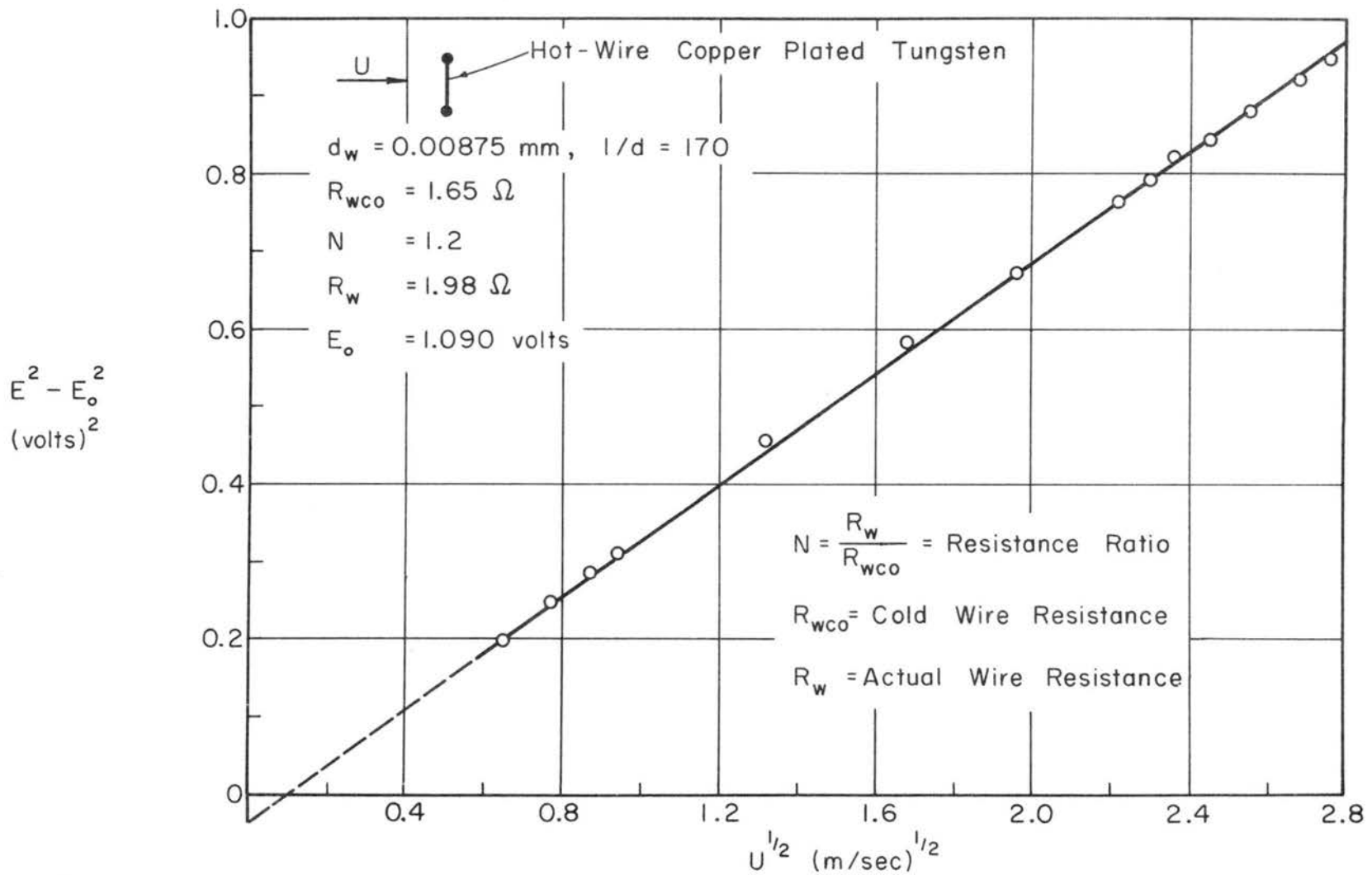


Fig. 4.1 Typical normal hot-wire calibration curve.

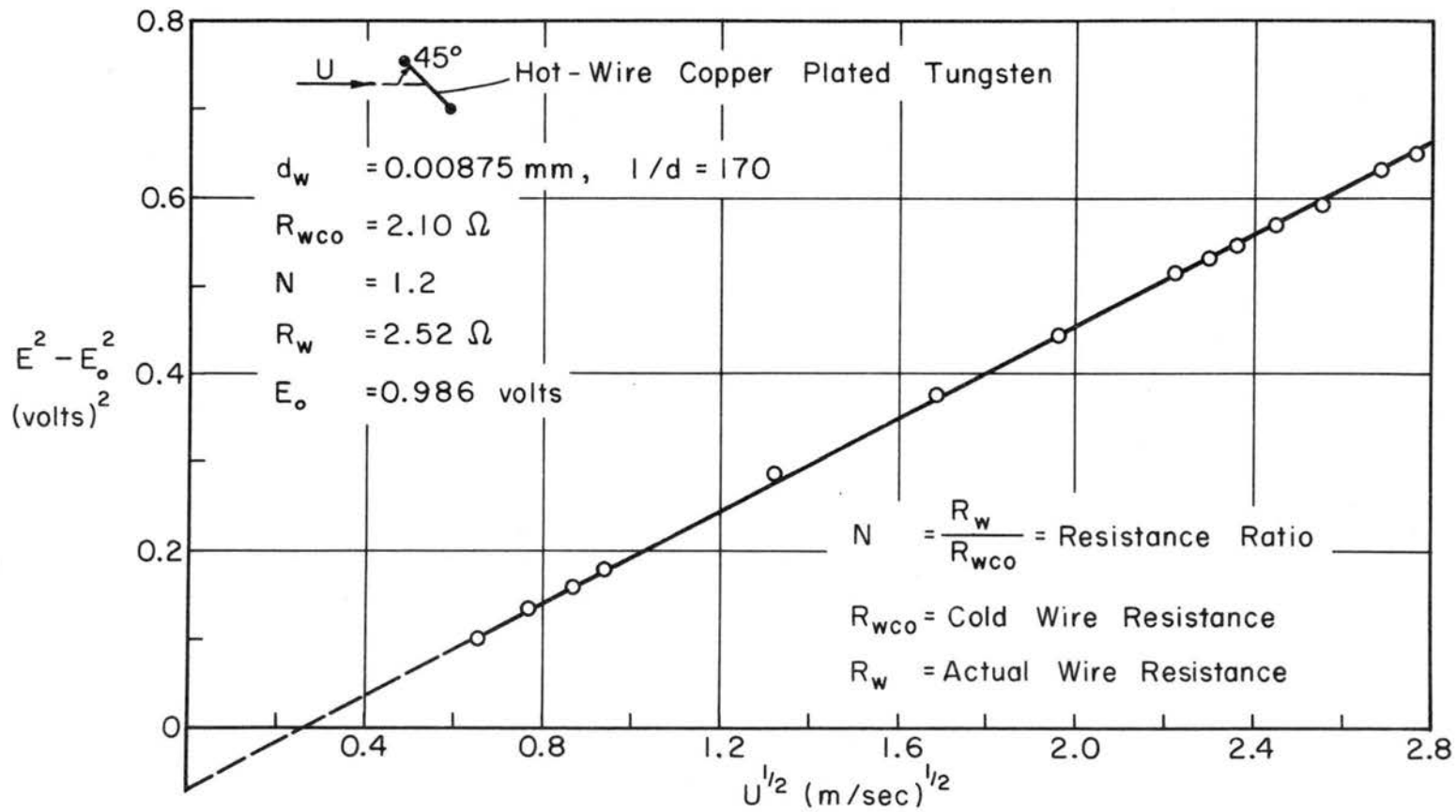


Fig. 4.2 Typical yawed hot-wire calibration curve.

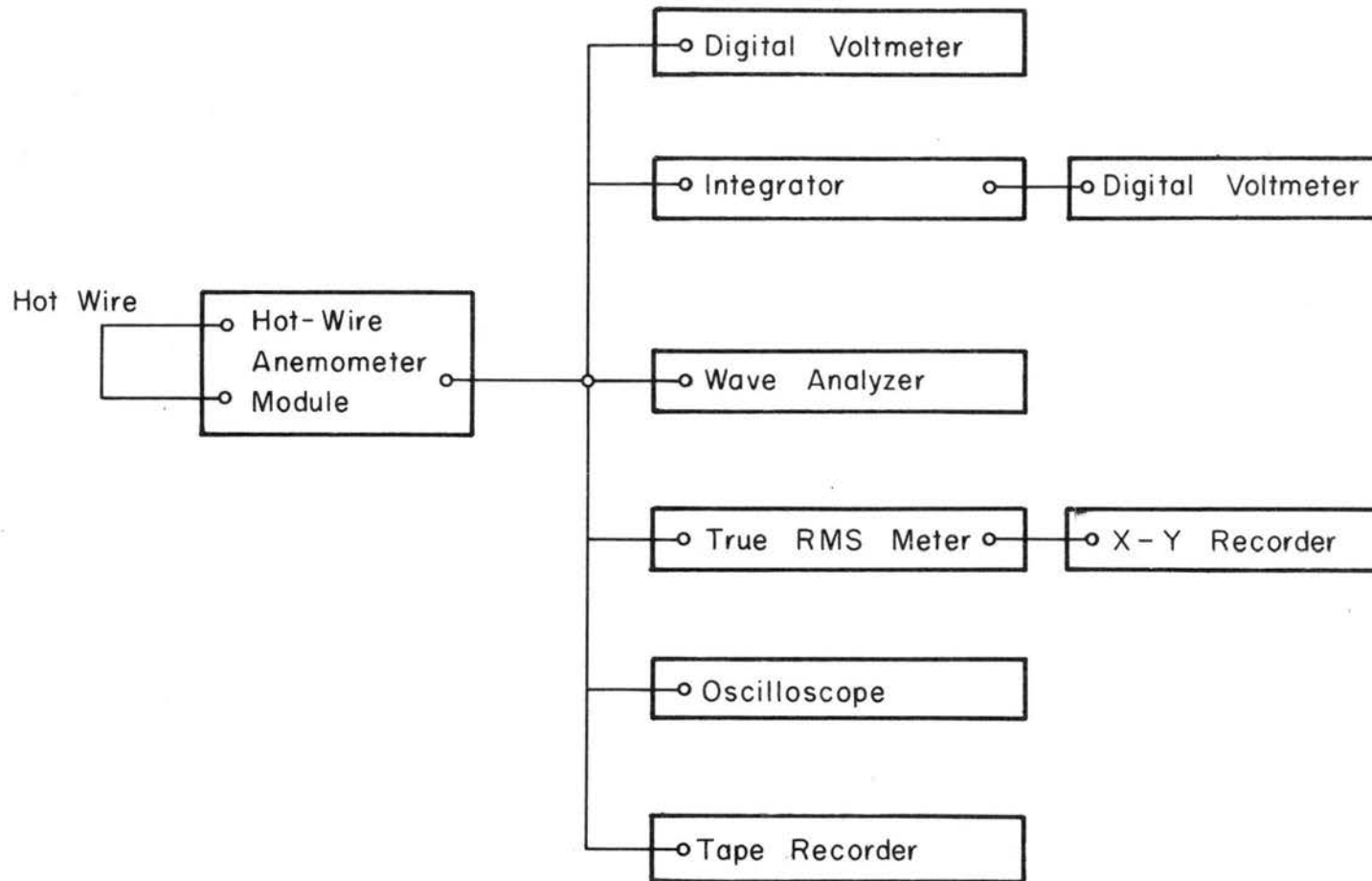


Fig. 4.3 Block diagram of hot-wire anemometer measuring system.

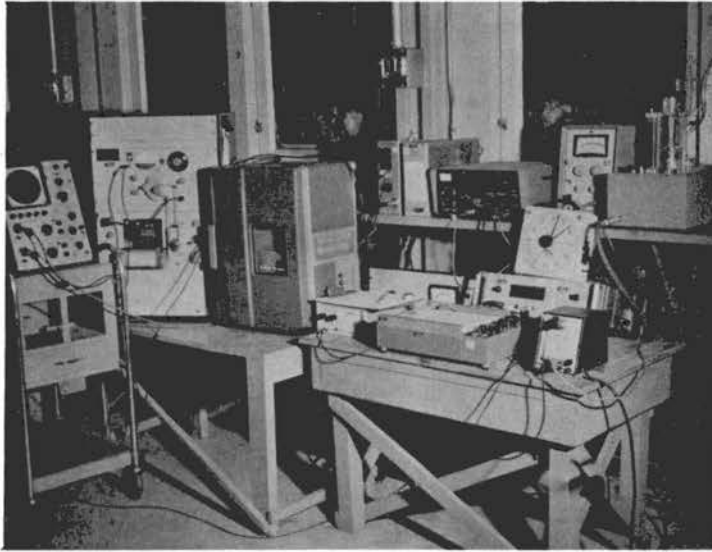


Fig. 4.4 General view of hot-wire anemometer system and additional equipments.

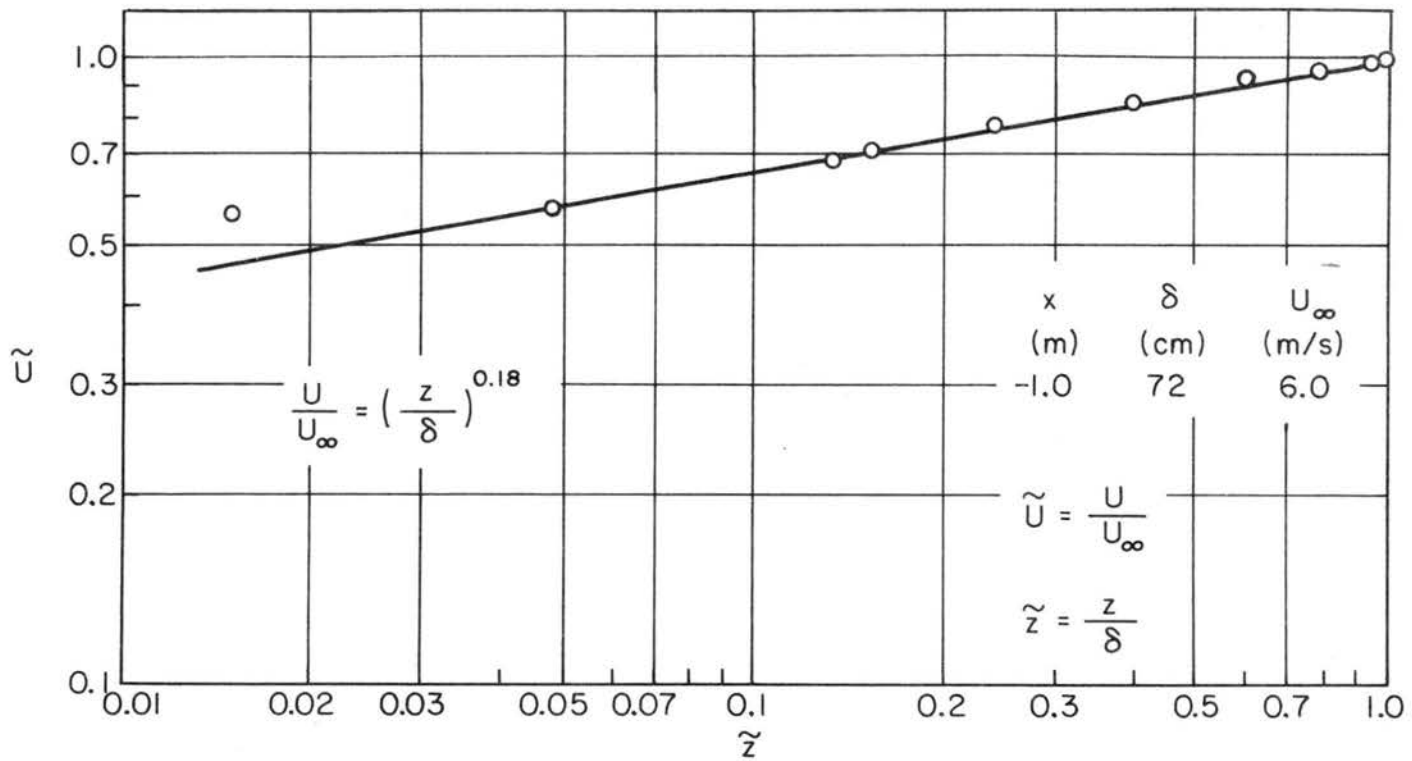


Fig. 5.1 Power law representation of upstream velocity profile.

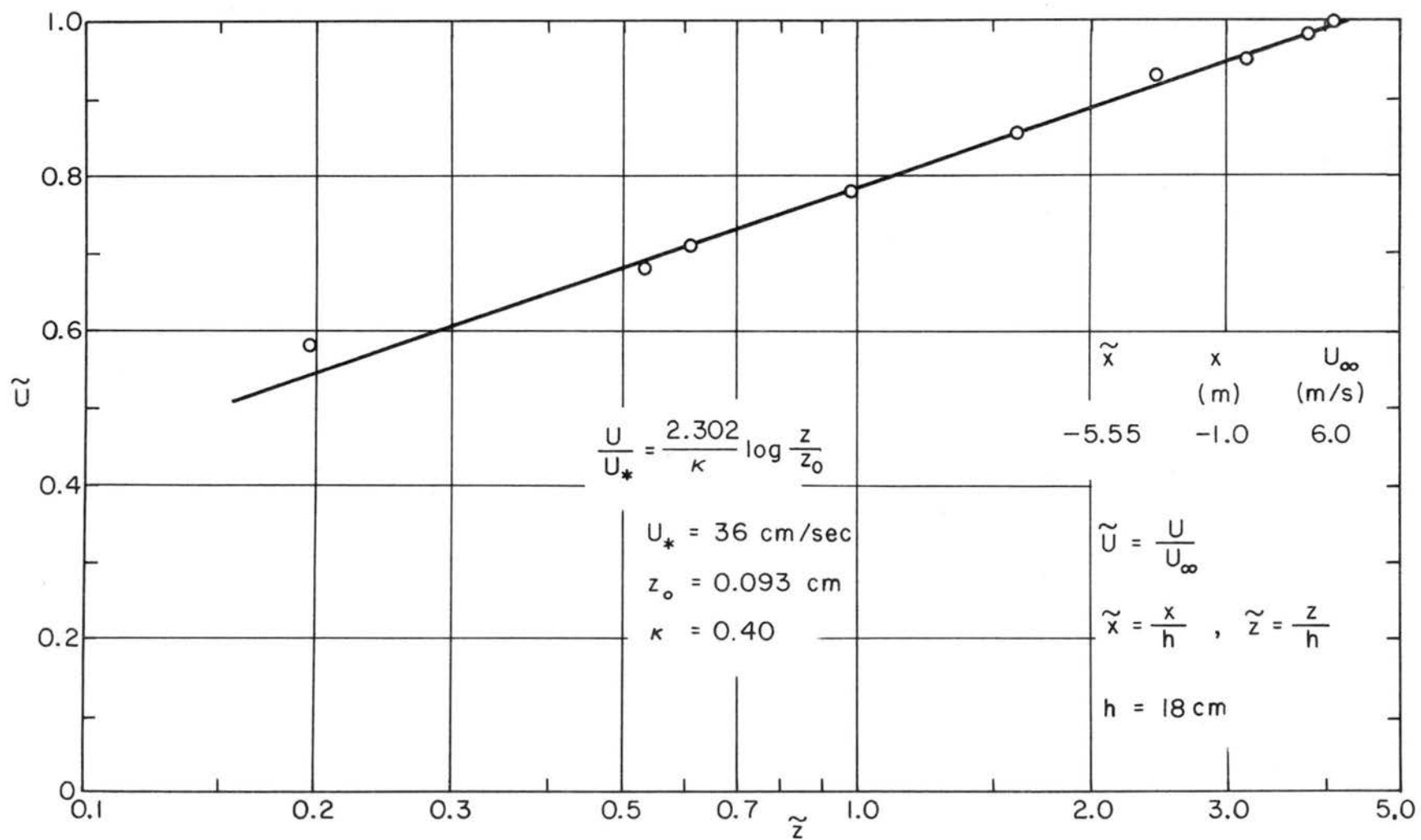


Fig. 5.2 Logarithmic law representation of upstream velocity profile.

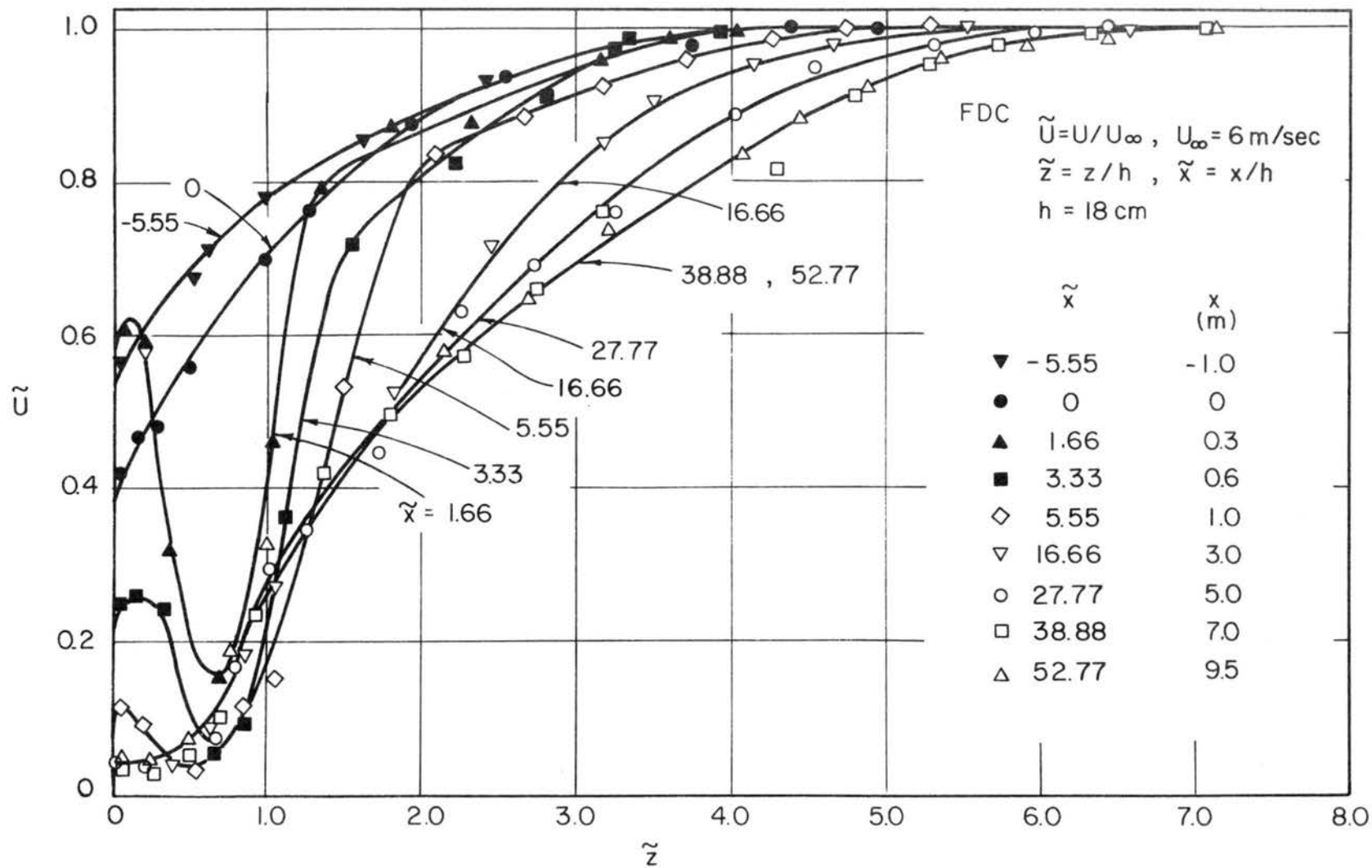


Fig. 5.3a Mean velocity profiles within and above the canopy for FDC case.

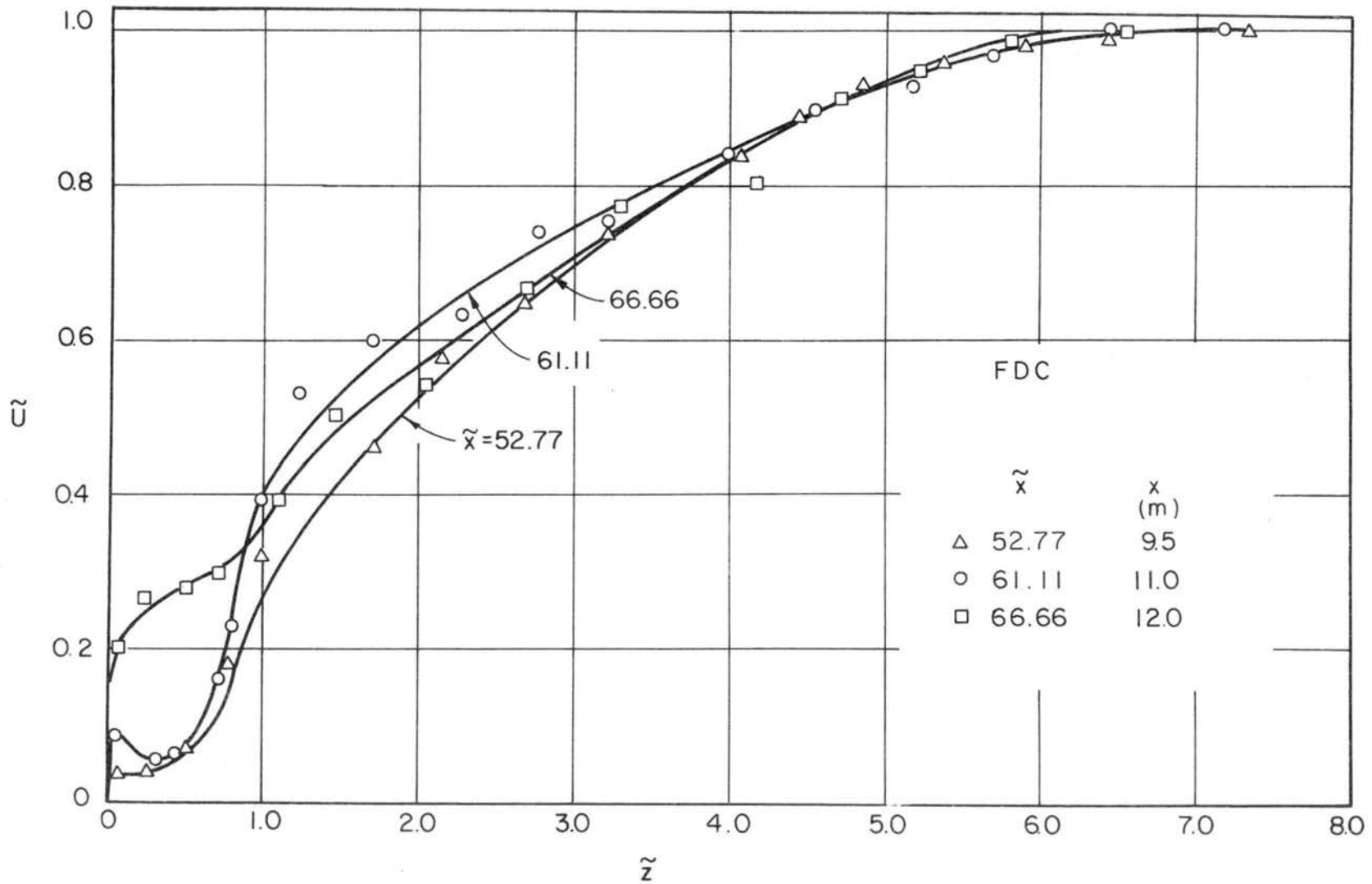


Fig. 5.3b Mean velocity profiles within and above the canopy for FDC case.

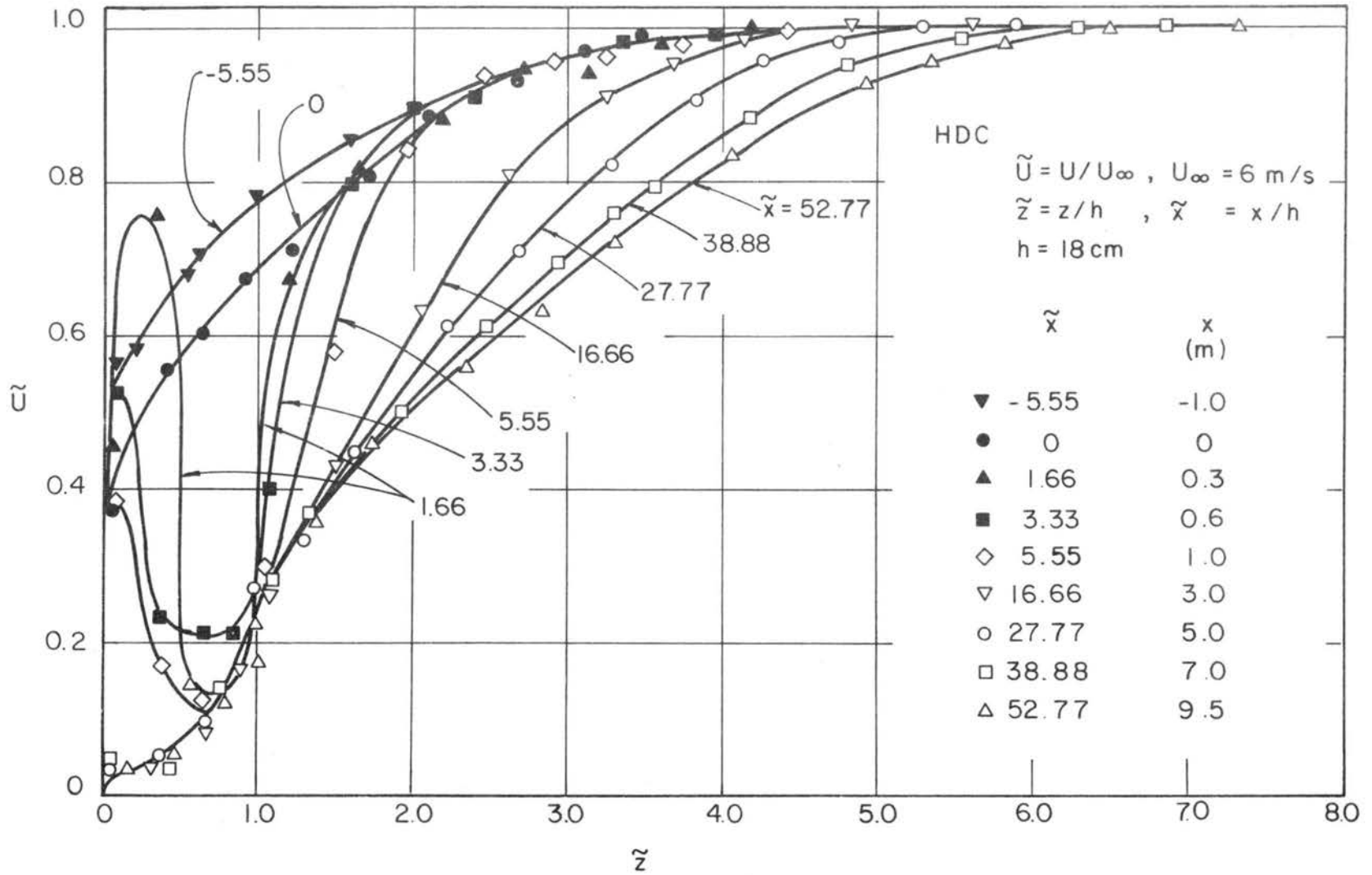


Fig. 5.4a Mean velocity profiles within and above the canopy for HDC case.

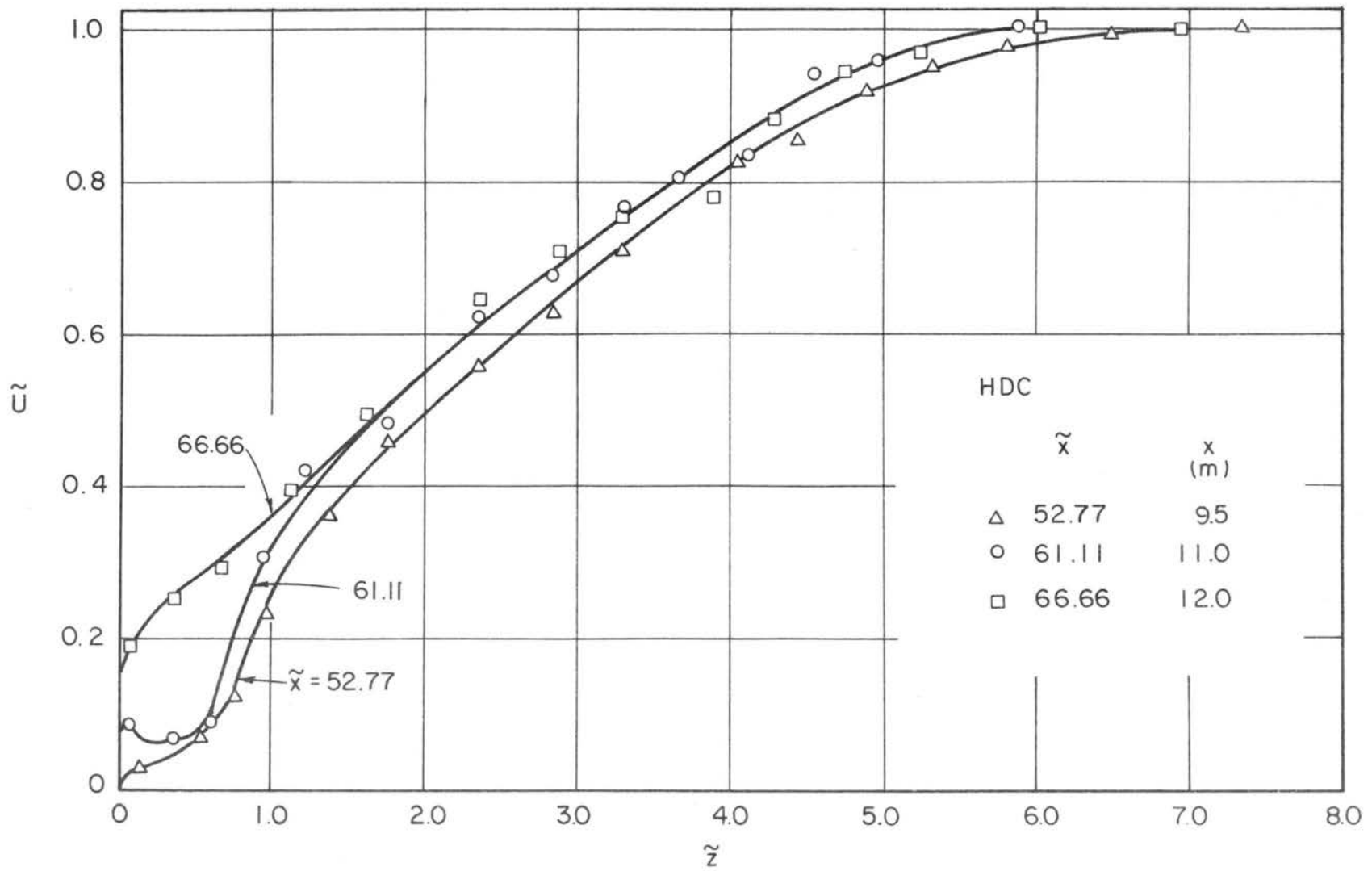


Fig. 5.4b Mean velocity profiles within and above the canopy for HDC case.

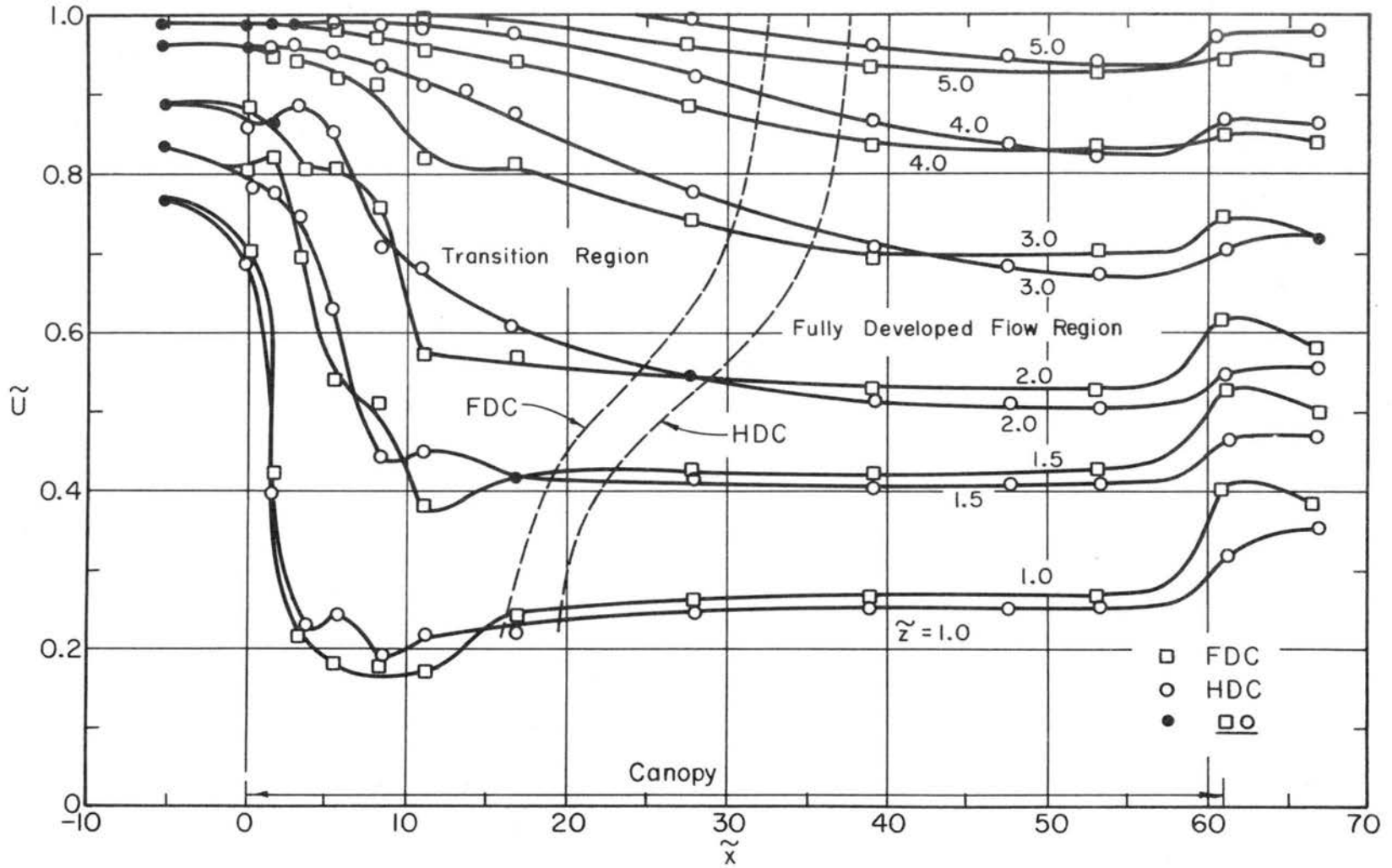


Fig. 5.5 Mean velocity variation along isoheights above the canopy; FDC and HDC.

$$\tilde{U} = \frac{U}{U_\infty}, U_\infty = 6 \text{ m/sec}$$

$$\tilde{x} = \frac{x}{h}, \tilde{z} = \frac{z}{h}, h = 18 \text{ cm}$$

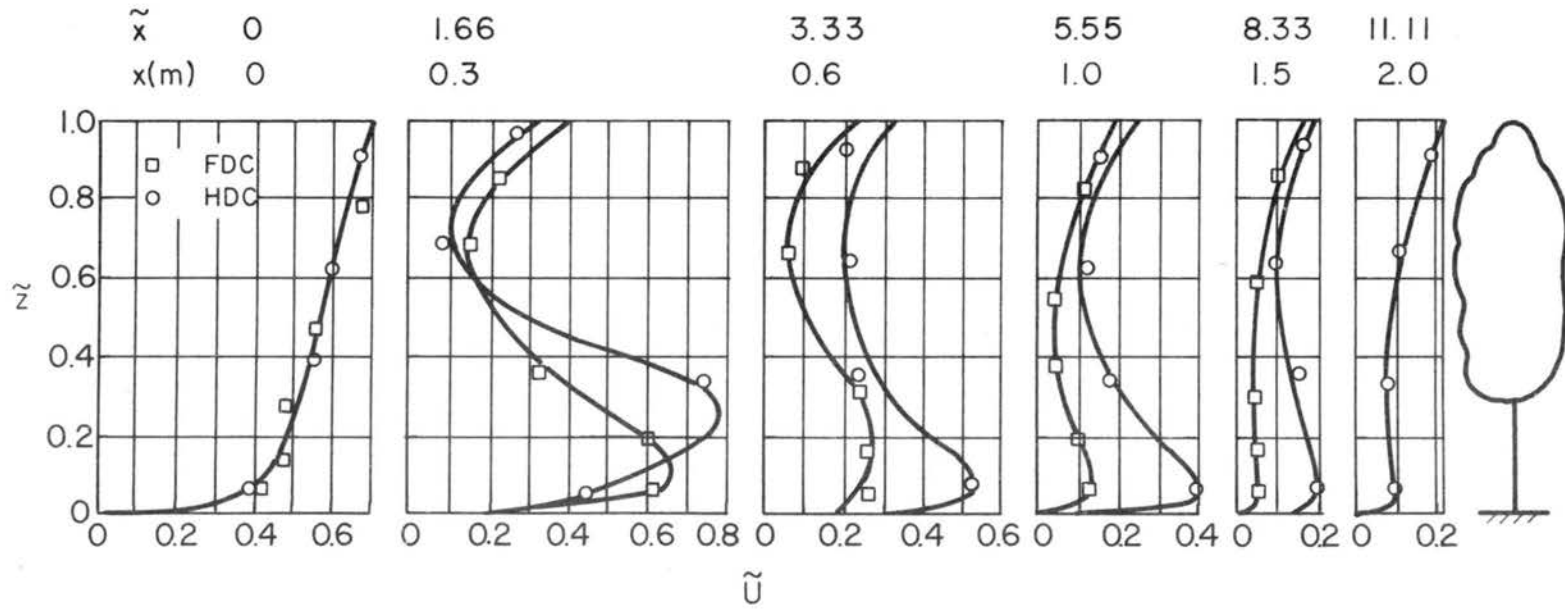


Fig. 5.6 Mean velocity profiles inside the canopy at 6 selected stations; FDC and HDC.

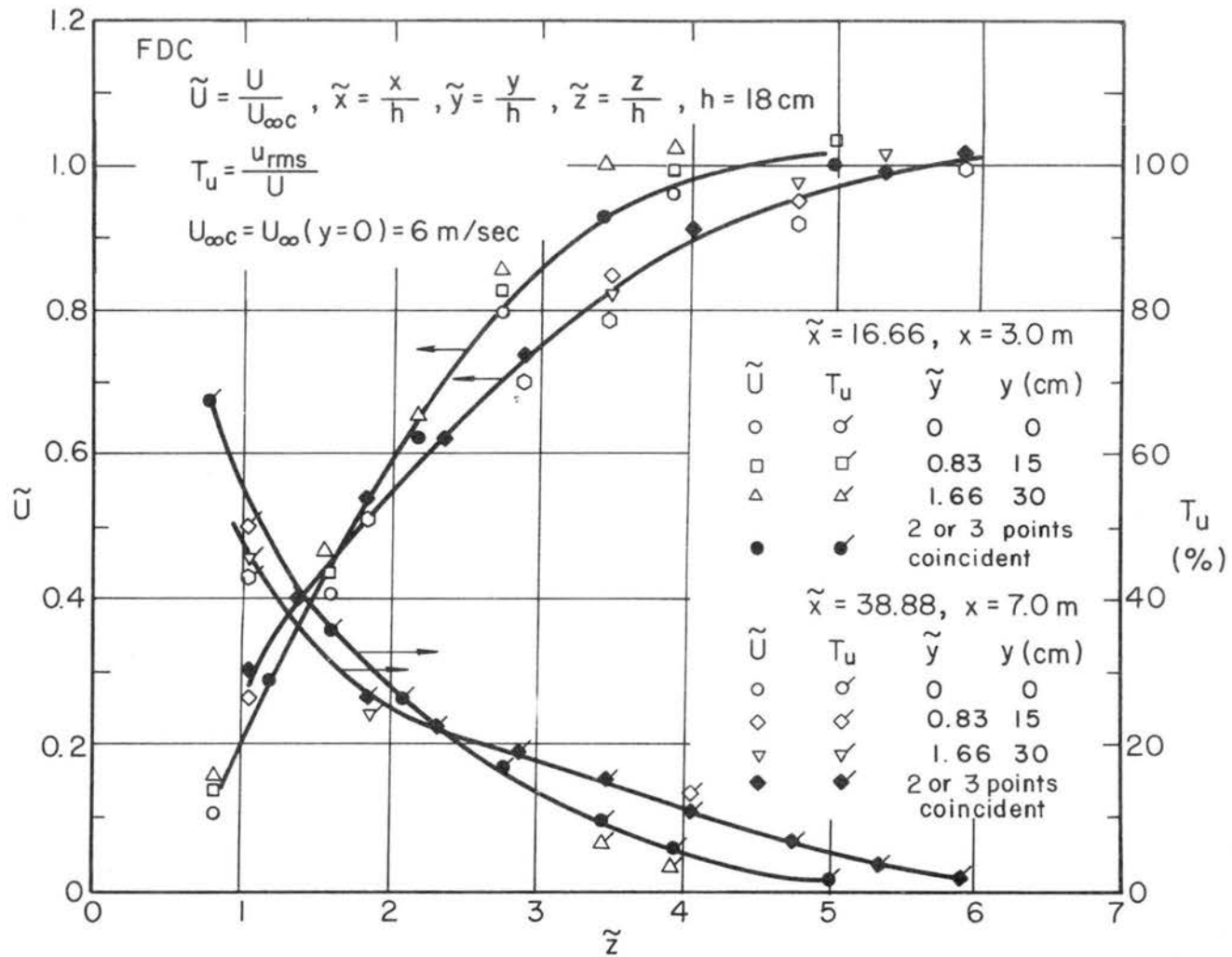


Fig. 5.7 Lateral variation in the mean velocity and turbulent intensity for FDC case over a distance of 30 cm off the center line.

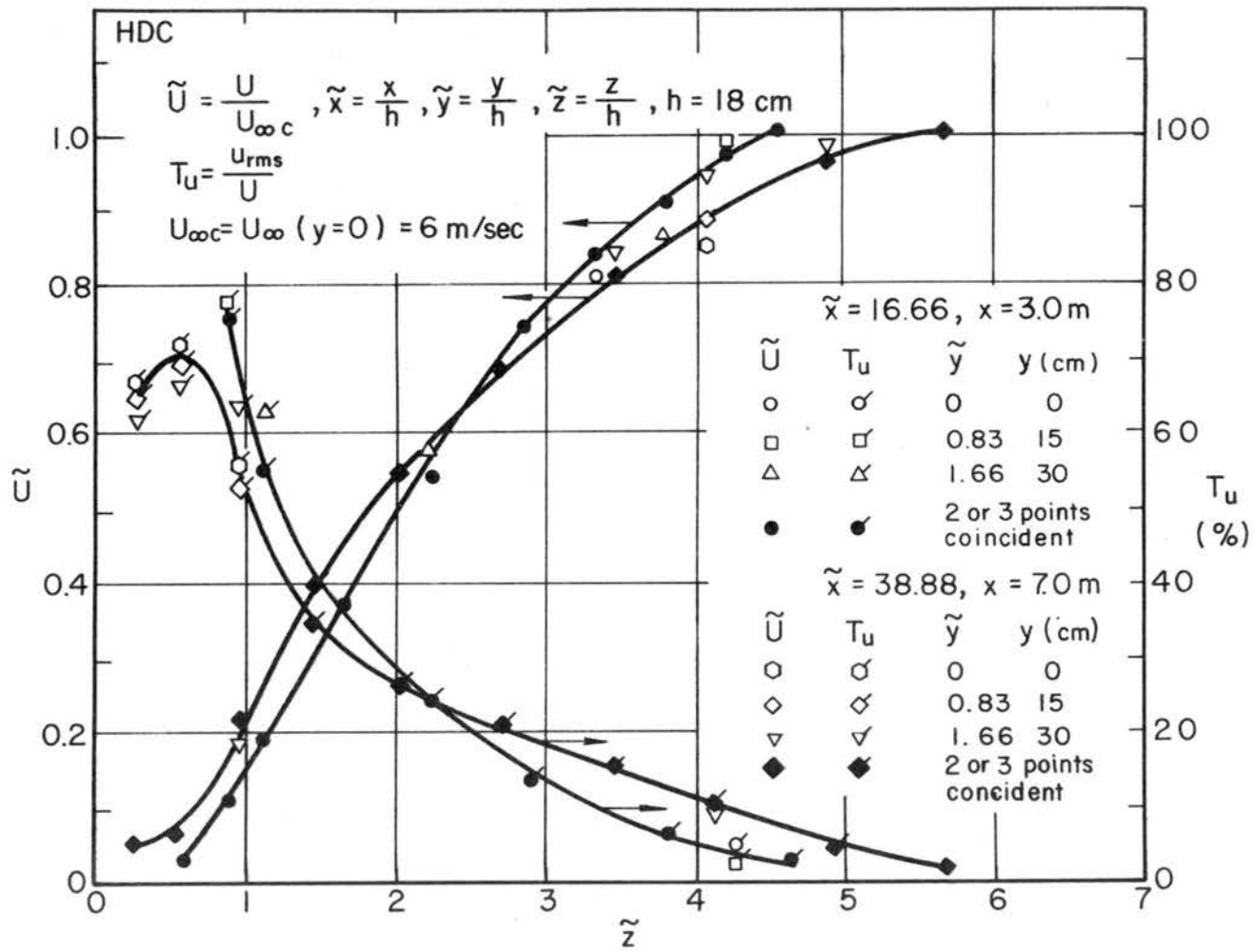


Fig. 5.8 Lateral variation in the mean velocity and turbulent intensity for HDC case over a distance of 30 cm off the center line.

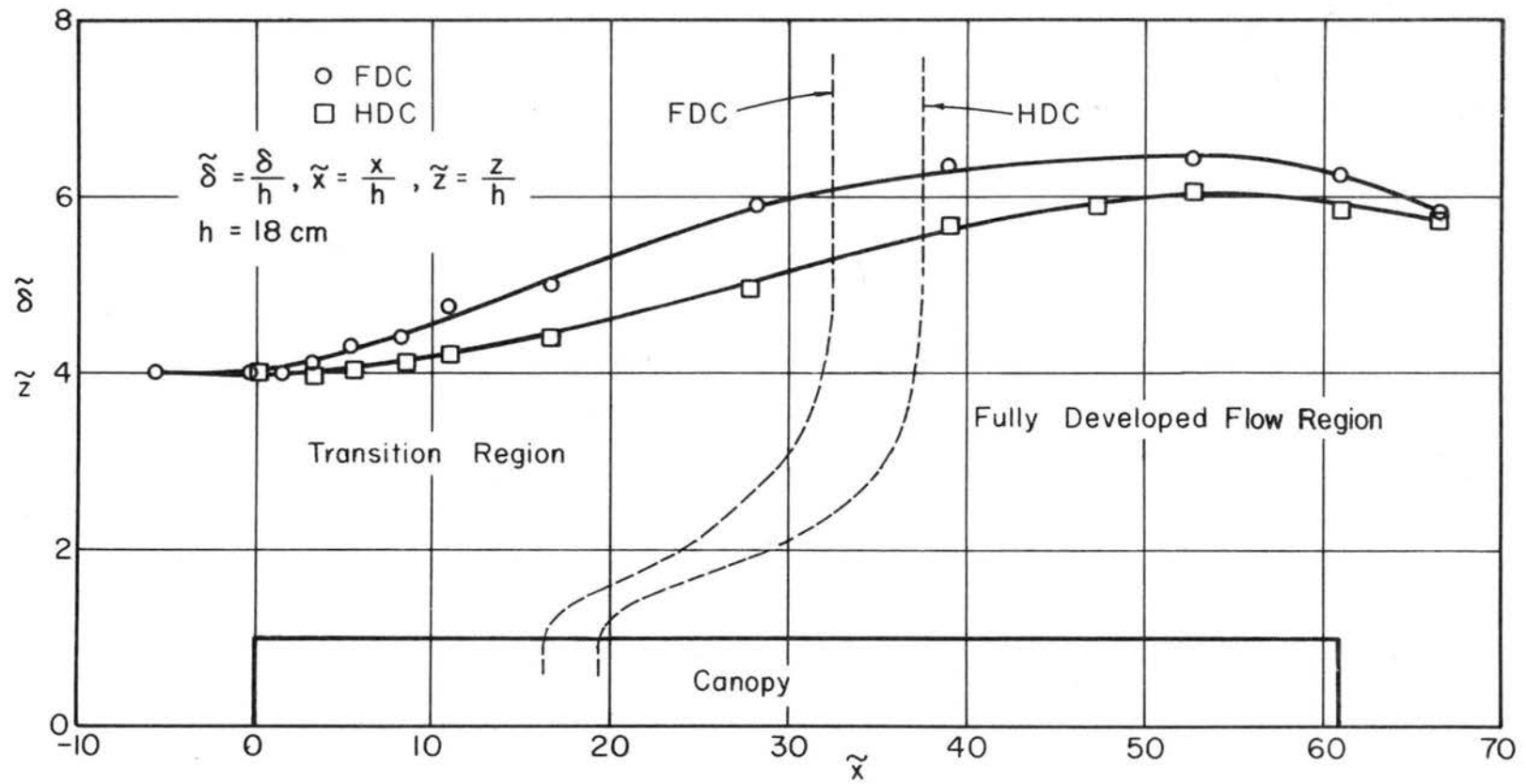


Fig. 5.9 Boundary-layer thickness growth and the boundary between the transition and fully developed flow regions; FDC and HDC.

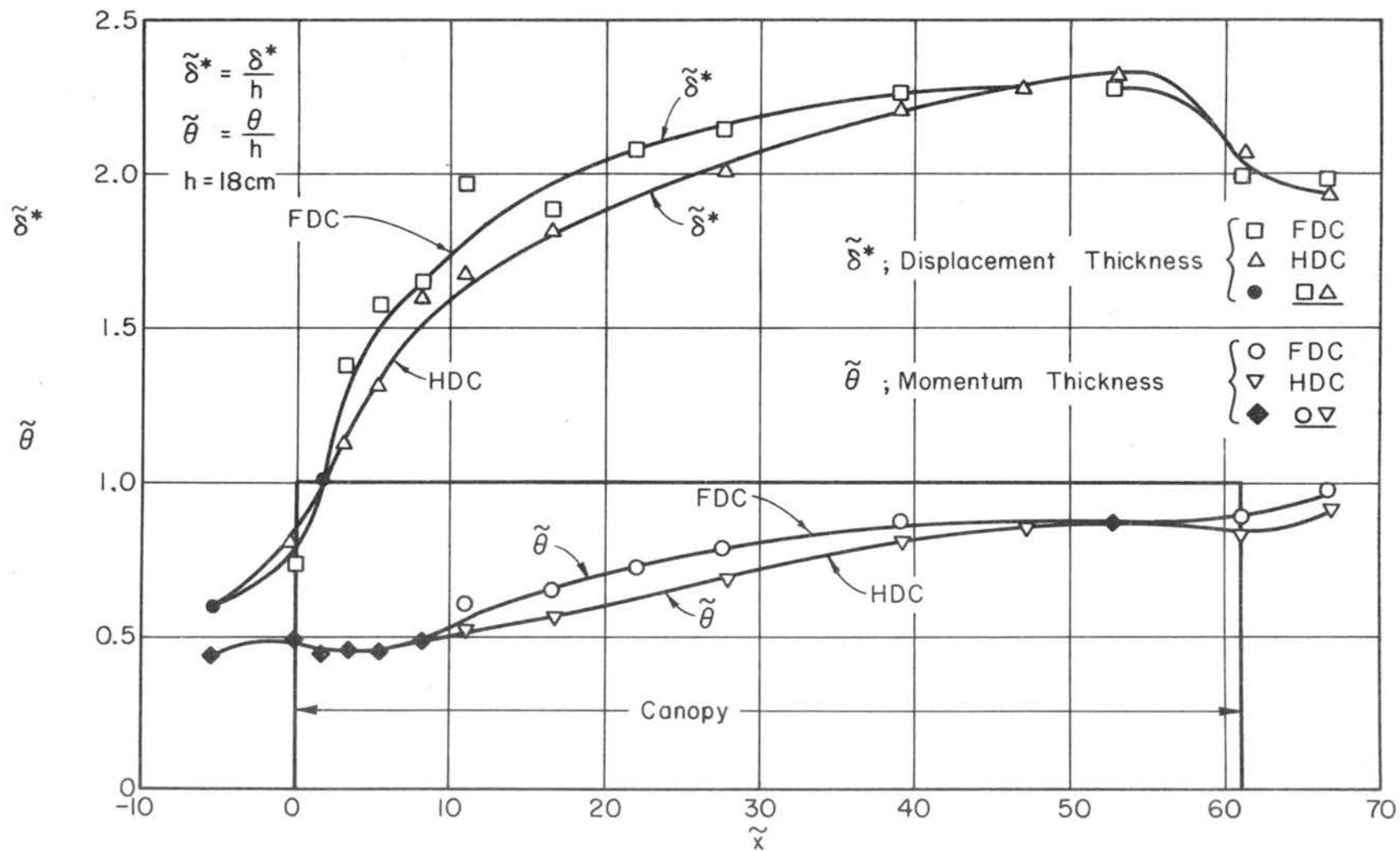


Fig. 5.10 Growth of displacement thickness and momentum thickness along the canopy; FDC and HDC.

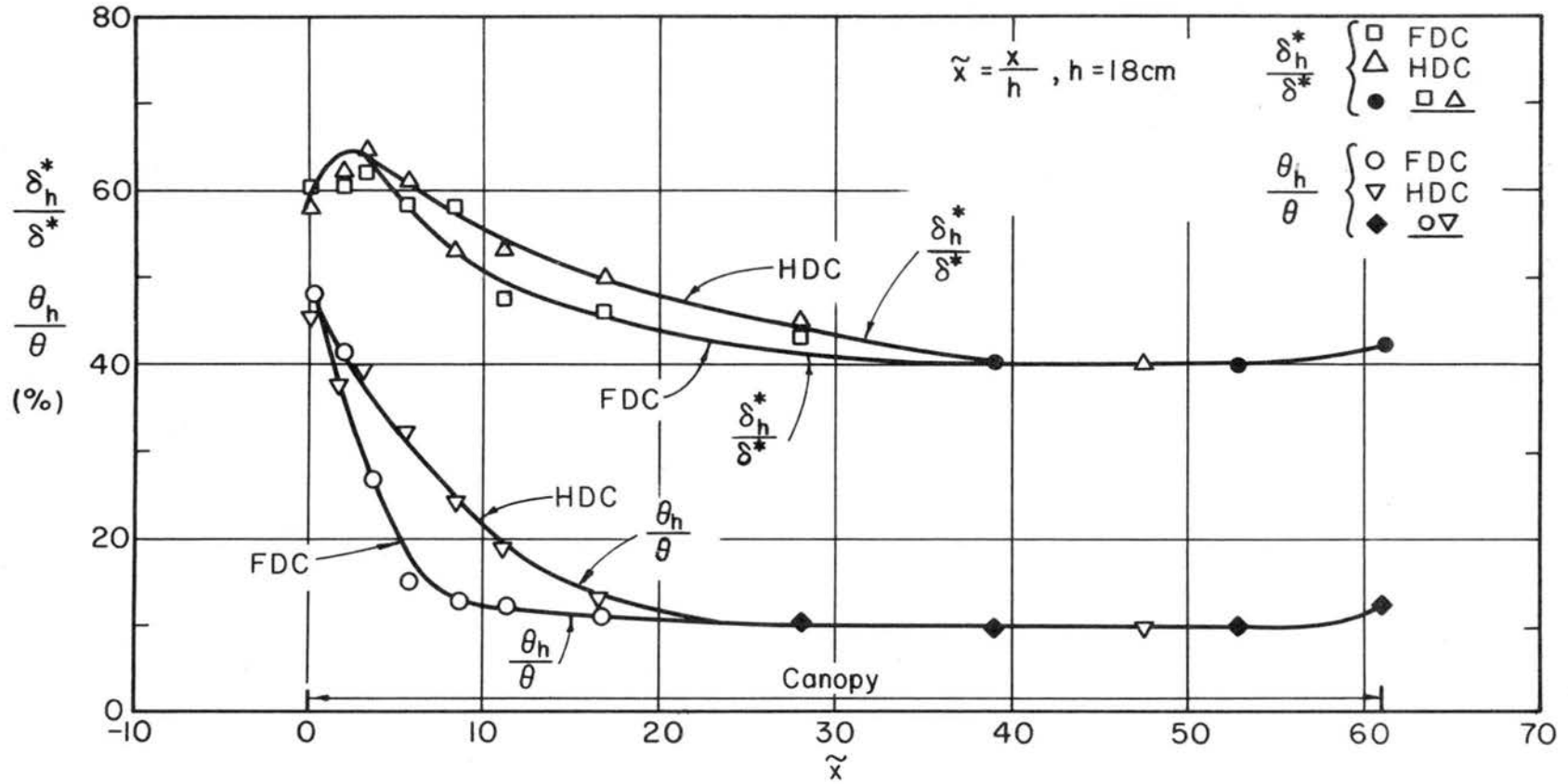


Fig. 5.11 Variation of the ratios of the displacement and momentum thicknesses within the canopy to the local total displacement and momentum thicknesses along the roughness; FDC and HDC.

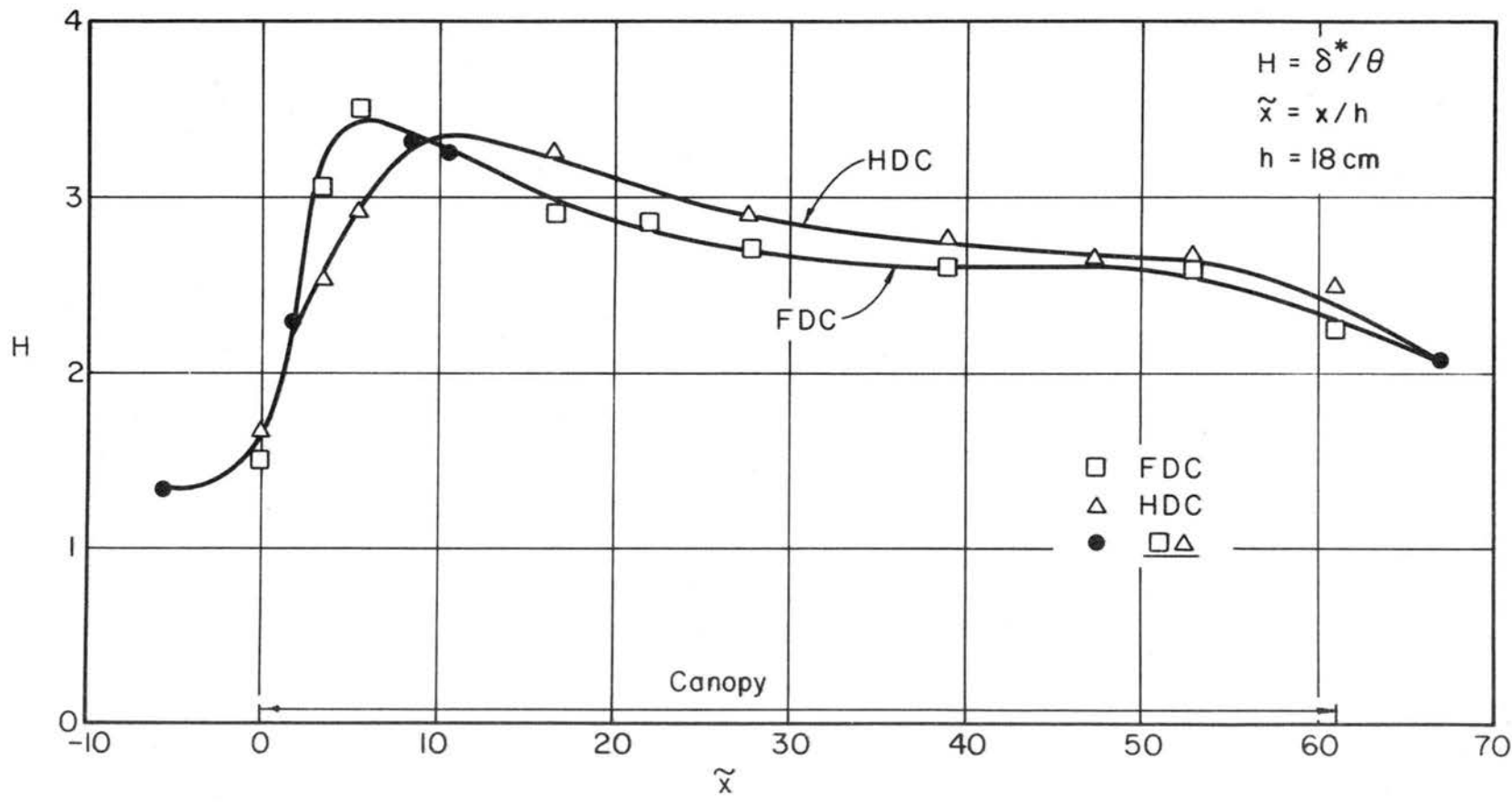


Fig. 5.12 Variation in the shape factor along the canopy; FDC and HDC.

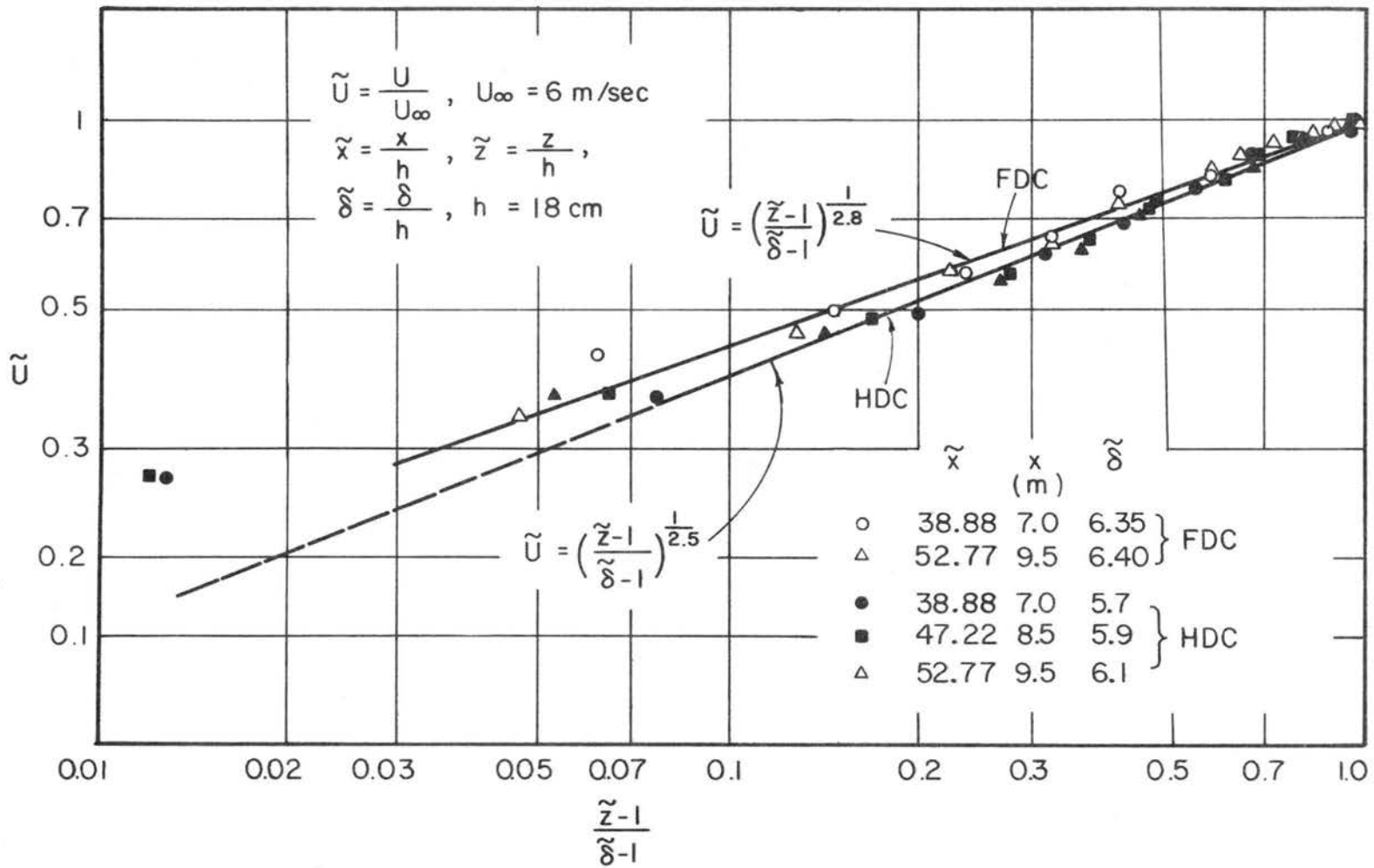


Fig. 5.13 Power law variation of the mean velocity above the canopy within the fully developed flow region; FDC and HDC.

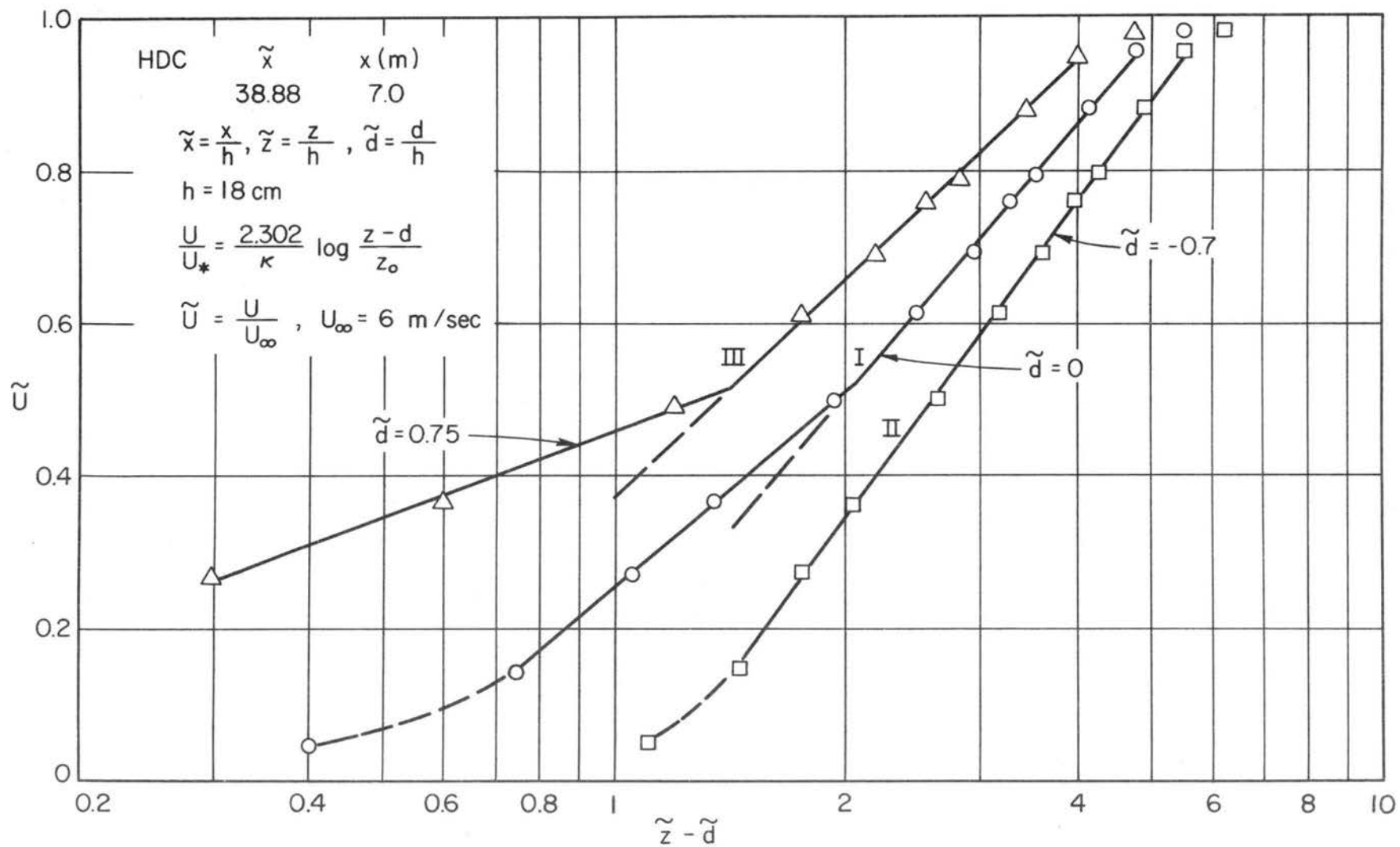


Fig. 5.14 Change in logarithmic law velocity representation with the zero-plane displacement; HDC case.

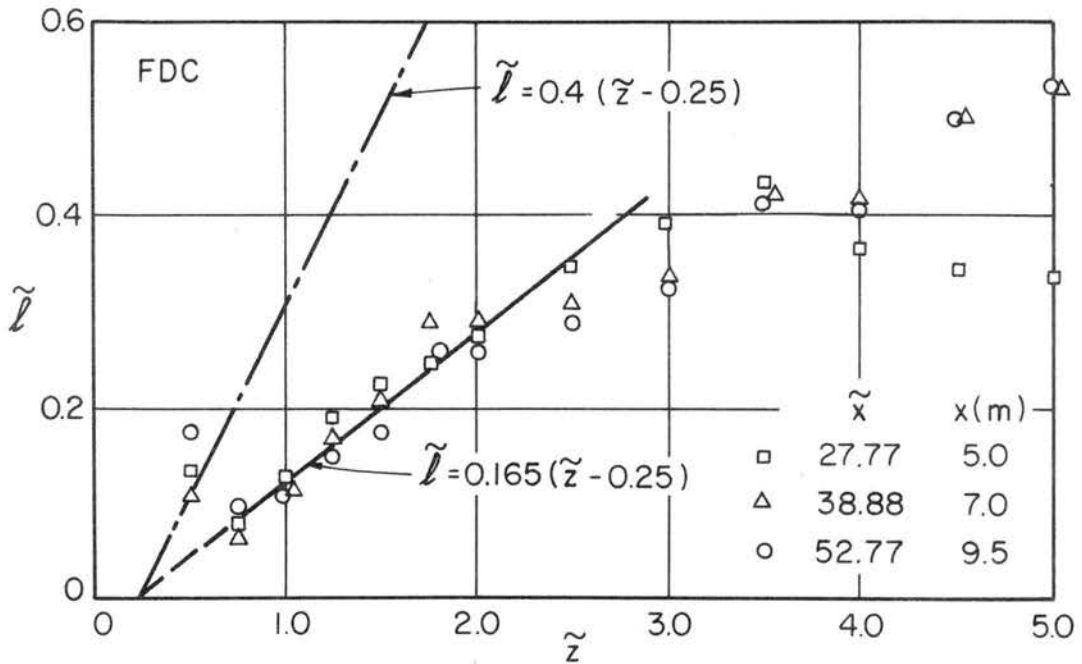
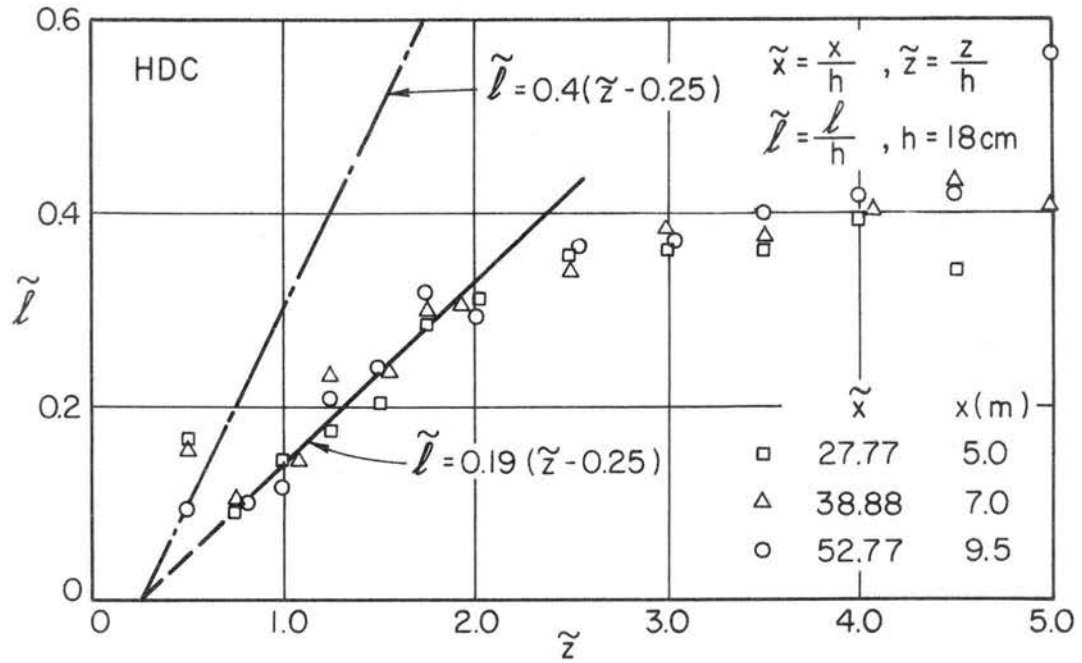


Fig. 5.15 Variation of the mixing length with height; FDC and HDC.

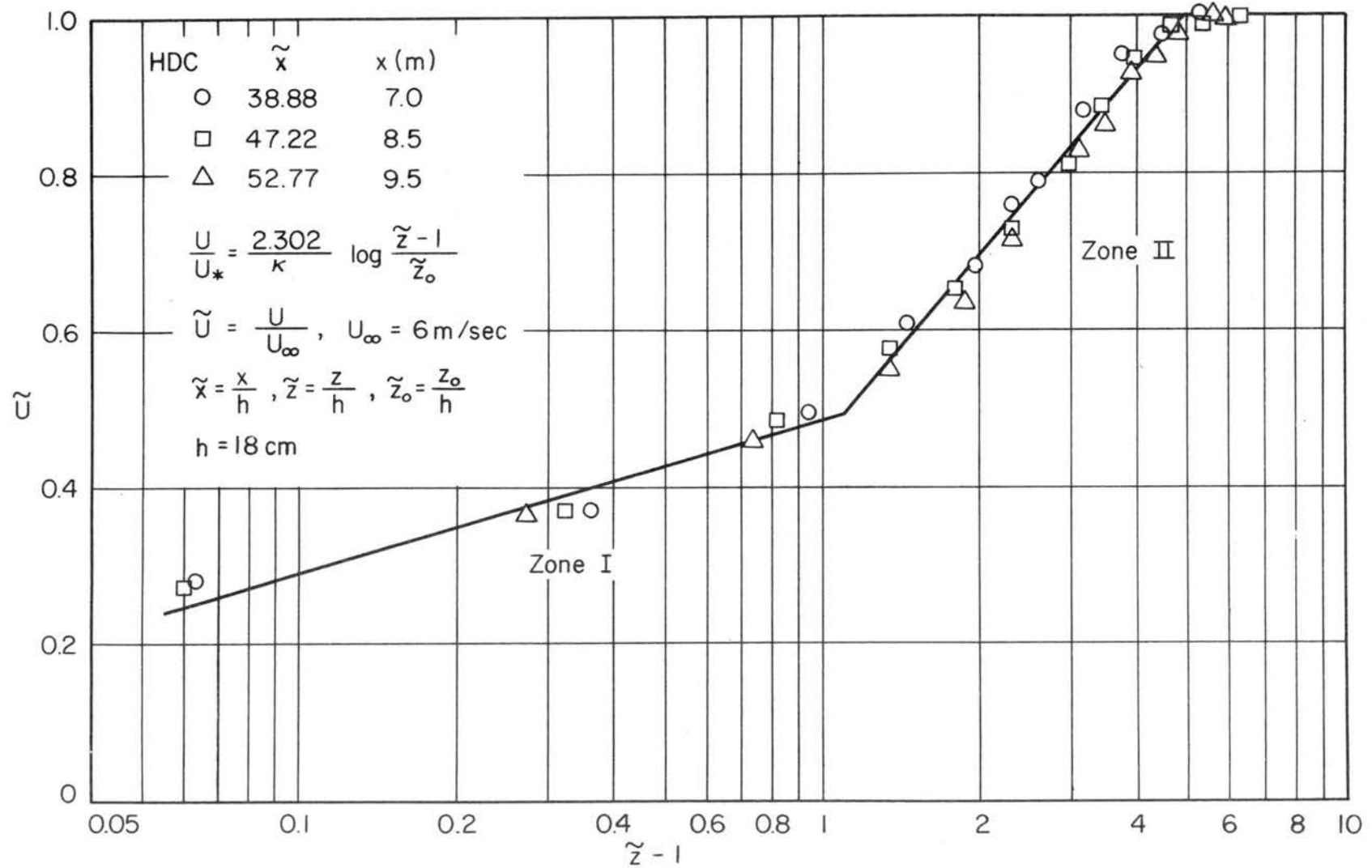


Fig. 5.16 Sample of modified logarithmic law description of the mean velocity profiles above the canopy within the fully developed flow region for HDC case.

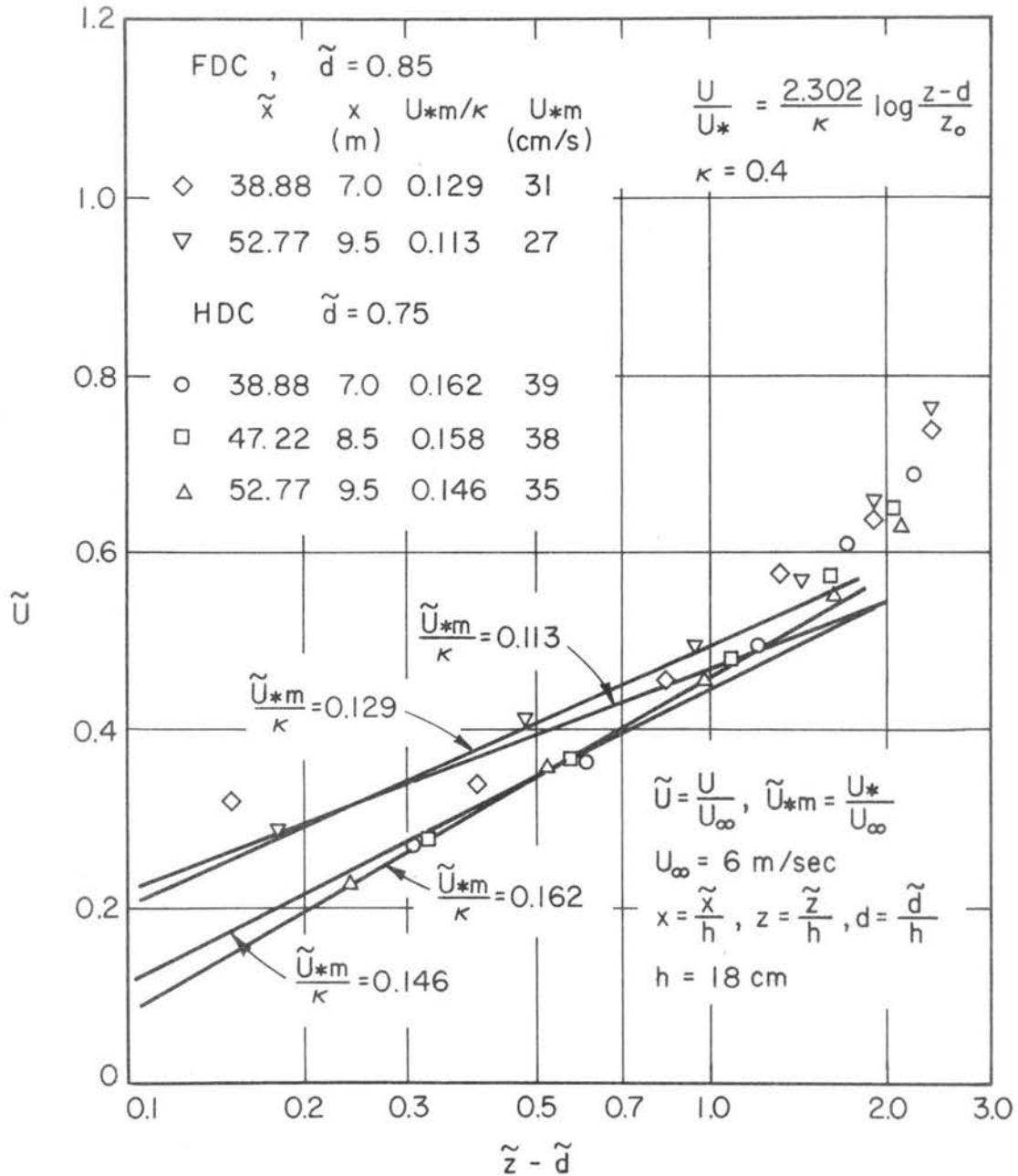


Fig. 5.17 Modified logarithmic law description of the mean velocity within the inner zone ( $z = 1.0$  to  $1.85$ ); FDC and HDC.

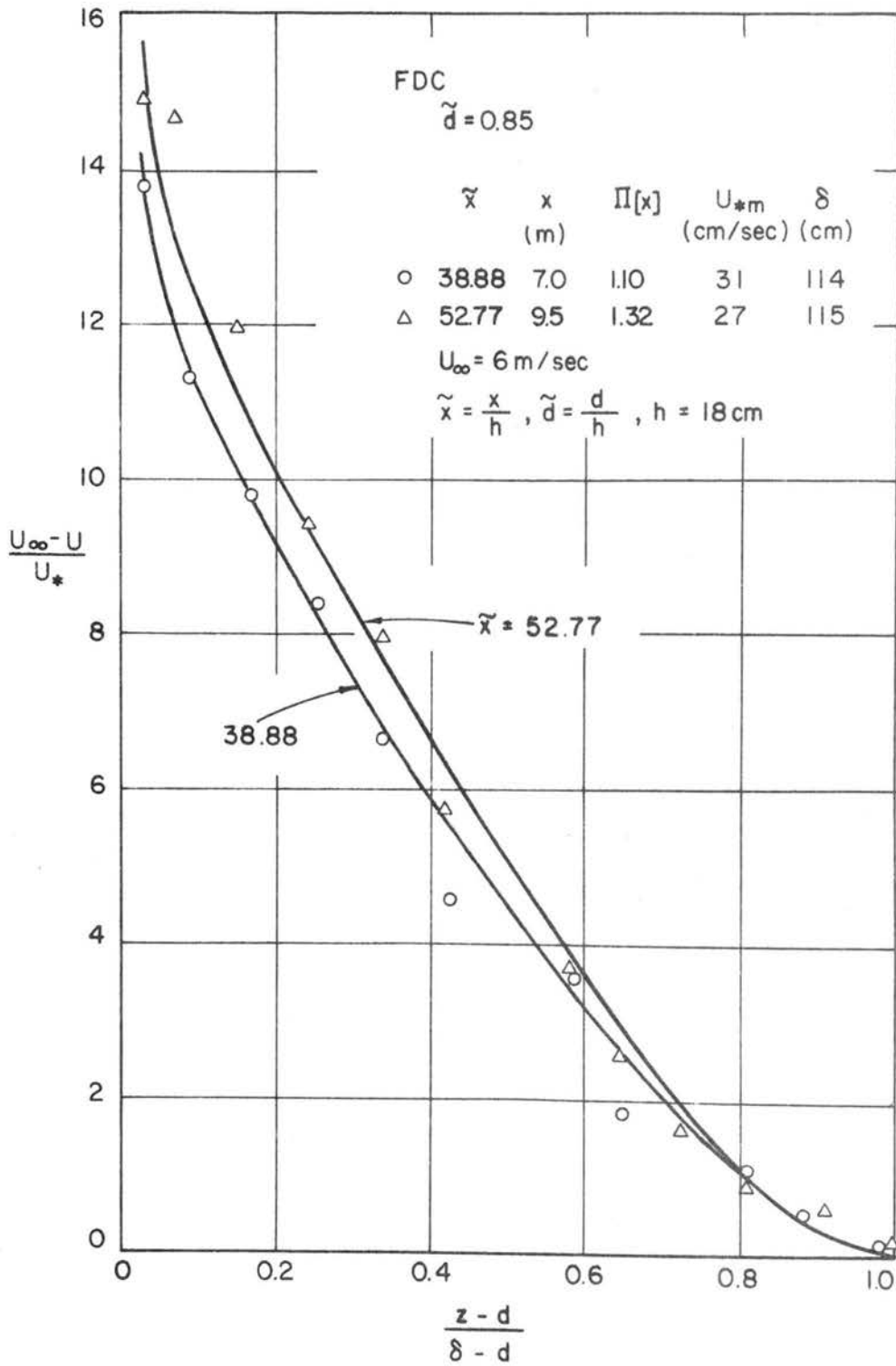


Fig. 5.18 Defect velocity profiles within the fully developed flow region in terms of the modified wake function; FDC case.

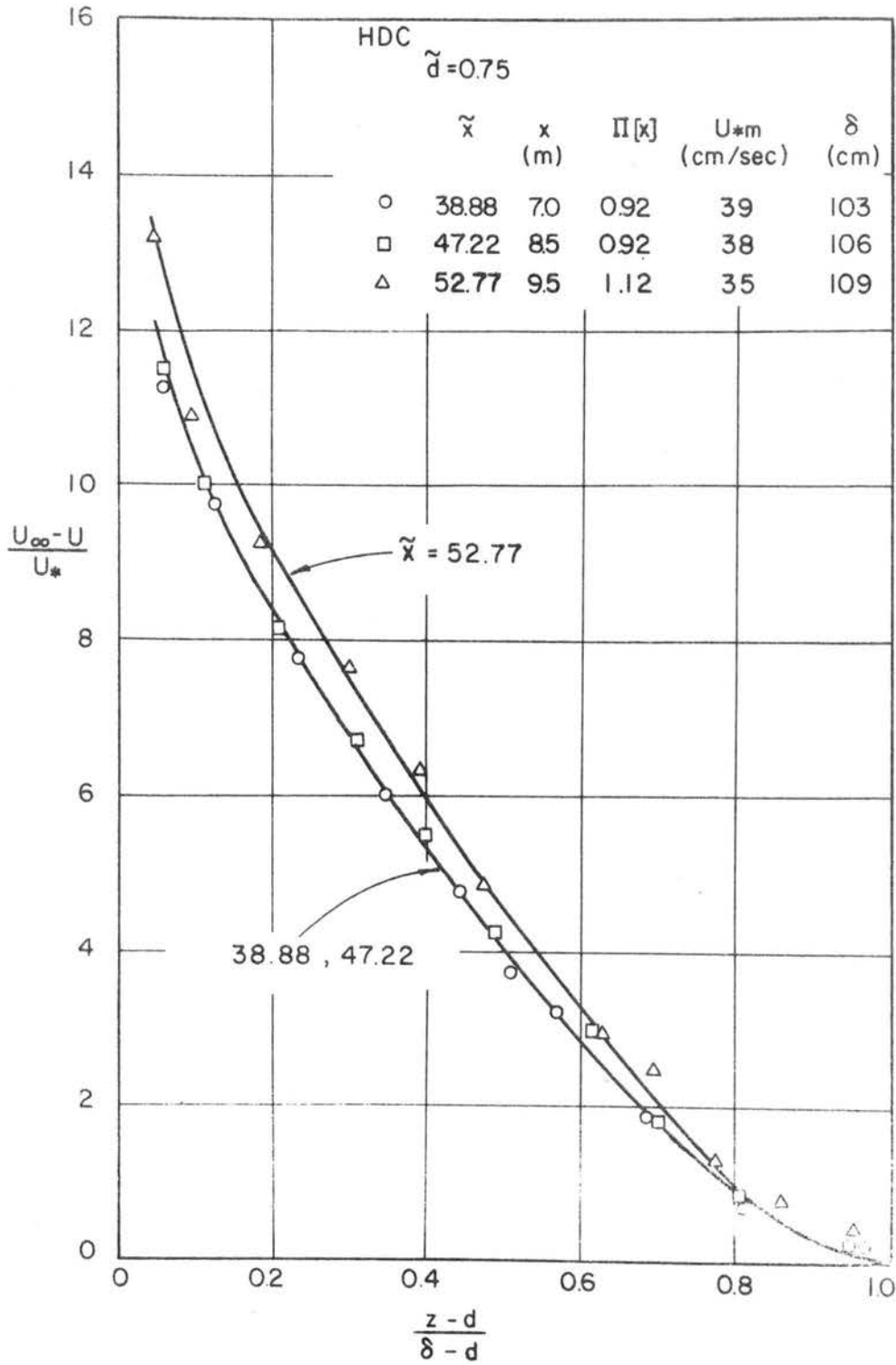


Fig. 5.19 Defect velocity profiles within the fully developed flow region in terms of the modified wake function; HDC case.

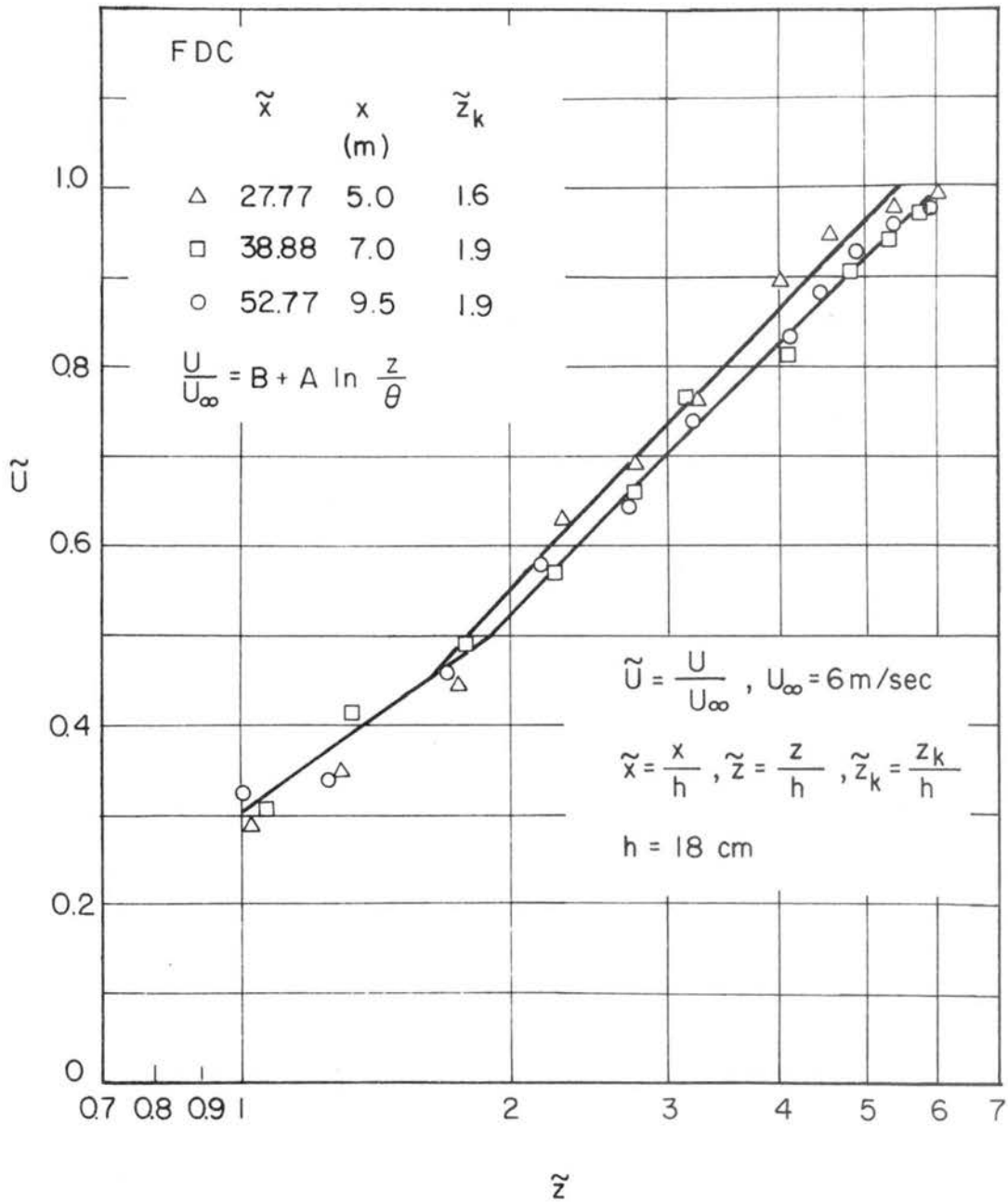


Fig. 5.20 Mean velocity profiles above the canopy within the fully developed flow region according to the generalized logarithmic law; FDC case.

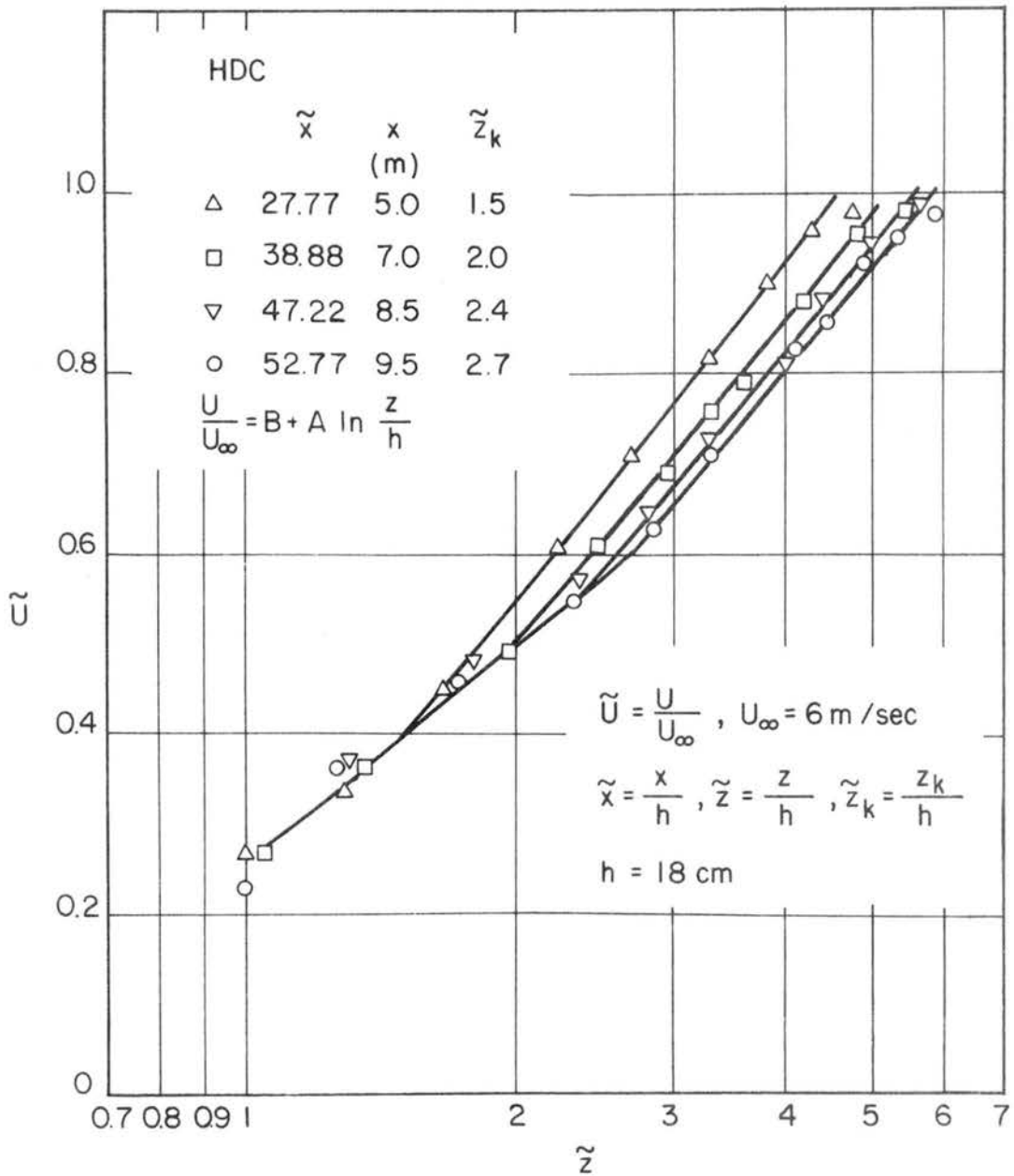


Fig. 5.21 Mean velocity profiles above the canopy in the fully developed flow region according to the generalized logarithmic law; HDC case.

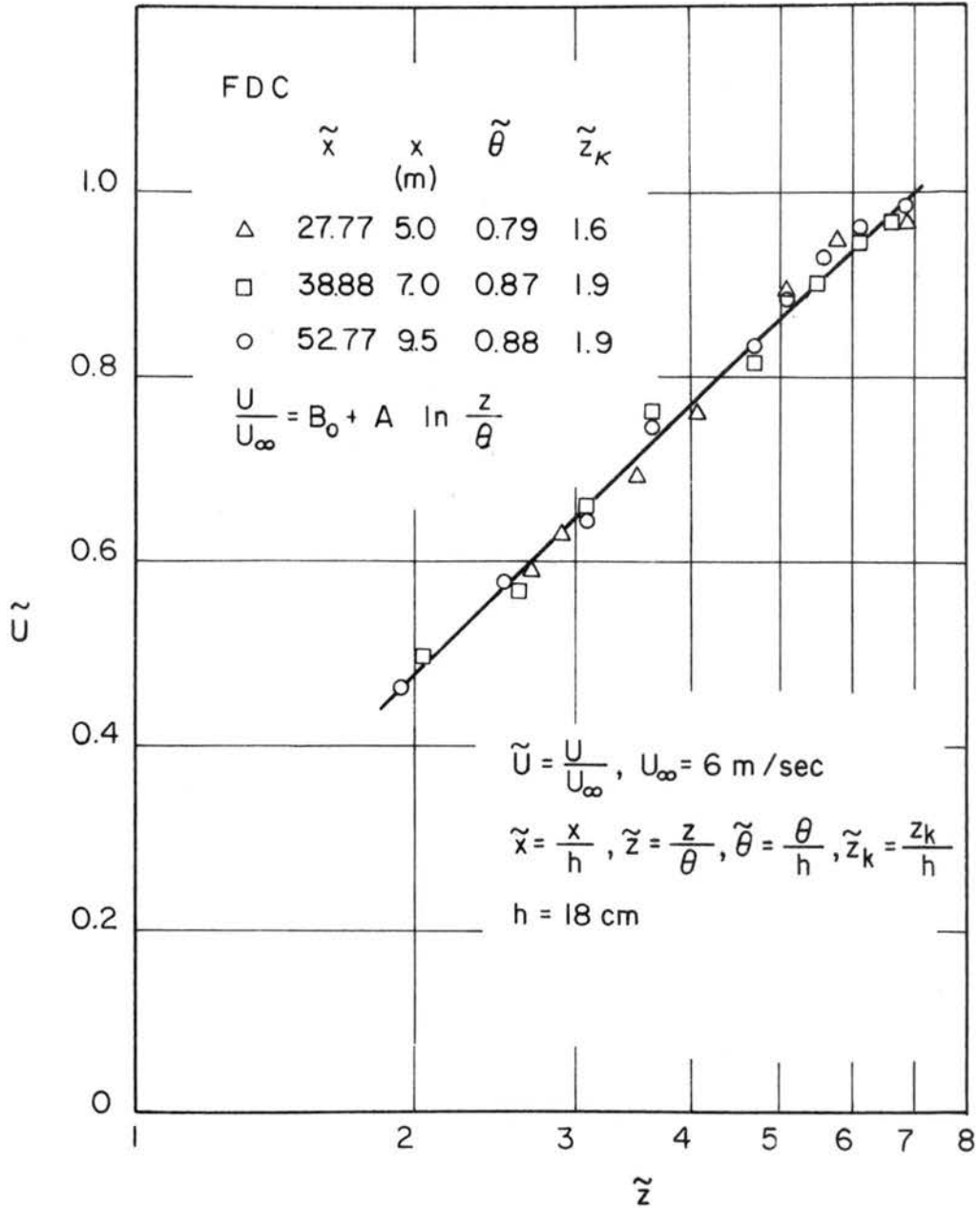


Fig. 5.22 Mean velocity profiles in the outer zone within the fully developed flow region described by the generalized logarithmic law; FDC case.

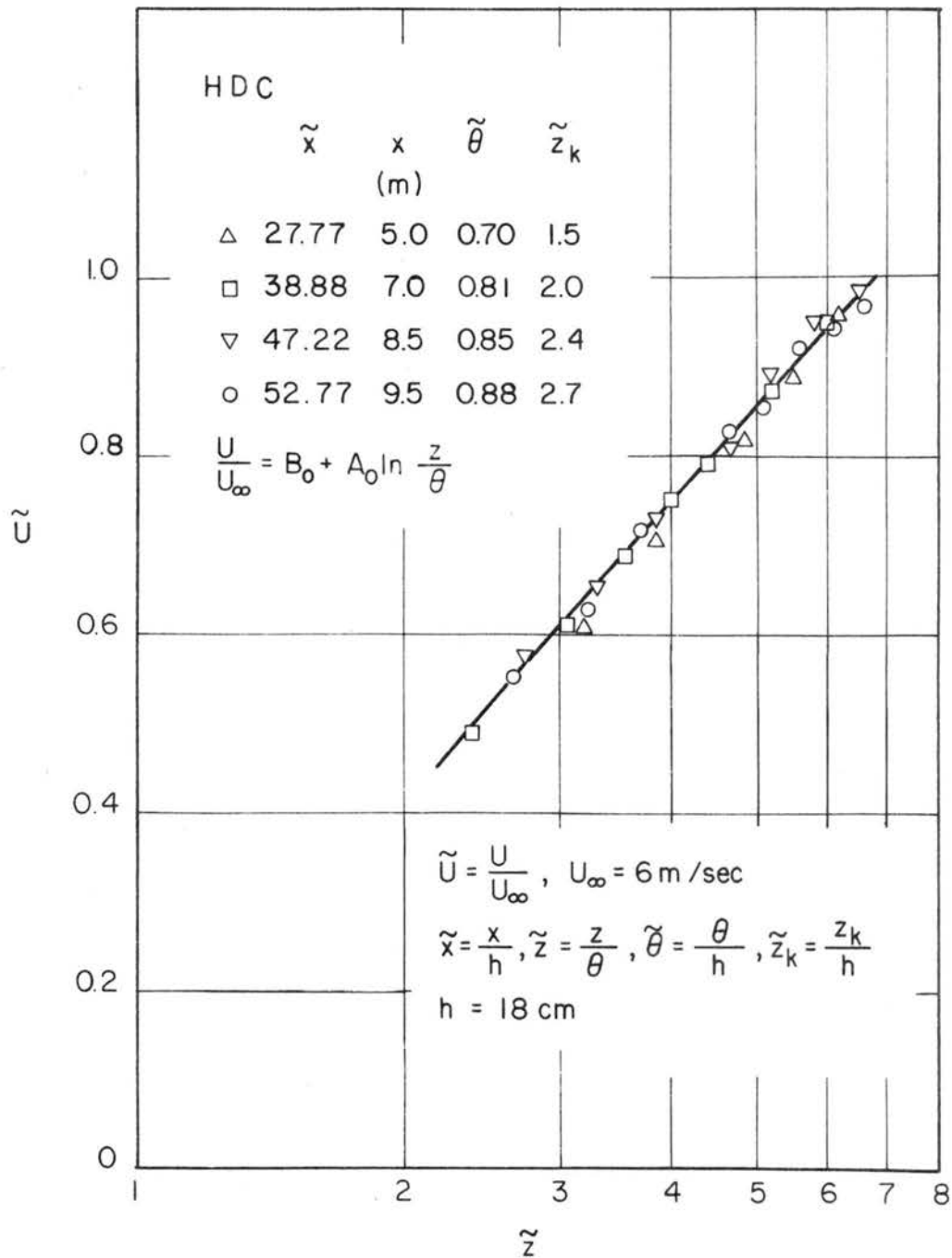


Fig. 5.23 Mean velocity profiles in the outer zone within the fully developed flow region described by the generalized logarithmic law; HDC case.

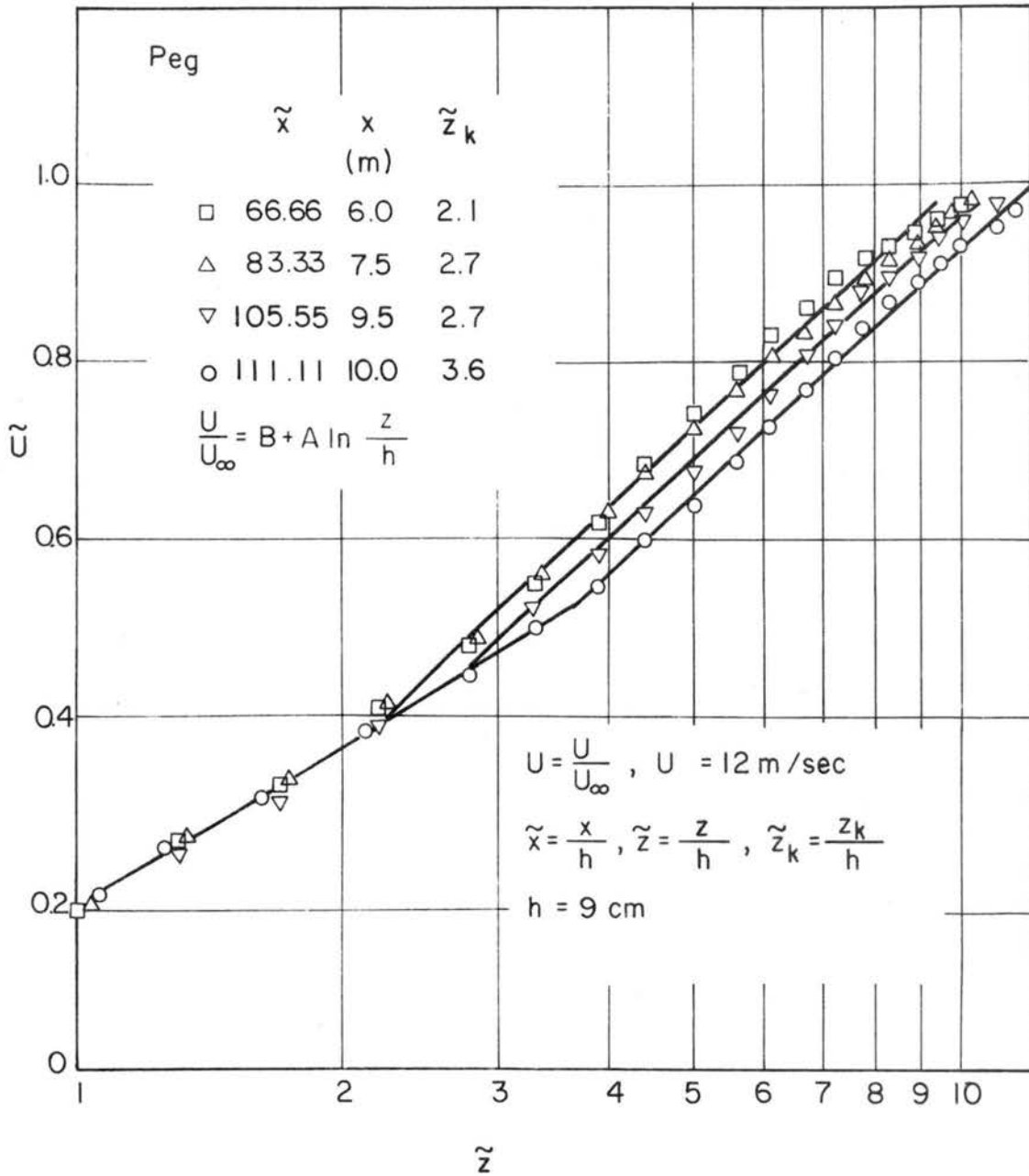


Fig. 5.24 Mean velocity profiles above a peg canopy within the fully developed flow region according to the generalized logarithmic law.

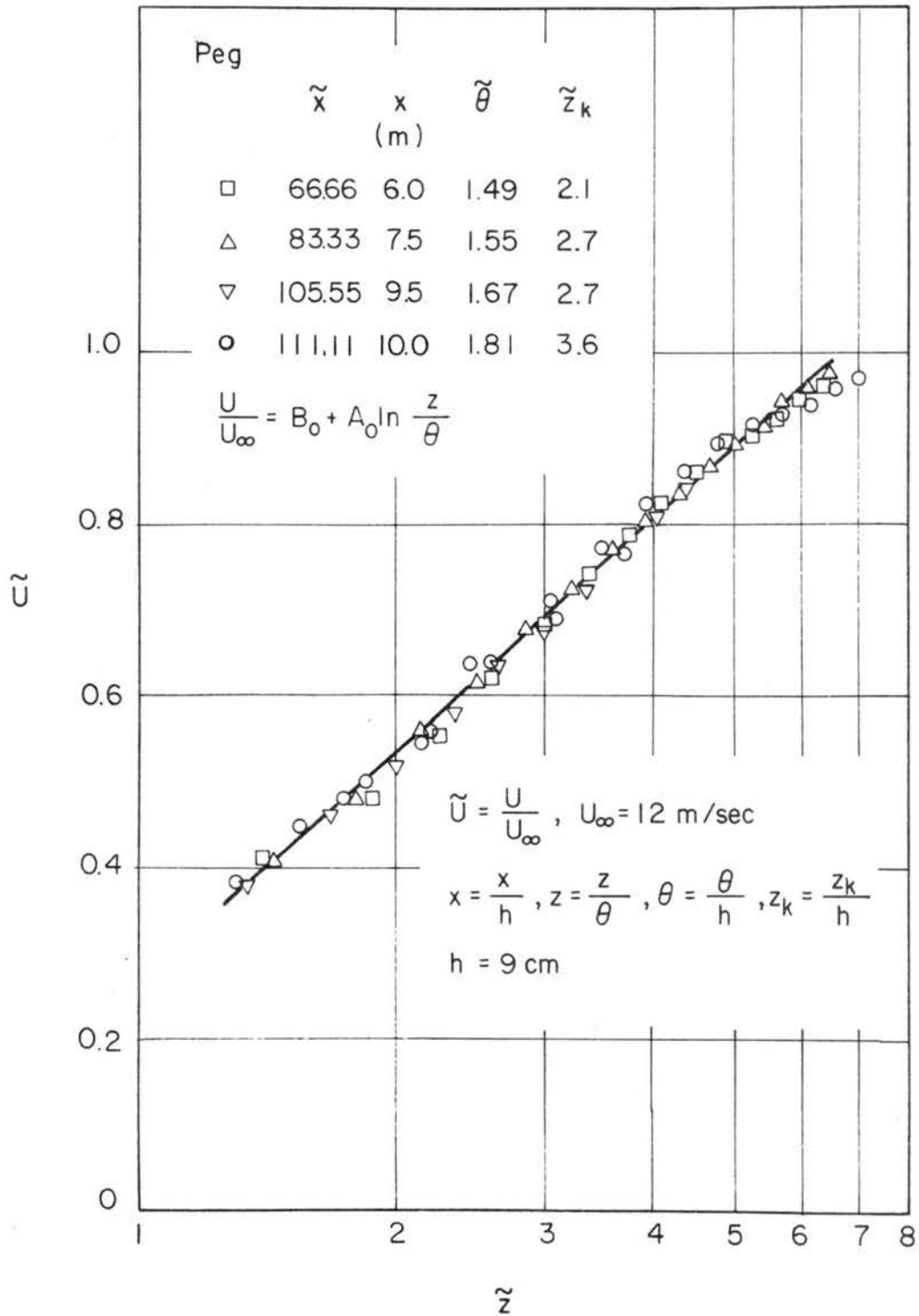


Fig. 5.25 Mean velocity profiles above a peg canopy in the outer zone within the fully developed flow region described by the generalized logarithmic law.

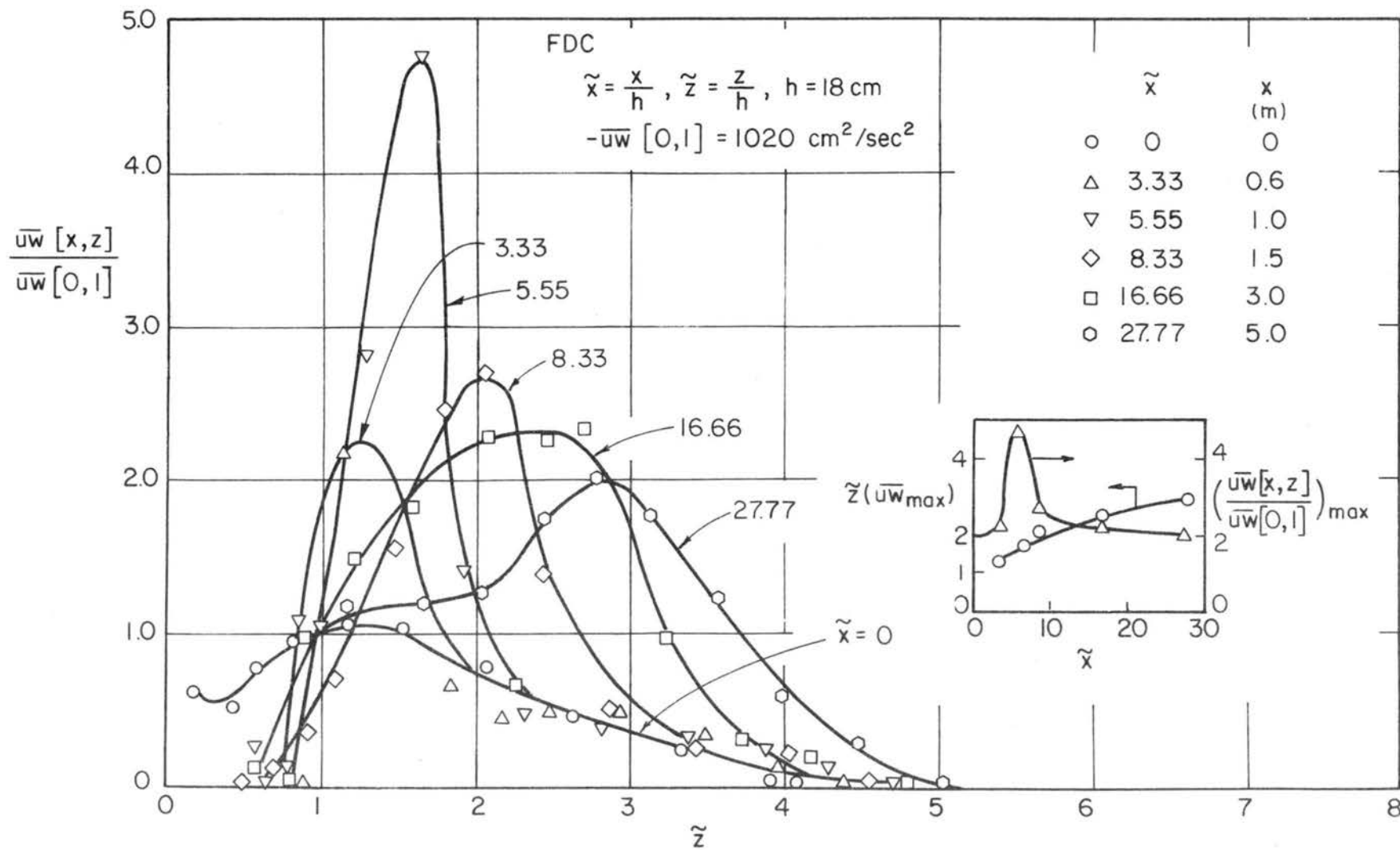


Fig. 5.26a Turbulent shear-stress distribution within and above the canopy; FDC case.

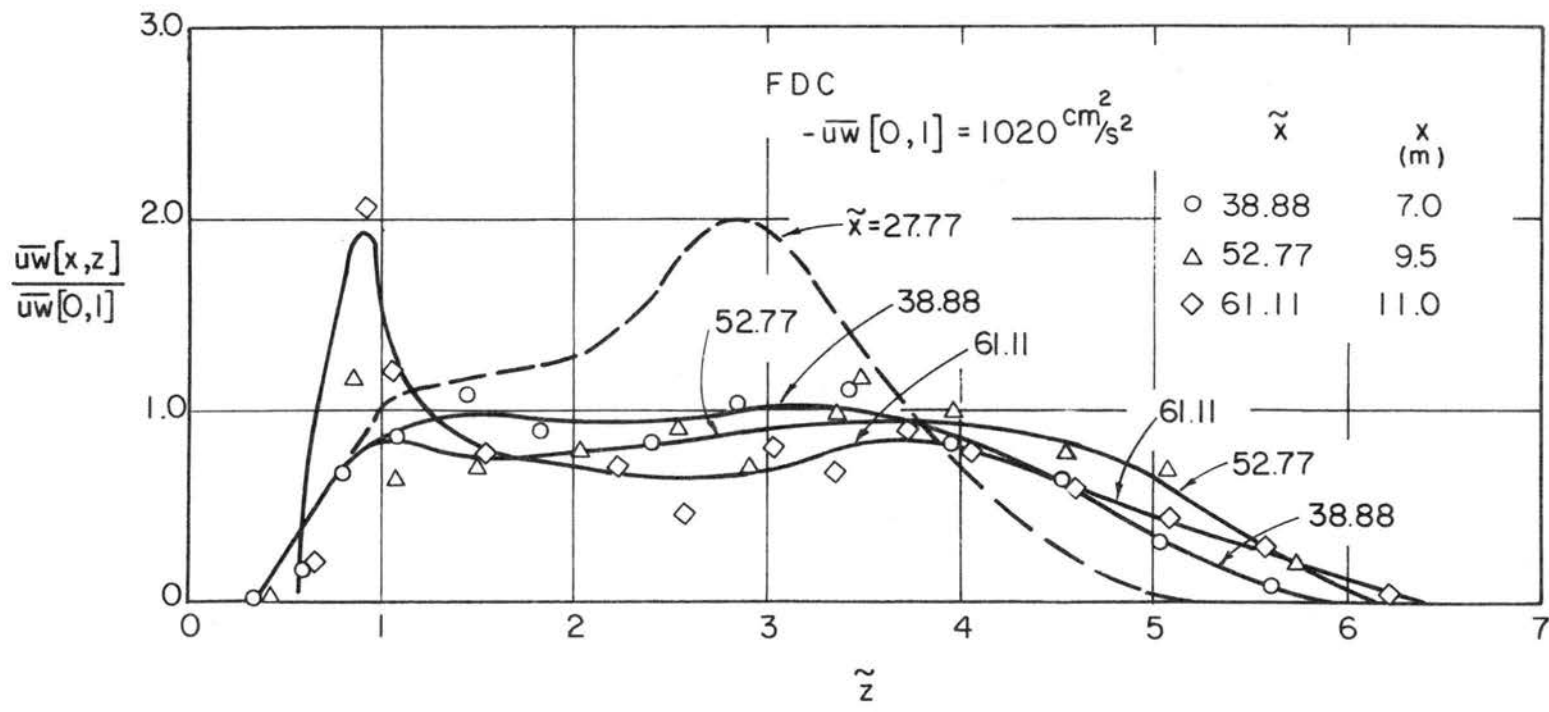


Fig. 5.26b Turbulent shear-stress distribution within and above the canopy; FDC case.

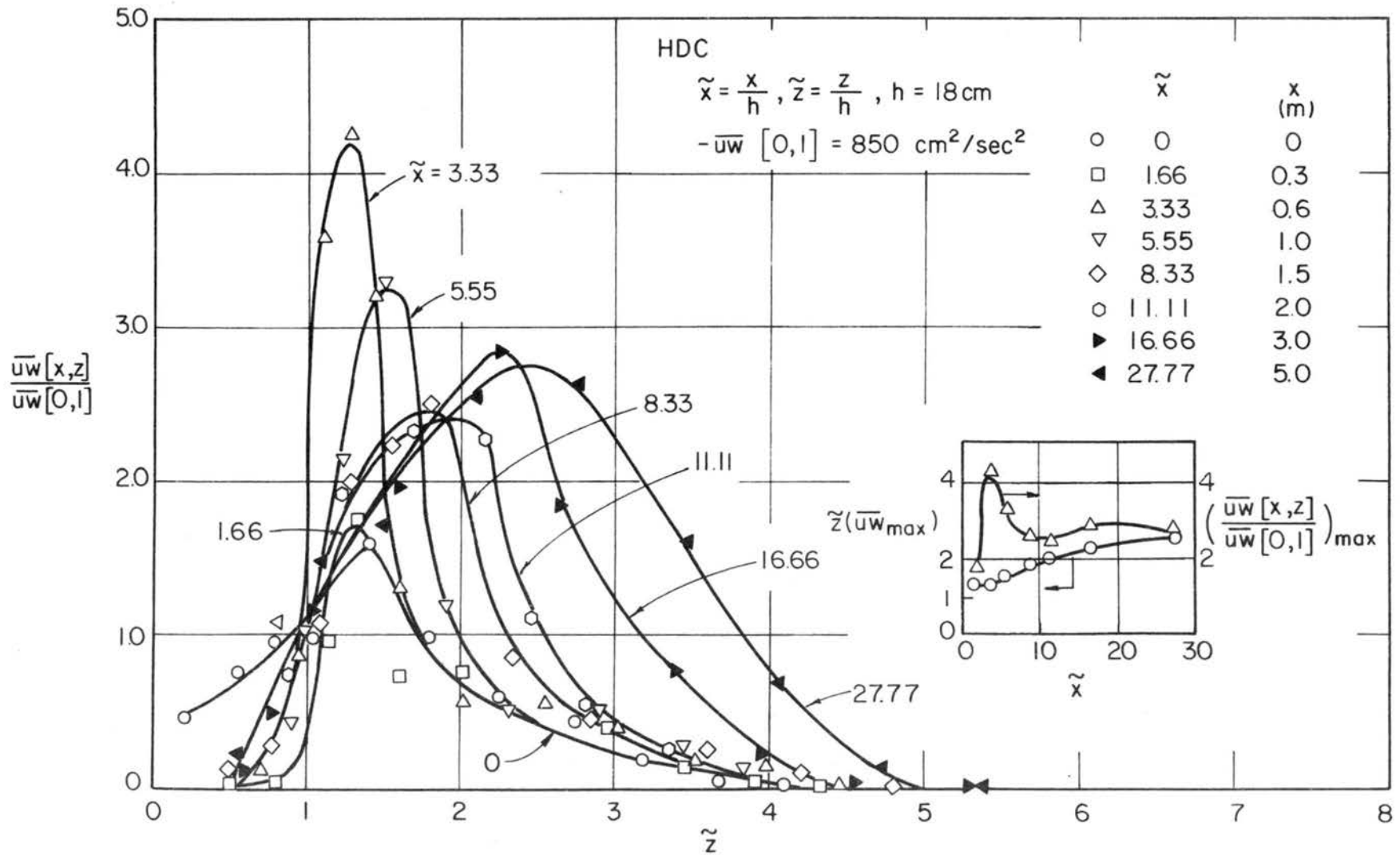


Fig. 5.27a Turbulent shear-stress distributions within and above the canopy; HDC case.

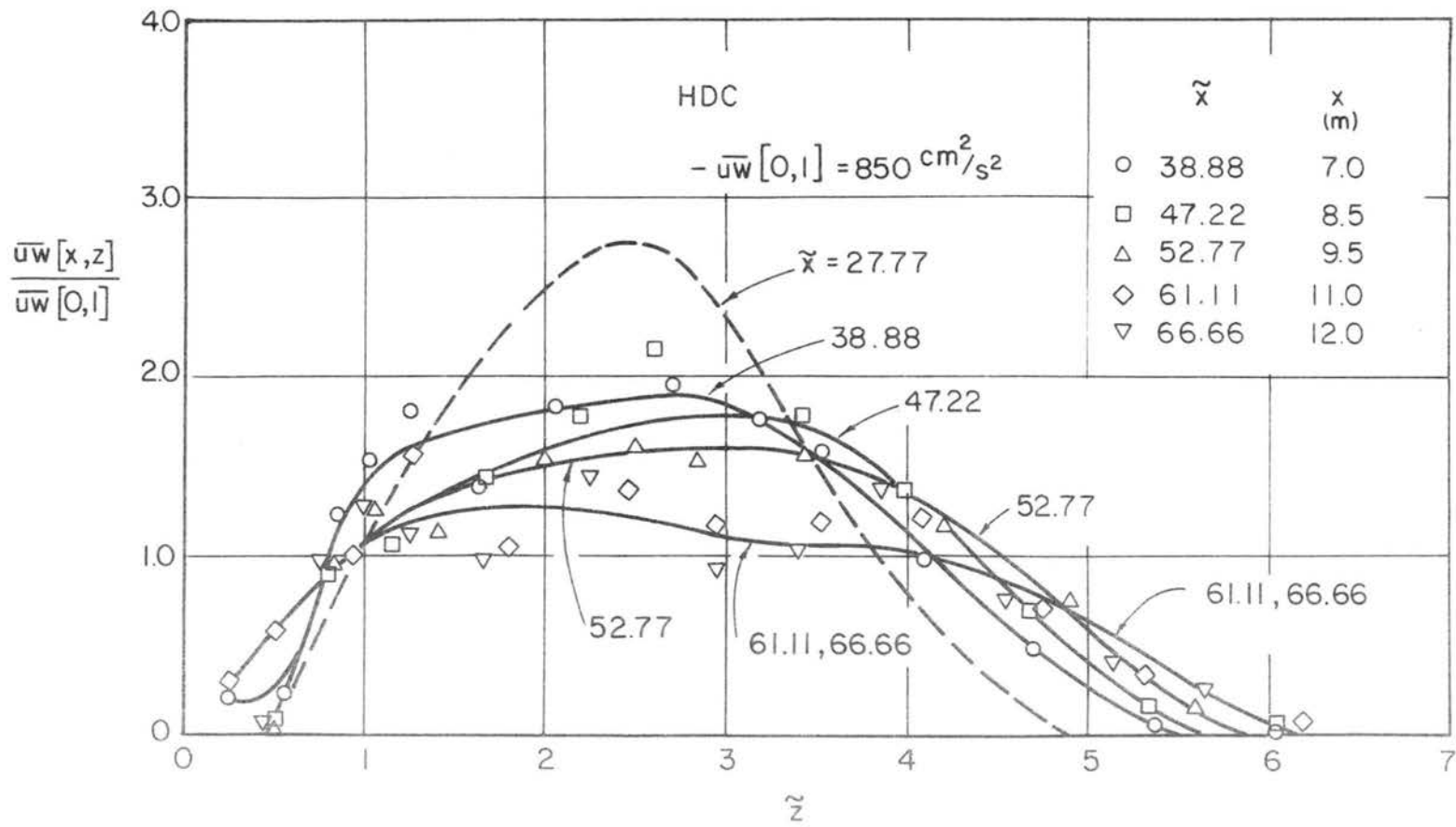


Fig. 5.27b Turbulent shear-stress distributions within and above the canopy; HDC case.

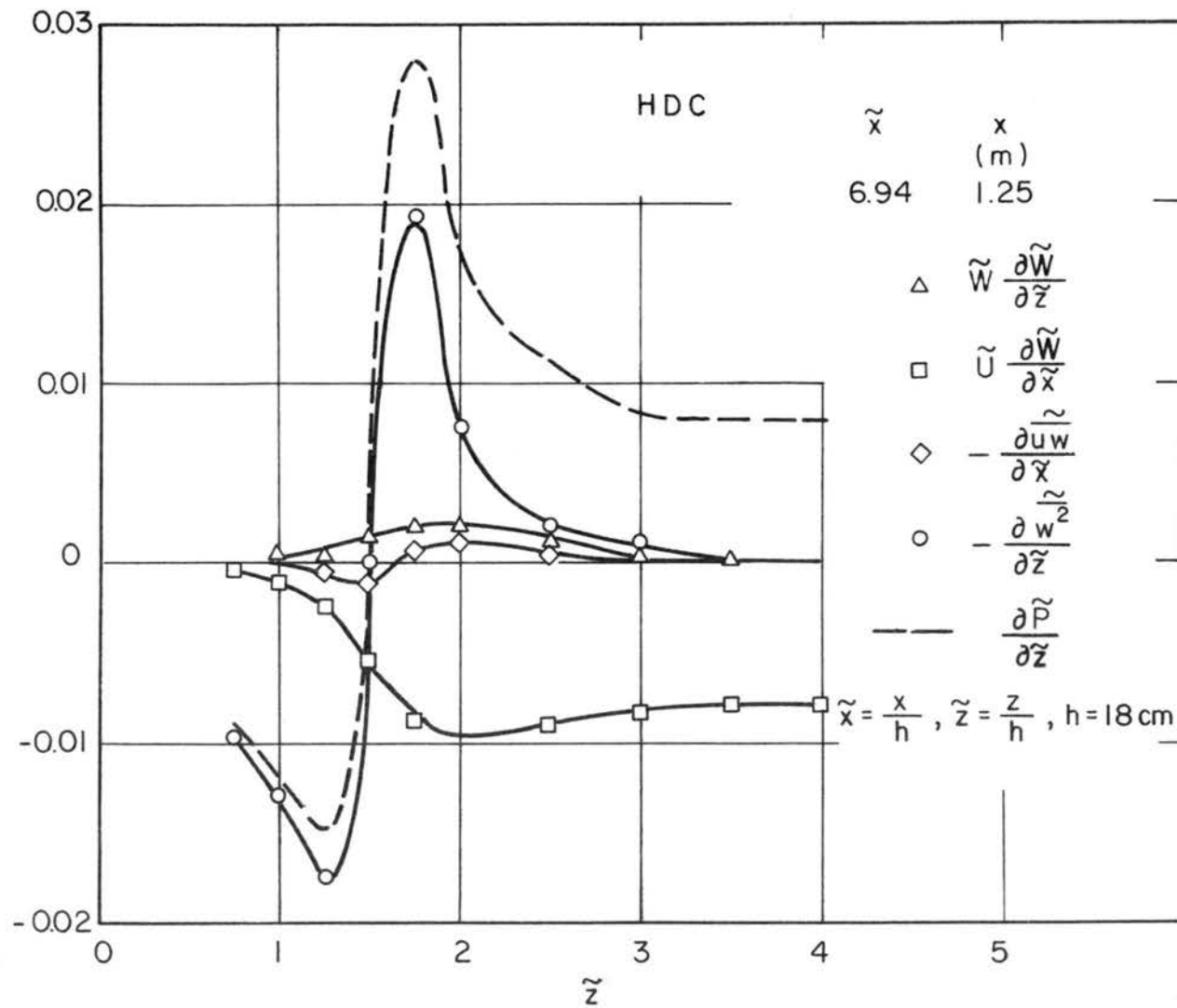


Fig. 5.28 Momentum balance in the transition region; HDC case.

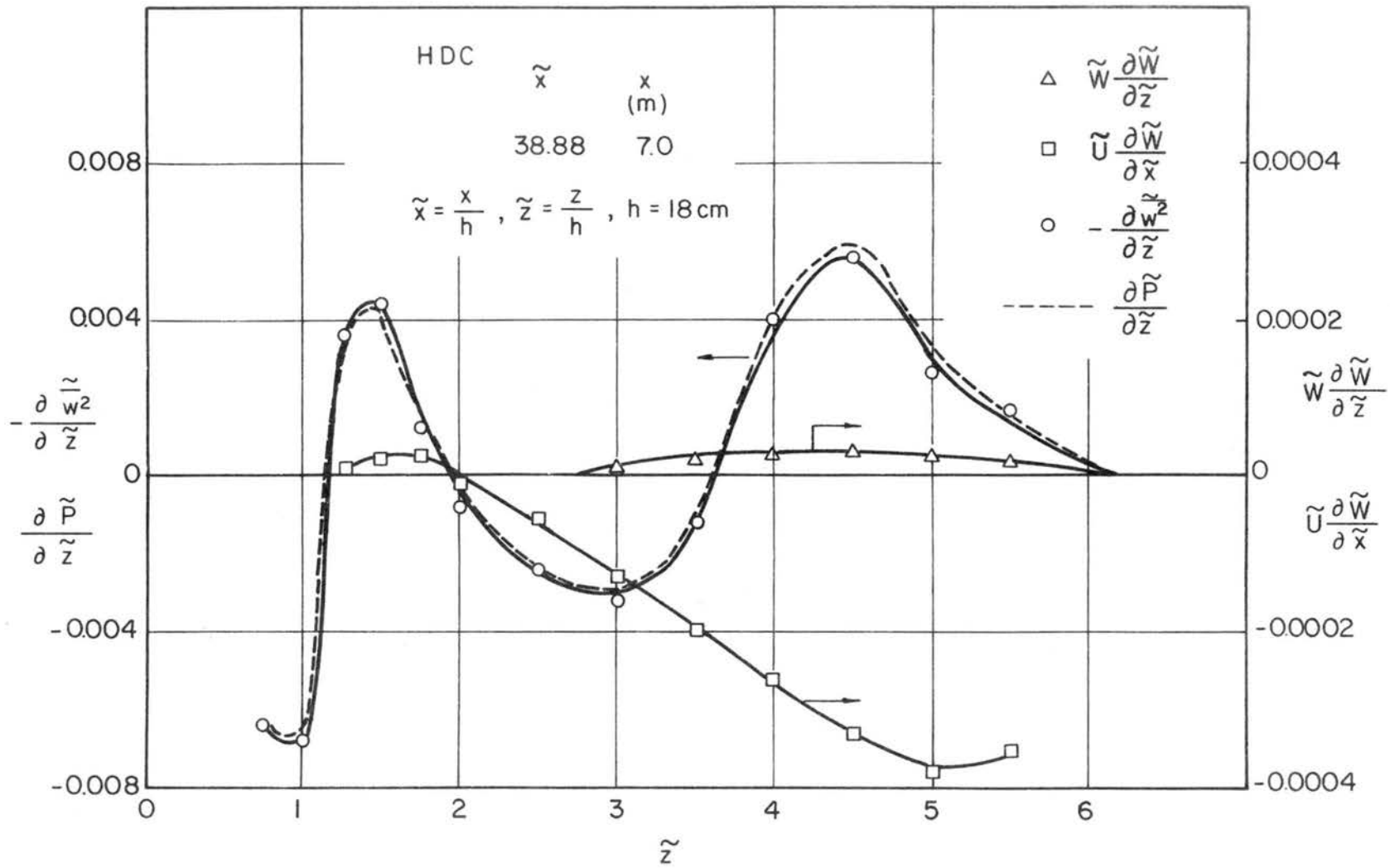


Fig. 5.29 Momentum balance in the fully developed flow region; HDC case.

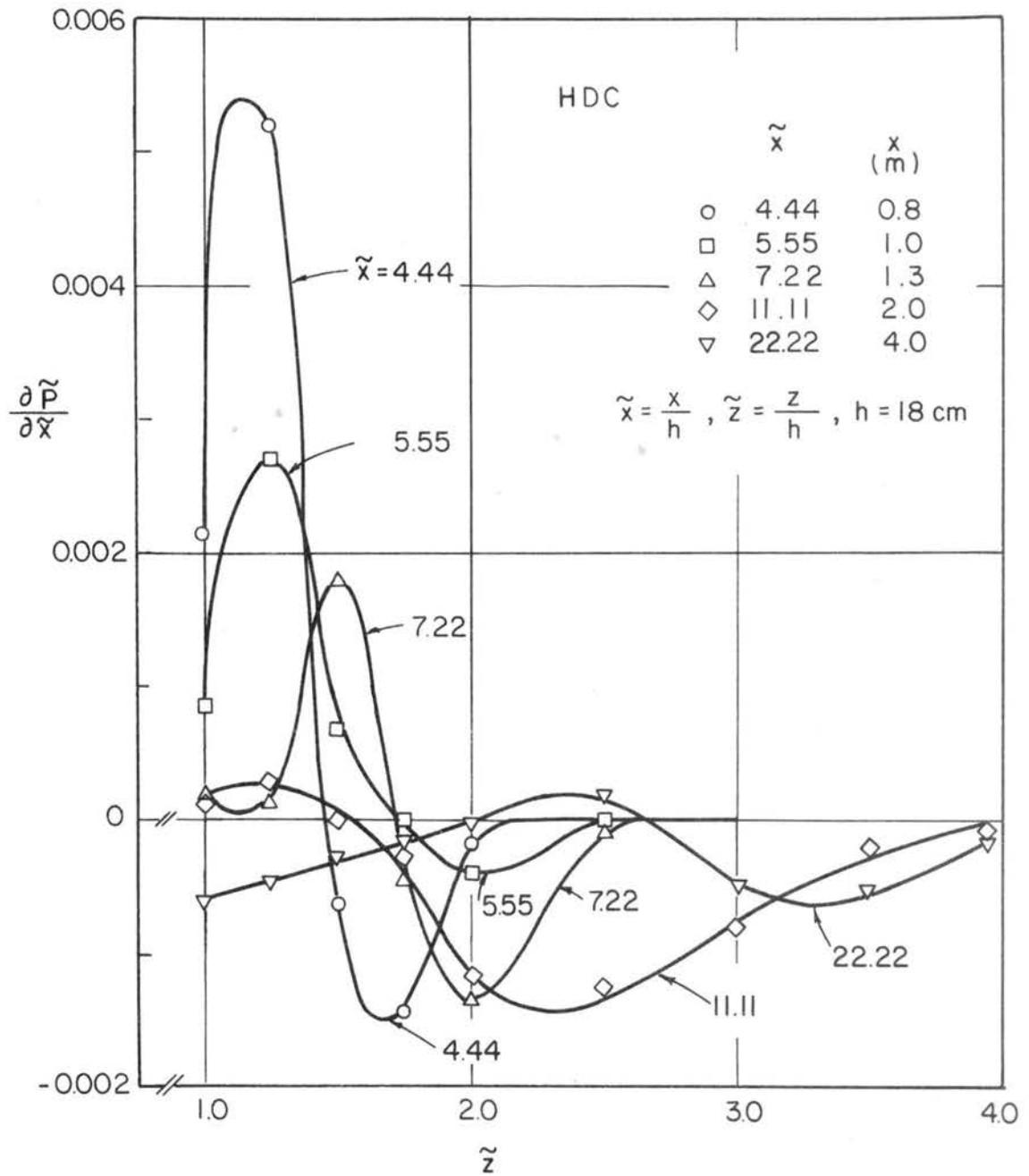


Fig. 5.30 Longitudinal pressure gradient above the canopy; HDC case.

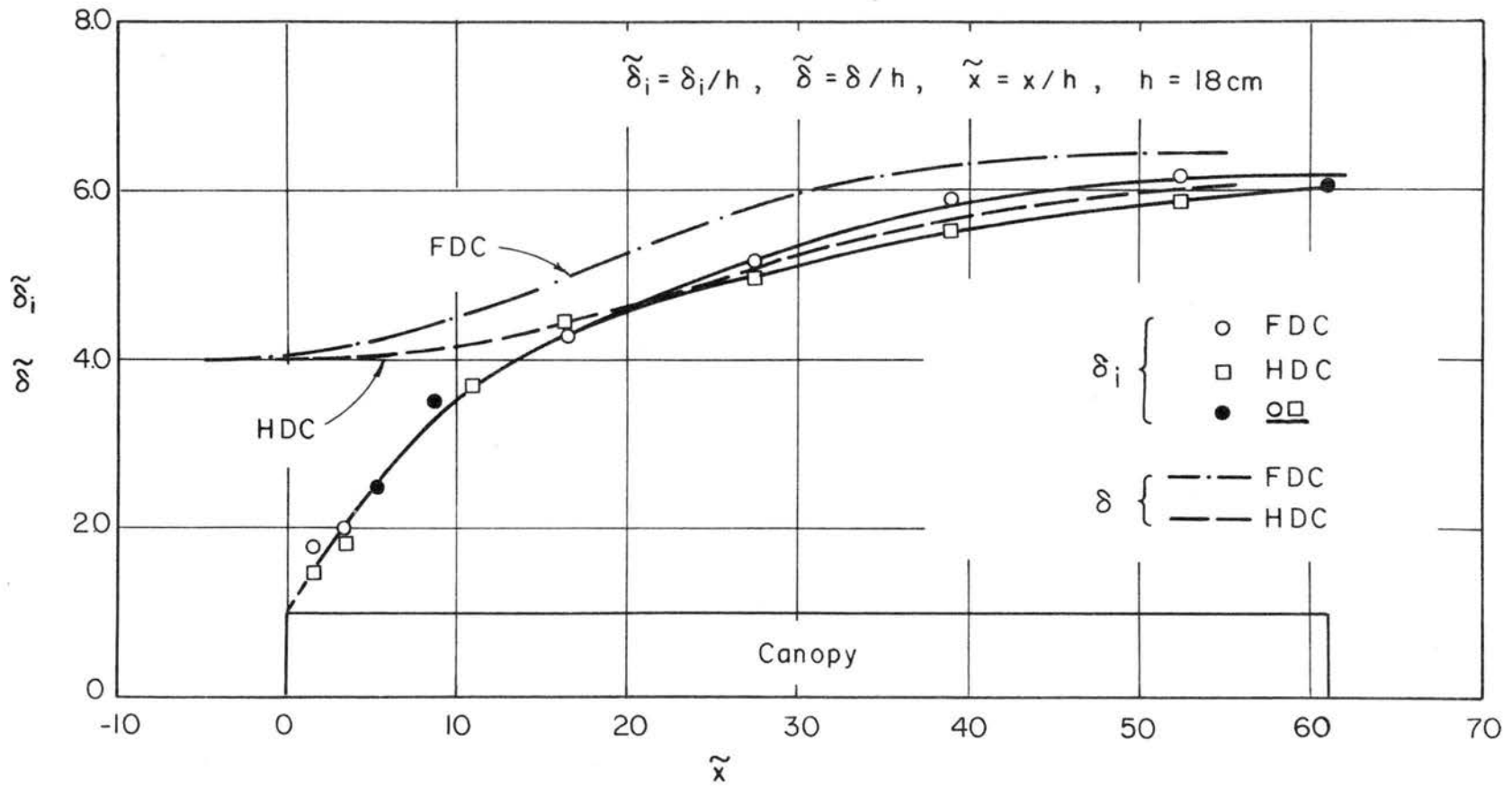


Fig. 5.31 Growth of the internal and total boundary layer thicknesses.

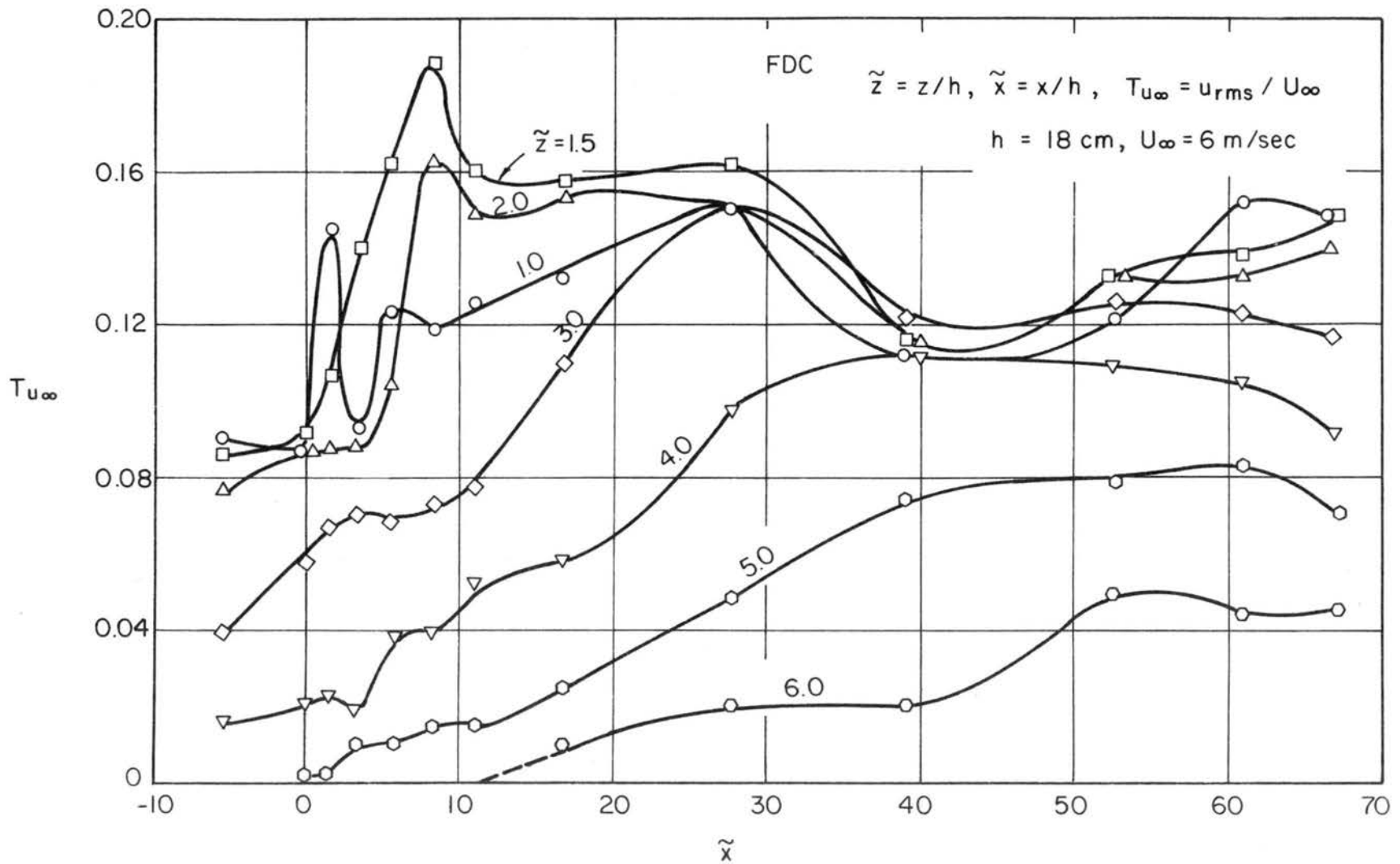


Fig. 5.32 Variation in longitudinal turbulent intensity above the canopy along isoheights; FDC case.

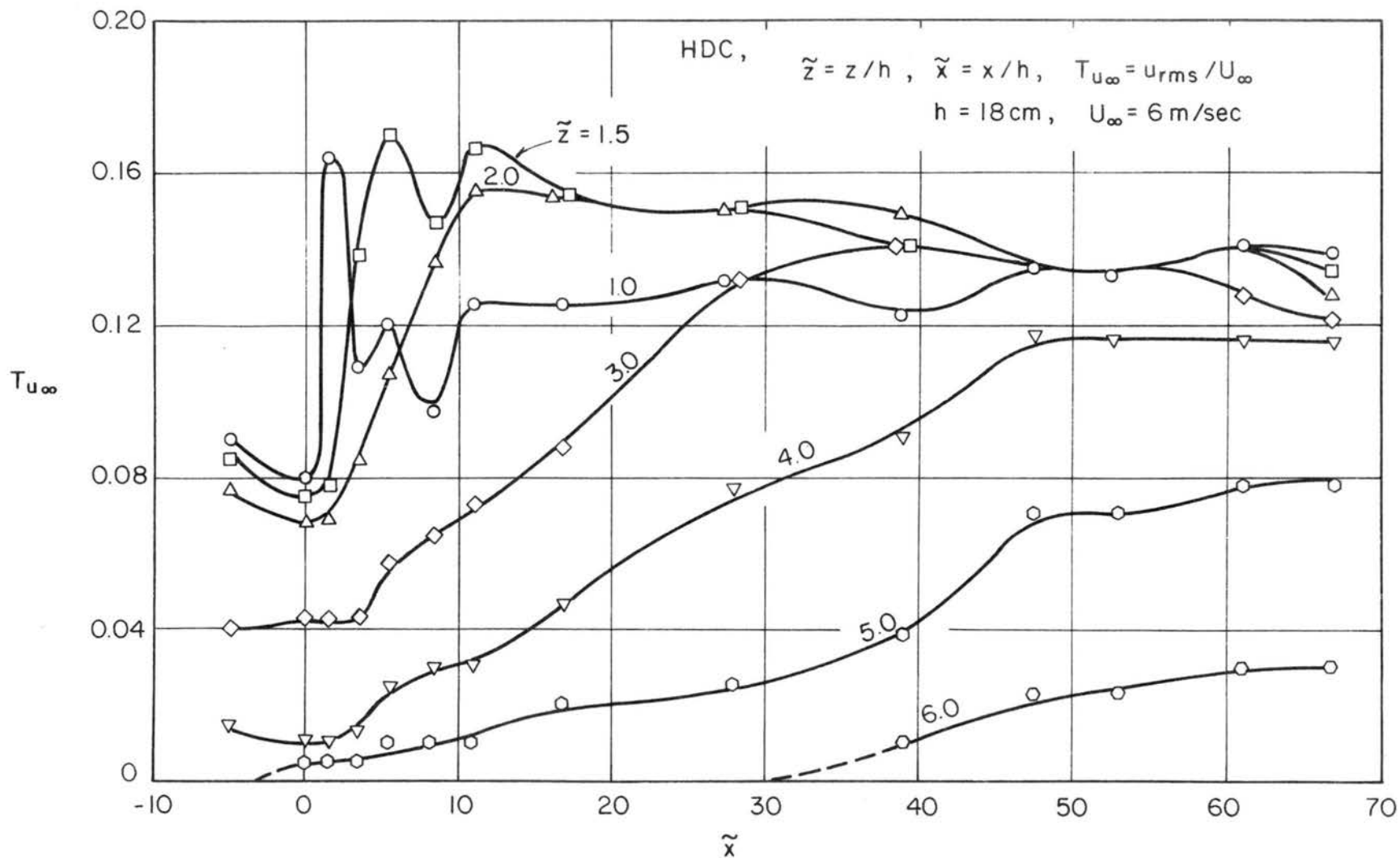


Fig. 5.33 Variation in longitudinal turbulent intensity above the canopy along isoheights; HDC case.

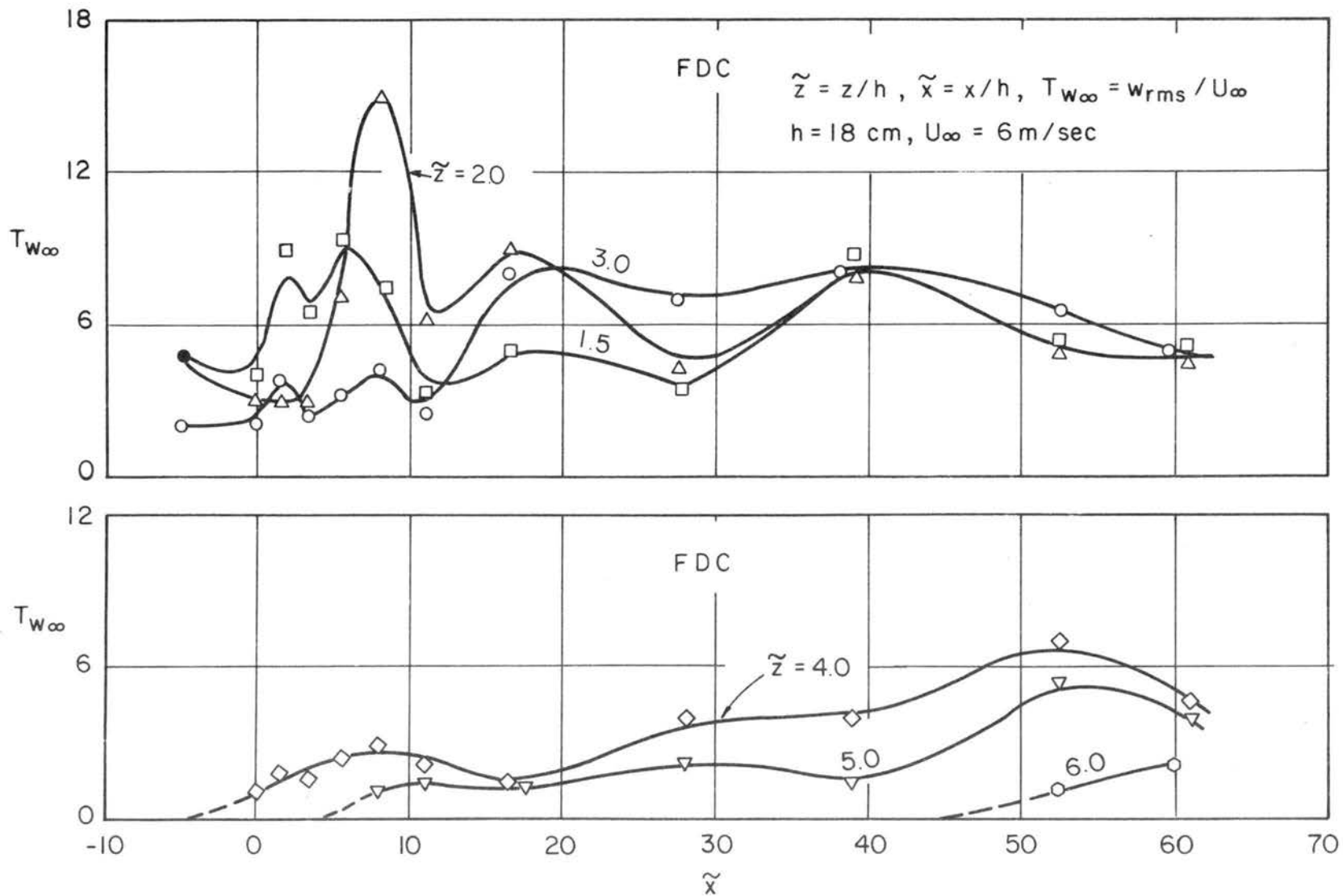


Fig. 5.34 Variation in vertical turbulent intensity above the canopy along isoheights; FDC case.

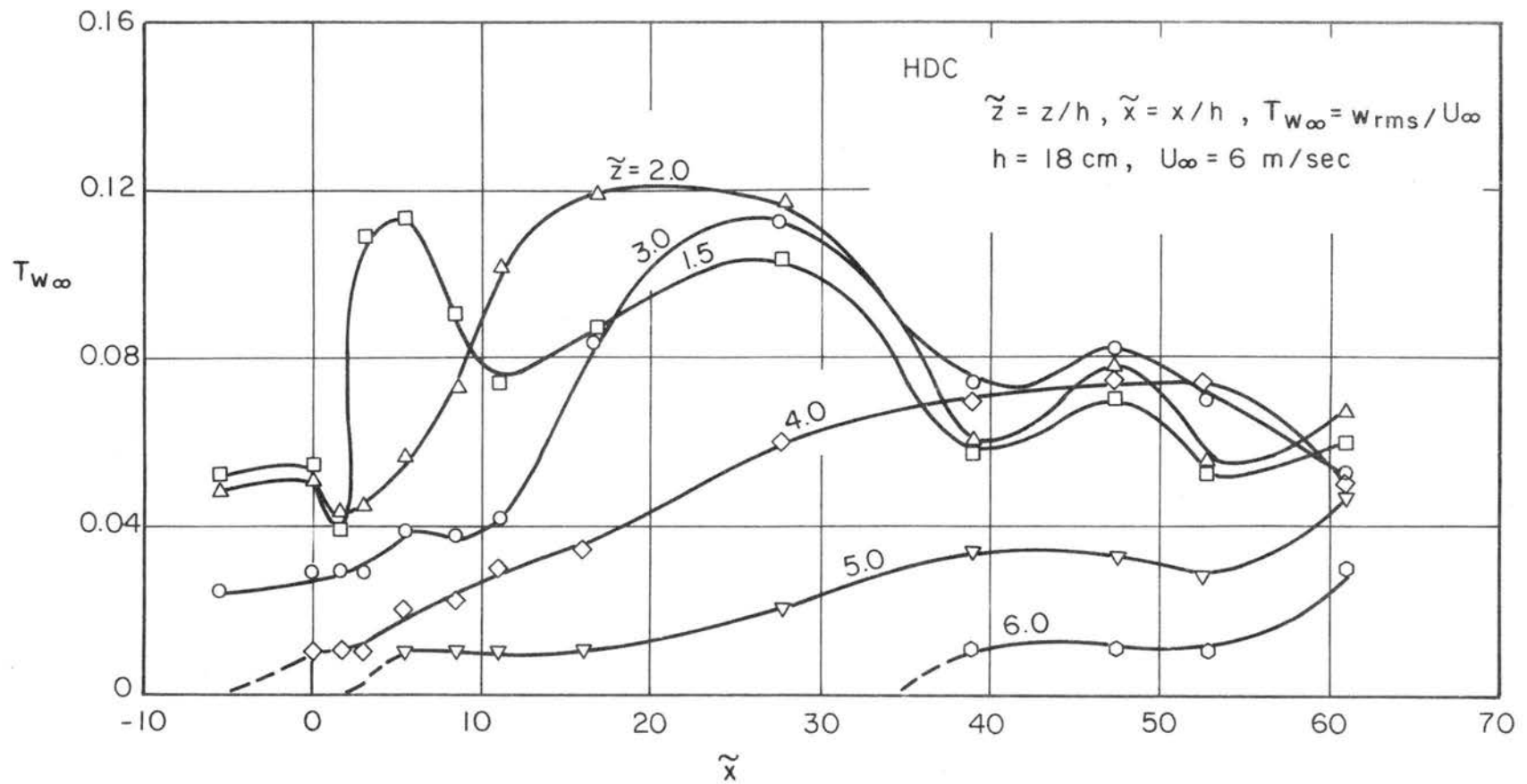


Fig. 5.35 Variation in vertical turbulent intensity above the canopy along isoheights; HDC case.

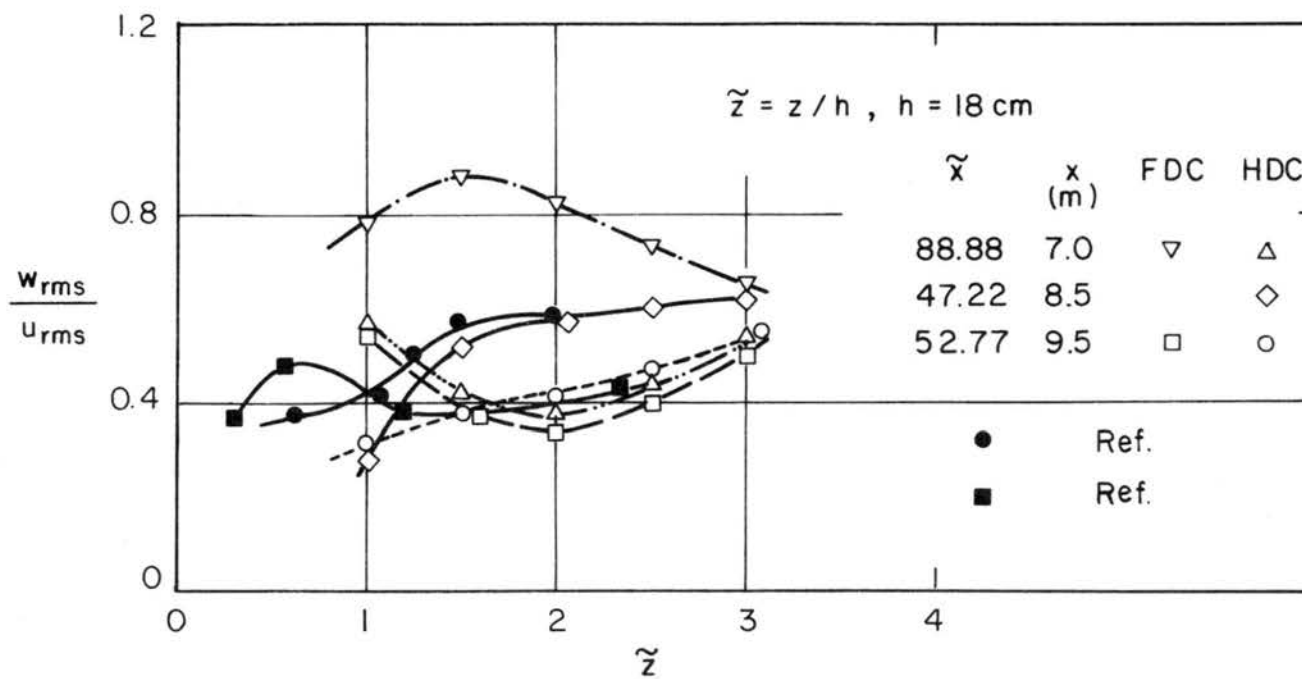


Fig. 5.36 Coefficient of anisotropy for the model forest canopy and for real forests.

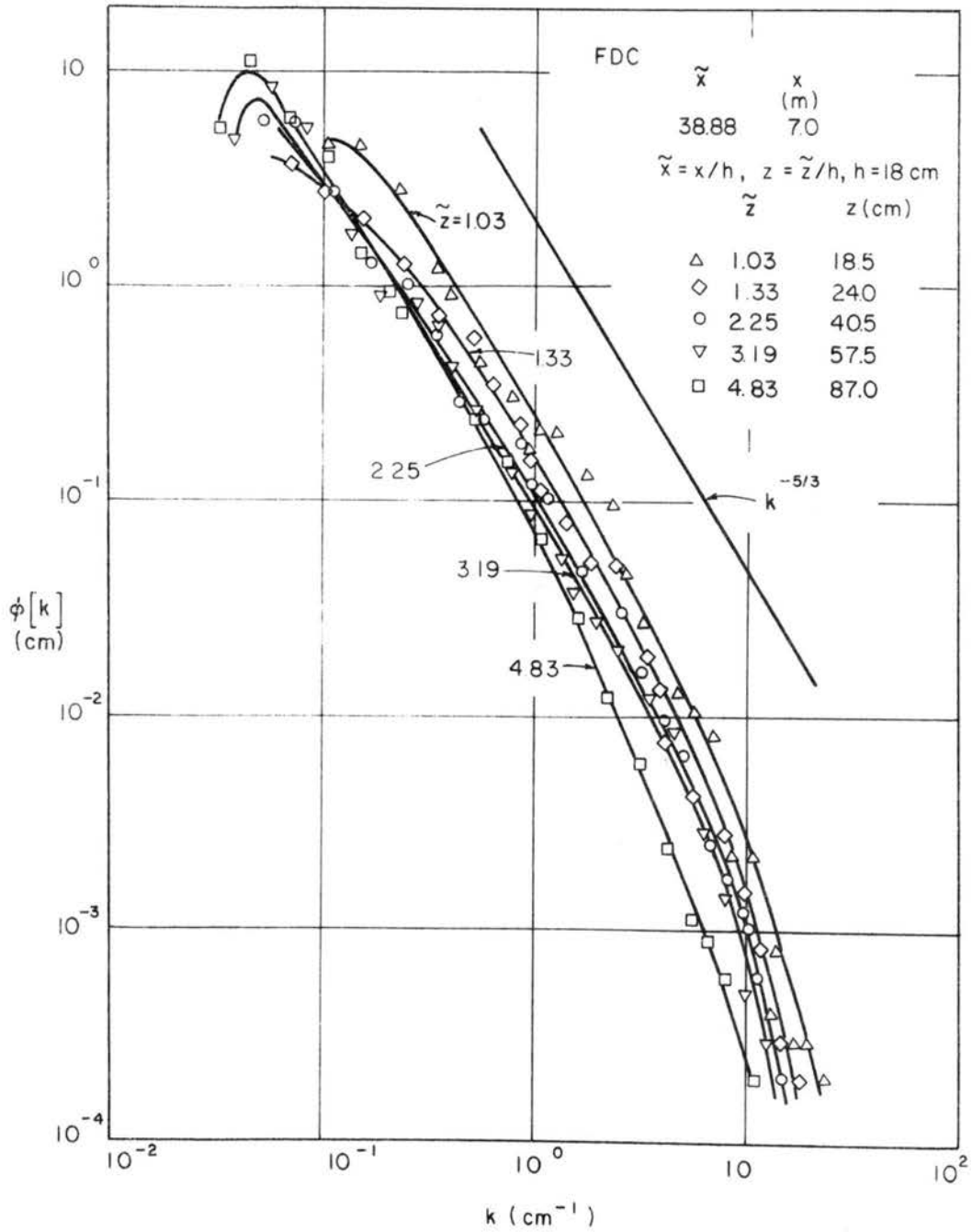


Fig. 5.37 Wave-number spectra above the canopy; FDC case.

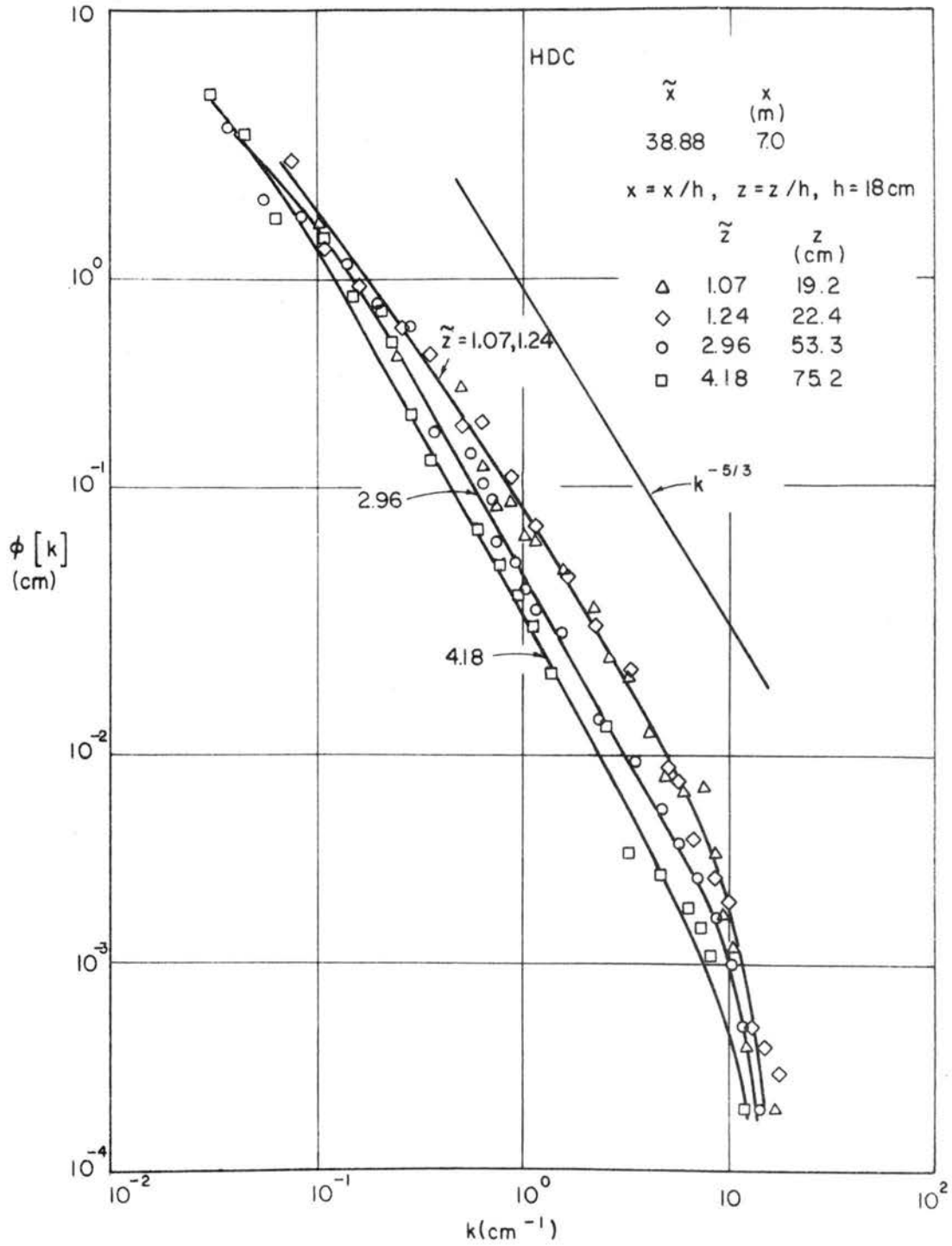


Fig. 5.38 Wave-number spectra above the canopy; HDC case.

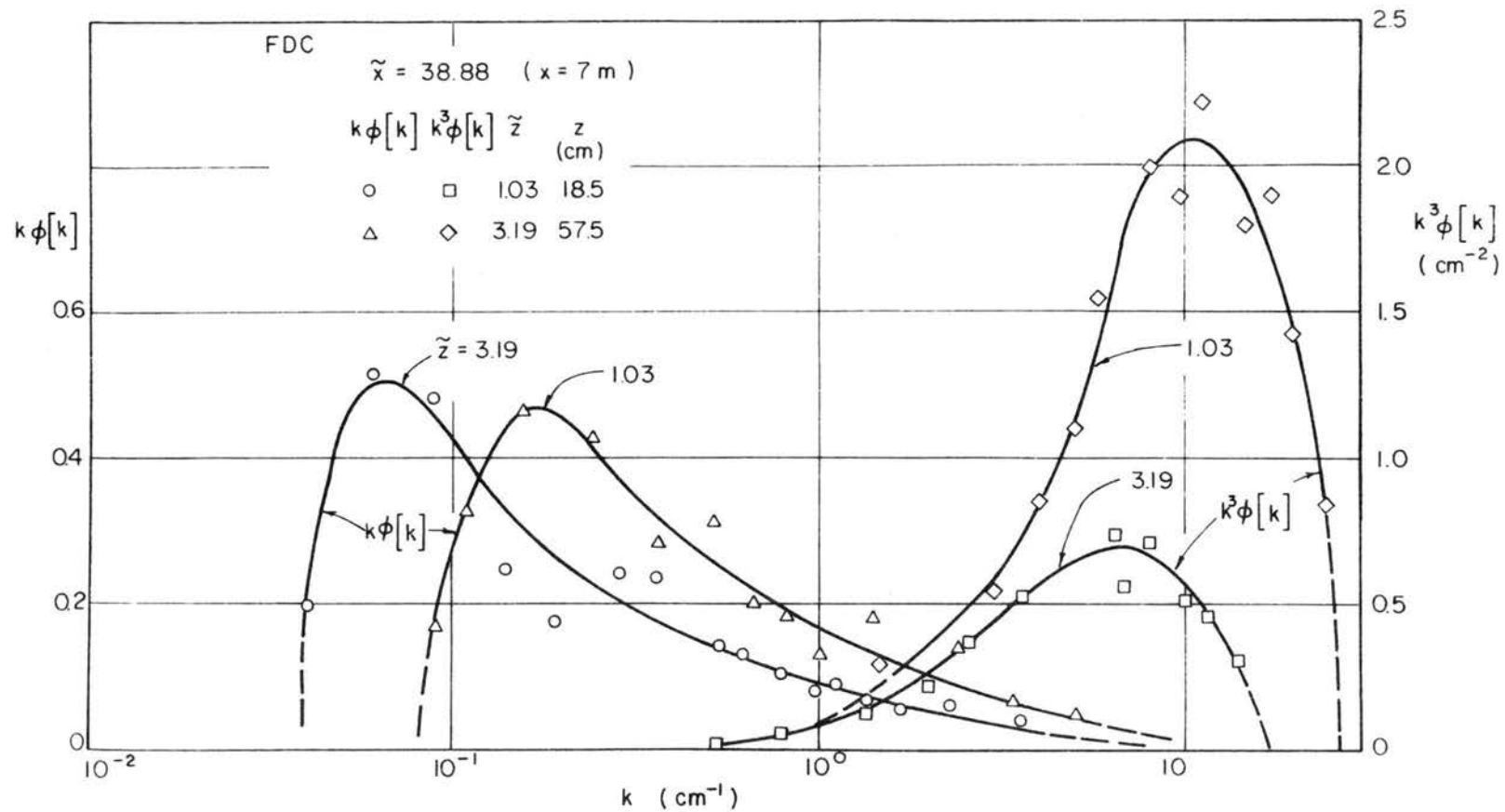


Fig. 5.39 Variation of energy-containing spectrum and energy-dissipation spectrum at two selected heights; FDC case.

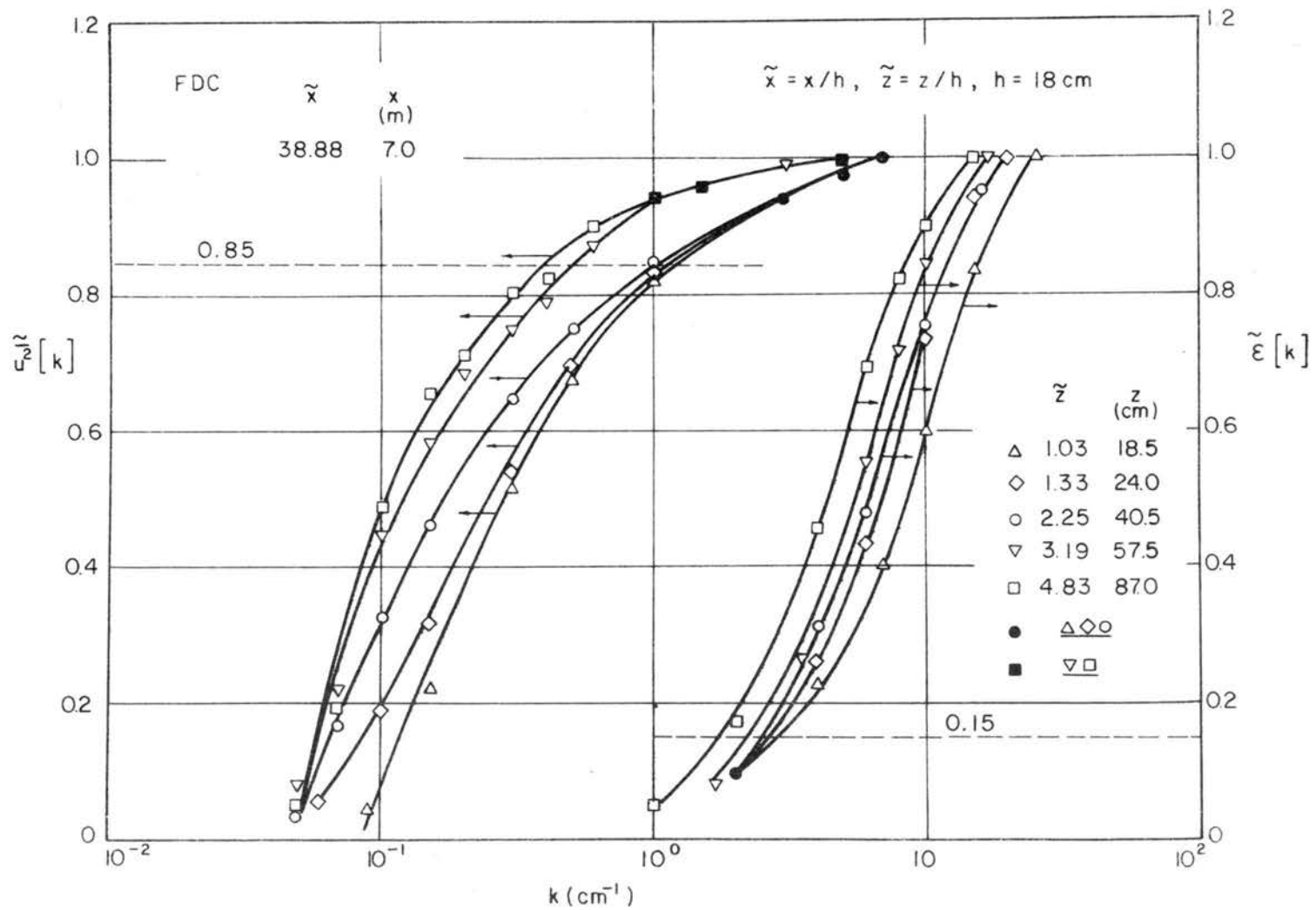


Fig. 5.40 Variation in turbulent kinetic energy and energy dissipation as function of the wave number; FDC case.

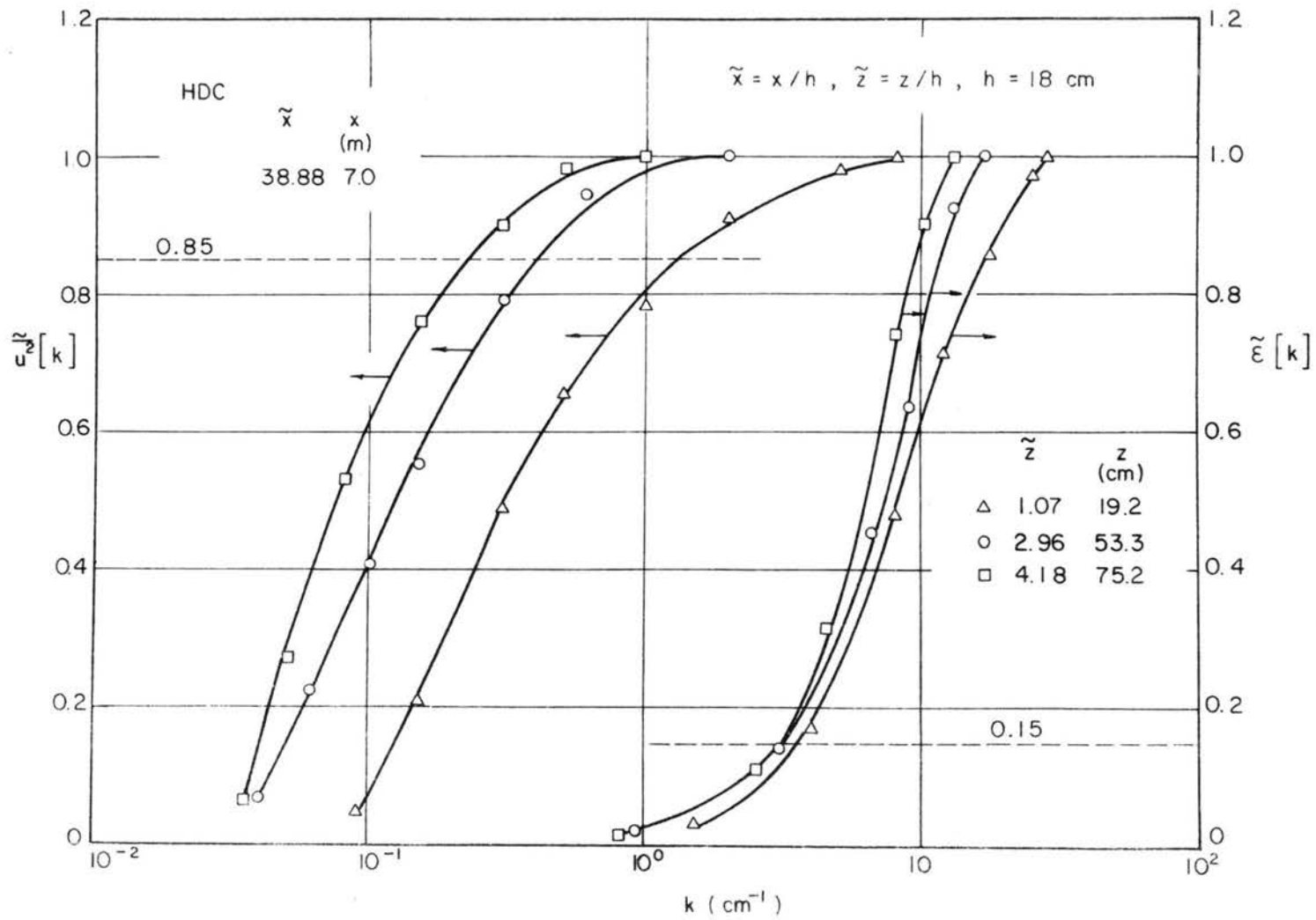


Fig. 5.41 Variation in turbulent kinetic energy and energy dissipation as function of the wave number; HDC case.

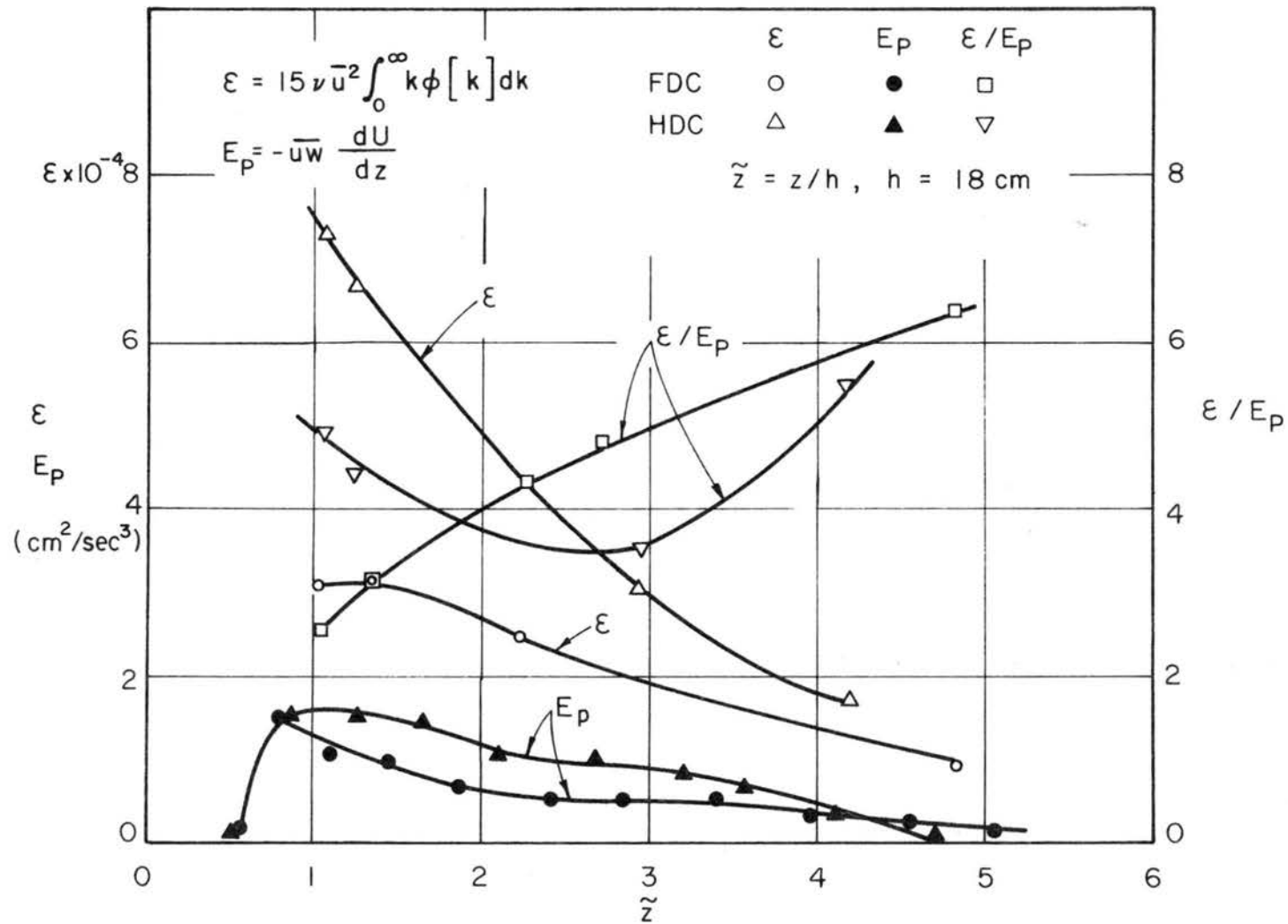


Fig. 5.42 Variations in energy dissipation, energy production and their ratio as function height; FDC and HDC.

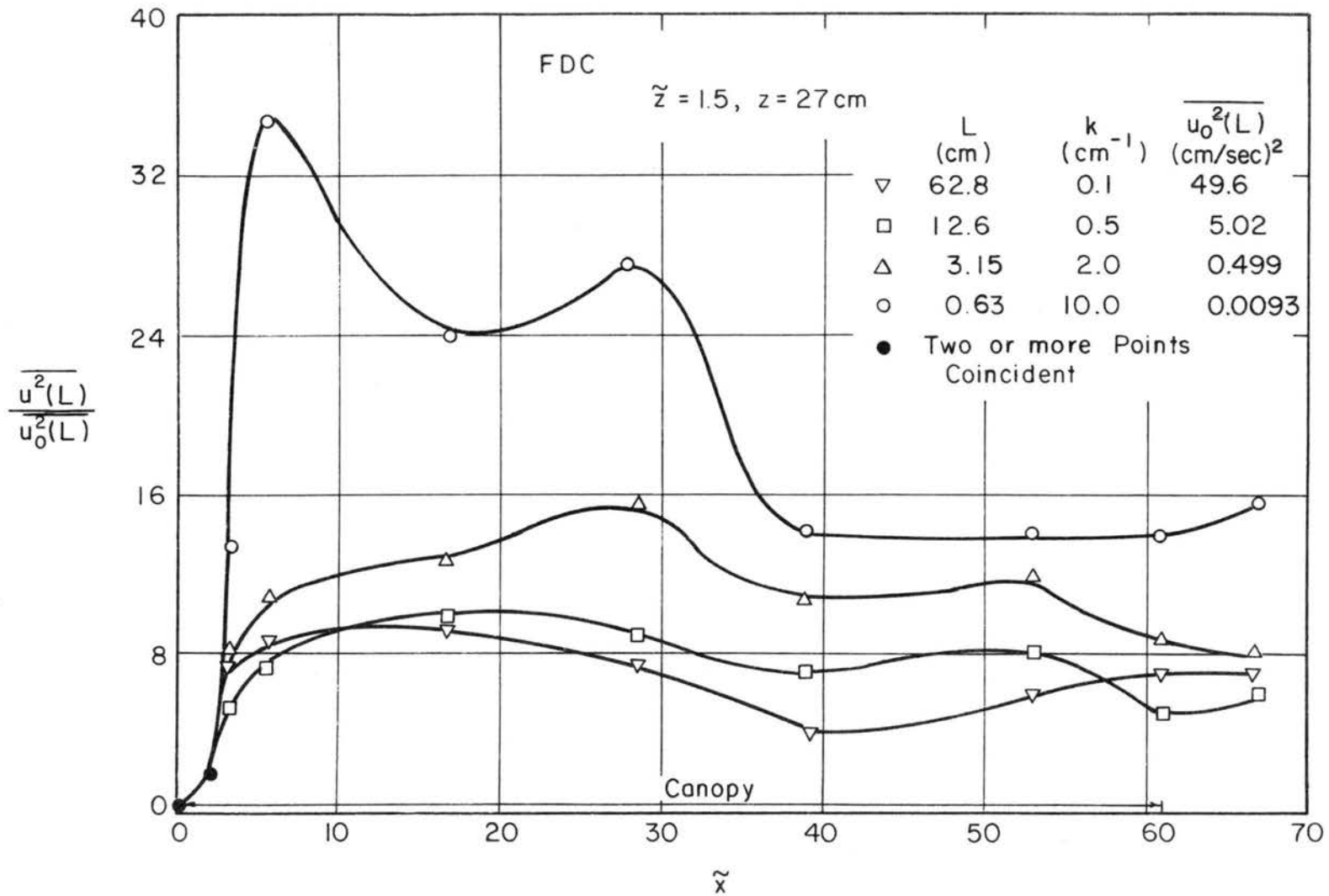


Fig. 5.43a Variation in the discretized energy at four eddy sizes; FDC case.

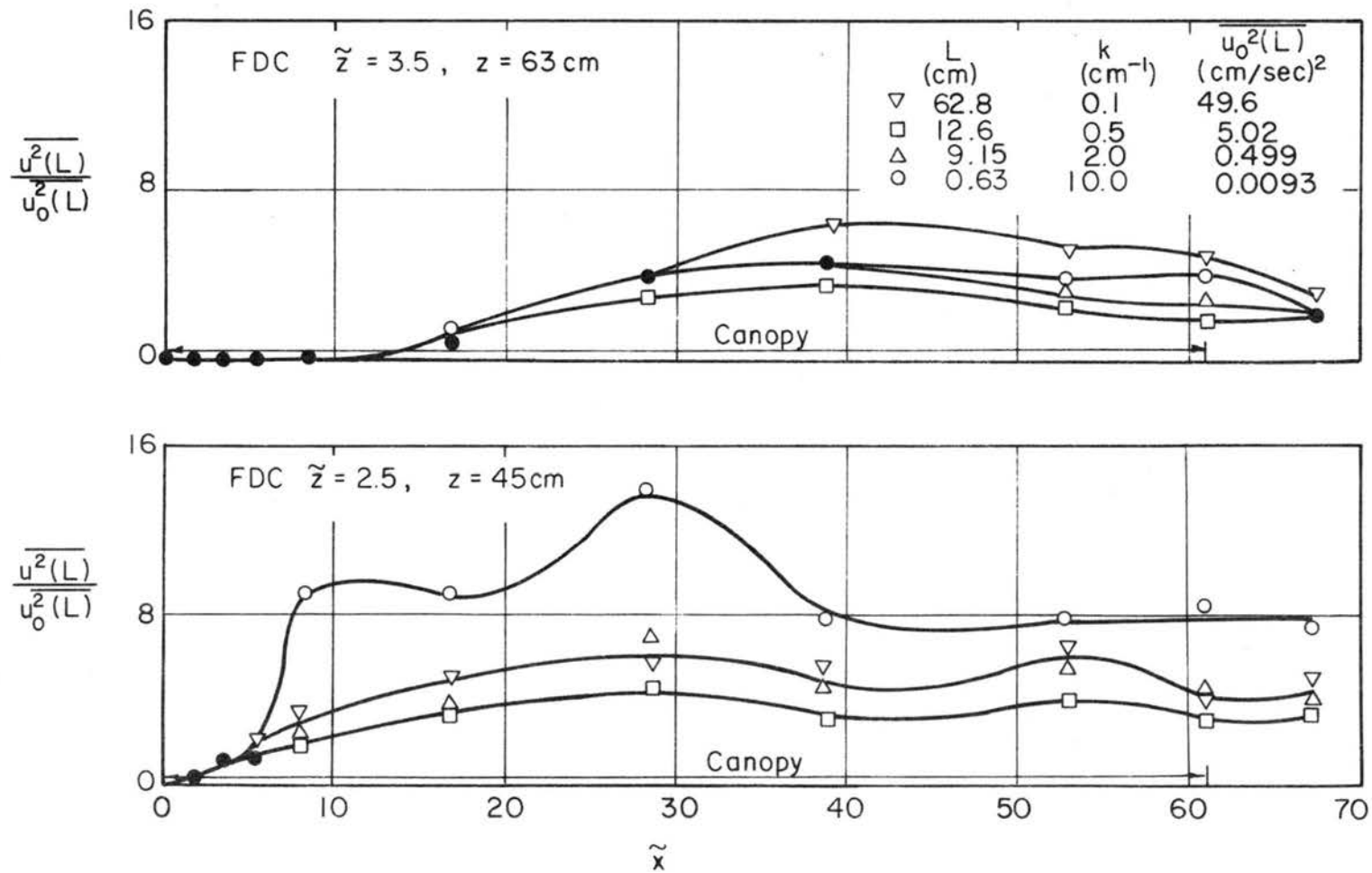


Fig. 5.43b Variation in the discretized energy at four eddy sizes; FDC case.

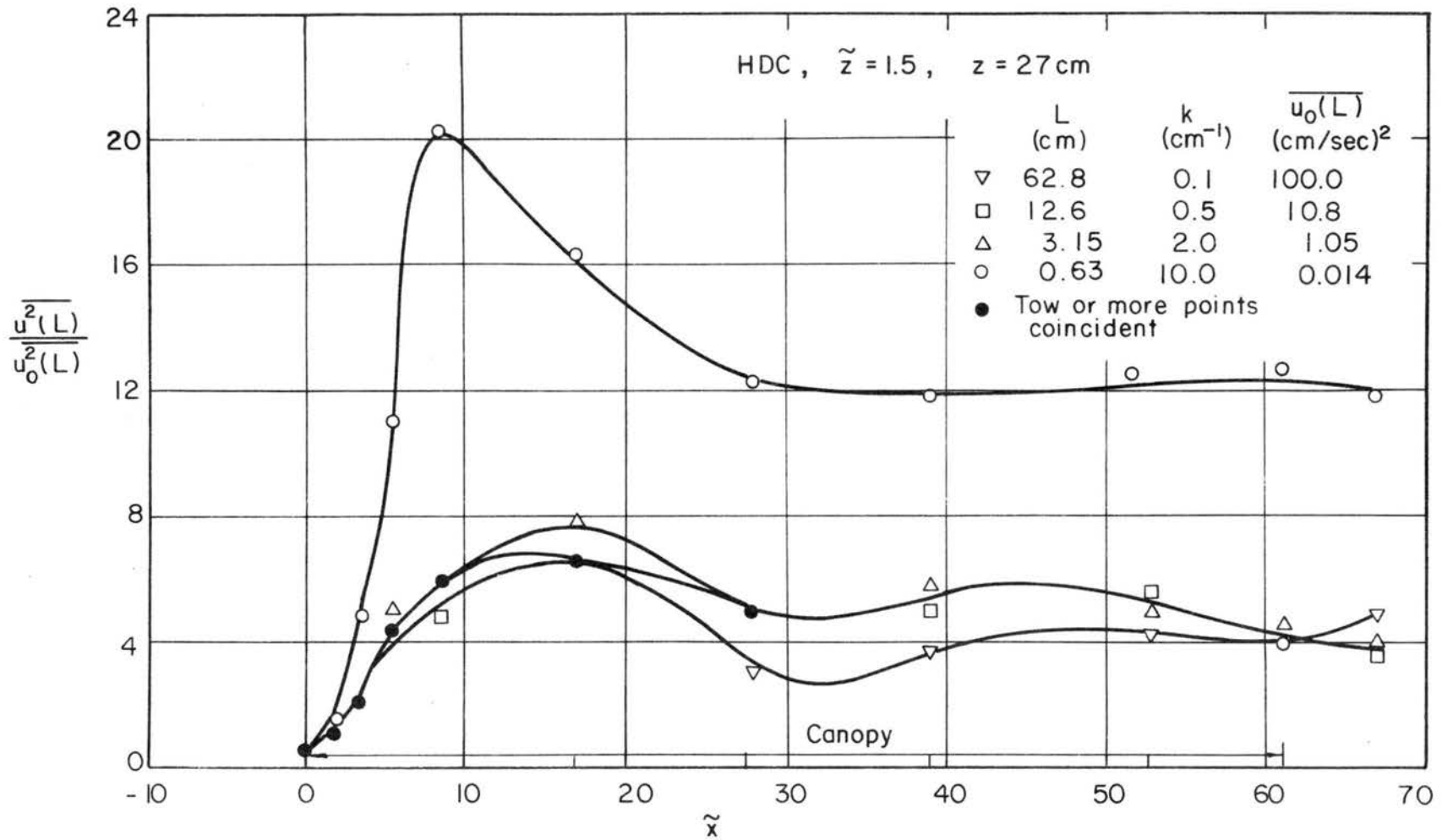


Fig. 5.44a Variation in the discretized energy at four eddy sizes; HDC case.

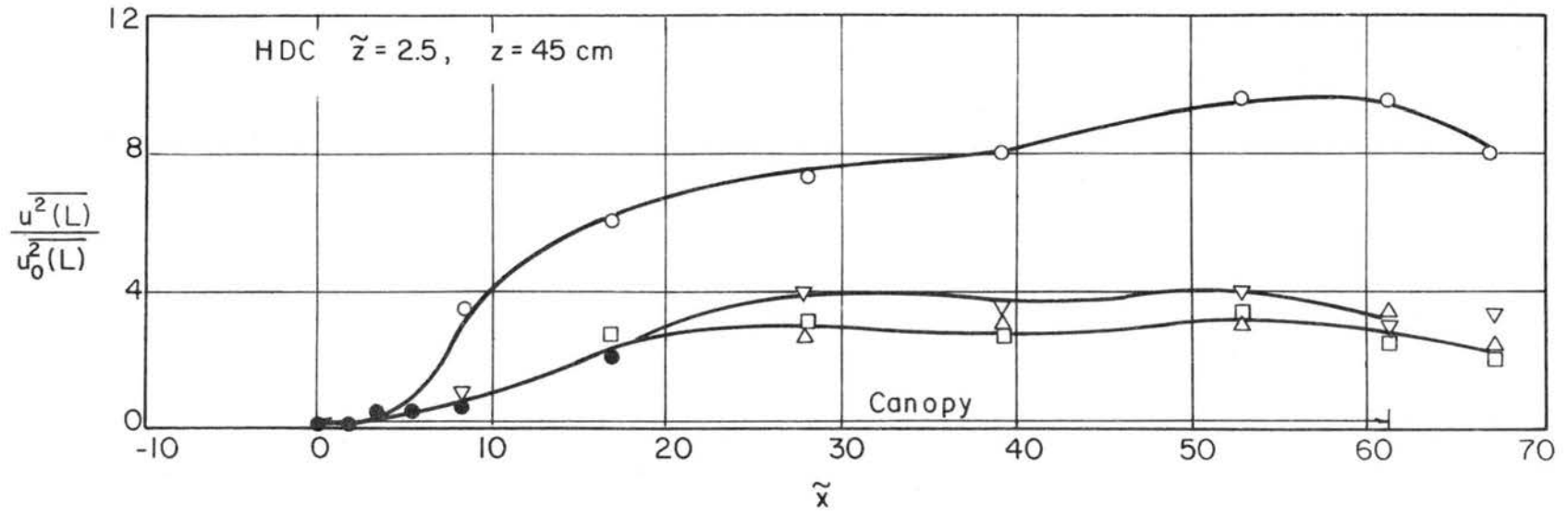
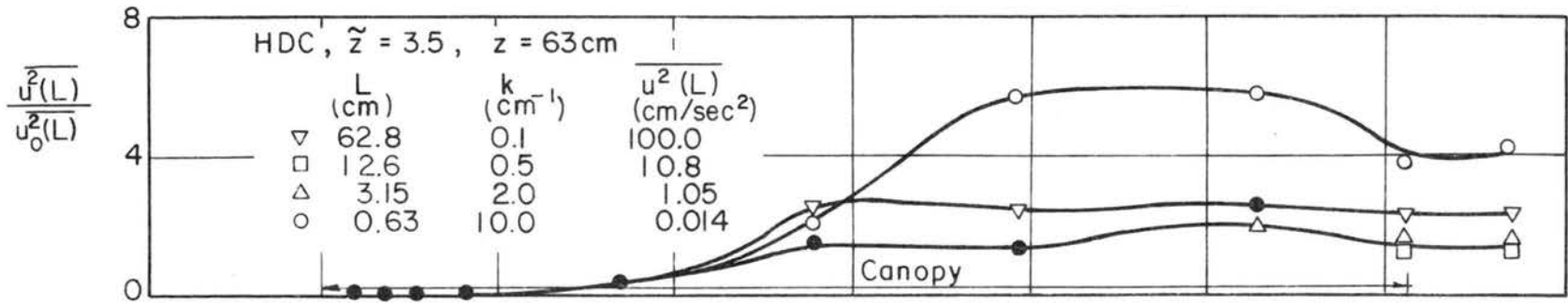


Fig. 5.44b Variation in the discretized energy at four eddy sizes; HDC case.

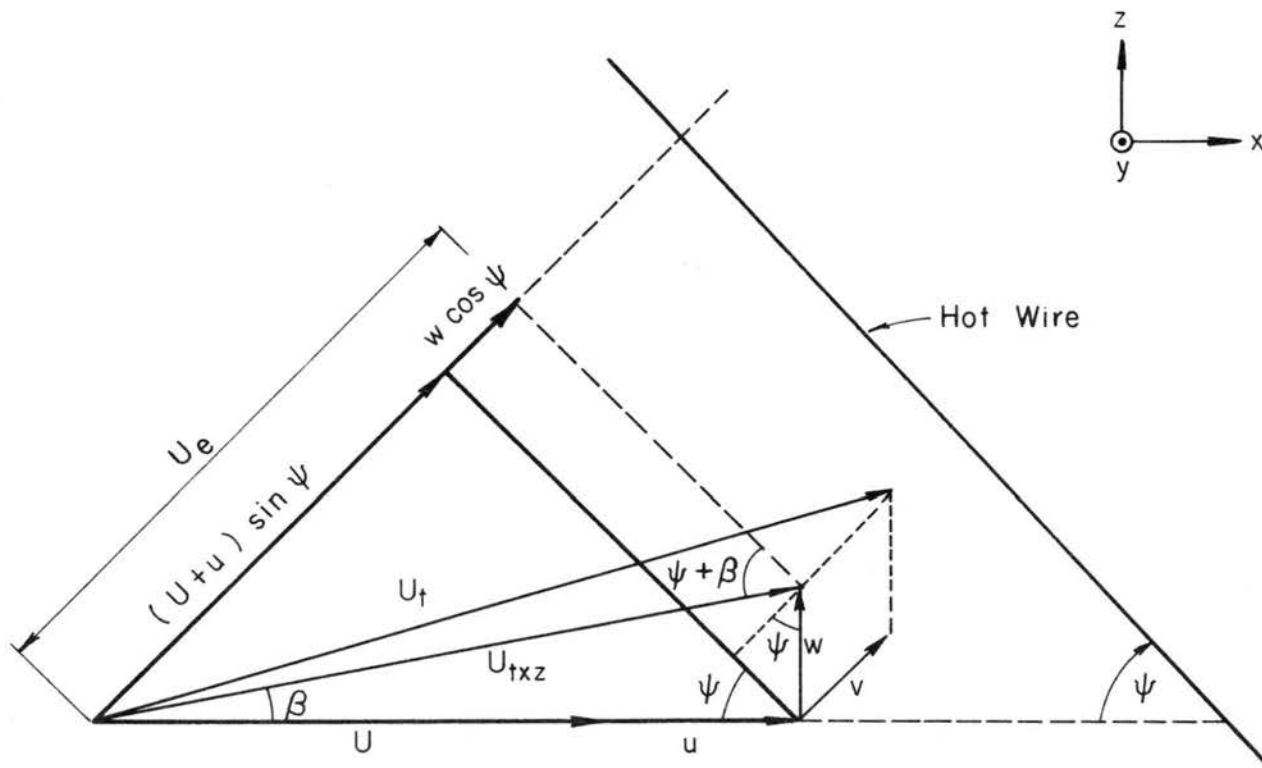


Fig. A.1 Hot wire yawed to the mean flow.

## APPENDIX II

## TABLES

## 1. Mean velocity

The measured mean velocity along the canopy center line, i.e., along the x-axis (see Figs. 3.1 and 3.2), are summarized in Table 1-FDC and 1-HDC. The mean velocity variation is shown in Figs. 5.3a and 5.3b for the FDC case and in Figs. 5.4a and 5.4b for the HDC case. In these tables the dimensionless coordinates are

$$\tilde{x}, \tilde{z} = x/h, z/h,$$

where  $h = 18$  cm (see Eq. (5.1)). The dimensionless mean velocity is

$$\tilde{U} = U/U_{\infty},$$

where  $U_{\infty} = 6$  m/sec (see Eq. (5.2)).

The downstream extent of the transition region for both FDC and HDC cases is tabulated in Table 1-TD. These extents are shown in Figs. 5.5 and 5.9 by the broken lines. In this table  $x_{td}$  denotes the longitudinal extent of the transition region, i.e., the boundary between the transition region and fully developed flow domain.

TABLE 1 - FDC  
 MEAN VELOCITY - Full Density Canopy

x(m)		-1.0				0				0.3				0.6						
x		-5.55				0				1.66				3.33						
z	U	U	U	U	z	U	U	U	U	z	U	U	U	U	z	U	U	U	U	
(cm)	(m/sec)	(m/sec)	(m/sec)	(m/sec)	(cm)	(m/sec)	(m/sec)	(m/sec)	(m/sec)	(cm)	(m/sec)	(m/sec)	(m/sec)	(m/sec)	(cm)	(m/sec)	(m/sec)	(m/sec)	(m/sec)	
1.0	0.06	3.42	0.262		1.0	0.06	2.59	0.415		1.0	0.06	3.84	0.614		1.0	0.06	1.60	0.252		
3.5	0.19	3.39	0.379		3.5	0.14	2.92	0.467		3.5	0.19	3.74	0.598		3.5	0.17	1.65	0.260		
9.5	0.53	4.17	0.681		9.5	0.24	3.08	0.482		9.5	0.36	2.00	0.520		9.5	0.33	1.35	0.244		
11.0	0.61	4.28	0.717		11.0	0.47	3.46	0.554		11.0	0.69	0.95	0.522		11.0	0.67	0.35	0.055		
17.5	0.97	4.72	0.780		17.5	0.78	4.18	0.669		17.5	0.86	1.39	0.222		17.5	0.89	0.55	0.087		
29.0	1.61	5.15	0.851		29.0	1.00	4.37	0.699		29.0	1.06	2.89	0.462		29.0	1.14	2.30	0.362		
43.5	2.42	5.62	0.929		43.5	1.28	4.77	0.763		43.5	1.36	5.02	0.803		43.5	1.53	4.58	0.721		
57.0	3.17	5.76	0.952		57.0	1.92	5.47	0.875		57.0	1.79	5.43	0.869		57.0	2.22	5.24	0.825		
68.5	3.81	5.95	0.983		68.5	2.56	5.84	0.934		68.5	2.33	5.48	0.877		68.5	2.67	5.66	0.891		
74.0	4.11	6.05	1.000		74.0	3.17	6.03	0.964		74.0	2.83	5.69	0.910		74.0	3.22	6.15	0.969		
86.5	4.81	6.05	1.000		86.5	3.75	6.10	0.976		86.5	3.17	6.03	0.965		86.5	3.31	6.22	0.980		
99.0	5.50	6.05	1.000		99.0	4.03	6.25	1.000		99.0	3.61	6.15	0.984		99.0	3.97	6.28	0.989		
109.5	6.08	6.05	1.000		109.5	4.39	6.25	1.000		109.5	4.06	6.15	0.984		109.5	4.50	6.35	1.000		
120.0	6.67	6.05	1.000		120.0	4.97	6.25	1.000		120.0	4.67	6.25	1.000		120.0	5.39	6.35	1.000		
					119.0	5.44	6.25	1.000		119.0	5.42	6.25	1.000		119.0	6.61	6.35	1.000		
					106.0	5.89	6.25	1.000		106.0	6.17	6.25	1.000							
					119.0	6.61	6.25	1.000		121.0	6.72	6.25	1.000							

x(m)		1.0				1.5				2.0				3.0					
x		5.55				9.33				11.11				16.66					
z	U	U	U	U	z	U	U	U	U	z	U	U	U	U	z	U	U	U	U
(cm)	(m/sec)	(m/sec)	(m/sec)	(m/sec)	(cm)	(m/sec)	(m/sec)	(m/sec)	(m/sec)	(cm)	(m/sec)	(m/sec)	(m/sec)	(m/sec)	(cm)	(m/sec)	(m/sec)	(m/sec)	(m/sec)
1.0	0.06	0.71	0.114		1.0	0.06	0.29	0.047		1.0	0.06	0.49	0.080		1.0	0.06	0.44	0.070	
3.5	0.19	0.34	0.087		3.5	0.17	0.29	0.047		3.5	0.19	0.34	0.056		3.5	0.19	0.42	0.066	
7.0	0.39	0.19	0.051		7.0	0.31	0.32	0.052		7.0	0.44	0.25	0.041		7.0	0.42	0.25	0.039	
10.0	0.56	0.19	0.031		10.0	0.58	0.29	0.047		10.0	0.72	0.59	0.096		10.0	0.67	0.53	0.084	
15.0	0.83	0.71	0.114		15.0	0.86	0.59	0.096		15.0	0.94	0.92	0.150		15.0	0.86	1.14	0.180	
18.5	1.03	0.94	0.151		18.5	1.06	1.37	0.223		18.5	1.11	1.09	0.178		18.5	1.06	1.69	0.267	
27.0	1.50	3.29	0.528		27.0	1.33	2.21	0.361		27.0	1.36	2.04	0.333		27.0	1.39	2.59	0.409	
37.5	2.08	3.24	0.841		37.5	1.94	4.34	0.741		37.5	1.89	3.35	0.546		37.5	1.83	3.31	0.523	
48.1	2.67	3.48	0.850		48.1	2.56	5.43	0.856		48.1	2.50	4.45	0.726		48.1	2.47	4.56	0.720	
57.0	3.17	3.74	0.921		57.0	3.17	5.71	0.931		57.0	3.17	4.95	0.808		57.0	3.17	5.38	0.849	
67.0	3.72	3.98	0.960		67.0	3.75	5.88	0.959		67.0	3.64	5.70	0.950		67.0	3.50	5.72	0.904	
77.5	4.31	6.10	0.979		77.5	4.19	5.98	0.956		77.5	4.33	6.91	0.964		77.5	4.14	6.00	0.948	
85.5	4.75	6.23	1.000		85.5	4.64	6.08	0.992		85.5	4.94	6.06	0.989		85.5	4.67	6.20	0.979	
95.5	5.31	6.23	1.000		95.5	5.30	6.13	1.000		95.5	5.75	6.13	1.000		95.5	5.53	6.33	1.000	
111.5	6.19	6.23	1.000		111.5	6.19	6.13	1.000		111.5	6.67	6.13	1.000		111.5	6.67	6.33	1.000	
120.0	6.67	6.23	1.000		120.0	6.67	6.13	1.000		120.0	6.67	6.13	1.000		120.0	6.67	6.33	1.000	

x(m)		4.0				5.0				7.0				9.5					
x		22.22				27.77				38.88				52.77					
z	U	U	U	U	z	U	U	U	U	z	U	U	U	U	z	U	U	U	U
(cm)	(m/sec)	(m/sec)	(m/sec)	(m/sec)	(cm)	(m/sec)	(m/sec)	(m/sec)	(m/sec)	(cm)	(m/sec)	(m/sec)	(m/sec)	(m/sec)	(cm)	(m/sec)	(m/sec)	(m/sec)	(m/sec)
1.0	0.06	0.38	0.063		1.0	0.06	0.25	0.042		1.0	0.06	0.17	0.028		1.0	0.06	0.22	0.037	
5.0	0.28	0.38	0.063		5.0	0.25	0.25	0.038		5.0	0.28	0.16	0.027		5.0	0.25	0.22	0.037	
9.0	0.50	0.23	0.038		9.0	0.44	0.26	0.043		9.0	0.53	0.30	0.050		9.0	0.50	0.42	0.070	
14.0	0.78	0.59	0.093		14.0	0.67	0.49	0.082		14.0	0.69	0.63	0.105		14.0	0.78	1.09	0.182	
17.5	0.97	1.25	0.194		17.5	0.81	1.04	0.173		17.5	0.89	1.38	0.230		17.5	1.00	1.93	0.322	
19.5	1.08	1.53	0.242		19.5	1.03	1.74	0.290		19.5	1.03	1.72	0.287		19.5	1.25	2.04	0.340	
26.0	1.44	2.72	0.430		26.0	1.28	2.06	0.343		26.0	1.33	2.50	0.417		26.0	1.69	2.77	0.462	
38.5	2.14	3.65	0.576		38.5	1.75	2.67	0.445		38.5	1.78	2.96	0.493		38.5	2.17	3.46	0.577	
48.5	2.69	4.39	0.693		48.5	2.38	3.78	0.630		48.5	2.35	3.40	0.567		48.5	2.74	3.86	0.643	
57.0	3.17	5.13	0.810		57.0	2.75	4.12	0.687		57.0	2.72	3.94	0.657		57.0	3.19	4.45	0.742	
62.5	3.47	5.31	0.838		62.5	3.25	4.56	0.760		62.5	3.19	4.56	0.760		62.5	4.08	5.00	0.833	
74.5	4.14	5.86	0.925		74.5	4.03	5.36	0.893		74.5	4.08	4.88	0.813		74.5	4.41	5.31	0.885	
83.0	4.61	6.00	0.947		83.0	4.56	5.69	0.948		83.0	4.83	5.43	0.905		83.0	4.86	5.57	0.928	
92.5	5.14	6.20	0.978		92.5	5.33	5.85	0.975		92.5	5.31	5.66	0.943		92.5	5.36	5.76	0.960	
102.0	5.67	6.20	0.978		102.0	6.00	5.95	0.992		102.0	5.72	5.83	0.972		102.0	5.89	5.86	0.977	
119.0	6.61	6.33	1.000		119.0	6.44	6.00	1.000		119.0	6.33	5.93	0.988		119.0	6.42	5.94	0.990	
					130.0	7.22	6.00	1.000		130.0	7.22	6.00	1.000		130.0	7.22	6.00	1.000	

x(m)		11.0				12.0			
x		61.11				66.66			
z	U	U	U	U	z	U	U	U	U
(cm)	(m/sec)	(m/sec)	(m/sec)	(m/sec)	(cm)	(m/sec)	(m/sec)	(m/sec)	(m/sec)
1.0	0.06	0.39	0.096		1.0	0.06	1.20	0.203	
5.5	0.31	0.31	0.031		5.5	0.25	1.55	0.263	
8.5	0.47	0.40	0.065		8.5	0.47	1.64	0.278	
13.0	0.72	1.00	0.163		13.0	0.72	1.69	0.286	
14.5	0.81	1.42	0.252		14.5	1.06	2.33	0.395	
17.5	0.97	2.43	0.396		17.5	1.44	2.96	0.502	
22.0	1.22	3.28	0.535		22.0	2.03	3.20	0.542	
30.5	1.69	3.57	0.586		30.5	2.67	3.88	0.658	
41.0	2.28	3.88	0.633		41.0	3.25	4.58	0.776	
50.0	2.78	4.54	0.741		50.0	4.17	4.75	0.806	
58.0	3.22	4.62	0.754		58.0	4.69	5.38	0.912	
72.0	4.00	5.13	0.837		72.0	5.22	5.59	0.947	
82.0	4.56	5.50	0.897		82.0	5.78	5.83	0.988	
93.0	5.17	5.71	0.931		93.0	6.50	5.90	1.000	
102.5	5.69	5.93	0.967		102.5	7.33	5.90	1.000	
115.5	6.42	6.10	0.995						
129.0	7.17	6.13	1.000						

TABLE 1 - HUC  
MEAN VELOCITY - Half Density Canopy

x(m)		0				0.5				0.6				1.0			
x		0				1.66				3.33				5.55			
z	z	U	U	z	z	U	U	z	z	U	U	z	z	U	U		
(cm)	(cm)	(m/sec)		(cm)	(cm)	(m/sec)		(cm)	(cm)	(m/sec)		(cm)	(cm)	(m/sec)			
1.0	0.06	2.33	0.388	1.0	0.06	2.65	0.442	1.0	0.06	3.17	0.526	1.0	0.06	2.34	0.390		
7.0	0.39	3.32	0.551	6.4	0.35	4.51	0.752	6.2	0.35	1.39	0.231	6.1	0.34	1.00	0.167		
11.2	0.62	3.60	0.600	12.5	0.69	0.48	0.079	11.8	0.65	1.32	0.219	11.2	0.62	0.72	0.119		
16.5	0.91	4.01	0.669	17.5	0.97	0.99	0.166	16.6	0.92	1.23	0.204	16.2	0.90	0.94	0.157		
21.4	1.19	4.28	0.713	21.7	1.20	4.09	0.682	19.1	1.06	3.42	0.403	18.6	1.03	1.74	0.291		
29.5	1.64	4.85	0.809	29.7	1.65	4.32	0.819	28.8	1.60	4.78	0.799	26.4	1.47	3.45	0.576		
37.9	2.11	5.30	0.883	39.3	2.18	5.29	0.882	35.7	1.98	5.31	0.896	34.8	1.94	5.02	0.837		
48.1	2.67	5.60	0.935	48.5	2.69	5.88	0.947	43.0	2.39	5.50	0.915	43.6	2.42	5.63	0.938		
56.5	3.14	5.73	0.954	56.5	3.14	5.88	0.947	60.0	2.35	5.89	0.980	52.1	2.89	5.72	0.953		
62.0	3.44	5.94	0.991	65.0	3.61	5.87	0.979	71.6	3.98	5.95	0.992	58.5	3.25	5.76	0.960		
77.2	4.29	6.00	1.000	75.7	4.20	5.97	0.995	83.3	4.65	6.00	1.000	59.5	3.31	5.76	0.963		
90.0	5.00	5.94	0.991	86.7	4.95	6.00	1.000	99.7	5.54	6.00	1.000	67.1	3.73	5.83	0.971		
102.0	5.67	6.00	1.000	102.0	5.67	6.00	1.000	110.0	6.11	5.97	0.995	79.5	4.42	5.99	0.999		
												92.9	5.16	6.00	1.000		
												107.0	5.94	6.00	1.000		

x(m)		1.5				2.0				3.0				5.0			
x		8.33				11.11				16.66				27.77			
z	z	U	U	z	z	U	U	z	z	U	U	z	z	U	U		
(cm)	(cm)	(m/sec)		(cm)	(cm)	(m/sec)		(cm)	(cm)	(m/sec)		(cm)	(cm)	(m/sec)			
1.0	0.06	1.22	0.203	1.0	0.06	0.56	0.094	1.0	0.06	0.22	0.037	1.0	0.06	0.19	0.031		
6.2	0.35	0.96	0.159	5.8	0.32	0.48	0.081	6.3	0.35	0.23	0.039	6.3	0.35	0.30	0.050		
11.4	0.64	0.57	0.094	12.1	0.67	0.61	0.102	11.9	0.66	0.50	0.084	11.7	0.65	0.61	0.102		
16.7	0.93	0.96	0.161	16.2	0.90	1.14	0.189	15.7	0.87	0.99	0.165	18.1	1.00	1.62	0.270		
20.1	1.12	1.45	0.241	19.1	1.06	1.33	0.255	19.1	1.06	1.58	0.263	23.1	1.28	2.05	0.341		
27.1	1.51	2.65	0.441	25.1	1.39	2.35	0.389	23.2	1.29	2.04	0.340	29.5	1.64	2.68	0.447		
34.7	1.93	4.04	0.674	34.3	1.90	3.83	0.638	28.5	1.58	2.69	0.448	40.1	2.23	3.65	0.609		
41.0	2.28	4.97	0.829	43.8	2.43	4.96	0.826	37.3	2.07	3.74	0.624	48.3	2.69	4.26	0.710		
48.0	2.67	5.36	0.895	51.7	2.87	5.35	0.891	46.9	2.61	4.35	0.808	59.0	3.28	4.91	0.818		
58.2	3.23	5.65	0.942	59.5	3.29	5.39	0.931	58.5	3.25	5.47	0.912	69.0	3.63	5.43	0.905		
68.5	3.79	5.94	0.991	69.0	3.83	5.88	0.980	66.5	3.69	5.69	0.949	76.8	4.27	5.77	0.961		
79.8	4.43	6.00	1.000	78.9	4.38	5.95	0.992	74.4	4.13	5.89	0.982	85.7	4.76	5.88	0.980		
92.0	5.11	5.99	0.999	92.5	5.13	6.00	1.000	87.3	4.85	6.00	1.000	95.6	5.31	6.00	1.000		
105.5	5.86	5.99	0.999	105.7	5.87	5.95	0.992	100.8	5.60	5.99	0.999	106.2	5.90	5.97	0.995		
				121.6	6.76	5.97	0.995	116.5	6.47	5.99	0.999	122.5	6.81	5.98	0.997		

x(m)		7.0				8.5				9.5				11.0			
x		38.88				47.22				52.77				61.11			
z	z	U	U	z	z	U	U	z	z	U	U	z	z	U	U		
(cm)	(cm)	(m/sec)		(cm)	(cm)	(m/sec)		(cm)	(cm)	(m/sec)		(cm)	(cm)	(m/sec)			
1.0	0.06	0.22	0.036	1.0	0.06	0.20	0.034	1.0	0.06	0.21	0.036	1.0	0.06	0.50	0.083		
7.4	0.41	0.28	0.047	7.0	0.39	0.26	0.043	7.3	0.41	0.23	0.038	6.1	0.34	0.38	0.063		
13.5	0.75	0.84	0.140	14.0	0.78	0.91	0.152	14.0	0.78	0.74	0.123	10.6	0.59	0.55	0.091		
19.0	1.06	1.62	0.270	19.1	1.06	1.64	0.273	17.8	0.99	1.39	0.232	16.9	0.94	1.82	0.304		
24.5	1.36	2.20	0.366	23.8	1.32	2.20	0.367	22.9	1.27	2.19	0.365	21.7	1.21	2.51	0.418		
34.8	1.94	2.97	0.495	32.7	1.82	2.90	0.483	31.1	1.73	2.76	0.460	31.6	1.76	2.90	0.983		
44.4	2.47	3.66	0.611	42.2	2.35	3.45	0.575	42.2	2.35	3.32	0.554	42.4	2.36	3.80	0.633		
53.3	2.96	4.14	0.689	50.4	2.80	3.91	0.652	51.1	2.84	3.79	0.631	50.7	2.82	4.09	0.682		
59.0	3.28	4.55	0.758	59.0	3.28	4.39	0.731	59.0	3.28	4.30	0.717	59.0	3.28	4.56	0.760		
64.5	3.58	4.74	0.790	71.5	3.97	4.88	0.813	74.0	4.11	4.97	0.829	66.0	3.67	4.84	0.807		
75.2	4.18	5.27	0.879	78.8	4.38	5.11	0.886	80.3	4.46	5.13	0.855	74.0	4.11	4.99	0.832		
86.2	4.79	5.72	0.953	88.6	4.92	5.68	0.947	88.3	4.90	5.55	0.925	81.6	4.53	5.66	0.943		
99.7	5.54	5.89	0.982	101.3	5.63	5.91	0.985	96.2	5.34	5.71	0.952	89.3	4.96	5.79	0.966		
113.6	6.31	6.00	1.000	114.3	6.35	5.96	0.993	105.4	5.85	5.85	0.975	97.6	5.42	6.00	1.000		
122.5	6.81	6.00	1.000	129.5	7.19	6.00	1.000	116.8	6.49	5.97	0.994	105.8	5.88	5.98	0.996		
								132.0	7.33	6.00	1.000	124.0	6.89	5.99	0.999		

x(m)		12.0			
x		66.66			
z	z	U	U	z	z
(cm)	(cm)	(m/sec)		(cm)	(cm)
1.0	0.06	1.17	0.194	1.0	0.06
6.4	0.36	1.54	0.256	6.4	0.36
12.1	0.67	1.77	0.295	12.1	0.67
20.0	1.11	2.38	0.396	20.0	1.11
29.2	1.62	2.97	0.496	29.2	1.62
42.2	2.35	3.73	0.639	42.2	2.35
51.7	2.87	4.26	0.711	51.7	2.87
59.0	3.28	4.52	0.753	59.0	3.28
69.7	3.87	4.73	0.788	69.7	3.87
77.6	4.31	5.29	0.881	77.6	4.31
85.5	4.75	5.66	0.944	85.5	4.75
94.7	5.26	5.80	0.967	94.7	5.26
109.3	6.07	6.00	1.000	109.3	6.07
124.5	6.92	6.00	1.000	124.5	6.92

TABLE 1 - TD  
TRANSITION REGION

z (cm)	$\tilde{z}$	Full Density Canopy		Half Density Canopy	
		$x_{td}$ (m)	$\tilde{x}_{td}$	$x_{td}$ (m)	$\tilde{x}_{td}$
18	1.0	2.80	15.5	3.50	19.5
27	1.5	3.42	19.0	4.05	22.5
36	2.0	4.40	24.5	5.20	29.0
54	3.0	5.40	30.0	6.30	35.0
72	4.0	5.75	32.0	6.65	37.0
90	5.0	5.85	32.5	6.75	37.5

$$\tilde{x}_{td} = x_{td}/h, \quad h = 18 \text{ cm}$$

## 2. Turbulence intensity

The measured turbulence intensity in the longitudinal and vertical directions, i.e., x and z directions, are summarized in Table 2-x-FDC, 2-z-FDC, 2-x-HDC and 2-z-HDC. The variations of the longitudinal and vertical turbulence intensities for the FDC case are shown in Figs. 5.32 and 5.34, respectively. For the HDC case the results are displayed in Fig. 5.33 and 5.35. In these tables the turbulence intensities based on both local velocity and free-stream velocity are tabulated. The turbulence intensities based on local velocity are denoted by

$$T_u = \frac{u_{rms}}{U} ,$$

and

$$T_w = \frac{w_{rms}}{U} .$$

When the turbulence intensities are based on free-stream velocity, they are designated by

$$T_{u_\infty} = \frac{u_{rms}}{U_\infty} ,$$

and

$$T_{w_\infty} = \frac{w_{rms}}{U_\infty} ,$$

where  $U_\infty = 6$  m/sec.

TABLE 2 - x - FDC  
LONGITUDINAL TURBULENCE INTENSITY - Full Density Canopy

x(m)				0				0.3				0.6			
x̄				0				1.66				3.33			
z (cm)	z̄	T <sub>u</sub>	T <sub>u<sub>w</sub></sub>	z (cm)	z̄	T <sub>u</sub>	T <sub>u<sub>w</sub></sub>	z (cm)	z̄	T <sub>u</sub>	T <sub>u<sub>w</sub></sub>	z (cm)	z̄	T <sub>u</sub>	T <sub>u<sub>w</sub></sub>
1.0	0.06	0.166	0.0945	1.0	0.06	0.212	0.0917	1.0	0.06	0.114	0.0728	1.0	0.06	0.304	0.0810
3.5	0.19	0.150	0.0875	2.5	0.14	0.215	0.1040	3.5	0.19	0.124	0.0775	3.0	0.18	0.232	0.0637
9.5	0.53	0.129	0.0885	5.0	0.28	0.205	0.1030	6.5	0.36	0.313	0.1040	6.0	0.33	0.442	0.1140
11.0	0.61	0.122	0.0870	8.5	0.47	0.174	0.1000	12.5	0.69	0.208	0.0330	12.0	0.67	1.03	0.0598
17.5	0.97	0.115	0.0903	14.0	0.78	0.135	0.0942	15.5	0.86	0.263	0.0608	16.0	0.89	0.784	0.0718
29.0	1.61	0.103	0.0883	16.0	1.00	0.124	0.0900	19.0	1.06	0.366	0.1770	20.5	1.14	0.321	0.1250
43.5	2.42	0.075	0.0696	23.0	1.28	0.114	0.0907	24.5	1.36	0.134	0.1120	27.5	1.53	0.200	0.1530
57.0	3.17	0.032	0.0308	34.5	1.92	0.097	0.0885	32.0	1.78	0.090	0.0810	40.0	2.22	0.094	0.0820
68.5	3.81	0.021	0.0212	46.0	2.56	0.080	0.0783	42.0	2.33	0.087	0.0795	48.0	2.67	0.083	0.0782
74.0	4.11	0.012	0.0123	57.0	3.17	0.054	0.0347	51.0	2.83	0.077	0.0735	58.0	3.22	0.067	0.0683
86.5	4.81	0.009	0.0092	67.5	3.75	0.028	0.0283	57.0	3.17	0.066	0.0667	59.5	3.31	0.049	0.0503
99.0	5.50	0.008	0.0082	72.5	4.03	0.023	0.0237	65.0	3.61	0.043	0.0445	71.5	3.97	0.015	0.0160
109.5	6.08	0.008	0.0075	79.0	4.39	0.016	0.0168	73.0	4.06	0.026	0.0264	81.0	4.50	0.014	0.0148
120.0	6.67	0.008	0.0078	89.5	4.97	0.012	0.0128	84.0	4.67	0.014	0.0150	97.0	5.39	0.010	0.0103
				98.0	5.44	0.010	0.0108	97.5	5.42	0.010	0.0105	119.0	6.61	0.008	0.0090
				106.0	5.89	0.009	0.0098	111.0	6.17	0.009	0.0090				
				119.0	6.61	0.009	0.0093	121.0	6.72	0.009	0.0090				

x(m)				1.0				1.5				2.0				3.0			
x̄				5.55				8.33				11.11				16.66			
z (cm)	z̄	T <sub>u</sub>	T <sub>u<sub>w</sub></sub>	z (cm)	z̄	T <sub>u</sub>	T <sub>u<sub>w</sub></sub>	z (cm)	z̄	T <sub>u</sub>	T <sub>u<sub>w</sub></sub>	z (cm)	z̄	T <sub>u</sub>	T <sub>u<sub>w</sub></sub>				
1.0	0.06	0.470	0.0573	1.0	0.06	0.869	0.0420	1.0	0.06	0.565	0.0462	1.0	0.06	0.777	0.0570				
3.5	0.19	0.765	0.0688	3.0	0.17	0.766	0.0370	3.5	0.19	0.736	0.0416	3.5	0.19	0.736	0.0515				
7.0	0.39	1.29	0.0410	5.5	0.31	0.668	0.0357	8.0	0.44	1.259	0.0525	7.5	0.42	1.035	0.0432				
10.0	0.56	1.29	0.0410	10.5	0.38	0.869	0.0420	13.0	0.72	0.951	0.0935	12.0	0.67	1.082	0.0955				
15.0	0.83	0.788	0.0933	15.5	0.58	0.889	0.0875	17.0	0.94	0.801	0.1230	15.5	0.86	0.775	0.1470				
18.5	1.03	0.789	0.1240	19.0	1.06	0.649	0.1480	20.0	1.11	0.702	0.1280	19.0	1.06	0.552	0.1560				
27.0	1.50	0.328	0.1800	24.0	1.33	0.470	0.1730	24.5	1.36	0.474	0.1610	25.0	1.39	0.397	0.1720				
37.5	2.08	0.118	0.1030	35.0	1.94	0.222	0.1690	34.0	1.89	0.308	0.1720	33.0	1.83	0.315	0.1730				
48.1	2.67	0.085	0.0777	46.0	2.56	0.092	0.0833	45.0	2.50	0.161	0.1190	44.5	2.47	0.203	0.1540				
57.0	3.17	0.072	0.0688	57.0	3.17	0.076	0.0723	57.0	3.17	0.086	0.0710	57.0	3.17	0.121	0.1090				
67.0	3.72	0.048	0.0480	67.5	3.75	0.055	0.0538	65.5	3.64	0.065	0.0622	63.0	3.50	0.086	0.0815				
77.5	4.31	0.026	0.0265	75.5	4.19	0.035	0.0347	78.0	4.33	0.042	0.0417	74.5	4.14	0.055	0.055				
85.5	4.75	0.016	0.0163	83.5	4.84	0.022	0.0222	89.0	4.84	0.016	0.0165	84.0	4.67	0.029	0.0297				
95.5	5.31	0.012	0.0123	99.0	5.50	0.013	0.0130	103.5	5.75	0.009	0.0097	99.5	5.53	0.017	0.0178				
111.5	6.19	0.009	0.0095	119.0	6.61	0.010	0.0105	120.0	6.67	0.008	0.0078	120.0	6.67	0.011	0.0113				
120.0	6.67	0.009	0.0088																

x(m)				4.0				5.0				7.0				9.5			
x̄				22.22				27.77				38.88				52.77			
z (cm)	z̄	T <sub>u</sub>	T <sub>u<sub>w</sub></sub>	z (cm)	z̄	T <sub>u</sub>	T <sub>u<sub>w</sub></sub>	z (cm)	z̄	T <sub>u</sub>	T <sub>u<sub>w</sub></sub>	z (cm)	z̄	T <sub>u</sub>	T <sub>u<sub>w</sub></sub>				
1.0	0.06	0.768	0.0487	1.0	0.06	1.160	0.0483	1.0	0.06	0.914	0.0258	1.0	0.06	0.885	0.0323				
5.0	0.28	0.570	0.0362	4.5	0.25	1.050	0.0402	5.0	0.28	0.793	0.0212	4.5	0.25	0.784	0.0287				
9.0	0.50	1.400	0.0538	8.0	0.44	0.978	0.0423	9.5	0.53	0.901	0.045	9.0	0.50	0.788	0.0552				
14.0	0.78	1.010	0.0992	12.0	0.67	0.900	0.0735	12.5	0.69	0.701	0.0737	14.0	0.78	0.589	0.1070				
17.5	0.97	0.656	0.1340	14.5	0.81	0.707	0.1230	16.0	0.89	0.519	0.1190	18.0	1.00	0.470	0.1510				
19.5	1.08	0.535	0.1360	16.5	1.03	0.535	0.1550	18.5	1.03	0.385	0.1110	22.5	1.25	0.378	0.1280				
26.0	1.44	0.337	0.1530	23.0	1.28	0.445	0.1530	24.0	1.33	0.277	0.1130	30.5	1.69	0.279	0.1290				
38.5	2.14	0.260	0.1380	31.5	1.75	0.339	0.1510	32.0	1.78	0.230	0.1140	39.0	2.17	0.226	0.1300				
48.5	2.69	0.207	0.1510	41.0	2.38	0.231	0.1580	40.5	2.25	0.202	0.1150	49.0	2.72	0.201	0.1290				
57.0	3.17	0.162	0.1380	49.5	2.75	0.224	0.1240	49.0	2.72	0.171	0.1120	57.5	3.19	0.170	0.1260				
62.5	3.47	0.115	0.1020	58.5	3.25	0.186	0.1410	57.5	3.19	0.188	0.1430	73.5	4.08	0.152	0.1100				
74.5	4.14	0.065	0.0637	72.5	4.03	0.103	0.0923	73.5	4.08	0.129	0.1050	80.0	4.44	0.119	0.1060				
83.0	4.61	0.045	0.0455	87.0	4.56	0.066	0.0630	87.0	4.83	0.096	0.0867	87.5	4.86	0.094	0.0872				
92.5	5.14	0.025	0.0255	96.0	5.33	0.031	0.0307	95.5	5.31	0.066	0.0622	96.5	5.36	0.070	0.0672				
102.0	5.67	0.017	0.0173	108.0	6.00	0.017	0.0165	103.0	5.72	0.030	0.0293	106.0	5.89	0.046	0.0447				
119.0	6.61	0.012	0.0128	116.0	6.44	0.014	0.0140	114.0	6.33	0.018	0.0178	115.0	6.42	0.023	0.0227				
				130.0	7.22	0.011	0.0108	130.0	7.22	0.012	0.0118	130.0	7.22	0.015	0.0152				

x(m)				11.0				12.0			
x̄				61.11				66.66			
z (cm)	z̄	T <sub>u</sub>	T <sub>u<sub>w</sub></sub>	z (cm)	z̄	T <sub>u</sub>	T <sub>u<sub>w</sub></sub>	z (cm)	z̄	T <sub>u</sub>	T <sub>u<sub>w</sub></sub>
1.0	0.06	0.425	0.0418	1.0	0.06	0.529	0.1060	1.0	0.06	0.529	0.1060
5.5	0.31	0.932	0.0982	4.5	0.25	0.454	0.1170	4.5	0.25	0.454	0.1170
8.5	0.47	0.760	0.0507	8.5	0.47	0.441	0.1210	8.5	0.47	0.441	0.1210
13.0	0.72	0.661	0.1100	13.0	0.72	0.465	0.1310	13.0	0.72	0.465	0.1310
14.5	0.81	0.608	0.1440	14.5	0.81	0.391	0.1520	14.5	0.81	0.391	0.1520
17.5	0.97	0.395	0.1600	17.5	0.97	0.288	0.1420	17.5	0.97	0.288	0.1420
22.0	1.22	0.301	0.1640	22.0	1.22	0.237	0.1260	22.0	1.22	0.237	0.1260
30.5	1.69	0.245	0.1460	30.5	1.69	0.186	0.1200	30.5	1.69	0.186	0.1200
41.0	2.28	0.207	0.1340	41.0	2.28	0.156	0.1190	41.0	2.28	0.156	0.1190
50.0	2.78	0.173	0.1310	50.0	2.78	0.118	0.0933	50.0	2.78	0.118	0.0933
58.0	3.22	0.160	0.1230	58.0	3.22	0.094	0.0842	58.0	3.22	0.094	0.0842
72.0	4.00	0.125	0.1070	72.0	4.00	0.072	0.0675	72.0	4.00	0.072	0.0675
82.0	4.56	0.109	0.1000	82.0	4.56	0.048	0.0472	82.0	4.56	0.048	0.0472
93.0	5.17	0.078	0.0742	93.0	5.17	0.023	0.0222	93.0	5.17	0.023	0.0222
102.5	5.69	0.055	0.0540	102.5	5.69	0.014	0.0135	102.5	5.69	0.014	0.0135
115.5	6.42	0.023	0.0232	115.5	6.42	0.014	0.0135	115.5	6.42	0.014	0.0135
129.0	7.17	0.014	0.0138	129.0	7.17	0.014	0.0138	129.0	7.17	0.014	0.0138

TABLE - 2 - z - FDC  
 VERTICAL TURBULENCE INTENSITY - Full Density Canopy

x(m)	-1.0				0				0.3				0.6			
$\bar{x}$	-5.55				0				1.66				3.33			
	z (cm)	$\bar{z}$	$T_w$	$T_{w_m}$	z (cm)	$\bar{z}$	$T_w$	$T_{w_m}$	z (cm)	$\bar{z}$	$T_w$	$T_{w_m}$	z (cm)	$\bar{z}$	$T_w$	$T_{w_m}$
	2.0	0.11	0.082	0.046	7.5	0.42	0.025	0.014	7.0	0.39	0.260	0.075	20.5	1.14	0.164	0.080
	5.5	0.31	0.056	0.033	11.0	0.61	0.068	0.043	12.5	0.69	0.156	0.029	27.0	1.50	0.098	0.069
	9.0	0.50	0.063	0.042	15.0	0.83	0.072	0.050	15.0	0.83	0.270	0.055	33.5	1.86	0.021	0.017
	14.0	0.78	0.061	0.045	16.0	0.89	0.058	0.041	19.0	1.06	0.328	0.187	45.0	2.50	0.022	0.020
	19.5	1.08	0.058	0.046	21.0	1.17	0.057	0.044	23.0	1.28	0.181	0.139	53.0	2.94	0.032	0.031
	26.5	1.47	0.061	0.052	28.0	1.56	0.038	0.032	31.0	1.72	0.036	0.032	65.0	3.50	0.034	0.035
	35.0	1.94	0.054	0.049	38.0	2.11	0.022	0.021	41.0	2.28	0.037	0.035	70.5	3.92	0.021	0.022
	44.5	2.47	0.038	0.036	48.0	2.66	0.022	0.022	50.5	2.81	0.034	0.033	79.5	4.39	0.005	0.005
	51.5	2.86	0.029	0.028	60.5	3.36	0.032	0.032	59.5	3.31	0.040	0.040				
	60.0	3.33	0.009	0.009	70.5	3.92	0.015	0.015	70.0	3.89	0.026	0.027				
	73.0	4.06	0.007	0.007	74.0	4.11	0.013	0.013	77.0	4.28	0.015	0.016				
					81.0	4.50	0.006	0.006								
					91.5	5.08	0.003	0.003								

x(m)	1.0				1.5				2.0				3.0			
$\bar{x}$	5.55				8.33				11.11				16.66			
	z (cm)	$\bar{z}$	$T_w$	$T_{w_m}$	z (cm)	$\bar{z}$	$T_w$	$T_{w_m}$	z (cm)	$\bar{z}$	$T_w$	$T_{w_m}$	z (cm)	$\bar{z}$	$T_w$	$T_{w_m}$
	29.5	1.64	0.152	0.103	26.5	1.47	0.118	0.054	51.0	1.72	0.089	0.043	22.0	1.22	0.067	0.024
	34.5	1.92	0.132	0.106	32.5	1.81	0.205	0.138	40.0	2.22	0.109	0.071	28.5	1.58	0.130	0.064
	42.0	2.33	0.023	0.021	37.0	2.06	0.200	0.153	49.0	2.72	0.041	0.032	37.5	2.08	0.155	0.102
	51.0	2.83	0.025	0.024	44.0	2.44	0.100	0.088	61.0	3.39	0.020	0.018	44.5	2.47	0.132	0.100
	61.0	3.39	0.029	0.028	52.0	2.59	0.034	0.032	64.5	3.58	0.022	0.020	49.0	2.72	0.134	0.109
	70.0	3.89	0.036	0.036	61.5	3.42	0.032	0.031	75.0	4.17	0.024	0.023	58.5	3.25	0.061	0.053
	77.0	4.28	0.025	0.025	72.5	4.03	0.035	0.035	87.5	4.86	0.014	0.014	67.5	3.75	0.006	0.006
	85.0	4.72	0.007	0.007	82.5	4.58	0.013	0.013	102.0	5.67	0.006	0.006	76.5	4.25	0.015	0.015
					93.5	5.19	0.012	0.012					85.5	4.75	0.014	0.014
													94.5	5.22	0.005	0.005
													102.5	5.69	0.001	0.001

x(m)	4.0				5.0				7.0				9.5			
$\bar{x}$	22.22				27.77				38.88				52.77			
	z (cm)	$\bar{z}$	$T_w$	$T_{w_m}$	z (cm)	$\bar{z}$	$T_w$	$T_{w_m}$	z (cm)	$\bar{z}$	$T_w$	$T_{w_m}$	z (cm)	$\bar{z}$	$T_w$	$T_{w_m}$
	23.5	1.31	0.158	0.058	15.5	0.86	0.130	0.063	10.5	0.58	0.295	0.021	2.5	0.14	0.133	0.005
	31.5	1.75	0.143	0.075	21.0	1.17	0.139	0.044	14.5	0.81	0.408	0.065	7.0	0.39	0.140	0.024
	41.0	2.28	0.119	0.079	30.0	1.68	0.057	0.026	19.5	1.08	0.297	0.091	11.0	0.61	0.597	0.073
	50.0	2.78	0.109	0.085	36.5	2.03	0.090	0.049	26.0	1.44	0.247	0.101	15.5	0.86	0.298	0.069
	60.0	3.33	0.100	0.088	44.0	2.44	0.127	0.081	33.0	1.83	0.213	0.105	19.0	1.06	0.233	0.071
	72.0	4.00	0.050	0.048	50.0	2.78	0.104	0.073	43.0	2.39	0.141	0.085	27.0	1.50	0.102	0.044
	79.0	4.39	0.027	0.027	56.5	3.14	0.078	0.060	51.5	2.86	0.120	0.081	36.5	2.03	0.083	0.045
	89.0	4.94	0.018	0.018	64.5	3.58	0.061	0.051	61.5	3.42	0.092	0.069	45.5	2.53	0.095	0.060
					72.0	4.00	0.044	0.039	71.0	3.94	0.058	0.048	52.0	2.89	0.075	0.052
					81.0	4.30	0.030	0.028	81.5	4.53	0.005	0.004	60.5	3.36	0.095	0.072
					91.0	5.06	0.013	0.012	91.0	5.06	0.014	0.013	62.5	3.47	0.102	0.079
									101.0	5.61	0.013	0.012	71.0	3.94	0.099	0.082
													82.0	4.56	0.081	0.072
													91.5	5.08	0.067	0.063

x(m)	11.0			
$\bar{x}$	61.11			
	z (cm)	$\bar{z}$	$T_w$	$T_{w_m}$
	11.5	0.64	0.071	0.008
	16.0	0.92	0.262	0.099
	21.5	1.19	0.133	0.064
	29.5	1.64	0.082	0.048
	40.0	2.22	0.054	0.036
	46.0	2.56	0.085	0.061
	54.5	3.03	0.050	0.039
	60.5	3.36	0.057	0.046
	67.0	3.72	0.062	0.052
	73.0	4.06	0.065	0.057
	82.5	4.58	0.044	0.040
	91.5	5.08	0.034	0.032

TABLE 2 - x - HOC  
LONGITUDINAL TURBULENCE INTENSITY - Half Density Canopy

x(m)	0				0.3				0.6				1.0			
$\bar{x}$	0				1.66				3.33				5.55			
	z (cm)	$\bar{z}$	$T_u$	$T_{u_m}$	z (cm)	$\bar{z}$	$T_u$	$T_{u_m}$	z (cm)	$\bar{z}$	$T_u$	$T_{u_m}$	z (cm)	$\bar{z}$	$T_u$	$T_{u_m}$
1.0	0.06	0.213	0.0826		1.0	0.06	0.160	0.0707	1.0	0.06	0.127	0.0671	1.0	0.06	0.192	0.0749
7.0	0.39	0.163	0.0703		6.4	0.35	0.242	0.1820	6.2	0.35	0.398	0.0919	6.1	0.34	0.471	0.0786
11.0	0.62	0.143	0.0858		12.5	0.69	0.674	0.0532	11.8	0.65	0.324	0.0710	11.2	0.62	0.513	0.0610
16.5	0.91	0.121	0.0869		17.3	0.97	0.585	0.0971	16.6	0.92	0.357	0.0728	16.2	0.90	0.549	0.0862
21.4	1.19	0.108	0.0770		21.7	1.20	0.190	0.1300	19.1	1.06	0.357	0.1440	18.6	1.03	0.478	0.1390
29.5	1.64	0.092	0.0744		29.7	1.65	0.080	0.0655	28.8	1.60	0.147	0.1170	26.4	1.47	0.290	0.1670
37.9	2.11	0.080	0.0706		39.3	2.18	0.076	0.0670	35.7	1.98	0.080	0.0717	34.8	1.94	0.121	0.1010
48.1	2.67	0.058	0.0541		48.5	2.69	0.062	0.0587	43.0	2.39	0.074	0.0677	43.6	2.42	0.074	0.0694
56.5	3.14	0.036	0.0343		56.5	3.14	0.046	0.0436	60.0	3.33	0.043	0.0421	52.1	2.89	0.067	0.0639
62.0	3.44	0.020	0.0198		65.0	3.61	0.023	0.0225	71.6	3.98	0.017	0.0169	58.5	3.25	0.053	0.0509
77.2	4.29	0.009	0.0090		75.7	4.20	0.010	0.00995	83.3	4.63	0.007	0.0070	59.5	3.51	0.050	0.0482
90.0	5.00	0.005	0.0050		88.7	4.93	0.005	0.005	99.7	5.54	0.004	0.0040	67.1	3.73	0.034	0.0330
102.0	5.67	0.004	0.0040		102.0	5.67	0.005	0.005	110.0	6.11	0.003	0.0030	79.5	4.42	0.012	0.0120
													92.9	5.16	0.005	0.0050
													107.0	5.94	0.004	0.0040

x(m)	1.5				2.0				3.0				5.0			
$\bar{x}$	8.33				11.11				16.66				27.77			
	z (cm)	$\bar{z}$	$T_u$	$T_{u_m}$	z (cm)	$\bar{z}$	$T_u$	$T_{u_m}$	z (cm)	$\bar{z}$	$T_u$	$T_{u_m}$	z (cm)	$\bar{z}$	$T_u$	$T_{u_m}$
1.0	0.06	0.361	0.0733		1.0	0.06	0.635	0.0597	1.0	0.06	1.000	0.037	1.0	0.06	1.000	0.0310
6.2	0.35	0.375	0.0914		5.8	0.32	0.777	0.0629	6.3	0.35	0.946	0.0369	6.3	0.35	0.859	0.0430
11.4	0.64	0.723	0.0680		12.1	0.67	0.781	0.0797	11.9	0.66	0.859	0.0721	11.7	0.65	0.842	0.0859
16.7	0.93	0.634	0.1020		16.2	0.90	0.610	0.1150	15.7	0.87	0.709	0.1170	18.1	1.00	0.505	0.1360
20.1	1.12	0.548	0.1320		19.1	1.06	0.548	0.1400	19.1	1.06	0.533	0.1400	23.1	1.28	0.397	0.1350
27.1	1.51	0.350	0.1540		25.1	1.39	0.400	0.1560	23.2	1.29	0.427	0.1450	29.5	1.64	0.353	0.1490
34.7	1.93	0.222	0.1500		34.3	1.90	0.257	0.1640	28.5	1.58	0.541	0.1530	40.1	2.23	0.253	0.1540
41.0	2.28	0.134	0.1110		43.8	2.43	0.145	0.1200	37.3	2.07	0.255	0.1590	48.3	2.69	0.202	0.1430
48.0	2.67	0.081	0.0723		51.7	2.87	0.034	0.0748	46.9	2.61	0.160	0.1290	59.0	3.28	0.143	0.1170
58.2	3.23	0.062	0.0584		59.3	3.29	0.066	0.0614	58.5	3.25	0.082	0.0748	69.0	3.83	0.096	0.0869
68.3	3.79	0.038	0.0376		69.0	3.83	0.043	0.0421	66.5	3.69	0.056	0.0531	76.8	4.27	0.059	0.0567
79.8	4.43	0.015	0.0150		78.9	4.38	0.020	0.0198	74.4	4.13	0.041	0.0403	85.7	4.76	0.030	0.0290
92.0	5.11	0.006	0.0060		92.3	5.13	0.008	0.0080	87.3	4.85	0.017	0.0170	95.6	5.31	0.016	0.0160
105.5	5.86	0.004	0.0040		105.7	5.87	0.003	0.0030	100.8	5.60	0.007	0.0070	106.2	5.90	0.009	0.0090
					121.6	6.76	0.004	0.0040	116.5	6.47	0.004	0.0040	122.5	6.81	0.006	0.0060

x(m)	7.0				8.5				9.5				11.0			
$\bar{x}$	38.88				47.22				52.77				61.11			
	z (cm)	$\bar{z}$	$T_u$	$T_{u_m}$	z (cm)	$\bar{z}$	$T_u$	$T_{u_m}$	z (cm)	$\bar{z}$	$T_u$	$T_{u_m}$	z (cm)	$\bar{z}$	$T_u$	$T_{u_m}$
1.0	0.06	0.976	0.0350		1.0	0.06	0.944	0.0320	1.0	0.06	0.834	0.0300	1.0	0.06	0.554	0.0460
7.4	0.41	0.890	0.0420		7.0	0.39	0.833	0.0360	7.3	0.41	0.850	0.0320	6.1	0.34	0.676	0.0420
13.5	0.75	0.700	0.0980		14.0	0.78	0.693	0.1050	14.0	0.78	0.718	0.0883	10.6	0.59	0.596	0.0540
19.2	1.06	0.493	0.1330		19.0	1.06	0.492	0.1340	17.8	0.99	0.564	0.1310	16.9	0.94	0.501	0.1520
24.5	1.36	0.374	0.1370		23.8	1.32	0.388	0.1420	22.9	1.27	0.373	0.1360	21.7	1.21	0.351	0.1470
34.8	1.94	0.294	0.1460		32.7	1.82	0.296	0.1430	31.1	1.73	0.298	0.1370	31.6	1.76	0.284	0.1370
44.4	2.47	0.237	0.1450		42.2	2.35	0.246	0.1410	42.2	2.35	0.254	0.1410	42.4	2.36	0.221	0.1400
53.3	2.96	0.198	0.1360		50.4	2.80	0.206	0.1340	51.1	2.84	0.212	0.1340	50.7	2.82	0.195	0.1330
59.0	3.28	0.185	0.140		59.0	3.28	0.180	0.1320	59.0	3.28	0.184	0.1320	59.0	3.28	0.169	0.1280
64.5	3.58	0.156	0.1230		71.5	3.97	0.140	0.1140	74.0	4.11	0.136	0.1130	66.0	3.67	0.151	0.1220
75.2	4.18	0.099	0.0870		78.8	4.38	0.110	0.0975	80.3	4.46	0.114	0.0975	74.0	4.11	0.130	0.1080
86.2	4.79	0.056	0.0534		88.6	4.92	0.078	0.0740	88.3	4.90	0.081	0.0750	81.6	4.53	0.105	0.0990
99.7	5.54	0.019	0.0186		101.3	5.63	0.030	0.0300	96.2	5.34	0.058	0.0550	89.3	4.96	0.078	0.0750
113.6	6.31	0.010	0.0100		114.3	6.35	0.015	0.0150	105.4	5.85	0.027	0.0260	97.6	5.42	0.055	0.0530
122.5	6.81	0.008	0.0080		129.5	7.19	0.008	0.0080	116.8	6.49	0.014	0.0140	105.8	5.88	0.031	0.0310
									132.0	7.33	0.009	0.0090	124.0	6.89	0.015	0.0150

x(m)	12.0			
$\bar{x}$	66.66			
	z (cm)	$\bar{z}$	$T_u$	$T_{u_m}$
1.0	0.06		0.470	0.0912
6.4	0.36		0.409	0.1050
12.1	0.67		0.420	0.1240
20.0	1.11		0.369	0.1465
29.2	1.62		0.273	0.1350
42.2	2.35		0.201	0.1280
51.7	2.87		0.176	0.1253
59.0	3.28		0.158	0.1190
69.7	3.87		0.136	0.1070
77.6	4.31		0.114	0.1000
85.5	4.75		0.089	0.0840
94.7	5.20		0.061	0.0590
109.3	6.07		0.027	0.0270
124.5	6.92		0.013	0.0132

TABLE 2 - z - HDC  
 VERTICAL TURBULENCE INTENSITY - Half Density Canopy

x(m)	0				0.3				0.6				1.0			
$\bar{z}$	0				1.66				5.33				5.55			
$\bar{z}$	$\bar{z}$	$T_w$	$T_{w_m}$													
(cm)	(cm)			(cm)	(cm)			(cm)	(cm)			(cm)	(cm)			
3.5	0.19	0.074	0.034	20.3	1.13	0.118	0.071	12.7	0.70	0.340	0.071	7.9	0.44	0.331	0.045	
9.5	0.53	0.066	0.038	23.1	1.26	0.052	0.037	17.1	0.95	0.295	0.078	12.1	0.67	0.271	0.030	
14.8	0.82	0.078	0.051	28.8	1.60	0.051	0.041	19.6	1.09	0.335	0.151	16.0	0.89	0.256	0.041	
18.7	1.04	0.076	0.053	35.8	1.99	0.057	0.049	22.9	1.27	0.229	0.144	18.1	1.01	0.239	0.057	
25.4	1.41	0.068	0.052	45.0	2.50	0.054	0.050	25.5	1.42	0.224	0.159	22.0	1.22	0.232	0.077	
32.1	1.79	0.074	0.061	53.2	2.95	0.046	0.044	29.0	1.61	0.062	0.049	27.0	1.50	0.183	0.114	
40.6	2.26	0.054	0.048	62.0	3.44	0.027	0.026	36.1	2.00	0.037	0.053	34.1	1.89	0.056	0.044	
49.5	2.75	0.041	0.038	69.9	3.88	0.013	0.013	44.9	2.50	0.045	0.042	41.5	2.31	0.040	0.038	
57.6	3.20	0.028	0.027	78.0	4.33	0.007	0.007	53.8	2.99	0.046	0.044	51.7	2.88	0.050	0.048	
66.0	3.67	0.011	0.011					62.6	3.48	0.029	0.028	62.0	3.44	0.038	0.037	
73.5	4.08	0.009	0.009					71.4	3.97	0.020	0.020	68.9	3.83	0.022	0.022	
								80.3	4.46	0.008	0.008	78.3	4.35	0.007	0.007	
								87.0	4.83	0.005	0.005	86.5	4.92	0.002	0.002	

x(m)	1.5				2.0				3.0				5.0			
$\bar{z}$	8.33				11.11				16.66				27.77			
$\bar{z}$	$\bar{z}$	$T_w$	$T_{w_m}$													
(cm)	(cm)			(cm)	(cm)			(cm)	(cm)			(cm)	(cm)			
9.2	0.51	0.122	0.013	15.7	0.87	0.216	0.038	13.9	0.77	0.119	0.014	9.3	0.52	0.405	0.032	
13.8	0.77	0.284	0.031	22.0	1.22	0.174	0.044	18.8	1.05	0.245	0.059	14.5	0.81	0.408	0.061	
19.5	1.08	0.299	0.068	29.4	1.63	0.160	0.082	29.0	1.61	0.199	0.090	19.5	1.08	0.336	0.095	
23.0	1.28	0.257	0.082	38.5	2.14	0.152	0.111	40.3	2.24	0.193	0.135	26.8	1.49	0.238	0.098	
28.0	1.56	0.207	0.096	44.1	2.45	0.092	0.075	47.6	2.65	0.146	0.119	37.4	2.08	0.204	0.115	
33.0	1.83	0.150	0.092	52.6	2.92	0.043	0.039	61.0	3.39	0.073	0.067	49.7	2.76	0.171	0.123	
41.8	2.32	0.048	0.040	61.0	3.59	0.041	0.039	71.0	3.94	0.038	0.037	62.0	3.44	0.119	0.101	
51.4	2.85	0.038	0.035	70.0	3.89	0.035	0.034	81.7	4.54	0.021	0.021	72.7	4.04	0.058	0.054	
64.8	3.60	0.033	0.032	77.6	4.31	0.023	0.023	95.0	5.28	0.006	0.006	84.9	4.72	0.028	0.027	
75.4	4.19	0.017	0.017	88.0	4.89	0.009	0.009					96.4	5.36	0.009	0.009	
86.0	4.78	0.008	0.008									109.0	6.06	0.007	0.007	

x(m)	7.0				8.5				9.5				11			
$\bar{z}$	38.88				47.22				52.77				61.11			
$\bar{z}$	$\bar{z}$	$T_w$	$T_{w_m}$													
(cm)	(cm)			(cm)	(cm)			(cm)	(cm)			(cm)	(cm)			
15.1	0.84	0.342	0.065	14.5	0.80	0.077	0.012	14.7	0.82	0.211	0.034	13.6	0.76	0.194	0.038	
18.3	1.02	0.272	0.071	20.7	1.15	0.180	0.056	18.7	1.04	0.143	0.039	18.2	1.01	0.153	0.050	
22.5	1.25	0.221	0.073	29.8	1.66	0.189	0.074	25.2	1.40	0.143	0.055	22.1	1.23	0.128	0.050	
29.4	1.63	0.114	0.048	39.7	2.21	0.149	0.082	36.0	2.00	0.109	0.054	29.9	1.66	0.129	0.063	
38.1	2.12	0.108	0.038	47.0	2.61	0.136	0.084	45.0	2.50	0.122	0.071	40.5	2.25	0.121	0.072	
48.7	2.71	0.108	0.070	50.5	2.81	0.124	0.081	51.0	2.83	0.114	0.073	52.9	2.94	0.072	0.051	
57.2	3.18	0.107	0.079	61.5	3.42	0.104	0.078	62.0	3.44	0.100	0.074	61.0	3.39	0.066	0.051	
65.6	3.53	0.105	0.083	71.7	3.92	0.076	0.063	75.8	4.21	0.076	0.065	70.4	3.91	0.070	0.059	
73.8	4.10	0.089	0.078	84.1	4.67	0.042	0.038	88.3	4.90	0.055	0.051	82.1	4.56	0.061	0.056	
84.8	4.71	0.052	0.049	96.5	5.36	0.018	0.017	100.9	5.60	0.031	0.030	92.7	5.15	0.040	0.039	
96.7	5.37	0.023	0.022	108.5	6.03	0.013	0.013	109.0	6.06	0.018	0.018	101.5	5.64	0.039	0.039	
108.5	6.03	0.012	0.012									110.0	6.11	0.028	0.028	

X(m)	12			
$\bar{z}$	66.66			
$\bar{z}$	$\bar{z}$	$T_w$	$T_{w_m}$	
(cm)	(cm)			
4.0	0.22	0.133	0.030	
9.4	0.52	0.102	0.029	
16.6	0.92	0.146	0.051	
22.4	1.24	0.188	0.077	
32.5	1.80	0.144	0.075	
44.0	2.44	0.140	0.088	
52.5	2.92	0.116	0.081	
63.1	3.51	0.092	0.072	
73.7	4.10	0.069	0.060	
84.7	4.71	0.048	0.045	
95.3	5.39	0.043	0.042	
110.5	6.14	0.022	0.022	

### 3. Shear Stress

The measured turbulent shear stress  $-\overline{uw}$  data are summarized in Tables 3-FDC and 3-HDC. The results for the FDC case are displayed in Figs. 5.26a and 5.26b. For the HDC case the results are shown in Figs. 5.27a and 5.27b. In these tables the shear stress is made dimensionless using  $-\overline{uw} [0,1]$ , i.e., the turbulent shear stress at the top of canopy leading edge (at  $\tilde{x}, \tilde{z} = 0, 1$ ).

TABLE 3 - FDC  
 TURBULENCE SHEAR STRESS - Full Density Canopy

$-\overline{uw}[0,1] = 1020 \text{ (cm/sec)}^2$

x(m) = -1.0				0				0.3				0.6			
x̄ = -5.55				0				1.66				3.33			
z (cm)	z̄	$-\overline{uw}$ (cm/s) <sup>2</sup>	$\frac{\overline{uw}(z,z)}{\overline{uw}[0,1]}$	z (cm)	z̄	$-\overline{uw}$ (cm/s) <sup>2</sup>	$\frac{\overline{uw}(z,z)}{\overline{uw}[0,1]}$	z (cm)	z̄	$-\overline{uw}$ (cm/s) <sup>2</sup>	$\frac{\overline{uw}(z,z)}{\overline{uw}[0,1]}$	z (cm)	z̄	$-\overline{uw}$ (cm/s) <sup>2</sup>	$\frac{\overline{uw}(z,z)}{\overline{uw}[0,1]}$
2.0	0.11	287	0.28	3.0	0.17	630	0.62	2.0	0.11	582	0.57	3.0	0.167	70	0.07
5.5	0.31	326	0.32	7.5	0.42	511	0.50	7.0	0.39	311	0.30	6.5	0.36	125	0.12
9.0	0.50	292	0.29	11.0	0.61	800	0.78	12.5	0.69	68	0.07	12.5	0.69	20	0.02
14.0	0.78	416	0.41	15.0	0.83	966	0.95	15.0	0.83	31	0.03	16.0	0.89	6	0.01
19.5	1.08	490	0.48	16.0	0.89	969	0.95	19.0	1.06	6732	6.66	20.5	1.14	2212	2.17
26.5	1.47	530	0.62	21.0	1.17	1081	1.06	23.0	1.28	2323	2.28	27.0	1.50	1671	1.64
35.0	1.94	462	0.45	28.0	1.36	1047	1.03	31.0	1.72	577	0.57	33.5	1.86	672	0.66
44.5	2.47	253	0.25	38.0	2.11	789	0.77	41.0	2.28	700	0.69	39.0	2.17	471	0.46
51.5	2.86	137	0.13	48.0	2.66	454	0.45	50.5	2.81	570	0.56	45.0	2.50	493	0.48
60.0	3.33	73	0.07	60.5	3.36	256	0.25	59.5	3.31	439	0.43	53.0	2.94	491	0.48
73.0	4.06	9	0.01	70.5	3.92	66	0.06	70.0	3.89	130	0.13	63.0	3.50	342	0.34
				74.0	4.11	37	0.036	77.0	4.28	73	0.07	70.5	3.92	157	0.15
				81.0	4.50	11	0.01					79.5	4.39	41	0.04
				91.5	5.08	6	0								

x(m) = 1.0				1.5				2.0				3.0			
x̄ = 5.55				8.33				11.11				16.66			
z (cm)	z̄	$-\overline{uw}$ (cm/s) <sup>2</sup>	$\frac{\overline{uw}(z,z)}{\overline{uw}[0,1]}$	z (cm)	z̄	$-\overline{uw}$ (cm/s) <sup>2</sup>	$\frac{\overline{uw}(z,z)}{\overline{uw}[0,1]}$	z (cm)	z̄	$-\overline{uw}$ (cm/s) <sup>2</sup>	$\frac{\overline{uw}(z,z)}{\overline{uw}[0,1]}$	z (cm)	z̄	$-\overline{uw}$ (cm/s) <sup>2</sup>	$\frac{\overline{uw}(z,z)}{\overline{uw}[0,1]}$
3.5	0.19	1	0	2.5	0.14	6	0.01	3.5	0.19	2	0	2.0	0.11	2	0
7.0	0.39	4	0	6.0	0.33	4	0	6.5	0.36	21	0.02	7.0	0.39	27	0.03
11.5	0.64	25	0.02	9.0	0.50	19	0.02	10.0	0.56	28	0.03	11.0	0.61	112	0.12
14.0	0.78	60	0.06	12.5	0.69	76	0.07	16.0	0.89	204	0.20	15.0	0.83	955	0.94
18.0	1.00	1055	1.03	16.0	0.92	368	0.36	19.5	1.08	312	0.31	22.0	1.22	1512	1.48
23.0	1.28	2869	2.81	20.0	1.11	726	0.71	23.5	1.31	940	0.92	28.5	1.58	1848	1.81
29.5	1.64	4830	4.74	26.5	1.47	1583	1.55	31.0	1.72	1650	1.62	37.5	2.08	2320	2.27
34.5	1.92	1435	1.41	32.5	1.81	2508	2.46	40.0	2.22	1554	1.52	44.5	2.47	2271	2.23
42.0	2.33	448	0.44	37.0	2.06	2765	2.71	49.0	2.72	657	0.64	49.0	2.72	2382	2.34
51.0	2.83	388	0.38	44.0	2.44	1406	1.38	61.0	3.39	210	0.21	58.5	3.25	1000	0.98
61.0	3.39	334	0.33	52.0	2.89	512	0.50	64.5	3.58	228	0.22	67.5	3.75	306	0.30
70.0	3.89	233	0.23	61.5	3.42	309	0.30	75.0	4.17	185	0.18	76.5	4.25	170	0.17
77.0	4.28	101	0.10	72.5	4.03	222	0.22	87.5	4.86	46	0.05	85.5	4.75	76	0.07
85.0	4.72	33	0.03	82.5	4.58	55	0.05	102.0	5.67	1	0	94.5	5.22	30	0.03
				93.5	5.19	9	0.01					102.5	5.69	4	0

x(m) = 4.0				5.0				7.0				9.5			
x̄ = 22.22				27.77				38.88				52.77			
z (cm)	z̄	$-\overline{uw}$ (cm/s) <sup>2</sup>	$\frac{\overline{uw}(z,z)}{\overline{uw}[0,1]}$	z (cm)	z̄	$-\overline{uw}$ (cm/s) <sup>2</sup>	$\frac{\overline{uw}(z,z)}{\overline{uw}[0,1]}$	z (cm)	z̄	$-\overline{uw}$ (cm/s) <sup>2</sup>	$\frac{\overline{uw}(z,z)}{\overline{uw}[0,1]}$	z (cm)	z̄	$-\overline{uw}$ (cm/s) <sup>2</sup>	$\frac{\overline{uw}(z,z)}{\overline{uw}[0,1]}$
2.0	0.11	35	0.03	2.0	0.11	41	0.04	2.0	0.11	0	0	2.5	0.14	20	0.02
6.5	0.36	46	0.03	6.5	0.36	32	0.03	6.5	0.36	5	0	7.0	0.39	45	0.04
11.5	0.64	55	0.05	10.5	0.58	244	0.24	10.5	0.58	168	0.16	11.0	0.61	424	0.42
15.0	0.83	339	0.33	15.5	0.86	1081	1.06	14.5	0.81	684	0.67	15.5	0.86	1195	1.17
18.0	1.00	772	0.76	21.0	1.17	1160	1.14	19.5	1.08	854	0.84	19.0	1.06	640	0.63
23.5	1.31	805	0.79	30.0	1.68	1219	1.20	26.0	1.44	1103	1.08	27.0	1.50	711	0.70
31.5	1.75	1461	1.43	36.5	2.03	1282	1.26	33.0	1.83	900	0.88	36.5	2.03	784	0.77
41.0	2.28	1881	1.84	44.0	2.44	1793	1.76	43.0	2.39	835	0.82	45.5	2.53	922	0.90
50.0	2.78	2290	2.25	50.0	2.78	2043	2.00	51.5	2.86	1049	1.03	52.0	2.89	707	0.69
60.0	3.33	979	0.96	56.5	3.14	1733	1.70	61.5	3.42	1122	1.10	60.5	3.36	1018	1.00
72.0	4.00	478	0.47	64.5	3.58	1251	1.23	71.0	3.94	846	0.83	62.5	3.47	1180	1.16
79.0	4.39	247	0.24	72.0	4.00	622	0.61	81.5	4.53	655	0.64	71.0	3.94	1035	1.01
89.0	4.94	110	0.11	81.0	4.50	303	0.30	91.0	5.06	320	0.31	82.0	4.56	788	0.77
				91.0	5.06	72	0.07	101.0	5.61	69	0.07	91.5	5.08	701	0.69
												103.0	5.72	207	0.20

x(m) = 11.0			
x̄ = 61.11			
z (cm)	z̄	$-\overline{uw}$ (cm/s) <sup>2</sup>	$\frac{\overline{uw}(z,z)}{\overline{uw}[0,1]}$
2.0	0.11	17	0.02
6.5	0.36	19	0.02
11.5	0.64	189	0.20
16.0	0.92	2119	2.07
21.5	1.19	1063	1.04
29.5	1.64	762	0.75
40.0	2.22	701	0.69
46.0	2.56	468	0.46
54.5	3.03	815	0.80
60.5	3.36	883	0.67
67.0	3.72	952	0.93
73.0	4.06	803	0.79
82.5	4.58	590	0.59
91.5	5.08	439	0.43
100.5	5.58	288	0.29
112.0	6.22	58	0.06

TABLE 3 - HDC  
TURBULENT SHEAR STRESS - Half Density Canopy

$-\overline{uw}[0,1] = 850 \text{ (cm/sec)}^2$

x(m) 0				0.3				0.6				1.0			
z̄				1.66				3.33				5.55			
z (cm)	z̄	$-\overline{uw}$ (cm/s) <sup>2</sup>	$\frac{\overline{uw}(x,z)}{\overline{uw}(0,1)}$	z (cm)	z̄	$-\overline{uw}$ (cm/s) <sup>2</sup>	$\frac{\overline{uw}(x,z)}{\overline{uw}(0,1)}$	z (cm)	z̄	$-\overline{uw}$ (cm/s) <sup>2</sup>	$\frac{\overline{uw}(x,z)}{\overline{uw}(0,1)}$	z (cm)	z̄	$-\overline{uw}$ (cm/s) <sup>2</sup>	$\frac{\overline{uw}(x,z)}{\overline{uw}(0,1)}$
3.5	0.19	364	0.43	4.0	0.22	53	0.06	5.5	0.19	81	0.096	4.0	0.22	156	0.18
9.5	0.53	632	0.74	9.0	0.50	22	0.026	8.3	0.46	121	0.142	7.9	0.44	394	0.46
14.8	0.82	817	0.96	15.2	0.73	24	0.028	12.7	0.70	97	0.114	12.1	0.67	4	0
18.7	1.04	826	0.97	20.3	1.13	806	0.95	17.1	0.95	731	0.86	16.0	0.89	354	0.42
25.4	1.41	1354	1.59	23.1	1.28	149	1.75	19.6	1.09	3047	3.58	18.1	1.01	858	1.01
32.1	1.79	830	0.98	28.8	1.60	624	0.73	22.9	1.27	4041	4.75	22.0	1.22	1813	2.15
40.6	2.26	498	0.59	35.8	1.99	629	0.74	25.5	1.42	2711	3.19	27.0	1.50	2792	3.28
49.5	2.75	367	0.43	45.0	2.50	505	0.59	29.0	1.61	1094	1.29	34.1	1.89	1010	1.19
57.6	3.20	146	0.17	53.2	2.95	343	0.40	36.1	2.00	473	0.56	41.5	2.31	419	0.49
66.0	3.67	39	0.05	62.0	3.44	125	0.15	44.9	2.50	497	0.58	51.7	2.88	422	0.50
73.5	4.08	6	0.01	69.9	3.88	37	0.04	53.8	2.99	365	0.43	62.0	3.44	235	0.28
				78.0	4.33	6	0.01	62.6	3.48	132	0.16	68.9	3.83	111	0.13
								71.4	3.97	120	0.14	78.3	4.35	15	0.02
								80.3	4.46	22	0.03	88.5	4.92	7	0.01
								87.0	4.83	7	0.01				

x(m) 1.5				2.0				3.0				5.0			
z̄				11.11				16.66				27.77			
z (cm)	z̄	$-\overline{uw}$ (cm/s) <sup>2</sup>	$\frac{\overline{uw}(x,z)}{\overline{uw}(0,1)}$	z (cm)	z̄	$-\overline{uw}$ (cm/s) <sup>2</sup>	$\frac{\overline{uw}(x,z)}{\overline{uw}(0,1)}$	z (cm)	z̄	$-\overline{uw}$ (cm/s) <sup>2</sup>	$\frac{\overline{uw}(x,z)}{\overline{uw}(0,1)}$	z (cm)	z̄	$-\overline{uw}$ (cm/s) <sup>2</sup>	$\frac{\overline{uw}(x,z)}{\overline{uw}(0,1)}$
3.5	0.19	74	0.09	3.0	0.17	31	0.04	3.0	0.17	20	0.02	4.0	0.22	11	0.01
9.2	0.51	114	0.15	9.7	0.54	167	0.19	10.0	0.56	98	0.12	9.3	0.52	168	0.20
13.8	0.77	233	0.27	15.7	0.87	637	0.75	13.9	0.77	411	0.48	14.5	0.81	909	1.07
19.5	1.08	907	1.07	22.0	1.22	1643	1.93	18.8	1.05	981	1.15	19.5	1.08	1255	1.48
23.0	1.28	1673	1.97	29.4	1.63	1976	2.32	29.0	1.61	1651	1.94	26.8	1.49	1452	1.71
28.0	1.56	1895	2.23	38.5	2.14	1920	2.26	40.3	2.24	2441	2.87	37.4	2.08	2170	2.55
33.0	1.83	2123	2.50	44.1	2.45	942	1.11	47.6	2.65	1583	1.86	49.7	2.76	2236	2.63
41.8	2.32	723	0.85	52.6	2.92	417	0.49	61.0	3.39	626	0.74	62.0	3.44	1357	1.60
51.4	2.85	404	0.48	61.0	3.39	216	0.25	71.0	3.94	180	0.21	72.7	4.04	574	0.68
64.8	3.60	217	0.26	70.0	3.89	127	0.15	81.7	4.54	50	0.06	84.9	4.72	124	0.15
75.4	4.19	92	0.11	77.6	4.31	60	0.07	95.0	5.28	3	0	96.4	5.36	14	0.02
86.0	4.78	6	0.01	88.0	4.89	8	0.01					109.0	6.06	3	0.004

x(m) 7.0				8.5				9.5				11.0							
z̄				38.88				47.22				52.77				61.11			
z (cm)	z̄	$-\overline{uw}$ (cm/s) <sup>2</sup>	$\frac{\overline{uw}(x,z)}{\overline{uw}(0,1)}$	z (cm)	z̄	$-\overline{uw}$ (cm/s) <sup>2</sup>	$\frac{\overline{uw}(x,z)}{\overline{uw}(0,1)}$	z (cm)	z̄	$-\overline{uw}$ (cm/s) <sup>2</sup>	$\frac{\overline{uw}(x,z)}{\overline{uw}(0,1)}$	z (cm)	z̄	$-\overline{uw}$ (cm/s) <sup>2</sup>	$\frac{\overline{uw}(x,z)}{\overline{uw}(0,1)}$				
4.5	0.25	18	0.21	3.5	0.19	8	0.01	3.5	0.19	1	0	3.0	0.17	2	0				
9.8	0.55	194	0.23	9.0	0.50	66	0.08	8.9	0.50	18	0.02	8.3	0.46	72	0.08				
15.1	0.84	1049	1.23	14.5	0.80	757	0.89	14.7	0.82	803	0.94	13.6	0.76	798	0.94				
18.3	1.02	1301	1.53	20.7	1.15	905	1.06	18.7	1.04	1068	1.26	18.2	1.01	1081	1.27				
22.5	1.25	1541	1.81	29.8	1.66	1197	1.41	25.2	1.40	951	1.12	22.1	1.23	928	1.09				
29.4	1.63	1172	1.38	39.7	2.21	1508	1.77	36.0	2.00	1295	1.52	29.9	1.66	825	0.97				
38.1	2.12	1554	1.83	47.0	2.61	1836	2.16	45.0	2.50	1361	1.60	40.5	2.25	1230	1.45				
48.7	2.71	1655	1.95	50.5	2.81	1303	1.53	51.0	2.83	1288	1.52	52.9	2.94	787	0.93				
57.2	3.18	1478	1.74	61.5	3.42	1515	1.78	62.0	3.44	1325	1.56	61.0	3.39	871	1.02				
63.6	3.53	1336	1.57	71.7	3.98	1176	1.38	75.8	4.21	994	1.17	70.4	3.91	1170	1.38				
73.8	4.10	825	0.97	84.1	4.67	594	0.70	88.3	4.90	636	0.75	82.1	4.56	625	0.74				
84.8	4.71	405	0.48	96.5	5.36	114	0.13	100.9	5.60	121	0.14	92.7	5.15	340	0.40				
96.7	5.37	41	0.05	108.5	6.03	42	0.05	109.0	6.06	53	0.06	101.5	5.64	222	0.26				
108.5	6.03	14	0.02									110.0	6.11	104	0.12				

x(m) 12.0			
z̄			
z (cm)	z̄	$-\overline{uw}$ (cm/s) <sup>2</sup>	$\frac{\overline{uw}(x,z)}{\overline{uw}(0,1)}$
4.0	0.22	202	0.24
9.4	0.52	485	0.57
16.6	0.92	843	0.99
22.4	1.24	1320	1.55
32.5	1.80	885	1.04
44.0	2.44	1168	1.37
52.5	2.92	991	1.17
63.1	3.51	1012	1.19
73.7	4.10	1049	1.23
84.7	4.71	575	0.68
95.3	5.29	251	0.30
110.5	6.14	30	0.04

#### 4. Boundary-layer thicknesses and integral parameters.

The boundary-layer thickness, displacement thickness, momentum thickness, shape factor and internal boundary-layer thickness data are tabulated in Tables 4-FDC and 4-HDC. In these tables the fractions of displacement thickness and momentum thickness over the canopy height are also summarized. The results are shown in Figs. 5.9, 5.10, 5.11, 5.12 and 5.31. The dimensionless thicknesses are referred to the canopy height  $h = 18$  cm.

TABLE 4 - FDC  
BOUNDARY-LAYER THICKNESSES AND INTEGRAL PARAMETERS - Full Density Canopy

x (m)	$\bar{x}$	$\delta$ (cm)	$\bar{\delta}$	$\delta^*$ (cm)	$\bar{\delta}^*$	$\theta$ (cm)	$\bar{\theta}$	H	$\delta_h^*$ (cm)	$\bar{\delta}_h^*$	$\theta_h$ (cm)	$\bar{\theta}_h$	$\delta_i$ (cm)	$\bar{\delta}_i$
-1.0	-5.55	72	4.00	10.8	0.60	7.7	0.43	1.40						
0	0	72	4.00	13.5	0.75	9.0	0.50	1.50						
0.3	1.66	72	4.00	18.4	1.02	8.1	0.45	2.27	8.1	0.45	4.4	0.24	3.15	1.75
0.6	3.33	72	4.15	24.8	1.38	8.1	0.45	3.06	12.2	0.67	3.4	0.19	36.0	2.00
1.0	5.55	77	4.30	28.4	1.58	8.1	0.45	3.51	15.4	0.85	2.1	0.12	44.1	2.45
1.5	8.33	79	4.40	29.7	1.65	9.0	0.50	3.30	16.5	0.92	1.2	0.07	63.0	3.50
2.0	11.11	86	4.75	35.6	1.98	10.8	0.60	3.30	17.2	0.96	1.2	0.07	66.6	3.70
3.0	16.66	90	5.00	33.8	1.88	11.3	0.63	3.00	16.7	0.93	1.3	0.07	75.6	4.20
5.0	27.77	106	5.90	38.7	2.15	14.2	0.79	2.73	15.5	0.86	1.4	0.08	92.7	5.15
7.0	38.88	114	6.35	40.9	2.27	15.7	0.87	2.61	16.6	0.92	1.5	0.08	105.3	5.85
9.5	52.77	115	6.40	41.0	2.28	15.8	0.88	2.60	16.4	0.91	1.6	0.09	110.7	6.15
11.0	61.11	113	6.25	36.0	2.00	16.2	0.90	2.22	16.4	0.91	1.6	0.09	109.0	6.05
12.0	66.66	104	5.80	35.6	1.98	17.6	0.98	2.02	15.5	0.86	2.1	0.12		

TABLE 4 - HDC  
BOUNDARY-LAYER THICKNESSES AND INTEGRAL PARAMETERS - Half Density Canopy

x (m)	$\bar{x}$	$\delta$ (cm)	$\bar{\delta}$	$\delta^*$ (cm)	$\bar{\delta}^*$	$\theta$ (cm)	$\bar{\theta}$	H	$\delta_h^*$ (cm)	$\bar{\delta}_h^*$	$\theta_h$ (cm)	$\bar{\theta}_h$	$\delta_i$ (cm)	$\bar{\delta}_i$
0	0	72	4.00	14.4	0.80	9.0	0.50	1.60	8.4	0.46	4.1	0.23		
0.3	1.66	72	4.00	18.4	1.02	8.1	0.45	2.26	11.5	0.64	3.1	0.17	26.1	1.45
0.6	3.33	72	4.00	20.3	1.13	8.1	0.45	2.51	13.2	0.73	3.2	0.18	32.4	1.80
1.0	5.55	73	4.05	23.8	1.32	8.1	0.45	2.93	14.5	0.81	2.6	0.15	44.1	2.45
1.5	8.33	74	4.10	28.8	1.60	9.0	0.50	3.20	15.3	0.85	2.2	0.12	63.0	3.50
2.0	11.11	76	4.20	30.2	1.68	9.5	0.53	3.17	16.0	0.89	1.8	0.10	66.6	3.70
3.0	16.66	79	4.40	32.8	1.82	9.9	0.55	3.31	16.4	0.91	1.3	0.07	79.2	4.40
5.0	27.77	89	4.95	36.4	2.02	12.2	0.68	2.97	16.4	0.91	1.2	0.07	88.2	4.90
7.0	38.88	103	5.70	39.6	2.20	14.4	0.80	2.75	15.8	0.88	1.4	0.08	99.0	5.50
8.5	47.22	106	5.90	41.0	2.28	15.3	0.85	2.68	16.4	0.91	1.5	0.09	103.5	5.75
9.5	52.77	109	6.05	41.9	2.33	15.8	0.88	2.65	16.8	0.93	1.6	0.09	105.3	5.85
11.0	61.11	105	5.85	37.4	2.08	14.9	0.83	2.51	15.7	0.87	1.9	0.10	108.9	6.05
12.0	66.66	103	5.70	35.1	1.95	17.1	0.95	2.05						

## 5. Turbulent energy

The one-dimensional wave-number density function data at  $x = 7\text{m}$  ( $\tilde{x} = 38.88$ ) are summarized in Tables 5-FDC and 5-HDC. The results are displayed in Figs. 5.37 and 5.38, respectively.

The energy dissipation and energy production for both canopy densities computed using Eqs. (5.27) and (5.32), respectively, are tabulated in Table 5- $\epsilon E_p$ .

The discretized energies at four selected wavelengths for the FDC and HDC cases are tabulated in Tables 5-DE-FDC and 5-DE-HDC, respectively. In these tables the discretized energy is made dimensionless employing the energy at same wavelength at the top of the canopy leading edge (at  $\tilde{x}, \tilde{z} = 0,1$ ) denoted by  $\overline{u_0^2}[L]$ . The results are displayed in Figs. 5.43a, 5.43b, 5.44a and 5.44b.

TABLE 5 - FDC  
ONE-DIMENSIONAL WAVE-NUMBER DENSITY FUNCTION - Full Density Canopy  
 $x = 7a, \bar{x} = 38.88$

$z$ (cm)	18.5			24.0			40.5			57.5			87.0		
$\bar{z}$	1.03			1.33			2.25			3.19			4.83		
$n$ (Hz)	$k$ (cm <sup>-1</sup> )	$\phi$ [k] (cm)	$n$ (Hz)	$k$ (cm <sup>-1</sup> )	$\phi$ [k] (cm)	$n$ (Hz)	$k$ (cm <sup>-1</sup> )	$\phi$ [k] (cm)	$n$ (Hz)	$k$ (cm <sup>-1</sup> )	$\phi$ [k] (cm)	$n$ (Hz)	$k$ (cm <sup>-1</sup> )	$\phi$ [k] (cm)	
3.0	0.11	4.7210	2.9	0.07	3.7976	3.0	0.06	5.9582	2.9	0.04	4.9212	2.6	0.03	5.4530	
4.2	0.15	4.6035	4.1	0.10	2.7958	4.1	0.08	5.8476	4.4	0.06	8.5663	4.3	0.05	11.2164	
6.4	0.24	2.8163	6.4	0.16	2.0888	6.2	0.12	2.8027	6.5	0.09	5.5529	6.1	0.07	5.9768	
9.8	0.36	1.2142	9.8	0.25	1.2683	9.5	0.18	1.2865	10.2	0.14	1.7693	9.5	0.11	4.0734	
14.1	0.51	0.9258	14.3	0.36	0.6251	13.9	0.26	1.0618	13.8	0.19	0.9078	13.0	0.15	1.4206	
18.1	0.66	0.4538	21.1	0.53	0.5816	19.2	0.35	0.5927	21.1	0.29	0.8583	18.2	0.21	0.9459	
22.1	0.81	0.3084	25.7	0.62	0.3562	24.5	0.45	0.2901	26.1	0.36	0.6582	20.8	0.24	0.7499	
26.4	0.97	0.1738	35.0	0.88	0.2311	31.8	0.59	0.2442	30.5	0.42	0.4178	46.7	0.54	0.2370	
29.4	1.07	0.2066	39.0	0.98	0.1524	48.0	0.89	0.1854	39.2	0.54	0.2661	65.7	0.76	0.1483	
33.9	1.24	0.2055	43.8	1.10	0.1080	53.5	0.99	0.1187	57.4	0.79	0.1322	93.4	1.08	0.0661	
50.5	1.85	0.1297	57.2	1.44	0.0798	64.3	1.19	0.1005	71.2	0.98	0.0853	143.5	1.66	0.0286	
65.2	2.38	0.0963	70.8	1.78	0.0522	92.3	1.71	0.0465	98.0	1.35	0.0542	193.7	2.24	0.0118	
77.5	2.83	0.0455	139.2	3.50	0.0187	140.0	2.59	0.0302	111.8	1.54	0.0373	278.4	3.22	0.0059	
91.9	3.25	0.0269	159.6	4.01	0.0130	178.8	3.30	0.0160	145.2	2.00	0.0268	460.0	5.32	0.0024	
134.0	4.98	0.0127	205.1	5.15	0.0075	225.1	4.16	0.0095	185.9	2.56	0.0200	570.6	6.60	0.0011	
159.7	5.83	0.0105	242.4	6.08	0.0047	278.6	5.15	0.0056	243.2	3.35	0.0117	703.8	8.14	0.0006	
197.9	7.23	0.0080	318.7	8.01	0.0028	374.7	6.92	0.0025	336.9	4.64	0.0083	953.7	11.13	0.0002	
238.1	8.69	0.0022	393.1	9.87	0.0015	451.9	8.35	0.0017	466.9	6.43	0.0028				
296.8	10.84	0.0023	465.8	11.77	0.0008	538.7	9.80	0.0012	582.3	8.02	0.0014				
384.0	14.02	0.0008	583.2	14.65	0.0003	560.5	10.35	0.0010	731.9	10.08	0.0005				
538.2	19.65	0.0003				613.0	11.32	0.0006	839.4	11.56	0.0003				
						813.7	15.03	0.0002							

TABLE 5 - HDC  
ONE DIMENSIONAL WAVE NUMBER DENSITY FUNCTION - Half Density Canopy  
 $x = 7a, \bar{x} = 38.88$

$z$ (cm)	19.2			22.4			53.3			75.2		
$\bar{z}$	1.07			1.24			2.96			4.18		
$n$ (Hz)	$k$ (cm <sup>-1</sup> )	$\phi$ [k] (cm)	$n$ (Hz)	$k$ (cm <sup>-1</sup> )	$\phi$ [k] (cm)	$n$ (Hz)	$k$ (cm <sup>-1</sup> )	$\phi$ [k] (cm)	$n$ (Hz)	$k$ (cm <sup>-1</sup> )	$\phi$ [k] (cm)	
2.8	0.11	3.7741	3.2	0.09	7.7407	2.6	0.04	10.9664	2.5	0.03	16.1813	
4.4	0.17	1.8924	4.2	0.12	2.8697	4.0	0.06	4.8921	4.2	0.05	10.2891	
6.5	0.25	1.5428	6.0	0.17	1.9095	5.9	0.09	4.0829	5.9	0.07	4.0280	
9.5	0.37	0.8807	9.8	0.28	1.1720	10.0	0.15	2.4112	10.1	0.12	3.1897	
14.2	0.55	0.6134	13.7	0.39	0.8844	14.5	0.22	1.5663	14.3	0.17	1.7070	
18.1	0.70	0.2534	19.3	0.55	0.4043	20.4	0.31	1.2007	18.5	0.22	1.5751	
20.6	0.80	0.1645	24.2	0.69	0.4238	26.4	0.40	0.3767	21.8	0.26	0.8581	
24.3	0.94	0.1698	33.3	0.95	0.2571	38.9	0.59	0.2082	26.0	0.31	0.4463	
28.6	1.11	0.1170	44.5	1.27	0.1321	44.8	0.68	0.1694	31.9	0.38	0.2703	
32.5	1.26	0.1124	61.3	1.75	0.0780	52.7	0.80	0.1086	53.7	0.64	0.1263	
45.9	1.78	0.0801	85.8	2.45	0.0432	64.6	0.98	0.0868	69.7	0.83	0.0841	
62.4	2.42	0.0626	114.2	3.62	0.0262	71.9	1.09	0.0642	84.8	1.01	0.0600	
72.8	2.82	0.0302	189.9	5.42	0.0088	82.4	1.25	0.0507	99.0	1.18	0.0432	
89.5	3.47	0.0238	208.4	5.95	0.0076	109.4	1.66	0.0399	120.0	1.43	0.0255	
112.2	4.35	0.0131	245.6	7.01	0.0040	166.8	2.53	0.0150	221.5	2.64	0.0139	
132.6	5.14	0.0081	318.1	9.08	0.0026	245.9	3.73	0.0094	276.1	3.29	0.0034	
161.5	6.26	0.0067	362.2	10.34	0.0020	330.3	5.01	0.0056	400.3	4.77	0.0027	
207.2	8.03	0.0072	479.6	13.69	0.0004	397.0	6.02	0.0038	551.4	6.57	0.0019	
234.0	9.07	0.0034	532.5	15.20	0.0004	490.4	7.44	0.0026	638.6	7.61	0.0015	
254.6	9.87	0.0017	631.9	18.04	0.0002	600.0	9.10	0.0017	853.5	10.17	0.0002	
284.3	11.02	0.0012				708.0	10.74	0.0010				
322.0	12.48	0.0004				795.7	12.07	0.0005				
441.7	17.12	0.0002				949.2	14.40	0.0002				

TABLE 5 -  $\epsilon E_p$   
 ENERGY DISSIPATION AND ENERGY PRODUCTION  
 $x = 7m, \tilde{x} = 38.88$

Full Density Canopy					Half Density Canopy				
$z$ (cm)	$\tilde{z}$	$\epsilon$ ( $\text{cm}^2/\text{sec}^3$ )	$E_p$ ( $\text{cm}^2/\text{sec}^3$ )	$\epsilon/E_p$	$z$ (cm)	$\tilde{z}$	$\epsilon$ ( $\text{cm}^2/\text{sec}^3$ )	$E_p$ ( $\text{cm}^2/\text{sec}^3$ )	$\epsilon/E_p$
18.5	1.03	30500	11950	2.55	19.3	1.07	73600	15000	4.91
23.9	1.33	31500	10000	3.15	22.4	1.24	66400	15000	4.43
40.5	2.25	23900	5500	4.35	53.3	2.96	30800	8700	3.54
57.4	3.19	20500	5000	4.10	75.2	4.18	16500	3000	5.50
86.9	4.83	9600	1500	6.40					

$\nu = 0.189 \text{ cm}^2/\text{sec}$

TABLE 5 - DE - FDC  
DISCRETIZED ENERGY - Full Density Canopy

		L(cm)		62.8		12.6		9.15		0.63	
x (m)	$\bar{x}$	x (cm)	$\bar{x}$	$\frac{\overline{u^2}[L]}{(cm/s)^2}$	$\frac{\overline{u^2}[L]}{u_0^2[L]}$	$\frac{\overline{u^2}[L]}{(cm/s)^2}$	$\frac{\overline{u^2}[L]}{u_0^2[L]}$	$\frac{\overline{u^2}[L]}{(cm/s)^2}$	$\frac{\overline{u^2}[L]}{u_0^2[L]}$	$\frac{\overline{u^2}[L]}{(cm/s)^2}$	$\frac{\overline{u^2}[L]}{u_0^2[L]}$
0	0	14.0	0.78	50.4	1.07	4.5	0.80	0.57	1.14	0.0096	1.10
		18.0	1.0	47.2	1.00	5.7	1.00	0.50	1.00	0.0087	1.00
		34.2	1.9	34.4	0.73	2.5	0.43	0.27	0.55	0.0042	0.48
		46.8	2.6	16.7	0.35	1.4	0.25	0.14	0.27	0.0011	0.13
		57.1	3.17	8.1	0.17	0.5	0.08	0.02	0.05	0.0011	0.13
0.3	1.66	15.5	0.86			36.2	6.40	6.05	12.20	0.0666	7.66
		19.1	1.06	601.0	12.70	67.0	1.80	5.78	11.65	0.2810	32.30
		32.0	1.78	55.6	1.14	5.2	0.92	0.71	1.44	0.0090	1.03
		57.1	3.17	35.0	0.74	3.2	0.56	0.24	0.49	0.0048	0.55
0.6	3.33	12.1	0.67					34.70	70.00	0.5010	57.60
		20.5	1.14	206.0	4.36	53.7	9.49	4.93	9.94	0.2180	25.00
		27.5	1.53	352.0	7.46	27.5	4.86	3.85	7.76	0.1170	13.40
		40.0	2.22	89.1	1.89	8.1	1.42	0.78	1.56	0.0162	1.86
		58.0	3.22	38.0	0.81	3.7	0.65	0.24	0.48	0.0040	0.46
1.0	5.55	18.5	1.03			285.0	50.40	19.30	38.90	0.4780	54.9
		27.0	1.50	406.0	8.60	40.8	7.21	5.42	10.90	0.3030	34.8
		37.4	2.08	177.0	3.75	10.0	1.77	1.50	3.00	0.0230	2.64
		57.4	3.17	17.9	0.38	1.4	0.25	0.13	0.27	0.0017	0.20
1.5	8.33	15.5	0.86			250.0	44.20	21.60	43.50	0.3970	45.6
		34.9	1.94	311.0	6.59	29.6	5.23	3.12	6.29	0.1630	18.7
		57.1	3.17	40.5	0.86	3.3	0.58	0.39	0.79	0.0068	0.78
3.0	16.66	12.1	0.67			244.0	45.10	36.80	74.20		
		19.1	1.06			197.6	34.90	18.80	37.90	1.0600	122.00
		25.0	1.39	451.0	9.56	60.5	10.70	7.11	14.30	0.2230	25.60
		44.5	2.47	234.0	4.96	19.6	3.46	2.00	4.03	0.0770	8.85
		63.0	3.50	65.3	1.34	4.7	0.83	0.51	1.02	0.0060	0.69
5.0	27.77	18.5	1.03			92.1	16.30	6.95	14.00	0.2170	24.90
		23.0	1.28	362.0	7.67	62.5	11.00	8.75	17.60	0.2770	31.80
		49.5	2.75	255.0	5.40	23.3	4.12	2.68	5.40	0.0937	10.80
		72.5	4.03	151.0	3.20	7.9	1.39	0.52	1.04	0.0101	1.16
7.0	38.88	18.5	1.03	268	5.68	48.4	8.55	5.93	12.00	0.1140	13.10
		23.9	1.33	174	3.69	34.3	6.06	3.03	6.11	0.0958	11.00
		40.5	2.25	241	5.11	16.7	2.95	2.17	4.38	0.0665	7.64
		57.4	3.19	327	6.93	20.6	3.64	2.30	4.64	0.0442	5.08
		86.9	4.83	142	3.01	8.1	1.43	0.50	1.01	0.0189	2.17
9.5	52.77	18.0	1.00	251	5.32	70.9	12.50	10.20	20.60	0.1730	19.90
		39.1	2.17	323	6.84	27.0	4.77	3.33	6.71	0.0854	9.82
		57.4	3.19	261	5.53	15.3	2.70	1.76	3.55	0.0383	4.40
11.0	61.11	17.5	0.97	806	17.10	60.8	10.70	6.79	13.70	0.2030	23.30
		22.0	1.22	485	10.30	32.1	5.67	4.24	8.55	0.1360	15.60
		41.0	2.28	178	3.77	20.3	3.59	2.35	4.74	0.090	10.34
		58.0	3.22	228	4.83	11.0	1.93	1.57	3.17	0.0436	5.01
		82.1	4.56	117	2.48	6.8	1.20	0.73	1.47	0.0144	1.66
12.0	66.66	13.0	0.72			77.8	13.70	8.03	16.20	0.2410	27.70
		19.1	1.06	359	7.61	75.9	13.40	7.93	16.00	0.2150	24.70
		36.5	2.03	266	5.64	22.5	3.98	2.57	5.18	0.1030	11.80
		58.5	3.25	174	3.69	14.7	2.60	1.26	2.54	0.0204	2.34
		84.6	4.70	74	1.57	6.1	1.07	0.44	0.90	0.005	0.57
		$\frac{\overline{u^2}[L]}{(cm/sec)^2}$		49.6		5.02		0.5		0.0093	

TABLE 5 - DE - HDC  
 DISCRETIZED ENERGY - Half Density Canopy

		L(cm)		62.8		12.6		9.15		0.63	
$x$ (#)	$\bar{x}$	$z$ (cm)	$\bar{Y}$	$\overline{u^2 [L]}$ (cm/s) <sup>2</sup>	$\frac{\overline{u^2 [L]}}{u_0^2 [L]}$						
0	0	11.2	0.62	145.0	1.45	16.10	1.49	1.45	1.38	0.0204	1.46
		21.4	1.19	86.4	0.85	8.52	0.79	0.88	0.84	0.0107	0.76
		48.1	2.67	68.2	0.68	1.61	0.15	0.19	0.18		
		56.5	3.14	29.4	0.29	0.58	0.05				
0.3	1.66	17.5	0.97			99.20	9.18	22.00	20.95	0.456	32.57
		21.8	1.21	162.4	1.62	19.60	1.81	3.12	2.97	0.133	9.50
		29.7	1.65	60.2	0.60	3.91	0.36	0.57	0.55	0.007	0.50
		56.5	3.14	27.5	0.28	0.77	0.07	0.04	0.04		
0.6	3.33	11.9	0.66			48.20	4.46	5.40	5.14	0.099	7.07
		19.1	1.06	373.2	3.73	55.50	5.14	4.41	4.20	0.209	14.93
		28.8	1.60	158.0	1.58	18.30	1.69	1.90	1.81	0.054	3.86
		43.0	2.39	51.2	0.51	4.21	0.39	0.52	0.50	0.007	0.47
1.0	5.55	11.2	0.62			81.70	7.56	9.95	9.48	0.264	18.86
		18.5	1.03	1191.0	11.91	85.80	7.94	7.06	6.72	0.228	16.28
		26.5	1.47	469.0	4.69	49.70	4.60	5.50	5.24	0.250	17.86
		43.6	2.42	63.6	6.36	3.53	0.33	0.49	0.47	0.006	0.43
59.6	3.31	32.2	3.22	2.17	0.20	0.11	0.11				
1.5	8.33	11.3	0.63			204.00	18.89	16.10	15.33	0.255	18.21
		20.2	1.12			123.00	11.39	8.72	8.30	0.291	20.78
		27.2	1.51	596.0	5.96	51.70	4.79	6.17	5.88	0.284	20.28
		34.6	1.92	278.0	2.78	17.10	1.58	2.28	2.17	0.129	9.21
58.1	3.23	34.5	0.34	2.74	0.25	0.22	0.21	0.002	0.14		
68.2	3.79	18.3	0.18	0.96	0.09	0.03	0.03				
3.0	16.66	19.1	1.06	1007.0	10.07	95.00	8.80	13.60	12.95	0.227	16.21
		37.3	2.07	355.0	3.55	44.30	4.10	4.10	3.90	0.228	16.28
		66.4	3.69	22.9	0.23	2.03	0.19	0.11	0.11		
		74.3	4.13	17.0	0.17	0.96	0.09	0.031	0.03		
5.0	27.77	18.0	1.00	640.0	6.40	100.00	9.26	12.00	11.43	0.254	18.14
		23.0	1.28	319.0	3.19	56.80	5.26	6.10	5.81	0.192	13.71
		40.1	2.23	403.0	4.03	38.90	3.60	3.11	2.96	0.119	8.50
		68.9	3.83	165.0	1.65	12.10	1.12	1.47	1.40	0.008	0.57
7.0	38.88	19.3	1.07	678.0	6.78	109.00	10.09	10.60	10.10	0.275	19.64
		22.4	1.24	379.0	3.79	58.00	5.37	6.76	6.44	0.183	13.07
		53.3	2.96	309.0	3.09	22.40	2.07	2.25	2.14	0.101	7.21
		75.2	4.18	93.2	0.93	3.38	0.31	0.38	0.36	0.005	0.36
86.2	4.79	37.5	0.38	1.38	0.13	0.09	0.08				
9.5	52.77	17.8	0.99	629.0	6.29	76.8	7.11	9.53	9.08	0.295	21.07
		22.9	1.27	284.0	2.84	63.7	5.90	6.60	6.28	0.214	15.28
		31.1	1.73	438.0	4.38	54.3	5.03	3.83	3.65	0.162	11.57
		51.1	2.84	305.0	3.05	31.4	2.91	2.66	2.53	0.123	8.78
59.0	3.28	168.0	1.68	20.5	1.90	2.52	2.40	0.088	6.28		
80.3	4.46			4.7	0.44	0.58	0.55	0.010	0.71		
11.0	61.11	16.9	0.94	488.0	4.88	74.4	6.89	7.90	7.52	0.241	17.21
		21.8	1.21	433.0	4.33	47.1	4.36	5.17	4.92	0.194	13.86
		42.5	2.36	322.0	3.22	28.2	2.61	3.72	3.54	0.141	10.07
		66.1	3.67	201.0	2.01	11.5	1.06	1.46	1.39	0.032	2.28
81.5	4.53	76.9	0.77	4.4	0.41	0.56	0.53	0.001	0.07		
12.0	66.66	20.0	1.11	590.0	5.90	49.9	4.62	5.33	5.08	0.224	16.00
		42.1	2.34	344.0	3.44	23.1	2.14	2.50	2.38	0.113	8.07
		69.7	3.87	180.0	1.80	10.3	0.95	1.34	1.28	0.041	2.93
		85.5	4.75	72.1	0.72	3.2	0.30	0.24	0.23		

 $\frac{\overline{u^2 [L]}}{u_0^2 [L]}$   
 (cm/sec)<sup>2</sup>

100.0

10.8

1.05

0.014

DOCUMENT CONTROL DATA - R & D

(Security classification of title, body of abstract and indexing annotation must be entered when the overall report is classified)

1. ORIGINATING ACTIVITY (Corporate author) Colorado State University Fort Collins, Colorado 80521		2a. REPORT SECURITY CLASSIFICATION	
		2b. GROUP	
3. REPORT TITLE AN INVESTIGATION OF FLOW OVER HIGH ROUGHNESS			
4. DESCRIPTIVE NOTES (Type of report and inclusive dates) Technical report			
5. AUTHOR(S) (First name, middle initial, last name) T. Kawatani and W. Z. Sadeh			
6. REPORT DATE August , 1971		7a. TOTAL NO. OF PAGES 142	7b. NO. OF REFS 69
8a. CONTRACT OR GRANT NO. DAAB07-68-C-0423 and N00014-68-A-0493-0001		9a. ORIGINATOR'S REPORT NUMBER(S) CER71-72TK-WZS3	
b. PROJECT NO.		9b. OTHER REPORT NO(S) (Any other numbers that may be assigned this report)	
c.			
d.			
10. DISTRIBUTION STATEMENT Distribution of this document is unlimited			
11. SUPPLEMENTARY NOTES		12. SPONSORING MILITARY ACTIVITY U.S. Army Materiel Command, Washington, D.C.	
13. ABSTRACT An experimental investigation of the atmospheric boundary-layer flow on high roughness was conducted by simulating the flow over a forest canopy in a meteorological wind tunnel. The model forest canopy used consisted of plastic simulated-evergreen trees. The measurements were carried out at constant free-stream velocity and under thermally neutral conditions. Two canopy densities were tested to explore the effects of the roughness density on the flow. One roughness density was half of the other. The results indicate that the mean velocity profiles within the fully developed flow region can be described by generalized logarithmic relationships. For the flow in the inner zone, the free-stream velocity and the roughness height are the similarity parameters for the velocity and the vertical distance, respectively. In the outer zone the free-stream velocity and the momentum thickness are the scaling parameters. The roughness density has a strong influence on the momentum loss and the upward flow displacement in the transition region. The shape of the roughness element affects the mean velocity distribution inside the canopy, i.e., jetting effect. The internal boundary-layer thickness was determined based on the turbulent shear-stress distribution. It is found that the flow near the canopy leading edge has two-dimensional wake-like characteristics. The latter are due to the canopy frontal area which is a drastic step obstruction. The existence of an inertial subrange in the fully developed flow region is doubtful although local isotropy occurs for eddies smaller than 2% of the total boundary-layer thickness. The evolution of turbulent energy associated with various size eddies along the canopy can be successfully described by a discretized-energy analysis.			

14. KEY WORDS	LINK A		LINK B		LINK C	
	ROLE	WT	ROLE	WT	ROLE	WT
Atmospheric Modeling Forest Canopies Turbulence Simulation Forest Meteorology Wind Tunnel Fluid Mechanics						

DISTRIBUTION LIST

DEPARTMENT OF DEFENSE

101 Defense Documentation Center  
Attn: DDC-TCA  
Cameron Station (Bldg. 5)  
\*20 Alexandria, Virginia 22314

102 Director of Defense Research & Engineering  
Attn: Technical Library  
Rm 3E-1039, The Pentagon  
1 Washington, D. C. 20301

103 Joint Chiefs of Staff  
Attn: Spec. Asst. Environmental Services  
1 Washington, D. C. 20301

106 Defense Intelligence Agency  
Attn: DIAAP-10A2  
1 Washington, D. C. 20301

108 Director, Defense Atomic Support Agency  
Attn: Technical Library  
1 Washington, D. C. 20305

DEPARTMENT OF THE NAVY

201 Naval Ships Systems Command Attn: Code 20526  
Tech. Lib. Main Navy Bldg. Rm 1528  
1 Washington, D. C. 20325

205 Director  
U. S. Naval Research Laboratory  
Attn: Code 2027  
2 Washington, D. C. 20390

206 Commanding Officer and Director  
U. S. Navy Electronics Laboratory  
Attn: Library  
1 San Diego, California 92152

207 Commander  
U. S. Naval Ordnance Laboratory  
Attn: Technical Library  
1 White Oak,  
Silver Springs, Maryland 20910

208 Officer in Charge  
Navy Weather Research Facility  
Bldg. R-48, Naval Air Station  
1 Norfolk, Virginia 23511

210 Commandant, Marine Corps  
HQ. U. S. Marine Corps  
Attn: Code A04C  
1 Washington, D. C. 20380

211 Commandant, Marine Corps  
HQ. U. S. Marine Corps  
Attn: Code A02F  
1 Washington, D. C. 20380

212 Marine Corps Development and  
Educ. Comd.  
Development Center  
Attn: C-E Division  
1 Quantico, Virginia 22134

213 Commander  
U. S. Naval Weapons Laboratory  
Attn: KXR  
1 Dahlgren, Virginia 22448

214 Commander, Naval Air Systems Command  
Meteorological Division (Air-540)  
1 Washington, D. C. 20360

216 Commander  
Naval Weather Service Command  
Washington Navy Yard (Bldg. 200)  
1 Washington, D. C. 20390

DEPARTMENT OF THE AIR FORCE

302 Air Force Cambridge Research Labs  
Attn: CREU  
L. G. Hanscom Field  
1 Bedford, Massachusetts 01730

303 Air Force Cambridge Research Labs  
Attn: CREW  
L. G. Hanscom Field  
1 Bedford, Massachusetts 01730

304 Air Force Cambridge Rsch. Labs.  
Attn: CRH  
L. G. Hanscom Field  
1 Bedford, Massachusetts 01730

305 Air Force Cambridge Rsch. Labs.  
Attn: CRER  
L. G. Hanscom Field  
1 Bedford, Massachusetts 01730

306 Electronic Systems Div. (ESSIE)  
L. G. Hanscom Field  
1 Bedford, Massachusetts 01730

307 Electronic Systems Division (ESTI)  
L. G. Hanscom Field  
2 Bedford, Massachusetts 01730

310 RFCON Central/AVRS.  
AF Avionics Laboratory  
1 Wright-Patterson AFB, Ohio 45433

311 HQ. Air Weather Service  
Attn: AWWAS/TF (R. G. Stone)  
1 Scott Air Force Base, Illinois 62225

312 U. S. Air Force Security Service  
Attn: TSG  
1 San Antonio, Texas 78241

313 Armament Development & Test Center  
Attn: ADBPS-12  
1 Eglin Air Force Base, Fla. 32542

314 HQ. Air Force Systems Command  
Attn: SCTSE  
1 Andrews AFB, Maryland 20331

319 Air Force Weapons Laboratory  
Attn: WLIL  
1 Kirtland AFB, New Mexico 87117

DEPARTMENT OF THE ARMY

401 OFC of Asst. CH. of Staff for DS-SSS  
Department of the Army  
Rm. 3C466, The Pentagon  
1 Washington, D.C. 20315

\* Increase to 50 copies if releasable to CFSTI.  
See para 6e(1) (b), ECOMR 70-31, for types of  
reports not to be sent to DDC.

Distribution List (Continued)

402	Asst. Ch. of Staff for Force Development CRR Nuclear Operations Directorate Department of the Army 1 Washington, D.C. 20310	437	Commanding General U.S. Army Munitions Command Attn: AMSMU-RE-R 1 Dover, New Jersey 07801
405	Ofc. Asst. Sec. of the Army (R&D) Attn: Asst. for Research Room 3-E-373, The Pentagon 1 Washington, D.C. 20310	438	Commanding General U.S. Army Munitions Command Operations Research Group 1 Edgewood Aresenal, MD 21010
406	Chief of Research and Development Department of the Army 2 Washington, D.C. 20315	439	Commanding General U.S. Army Munitions Command Attn: AMSMU-RE-P 1 Dover, New Jersey 07801
407	Chief of Research and Development Department of the Army Attn: CRD/M 1 Washington, D.C. 20310	442	Commanding Officer Harry Diamond Laboratories Attn: Library 1 Washington, D.C. 20438
409	Commanding General U.S. Army Materiel Command Attn: AMCMA-EE 1 Washington, D.C. 20315	445	Commanding General U.S. Army Natick Laboratories Attn: AMXRF-EG 1 Natick, Mass. 01760
414	Commanding General U.S. Army Materiel Command Attn: AMCRD-TV 1 Washington, D.C. 20315	448	Commanding Officer Picatinny Arsenal Attn: SMUPA-TV1 1 Dover, New Jersey 07801
416	Commanding General U.S. Army Materiel Command Attn: AMCRD-TV 1 Washington, D.C. 20315	449	Commanding Officer Picatinny Arsenal Attn: SMUPA-V46, Bldg. 59 2 Dover, New Jersey 07801
418	Commanding General U.S. Army Missile Command Attn: AMSMI-RRA, Bldg. 5429 1 Redstone Arsenal, Alabama 35809	453	Commanding Officer Fort Detrick Attn: SMUFD-AS-S 1 Frederick, Maryland 21701
421	CT. U.S. Army Missile Command Redstone Scientific Info. Center Attn: Chief, Document Section 3 Redstone Arsenal, Alabama 35809	454	Commanding Officer Fort Detrick Attn: Tech Library SMUFD-AE-T 1 Frederick, Maryland 21701
427	Commanding General U.S. Army Combat Developments CMD Combat Support Group 2 Fort Belvoir, Virginia 22060	459	Commanding Officer Edgewood Arsenal Attn: SMUEA-TSTI-TL 1 Edgewood Arsenal, Maryland 21010
428	Commanding General U.S. Army Combat Developments Command Attn: CDCMR-E 1 Fort Belvoir, Virginia 22060	460	Commanding Officer U.S. Army Nuclear Defense Lab. Attn: Library 2 Edgewood Arsenal, Maryland 21010
430	Commanding Officer USACDC CBR Agency Attn: Mr. N. W. Bush 1 Fort McClellan, Alabama 36201	463	President U.S. Army Artillery Board 1 Fort Sill, Oklahoma 73503
432	Commanding Officer USACDC Artillery Agency 1 Fort Sill, Oklahoma 73503	464	Commanding Officer Aberdeen Proving Ground Attn: Technical Library, Bldg. 313 2 Aberdeen Proving Ground, Md. 21005
435	Commanding General U.S. Army Test & Eval. Command Attn: AMSTE-EL, -FA, -NBC 3 Aberdeen Proving Ground, Md 21005	469	Commanding Officer U.S. Army Ballistics Rsch. Labs. Attn: Tech. Information Division 1 Aberdeen Proving Ground, Md. 21005
436	Commanding General U.S. Army Test & Eval. Command Attn: NBC Directorate 1 Aberdeen Proving Ground, Md 21005	470	Commanding Officer U.S. Army Ballistic Research Labs. Attn: AMXBR-B & AMXBR-1A 2 Aberdeen Proving Ground, Md. 21005

Distribution List (Continued)

<p>472 Commanding Officer U.S. Army Limited Warfare Lab. Attn: CRDLWL-7C 1 Aberdeen Proving Ground, Md. 21005</p> <p>475 Commanding Officer USA Garrison Attn: Technical Reference Division 1 Fort Huachuca, Arizona 85613</p> <p>483 Commander U.S. Army Research Office (Durham) Box CM-Duke Station 1 Durham, North Carolina 27706</p> <p>488 USA Security Agency Combat Dev. Actv. Attn: IACDA-P(T) and IACDA-P(L) Arlington Hall Station, Bldg. 420 2 Arlington, Virginia 22212</p> <p>489 U.S. Army Security Agency Proc. Ctr. Attn: TAVAPC-R&amp;D Vint Hill Frams Station 1 Warrenton, Virginia 22186</p> <p>490 Technical Support Directorate Attn: Technical Library Bldg. 3330 1 Edgewood Arsenal, Maryland 26010</p> <p>491 Commandant U.S. Army Chemical Center &amp; School Micrometeorological Section (Chem. Br.) 1 Fort McClellan, Alabama 36201</p> <p>492 Commandant U.S. Army Air Defense School Attn: C&amp;S Dept. MSL Science Division 1 Fort Bliss, Texas 79916</p> <p>493 Director U.S.A. Engr. Waterways Exper. Station Attn: Research Center Library 2 Vicksburg, Mississippi 39180</p> <p>495 CG, Deseret Test Center Attn: STEDO-TT-ME(S) MET Div. Bldg. 103, Soldiers Circle 1 Fort Douglas, Utah 84113</p> <p>496 Commanding General USA CDC Combat Arms Group 1 Ft. Leavenworth, Kansas 66027</p> <p>497 Commanding Officer USA Aviation Materiel Lab. Attn: Technical Director 1 Fort Eustis, Virginia 23604</p> <p>503 Director U.S. Army Advanced Matl. Conc. Agency Attn: AMXAM 1 Washington, D.C. 20315</p> <p>596 Commanding Officer U.S. Army Combat Dev. Command Communications-Electronics Agency 1 Fort Monmouth, New Jersey 07703</p> <p>597 Commandant U.S. Army Signal School Attn: Meteorological Department 1 Fort Monmouth, New Jersey 07703</p>	<p><u>U.S. ARMY ELECTRONICS COMMAND</u></p> <p>*604 U.S. Army Liaison Office MTT. Bldg. 26, Rm. 131 77 Massachusetts Avenue 1 Cambridge, Mass. 02139</p> <p>605 U.S. Army Liaison Office MTT-Lincoln Laboratory, Rm. A-210 P. O. Box 73 1 Lexington, Mass. 02173</p> <p>606 Headquarters U.S. Army Combat Dev. Command Attn: CDCLN-EL 1 Fort Belvoir, Virginia 22060</p> <p>607 Commanding General U.S. Army Tank-Automotive Command Attn: AMSTA-Z, Mr. R. McGregor 1 Warren, Michigan 48090</p> <p>608 USAECOM Liaison Office, Stanford University Solid State Electronics Lab. McCul. Bldg. 1 Stanford, California 94305</p> <p>613 Chief, Atmos. Sciences Res. Div. ASL, USAECOM, Attn: AMSEL-BL-RD 1 Fort Huachuca, Arizona 85613</p> <p>680 Commanding General U.S. Army Electronics Command Fort Monmouth, N.J. 07703</p> <p>1 AMSEL-EW 1 AMSEL-ME-NMP-PS 2 AMSEL-TD-TI 1 AMSEL-RD-MT 1 AMSEL-XL-D 1 AMSEL-NL-D 1 AMSEL-VL-D</p> <hr/> <p>*Unclassified, unlimited reports only. **Or number specified in contract. Add COTR's mail symbol</p> <hr/> <p>(5) Commanding Officer Atmospheric Sciences Laboratory US Army Electronics Command White Sands Missile Range, N.M. 88002</p> <p><u>OTHER RECIPIENTS</u></p> <p>504 Commanding General U.S. Army Materiel Command Attn: AMCRD-R (H. Cohen) 1 Washington, D.C. 20315</p> <p>702 Institute of Science and Technology The University of Michigan P.O. Box 618, (Iria Library) 1 Ann Arbor, Michigan 48107</p> <p>703 NASA Scientific &amp; Tech. Information Fac. Attn: Acquisitions Branch (S-AK/DL) P.O. Box 33 2 College Park, Maryland 20740</p> <p>707 Target Signature Analysis Cen. Willow Run Labs-Inst. of Sci. &amp; Tech. University of Michigan, P.O. Box 618 1 Ann Arbor, Michigan 48107</p>
--	---

Distribution List (Continued)

- 709 Battelle-Defender Information Center  
Battelle Memorial Institute  
505 King Avenue  
1 Columbus, Ohio 43201
- 714 Infrared Information & Analysis Center  
University of Michigan  
Institute of Science and Technology  
Box 618  
1 Ann Arbor, Michigan 48107
- 721 Vela Seismic Information Center  
University of Michigan  
Box 618  
3 Ann Arbor, Michigan 48107
- 
- Note: Distribute only unclassified reports  
to the following addresses. Consider  
intent of distribution statement.
- 
- 901 Head, Atmospheric Sciences Sect.  
National Science Foundation  
1800 G. Street, N.W.  
1 Washington, D.C. 20550
- 902 Director, Systems R&D Service  
Federal Aviation Administration  
800 Independence Avenue, S.W.  
1 Washington, D.C. 20590
- 903 Atmospheric Sciences Library  
Environmental Science Svcs Admin.  
1 Silver Spring, Maryland 20910
- 904 Division of Meteorology & National  
c/o Air Pollution Control Administration  
3820 Merton Drive  
1 Raleigh, N.C. 27609
- 905 U.S. Department of Agriculture  
Attn: William A. Main  
University of Minnesota  
1 St. Paul, Minnesota 55101
- 907 Chief, Fallout Studies Branch  
Division of Biology and Medicine  
Atomic Energy Commission  
1 Washington, D.C. 20545
- 908 NASA Headquarters  
Meteorology & Sounding Br. (Code SAM)  
Space Applications Programs  
1 Washington, D.C. 20546
- 910 Director  
Atmospheric Physics & Chemistry Lab R31  
ESSA-Department of Commerce  
1 Boulder, Colorado 80302
- 911 National Center for Atmospheric Research  
NCAR Library, Acquisitions-Reports  
1 Boulder, Colorado 80302
- 912 OCE, Bureau of Reclamation  
Attn: D755, Bldg. 67  
1 Denver, Colorado 80225
- 913 National Oceanographic Data Center  
Code 2220  
Building 160, WNY  
1 Washington, D.C. 20390